Cardiff University

Mutual Interactions of basic peptides with nucleic and fatty acids – Amyloid nucleation, Membrane disruption, and hybridisation

Thesis submitted for the degree Doctor of Philosophy

Sebastian Braun
20th February 2013

DECLARATION

This work has not been submitted in substance for any other degree or award at this or any other university or place of learning, nor is being submitted concurrently in candidature for any degree or other award.

Signed ...S. Braun..... (candidate) Date ...20/02/2013....

STATEMENT 1

This thesis is being submitted in partial fulfilment of the requirements for the degree of Doctor of Philosophy (Ph.D.).

Signed ...S. Braun..... (candidate) Date ...20/02/2013...

STATEMENT 2

This thesis is the result of my own independent work/investigation, except where otherwise stated.

Other sources are acknowledged by explicit references. The views expressed are my own.

Signed ...S. Braun..... (candidate) Date ...20/02/2013....

STATEMENT 3

I hereby give consent for my thesis, if accepted, to be available for photocopying and for inter-library loan, and for the title and summary to be made available to outside organisations.

Signed ...S. Braun..... (candidate) Date ...20/02/2013....

Major parts of this work were previously published in a peer-reviewed research article in PLoS ONE and in an addendum in Communicative and Integrative Biology.

- Braun S, Humphreys C, Fraser E, Brancale A, Bochtler M, Dale TC (2011) Amyloid-Associated Nucleic Acid Hybridisation. PLoS ONE 6(5): e19125. doi:10.1371/journal.pone.0019125
- Braun S, Humphreys C, Dale TC (2012) Evolutionary routes from a prebiotic ANA-world. Communicative & Integrative Biology 5: 0-3. doi:10.4161/cib.5.2.18892

CONTENTS

1. ACKNOWLEDGEMENTS

I am grateful for my parents for supporting me throughout my career as student of biochemistry in Leipzig and young scientist in Cardiff and their blissful ignorance for what I am actually working on. I am thankful for my supervisor Trevor Dale who caught my interest in this project during my short Erasmus exchange in Cardiff, organised a PhD position for me and guided and supported me throughout.

This project was originally started by Elizabeth Fraser, who collected some data on gel formation and recorded the electron micrographs of $(KL)_4$. Special thanks go to Christine Humphreys who was my first point of contact during both my Erasmus exchange project and my PhD study, supporting me in my daily work. Her work helped getting the grant for my studies, and she recorded together with me the confocal microscopy images and undertook the first systematic gel strength analysis.

I was introduced to the theoretical and more importantly practical aspects of time-resolved FRET by Amal Kasry, and received a good physical blast on that topic from Paola Borri, whose equipment I used. Richard Perrins wrote a Perl script that greatly helped with the processing of the raw data.

Light microscopy on the complex formation of fatty acid vesicles with amyloidogenic peptides was carried out by Lewis Price during his final year project and supported by Pete Watson whose microscope we were using.

The technical side of electron microscopy was carried out and supported by Ant Hann and Guy Pitt of the Imaging Unit of the School of Biosciences and by Jan Hobot of the Medical Microscopy Unit. Sara Rey helped me generating samples for a 24 h time course

of fibre growth that never made it into this thesis. The confocal images were taken under supervision of Anthony Hayes and Marc Isaacs.

I am grateful to Sarah Meehan from Chris Dobson's group in Cambridge who introduced me to X-ray fibre diffraction, and to Matthias Bochtler and Anja Piasecka who let me use their X-ray generator in Cardiff. Matthias was also a great 'advocatus diaboli' for my first paper.

The CD spectroscopy was done on the instrument of the Rudolf Allemann lab (Cardiff University) with support initially from Veronica Gonzalez and later Joel Loveridge. The same lab also synthesised and donated some peptides.

I was introduced to the Thioflavin T assay and the insulin amyloid control by Beth Bromley from Derek M. Woolfson's lab in Bristol, who also synthesised some peptides for me.

Louise Serpell invited me to Sussex University for some general discussion of the fibre diffraction patterns generated in the course of this work and I received some useful suggestions. With support of Kyle Morris I recorded some CD spectra and fibre diffraction patterns.

I want to thank my friends Sara Rey, Jonny Ryves, Kenneth Ewan, Richard Perrins and Regina Teo for their support, help with experiments, discussion of results and bearing my constant moaning about the suboptimal work and study conditions at Cardiff University. I cannot thank Richard Perrins, Dean Yearsley, Kenneth Ewan and especially Sara Rey enough for their kindness to proof-read this thesis.

This work was funded primarily by Alzheimer's Research UK (previously Alzheimer's Research Trust) and additionally supported by Cancer Research UK and The Leverhulme Trust.

2. ABBREVIATIONS

ANA	Amyloid-Nucleic Acid
a.u.	absorbance unit
Bicine	N,N-Bis(2-hydroxyethyl)glycine
CD	Circular Dichroism
DEP	Diethyl Phosphate
DNA	Deoxyribonucleic Acid
dsDNA	double-stranded DNA
HBS	HEPES-Buffered Saline
HEPES	4-(2-HydroxyEthyl)-1-PiperazineEthaneSulfonic acid
HT DNA	DNA from herring testes
IAPP	Islet Amyloid Polypeptide
FRET	Förster Resonance Energy Transfer
MES	2-(N-Morpholino)EthaneSulfonic acid
NMR	Nuclear Magnetic Resonance
BY RNA	Baker's Yeast RNA
PA RNA	poly(A) RNA
PMCA	Protein Misfolding Cyclic Amplification
PrP	Prion Protein
RMSD	Root Mean-Sqare Distance
RNA	Ribonucleic Acid
SH3	SRC Homology 3 [Domain]
ssDNA	single-stranded DNA
ST DNA	DNA from salmon testes
TEM	Transmission Electron Microscopy

ThT	Thioflavin T
TR-FRET	Time-Resolved Förster Resonance Energy Transfer

3. SUMMARY

Anions including nucleic acids and lipids have been found to promote amyloid formation in diseases including neurodegenerative conditions such as Alzheimer's and Creutzfeldt-Jakob disease. However, the direct effects of these close charge-based interactions are not well understood. It is unclear what effect amyloidogenic peptides would have on nucleic acid integrity. Similarly, the direct effects of amyloidogenic polypeptides on liposomes are not well understood. Here I have used a simplified system of short basic peptides with alternating hydrophobic and hydrophilic amino acid residues to study their interactions with polyanionic nucleic acids and fatty acid liposomes. Employing biophysical techniques including X-ray fibre diffraction, circular dichroism spectroscopy and electron microscopy I showed that the polymerized charges of nucleic acids and pseudo-polymerised charges of lipid membranes concentrated and enhanced the formation of amyloid from short basic peptides, many of which would not otherwise form fibres under the conditions explored. In turn, the same peptides bound nucleic acids and promoted their hybridisation at concentrations below their solution K_d, as shown by time-resolved FRET studies. The mutual interactions between peptides and nucleic acids lead to the formation of amyloid nucleic acid (ANA) fibres, which in addition to their importance in disease might have a potential in nano-engineering of biomaterials.

4. INTRODUCTION

4.1. Amyloid in Disease and Function

More than 30 polypeptides have been shown to form disease-relevant amyloid fibrils as an alternative ordered conformation to their native fold and are thought to propagate *in vivo* by templating the misfolding of their own monomeric precursors [1-3]. One of the best-studied examples is Alzheimer's disease, where Aβ peptides are found in extracellular plaques, while the usually tubulin-associated, hyperphosphorylated tau creates intracellular tangles [4,5]. Parkinson's disease has been proposed to be associated with deposition of α-synuclein in Lewy bodies [5,6]. The aggregation of huntingtin protein correlated with an extended polyglutamine-tract has been shown to give rise to Huntington's disease [7-9]. For prion diseases like scrapie in sheep, bovine spongiform encephalopathy in cattle and Creutzfeldt-Jakob disease in humans the protein-only hypothesis postulates that the infectious agent consisted only of misfolded protein, which was thought to be found in the amyloid form of prion protein (PrP) [10-15]. However, more recent studies have shown that the infectious particle might not be an amyloid fibril, but a complex of the protein with other cofactors [16-19]. Dialysis-related amyloidosis leads to the accumulation of β_2-microglobulin in the blood and proteinaceous deposits develop particularly in the joints [20]. Some forms of type II diabetes have been found to be associated by amylin/ islet amyloid polypeptide aggregation in the pancreas [21,22]. Also associated with diabetes, but not related to the cause of the disease, is the formation of insulin amyloid aggregates at injection sites [23].

The amyloid fold is not only associated with deleterious effects. Tightly controlled transition of proteins into an amyloid conformation has been found found to be

employed by many host organisms in positive roles [1,24-26]. The yeast prion Ure2p was involved in regulation of nitrogen catabolism in *Saccharomyces cerevisiae* and formed cytoplasmic amyloid via its C-terminal prion domain. As a result, its regulatory N-terminal domain becomes sterically inaccessible for the binding of the transcription factors Gln3p and Gat1, which then translocated into the nucleus, giving rise to the [URE3] prion state [26-29]. Another prion state in *S. cerevisiae*, [PSI^{+}], is based on the unavailability of the translation termination factor Sup35 either by complete inactivation or at least sterical hindrance due to its amyloid fibre formation, leading to nonsense suppression [26,28-31]. The conversion into and maintenance of the prion state is regulated by the chaperone proteins Hsp104, Hsp70 and Hsp40, which can both inhibit and promote prion nucleation and seeding from mature fibres by interacting with oligomers and prion amyloid fibres [30] (also see below in chapter 4.2). In *Podospera anserina*, heterocaryon compatibility was found to be influenced by the HET-s protein and its associated [Het-s] prion state that consisted of amyloid aggregates [28,32,33]. The combination of the generic amyloid structure formed by a prion domain in combination with a regulatory domain (usually transcription factors and RNA-processing factors) appears to be a wide-spread mechanism for phenotypic inheritance in wild yeast, often generating beneficial traits under selective conditions [25]. Fibres of mammalian Pmel17 are utilised for binding and orientation of toxic reactants during melanin synthesis [34]. Some peptide hormones of the human endocrine system were shown to be stored as amyloid aggregates [35,36] (see also below in chapter 4.4). *E. coli* curli fibres [37] and *C. albicans* als fibres [38], used for biofilm formation, have been shown to be amyloid fibrils, and *Streptomyces coelicolor* requires chaplin amyloid fibres for its aerial hyphae and spores [39] (also see below in chapter 4.4). The adhesive

cement of the barnacle *Balanus amphitrite* contains amyloid material mixed with globular proteins [40].

Even proteins that have not been found to be associated with pathological conditions or functional amyloid might be induced to change to the amyloid conformation. The all-α-helical apomyoglobin can be converted to amyloid, whereupon it switches to an all-β-sheet conformation [41-43], similar to apocytochrome [44]. The SH3 domain of phosphatidyl-inositol-3'-kinase readily forms well-defined fibres *in vitro* [45], as does the hydrogenase maturation factor HypF [46]. These examples show that proteins can adopt conformations that are not encoded in their primary sequence, maybe in contradiction of the Anfinsen hypothesis [47].

Fragments and small peptide derivatives of larger polypeptides and proteins have been regularly identified and studied as drivers of amyloid aggregation *in vitro*. These include peptides with diverse sequences derived from IAPP [48], Aβ [49-52], β_2-microglobulin [53], prolactin [36], PrP [52,54], insulin [52], Sup35 [52,55], tau [52,56], and others [2,57]. Differential phosphorylation of a tau-derived peptides showed that not only the number, but also the position of charges determines the likelihood of its amyloid formation due to charge interactions within and between the amyloid β-sheets [56]. X-ray microcrystallography studies has revealed generic steric zippers in microcrystals of peptides derived from amyloidogenic proteins like Sup35, Aβ, and insulin and might provide insight into the fine structure of amyloid fibrils [23,24,52,55,58]. Detailed biophysical studies have frequently been conducted on amyloidogenic peptides derived from their parent proteins, in a range of lengths from 5mers to 30mers [2]. For example, Aβ fibril structures were frequently studied using hexamers [59], and the cytotoxity of

IAPP was examined using pentamers [48]. The core sequence of the amyloid tau paired helical filaments was identified by using 3mer to 6mer sequences [60]. The amyloidogenic core of β_2-microglobulin has been described as 21mer [53], and the one of α-synuclein was identified as 8mer to 10mer [61,62]. The shortest reported amyloidogenic sequence is a phenylalanine dipeptide that seemed to form amyloid-like hollow nanotubes [63]. This shows that amyloidogenic proteins were associated with both beneficial and deleterious effects *in vivo* and that such proteins could be used to generate and examine amyloid aggregates *in vitro* [2,24,64,65].

4.2. Common Properties of Amyloid Aggregates

Despite the fact that that they are based on varying polypeptides with different properties and origins all amyloid aggregates are thought to share common features. Originally amyloid deposits in the brain were identified as starch-like by Virchow, who saw that certain areas in the brain stained with iodine, and he gave these deposits their name (amylum (Latin) = starch) [66,67]. Later the proteinaceous nature of these amyloid deposits became evident. The dyes Congo Red [68] and Thioflavin T [69] allow the identification of amyloid deposits in tissue sections and *in vitro*. Congo Red was found to exhibit birefringence and red-shift [68,70-73] upon binding of amyloid aggregates, while Thioflavin T emits a characteristic fluorescence [69,72,74,75]. Both dyes were used extensively to identify and characterise these proteinaceous deposits. Electron microscopy revealed their fibrous nature as another central characteristic of all amyloid aggregates [76]. Resistance to proteolysis is another macroscopic hallmark of the conversion of native proteins to amyloid conformation [3,77]. Relatively early the characteristic diffraction pattern of amyloid fibres, a cross-β pattern, was discovered [78], but detailed underlying structures have only been elucidated relatively recently

[23,52,59,79]. Based on some of these properties, amyloid aggregates are strictly defined as "extracellular deposits of protein fibrils with a characteristic appearance in the electron microscope, a typical X-ray diffraction pattern and affinity for Congo Red with concomitant green birefringence" [2,80] (see also chapter 4.3).

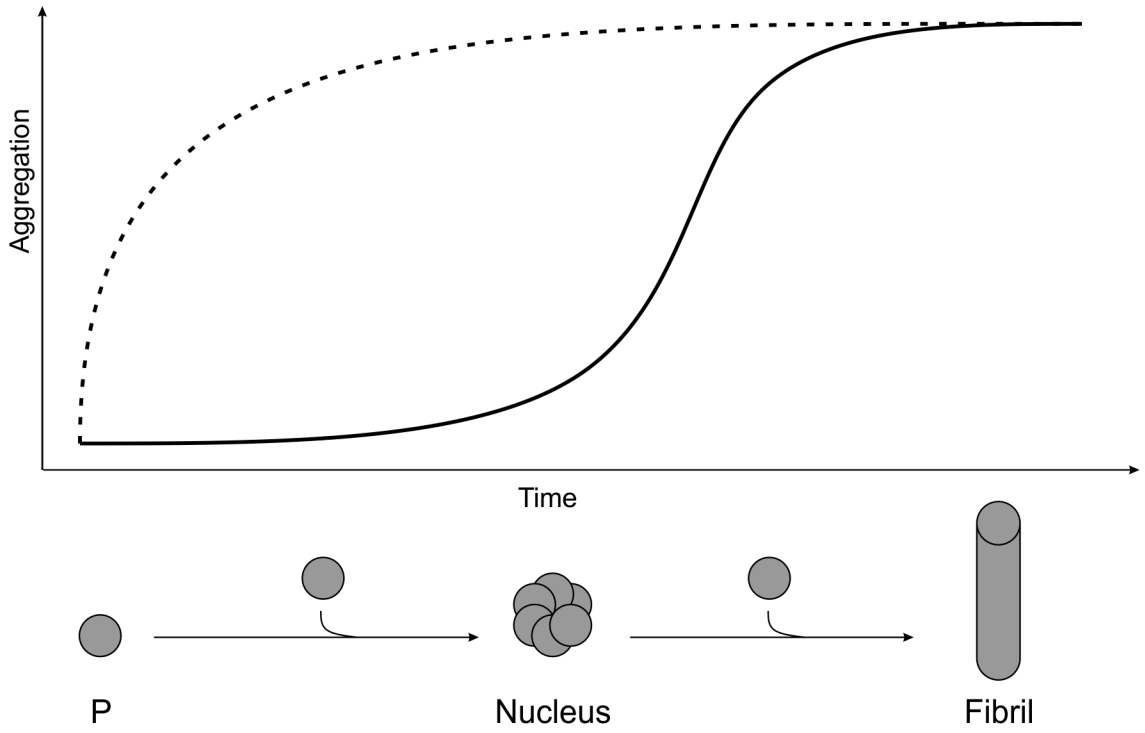

Figure 4-1: Nucleation polymerisation model of aggregation. The aggregation of a protein (P) into amyloid fibrils typically begins with a lag phase in which no aggregation is observed. During this time, the entropically unfavourable process of initial association occurs. Once the aggregation process begins and a critical nucleus is formed, the aggregation proceeds rapidly into amyloid fibrils (solid line). The lag phase, however, can be overcome (dotted line) by the addition of a pre-formed nucleus (i.e., an aliquot of solution containing pre-formed fibrils). Adapted from Nilsson (2004) and Jarret & Lansbury (1993) [72,81].

Amyloid formation kinetics are usually described as following a nucleated growth mechanism with a lag phase with slow rate-limiting nucleus formation, and an elongation phase with rapid fibril extension [1,81,82] (see Figure 4-1). A key characteristic of this nucleation-dependent phase was that it can be overcome by seeding (see Figure 4-1) [81,83-86]. The amyloid assembly kinetics can be studied by a wide range of techniques including dye-binding, CD and FTIR spectroscopy, light scattering, electron and atomic force microscopy, NMR, and X-ray fibre diffraction. For example, β-lactoglobulin aggregation was examined by Thioflavin T fluorescence and AFM [87], and amyloid fibre formation by a murine FBP28 WW domain was followed by light scattering, electron microscopy and X-ray fibre diffraction [88]. Light microscopy, AFM, Thioflavin T binding, and light scattering were used to distinguish insulin amyloid fibre formation from amorphous aggregation during the lag phase [89]. By contrast, some studies suggested that nucleation might be driven by amyloid-independent interactions, for example in the case of glutamine-rich peptides derived from huntingtin that were shown by mathematical fitting to require only a single monomer or less as a nucleus [82,90]. This is consistent with studies by Knowles *et al.* who fitted master equations to self-collected or previously reported data to determine secondary nucleation as a rate-limiting factor during the lag phase of amyloid aggregation [87,88,91]. These studies suggested that primary nucleation from monomers might not be the main rate-determining factor of the lag phase, but that instead fragmentation of mature fibres and the resulting secondary nucleation was the major factor, i.e. seeding after the initial primary nucleation. It appeared that the lag time was inversely correlated with the maximum growth rate of the amyloid fibres, i.e. faster growing fibres reached quicker a critical length at which breakage and seed formation would occur [91].

Partial unfolding has been found to be necessary for most polypeptides to adopt the β-sheet-rich amyloid conformation, often supported by amino acid mutations or changes in the environment like pH and temperature variation leading to protein denaturation [2,43,92,93]. For example, myoglobin assembled into fibrils via unordered segments of its native structure, but did not fully convert to a monomeric all-β-sheet conformation [43]. The conformational conversion to β-sheet-rich polypeptides could occur after initial native-like aggregates were formed like in the case of insulin [94], and could be accompanied or followed by the appearance of protofibrils, spherical aggregates consisting of about 20 monomers with 2 to 5 nm diameter detectable by TEM or AFM [1,94-99]. Atomic force microscopy revealed the hierarchical build-up of amyloid fibrils from β_2-microglobulin, going from native polypeptides to a partially unfolded state to protofilaments that mature into amyloid fibres (see Figure 4-2) [100]. α-synuclein has been suggested to be a natively unfolded protein which forms amyloid fibrils *in vitro*, a process that was enhanced by mutations linked to early-onset-Parkinson's disease [101,102]. However, Bartels *et al.* suggested that aggregation of α-synuclein as measured by *in vitro* biochemical assays was a poor measure of physiological aggregation since the protein may be expressed as native tetramer and might require chaperone-mediated folding *in vivo* [40].

The slow initial nucleation is usually described as being followed by rapid amyloid fibre elongation by addition of monomeric polypeptides to the ends [82,91]. The peptides are assumed to dock to a fibre end and change their conformation according to a template consisting of peptides already locked in the fibre [103,104]. This mechanism is supported by increased amyloid fibre formation rates when fibrils are sheared and more free ends are provided (seeding and secondary nucleation) [86,87,91]. In *S. cerevisiae*,

the dependence of Sup35 on primary and secondary nucleation for amyloid fibre formation is used to control and maintain the [*PSI*+] prion state [30,105]. The chaperone Hsp104 promotes the formation of Sup35 oligomers for nucleation and also fragmented mature and nascent Sup35 amyloid fibrils to provide nucleation seeds, resulting in a reduction or elimination of lag phase [29,56,106]. This activity is dose-dependent on the enzyme. The effects have been described as occurring at intermediate Hsp104 concentrations, while at low concentrations the lack of nucleation promotion by fibre fragmentation or formation of oligomeric Sup35 species delays amyloid fibril formation (lag phase). At high Hsp104 concentrations amyloid Sup35 fibres are broken down so that the [PSI+] state could not be maintained [30,56,106].

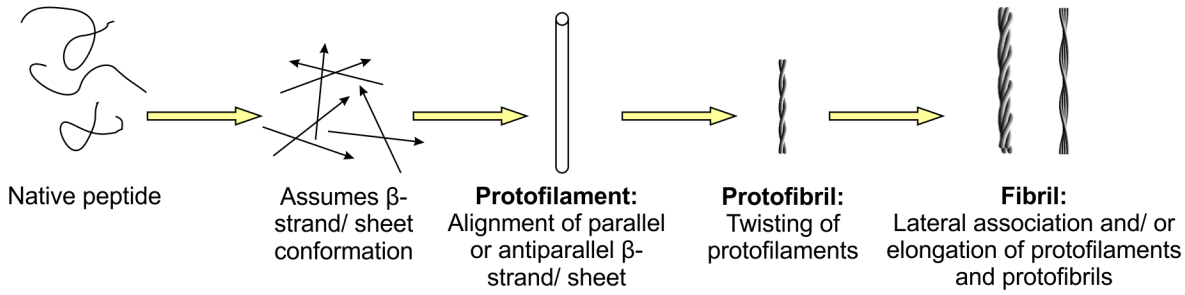

Figure 4-2: Hierarchy of amyloid formation. Native protein or peptide unfolds and acquires β-strand secondary structure. These β-strands align (both parallel and anti-parallel arrangement have been observed [24]) to form sheets and protofibrils with the direction of the β-strand perpendicular to the fibril axis (cross-β structure). For more details on the amyloid structure see Figure 4-1. Adapted from Kad *et al*. (2003) and Harrison *et al*. (2007) [2,100].

In disease, the focus is on identifying the toxic species. A number of studies suggested that protofibrils and early oligomers and not mature amyloid fibres are the toxic species [107-112]. Several mechanisms have been suggested to drive the formation of toxic aggregates. Interactions with membranes appeared to be a dominant theme: Interactions of Aβ oligomers with cellular membranes during amyloid fibril assembly were seen as cause for membrane disruption and cytotoxicity [107,113,114], and recently Aβ dimers were found to interfere with synaptic function in the brain and to induce dendritic spine loss in the hippocampus of rodents, while larger aggregates with mature fibres did not have these effects [110,115]. The Aβ sequence contains parts of the extracellular and transmembrane domains of its precursor, which have been thought to allow it to specifically interact with ganglioside lipids , enhancing aggregation on membranes and thereby disrupting them [116-120]. Contact of human IAPP aggregates with pancreatic islet cells triggered apoptosis [121,122]. Aβ and IAPP were suggested to introduce defects into membranes, as detected by AFM studies of peptide-membrane complexes [123]. Intracellularly, integration of tau into paired helical filaments impaired its ability to bind and regulate microtubule assembly, which consequently affected intracellular transport in neurons [5]. α-synuclein was found to interact with membranes more strongly when complexed in protofibrils in contrast to monomers and mature fibrils [107], and the protofibrils were also shown to permeabilise synthetic vesicles [107,124,125]. Prion diseases were correlated with endoplasmic reticulum stress and dysfunction of the proteasome, perhaps interfering with these important quality control systems of protein biosynthesis [126]. In Huntington's disease interactions of pre-aggregated huntingtin with key transcription factors like the TATA-box binding protein has been suggested as mechanism for toxicity [2]. Interestingly, *in vitro* studies showed that amyloid aggregates of proteins that were not associated with

disease, like the hydrogenase maturation factor N-terminal domain (HypF), interacted with membranes and increased Ca^{2+} permeability, perhaps suggesting that interference with membrane function was a relatively sequence-independent and common mechanism for cytotoxity following protein aggregation [46,127-129].

4.3. Amyloid Structure in Detail

High-resolution electron microscopy has revealed that amyloid fibres comprise several protofilaments winding around each other [43,45]. Considerable polymorphism regarding the number and the mode of coiling of the protofilaments even within samples of the same polypeptide may arise from different lateral association modes that originated from conformational differences of the fibres such that distinct conformations would expose different functional groups at the fibre surface [130]. Polymorphisms like this have been thought to be the basis for different prion strains in yeast [1,131,132], as well as responsible for strains of the prion protein pathologies [24,133].

Figure 4-3: Underlying Structure of Amyloid Fibrils. (**A**) Amyloid fibrils are composed of long filaments that are visible in negatively stained transmission electron micrographs. (**B**) The schematic diagram of the cross-β sheets in a fibril, with the backbone hydrogen bonds represented by dashed lines, indicates the repetitive spacings that give rise to (**C**) the typical fibre diffraction pattern with a meridional reflection at ~4.7 Å (black dashed box) and an equatorial reflection at ~6-11 Å (white dashed box). Adapted from Greenwald, Riek (2010) [24].

All amyloid fibres exhibit a common cross-β pattern (see Figure 4-3) in fibre diffraction experiments, which arises from peptide β-strands lying perpendicular to the amyloid fibre axis in a β-sheet sandwich [52,79,134]. The aforementioned X-ray microcrystallography studies (see chapter 4.1) on a range of short peptides derived from amyloidogenic regions of larger polypeptides such as Sup35, Aβ, tau, and insulin revealed that the interface between the β-sheets might consist of a water-free steric

zipper of hydrophobic amino acid residues, while more hydrophilic residues would be presented on the water interface of the β-sheet sandwich (see Figure 4-4) [23,52,55,58,135]. A similar study based on fibre-forming segments of Aβ revealed a variety of steric zipper conformations even for the same peptide sequence, which could, if such structures occurred in amyloid fibres, give rise to amyloid fibre polymorphisms [59]. Steric zippers as shown by microcrystallography might also be a generic feature of amyloid, agreeing with the finding that sequences with a simple alternating pattern of hydrophobic and hydrophilic residues are suppressed due to their high propensity to form such steric zippers [136-138]. The cross-β structure was not seen as sequence-specific and might be primarily mediated by main chain interactions leading to the formation of hydrogen-bonded β-sheets [138]. A good example for this is the amyloid formation by amino acid homopolymers like poly-L-lysine and poly-L-glutamate, which were found to aggregate, similar to poly-L-threonine, when their side chain charges were neutralised at pH 11 and pH 4, respectively. The absence of any protein-like amino acid sequences pointed towards a generic potential for all (poly-)peptide sequences to form amyloid via backbone interactions [139]. Fändrich and Dobson suggested that the probability of this intermolecular interaction leading to amyloid fibre formation would be strongly regulated by amino acid side chain identity and the environment [139]; in this case the primary polypeptide sequence would not determine the 3-dimensional protein fold as proposed by Anfinsen [47]. Indeed, interactions of the polypeptide backbone might generally be a more important driver of protein folding than side chain interactions [140].

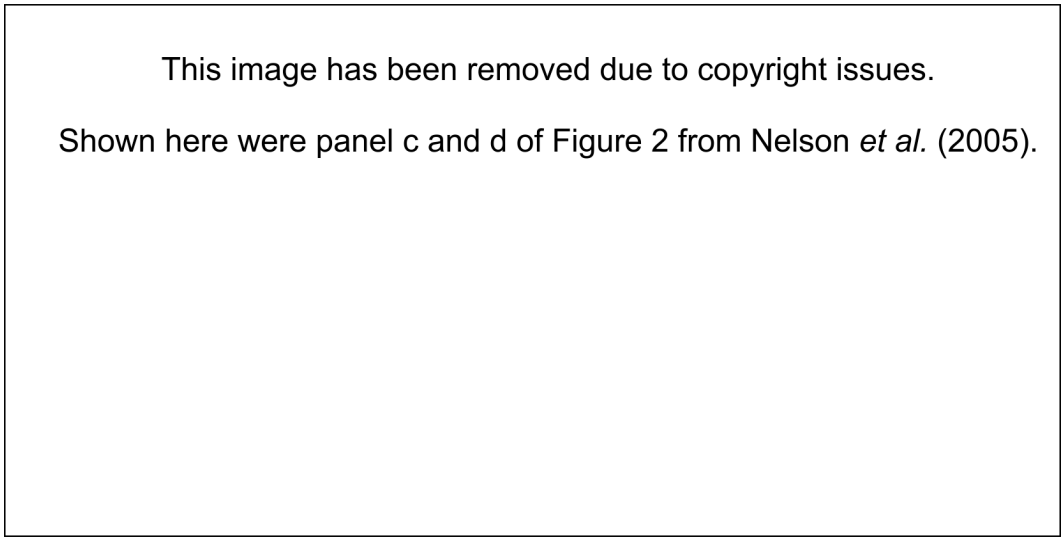

Figure 4-4: The steric zipper of GNNQQNY from Sup35. (**A**) The GNNQQNY crystal viewed down the sheets (along the b axis parallel to the 2_1 screw axis of the crystal). Six rows of β-sheets run horizontally. Peptide molecules are shown in black and water molecules are red plus signs. The atoms in the lower left unit cell are shown as spheres representing van der Waals radii. The water-free dry interface is shown with a grey background, the wet interface with a red background in the bottom right corner. (**B**) The steric zipper. This is a close-up view of a pair of GNNQQNY molecules from the same view as panel A, showing the remarkable shape complementarity of the asparagine and glutamine side chains protruding into the dry interface. $2F_0 - 2F_c$ electron density is shown, and the position of the central screw axis is indicated. Adapted from Nelson *et al.* (2005) [55].

These generic properties have been exploited to design *de novo* amyloidogenic peptides and proteins which provided insight into the amyloid formation process [138,141-143]. A library of small proteins based on heptamer peptides with alternating hydrophobic and hydrophilic amino acid residues linked by tetramer turn or linker sequences has

been created, and these artificial small proteins readily formed amyloid [138,144]. This behaviour could be broken by introduction of lysine residues on edge strands of the β-sandwich-like polypeptides so that charge repulsion prevented fibre formation, a strategy common in natural proteins to avoid edge-to-edge aggregation of β-sheets (see Figure 4-5) [136,138,145]. In contrast, charge interactions could also have a positive ordering effect during amyloid fibre formation: In a *de novo* peptide study based on STVIIE sequence and modification variants (N-terminal acetylation and/ or C-terminal amidation) the examined 6mer peptides required a +1 or -1 net charge for amyloid fibril formation, but formed amorphous aggregates at 0 net charge [142,143].

This image has been removed due to copyright issues.

Shown here were panel A to D of Figure 1 from Wang and Hecht (2002).

Figure 4-5: Conversion of a β-sheet protein from an amyloid fibre into globular units. β-strands are shown in green, and turns in silver. Polar side chains are shown in red and nonpolar side chains in yellow. (**A**) Schematic representation of a fibril formed by open-ended oligomerisation of a twelve-stranded β-sheet protein, burying hydrophobic residues in the steric zipper of a β-sheet sandwich. (**B**) Monomeric twelve-stranded β-sandwich (rotated 90° relative to A). It consists of 12 heptamer β-sheet strands (green backbone) linked by 5 tetramer linkers (grey backbone). In the monomer, the hydrophobic side chains of the edge stands are exposed to solvent. (**C**) Monomeric twelve-stranded β-sandwich in which two hydrophobic residues are substituted with lysine side chains (blue). In the monomeric structure, the charged ends of the lysine side chains on the edge strands are exposed to solvent, but would lead to unfavourable charge interactions within the β-sandwich and thereby maintain the protein as monomer. (**D**) Same as C, rotated by 90°. Adapted from Wang, Hecht (2002) [138]

The common core structure and the potential ability of all (poly-)peptides to form amyloid fibres make a wider definition of amyloid aggregates necessary to include the multitude of *in vitro* designed and generated peptides and proteins that could adopt this conformation: Amyloid structure comprises an "unbranched protein fibre whose repeating substructures consist of β-strands that run perpendicular to the fibre axis, forming a cross-β sheet of indefinite length" (see Figure 4-3) [24].

The generic nature of the amyloid conformation has been suggested to be an important factor before and during the evolution of cellular life. The thermodynamic stability under harsh conditions, especially extreme temperatures, made amyloid fibres a very likely conformation for peptides under prebiotic conditions. The self-propagating fibre elongation and inheritance of strain properties could form the basis for an 'amyloid-world' [146-148] that preceded the 'RNA-world' which is based on the sequence-dependent catalytic activities of 3-dimensionally folded RNA molecules [149,150]. The 'amyloid-nucleic acid-world' combines both amyloid fibre elongation and nucleic acid catalytic activity [151-153].

4.4. Factors Mediating and Controlling Amyloid Formation

The formation of functional amyloid was shown to be tightly controlled. This was especially important for protein fibres that were destined to form under a wide variety of environmental conditions like *E. coli* curli fibrils whose CsgA monomers were shown to be nucleated by another protein, CsgB, on the membrane surface [37,154]. Potentially toxic intermediate species during amyloid formation are avoided during Pmel17 fibre assembly by membrane sequestration, proteolytic processing and a sequence optimised

for very fast amyloid fibrillisation [34]. *Streptomyces coelicolor* chaplin fibres have been shown to require several proteins to form amyloid fibrils and also seemed to be selected for rapid amyloid formation in order to avoid toxic intermediates [39,155]. The use of the amyloid structure for storage of pituitary hormones like ACTH, oxytocin, etc. implied that this type of aggregation could under certain circumstances be reversible to release active monomers [35]; for example, ACTH coaggregated with β-endorphin in amyloid complexes within secretory granules of cells in the pituitary gland. Monomers of both peptides could be released upon dilution of the contents of the granules, which would occur *in vivo* when the granules fused with the cellular membrane for hormone release. The concentration of both peptides within the granules appeared to be the most important driving factor for amyloid aggregate formation, while the pH difference between granule (pH 6) and blood stream (pH 7.4) seemed to play only a minor role [35]. There is a kinetic and thermodynamic competition between the native folding pathway and the formation of amyloid [1]. In a limited number of cases inclusion bodies of mammalian proteins expressed in bacteria were found to contain amyloid aggregates, which have been suggested to be thermodynamic and kinetic traps for the unfolded proteins in the absence of chaperones [156]. Like peptide hormones, the release of Aβ monomers from amyloid fibrils could be initiated by dilution [35,157]. Aβ slowly dissociated from its fibre, indicating a readily reversible equilibrium, although the dissociation rate was much smaller than the association rate [157]. Monomers might be recycled between amyloid fibres as shown for the SH3 domain of bovine phosphatidylinositol-3'-kinase, suggesting constant assembly and disassembly of amyloid complexes with competition of the protofibrils for their building blocks (see Figure 4-6) [158].

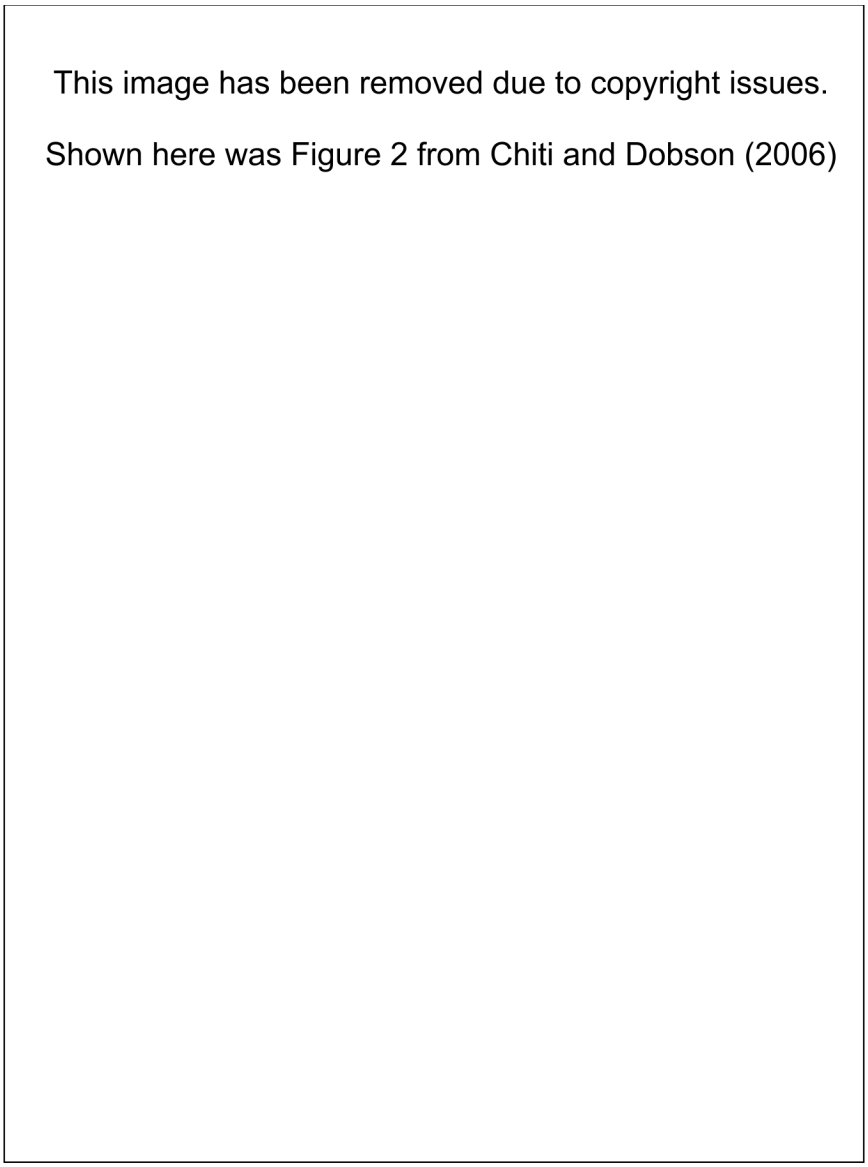

Figure 4-6: Schematic representation of the many conformational states that can be adopted by polypeptide chains and of the means by which they can be interconverted. The transition from β-structured aggregates to amyloid fibrils can occur by addition of either monomers or protofibrils (depending on protein) to preformed β-aggregates. All of these different conformational states and their interconversions are carefully regulated in the biological environment, much as enzymes regulate all the chemistry in cells, by using

machinery such as molecular chaperones, degradatory systems, and quality control processes. Adapted from Chiti, Dobson (2006) [1].

In contrast, pathological amyloid deposits were not regulated by their host and could involve interaction with partners such as glycosaminoglycans, collagen and nucleic acids [20,22,159-163]. Polyionic interactions of Heparan sulphate and heparin were shown to promote the fibrillisation of Aβ [164,165], tau [4,166], α-synuclein [167], and β_2-microglobulin [168]. DNA promoted amyloid fibre formation by murine PrP and α-synuclein [6,169,170]. RNA could also promote the formation of intracellular paired helical filaments from tau [171]. Recent studies have shown a critical role for polynucleotides and lipids in the conversion of bacterially-expressed hamster PrP into infectious prion particles *in vitro* during protein misfolding cyclic amplification (PMCA) (see Figure 4-7) [172-175]. Although the structure of these prion particles has not yet been determined, they might contain amyloid similarly to mouse PrP-DNA complexes [162,169]. This finding conflicts with the 'protein only' hypothesis of prion diseases [12,13], which is supported by the ability of PrP amyloid fibrils to induce scrapie in hamsters and mice, albeit with low infectivity [14,15]. However, the exact nature of the infectious agent may be difficult to establish in many assays since *in vitro* protein-only aggregates may associate with host-derived nucleic acid and lipid components following inoculation [14,19,176,177]. The nucleic acids and lipids required for high infectivity might either alter PrP aggregates into infectious conformations and/ or may indirectly regulate access to sites where toxic responses are observed (see Figure 4-7) [16,18,175,177]. Interestingly, there was some selectivity of PrP during PMCA for certain types of RNA composition [18]. Only polypyrimidines like $(dT)_{100}$ and $(dC)_{100}$

facilitated prion propagation and bound PrP aggregates, while same length 100mer polypurines $(dA)_{100}$ and $(dG)_{100}$ had no effect. $(dT)_{100}$ closely associated with PrP aggregates and was protected from nuclease digestion, while poly(dA)100 hardly attached to the aggregates. Also, a minimum length of about 40 bases of homo-poly(dT) was found to be required [18]. Interestingly, sequence-preference in PMCA-driven infectivity also extended to differences between cellular RNA extracted from mouse and rat brain (more efficacious) and non-mammalian RNA (*E. coli, S. cerevisiae, C. elegans, D. melanogaster*) which was less efficacious [176]. Whether this was due to an underlying species-specific base composition was not explored. The polymerized charges of nucleic acids, heparin, heparan sulphate and even nucleotides (with increasing effect from AMP over ADP to ATP [163]) associated with basic residues on polypeptides like acylphosphatase and lysozyme to concentrate and enhance their rate of amyloid formation [163]. In addition to charge-compensation by polyelectrolytes the concentration of amyloidogenic peptides could be increased locally by crowding and surface attachment, thereby enhancing the rate of nucleation and amyloid fibre extension [20,178-180]. Another *in vitro* approach to accelerate amyloid aggregation was to covalently link amyloidogenic peptide sequences, either via graft copolymers [181] or short peptide linkers [138,144].

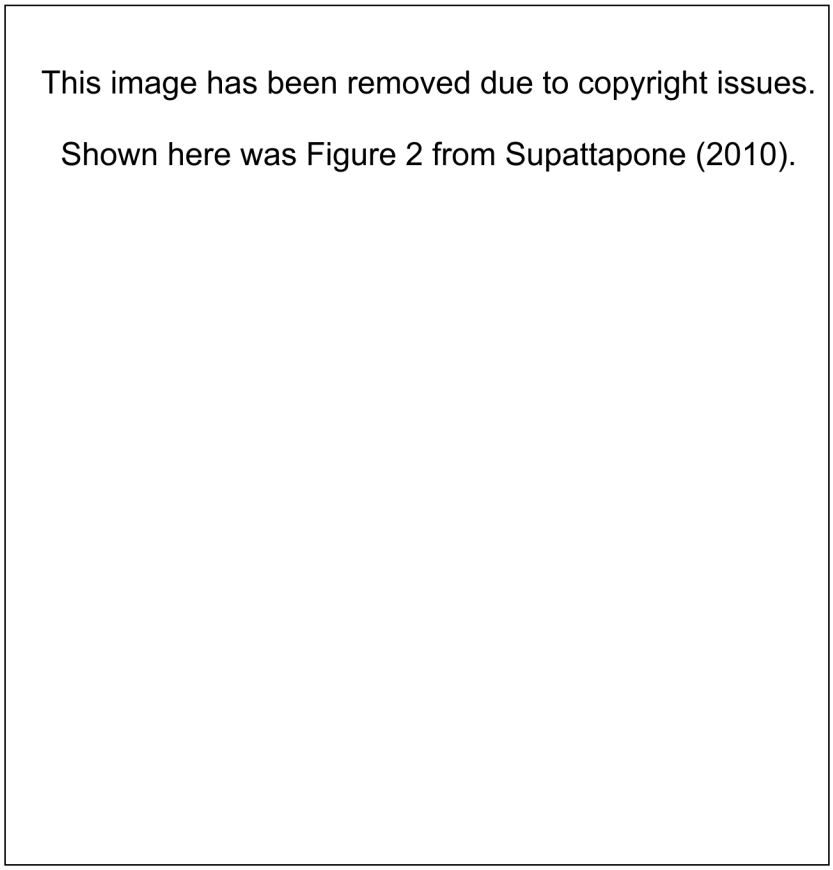

Figure 4-7: Nucleic acids and lipids increase infectivity of recombinant prion protein. Two different biochemical protocols yield recombinant PrP with different infectivity. (**Left**) Minimally infectious amyloid fibrils are formed by incubating recombinant PrP with chemical denaturants. (**Right**) Mixing recombinant PrP with phospholipid and RNA produces highly infectious prions of yet undetermined structure. Adapted from Supattapone (2010) [16].

Similar to linear polyanions, the complex interactions of lipids with amyloidogenic polypeptides are not well understood. Anionic lipids have been found to be essential for the conversion of bacterially expressed PrP into infectious prion particles where they acted in combination with nucleic acids (see Figure 4-7) [22,112,174,175,177]. The interaction of the N-terminal domain of apolipoprotein A with zwitterionic

dihexanoylphosphatidylcholine prevented the conformational switch to amyloid fibrils [64]. The interactions of Aβ with membranes were found to be complex: While membrane anchoring could prevent fibril formation, release of the peptide has been suggested to lead to aggregation that has been postulated to be supported by the membrane as a two-dimensional aggregation template, eventually leading to membrane disruption [112,114]. Also, interactions of amyloidogenic protein oligomers and protofibrils with membranes have been recognised as a possible cause for amyloid cytotoxicity as mentioned above [108-112,116-120,122,124,125,128,129,182].

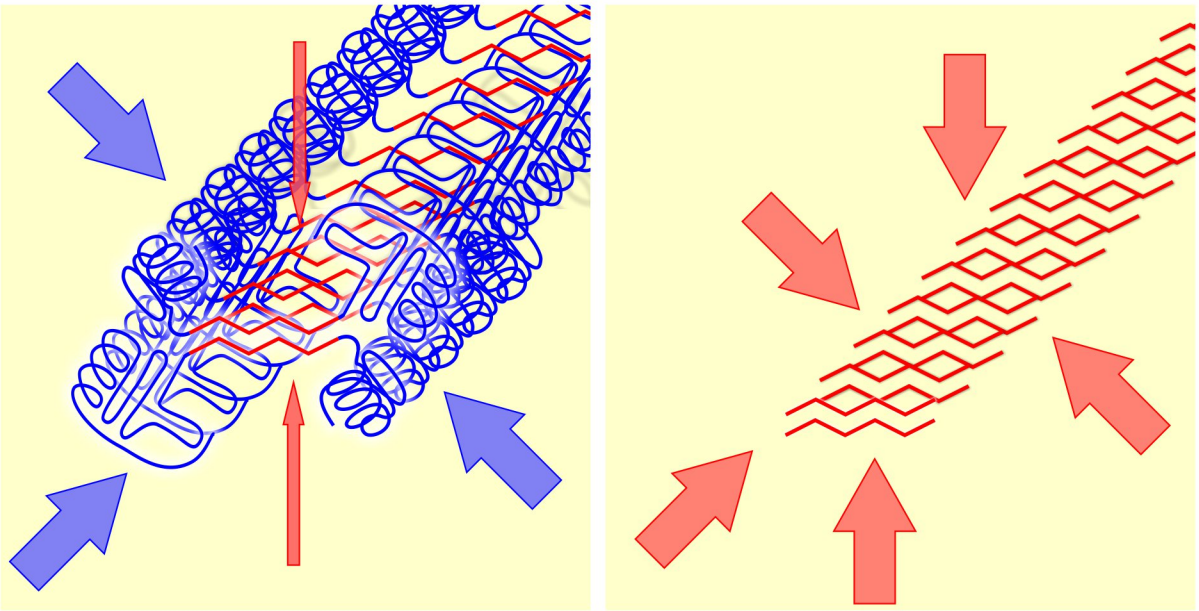

Figure 4-8: Interaction with decorating sequences or amyloid core. (**A**) Large binding partners like nucleic acids or membrane surfaces to an amyloid fibre from large polypeptides or proteins are more likely to interact with decorating (native-like) peptide structures (blue) because the amyloid core (red) is less accessible. (**B**) Fibres formed from short peptides consisting of only the amyloid core can interact directly with binding partners. Interactions with the amyloid core are shown by red arrows, with the decorating sequences indicated with blue arrows. Illustration is not to scale.

Generally, the interactions of polyanions with amyloidogenic polypeptides have been shown to be highly complex. Amyloid fibres from long peptide chains comprise discrete sequences forming the cross-β spine and unincorporated sequences that decorate the core (see Figure 4-8) [183,184]. More generally, it is not known whether polyanion promotion of amyloid aggregate formation is based on direct interactions with the core cross-β spine or indirectly via the decorating sequences.

Due to the significance of amyloid fibrils in disease and pathology research is concentrating on finding therapeutics that can modulate their formation. Various small molecules have been tested for their ability to inhibit amyloid aggregate formation. Among them is the dye Congo Red which is usually used to detect amyloid aggregates [185]. It is able to reduce Aβ toxicity, potentially by blocking interactions between cytotoxic oligomers and membranes, but its exact mechanism of actions remains unclear [186]. Antibodies raised against Aβ amyloid complexes can initiate the clearance of Aβ aggregates from the central nervous system of transgenic mouse models by stimulating the host immunoresponse and could be used as diagnostic markers for pre-symptomatic Aβ aggregation [187-191]. Passive immunisation of Alzheimer's patients is currently being examined in several clinical trials [192]. As an alternative to antibodies several peptides are being studied that can modulate or prevent the amyloid aggregation by disturbing the fibre assembly and oligomerisation [193,194]. Short oligonucleotides were able to inhibit the aggregation of huntingtin, the protein associated with Huntington's disease, but the mechanism remains unclear [195,196].

4.5. AIMS AND OBJECTIVES

A long-term goal is the development of therapeutics that can alleviate effects and prevent or remove the cause of amyloid deposit-associated neurodegenerative conditions such as Alzheimer's or Parkinson's disease. For this we needed a deeper understanding of the basic processes that lead to polypeptide aggregation and amyloid fibre formation as part of complexes with other biomolecules. Such changes in polypeptide properties would have a direct effect on their biological activity, An example is making the aggregating polypeptide inaccessible by providing amyloid fibrils as novel interaction partners, or by forming toxic oligomers [24]. The formation of amyloid fibrils depends on generic, primarily backbone-based, interactions, but charged residues are likely to play a major role because they can both inhibit the formation of amyloid structures [136,138] as well as support and enhance it [163]. Charge interactions appear to be an important factor modulating nucleation, but they have been studied *in vitro* either with short peptides without any binding partner, or with full-length proteins [163]. In the latter case it is difficult to distinguish between interactions that are mediated by 'decorating' sequences and those that are driven by interaction with the amyloid core (see Figure 4-8).

Here, I used a simplified system of short basic peptides with alternating hydrophobic and hydrophilic amino acid residues to study interactions of amyloidogenic peptides with nucleic acids and fatty acids under physiological conditions. Particular focus was on the formation of amyloid-nucleic acid (ANA) complexes consisting of (poly-)peptides associated non-covalently via charge interactions with nucleic acids.

To gain insight into the nucleation and fibre formation process of amyloid aggregates I studied the formation of complexes from peptides with nucleic acids or fatty acids using a range of biophysical techniques. Assays utilising Thioflavin T and Congo Red binding allowed the detection of amyloid aggregates, and peptide conformation changes could be followed by circular dichroism spectroscopy. Bright field, confocal and electron microscopy enabled us to examine the morphology of the formed complexes. X-ray fibre diffraction allowed us to detect the amyloid fibril-specific cross-β pattern and gave insight into the fine structure of the ANA complexes. Not only were the effects of polyanions on amyloid nucleation examined, but also the potentially disruptive effects of the fibres on nucleic acid integrity. For the latter, I looked at hybridisation using a BIAcore assay, the double-strand specific fluorescence of PicoGreen and time-resolved FRET.

I showed that nucleic acids and fatty acid liposomes promoted aggregation and amyloid fibre formation from peptides, many of which would not aggregate under the conditions explored. In turn, the peptides enhanced the hybridisation of associated nucleic acids. In my studies, reciprocal interactions of peptides with nucleic acids led to formation of amyloid-nucleic acid (ANA) complexes with properties that were discrete from those of their composite polymers. These mutual interactions under conditions that were compatible with nucleic acid secondary structure supported the idea that nucleic acid structure may in future be used to modulate amyloid fibre formation, both in therapeutic and nano-engineering roles.

The first results section concentrates on the aggregation of peptides with alternating polar and apolar amino acid residues in complex with either nucleic acids or fatty acid

liposomes. The results shown are from spectrophotometric assays including Thioflavin T fluorescence, Congo Red absorbance, and circular dichroism, as well as bright field, confocal and electron microscopy, and X-ray fibre diffraction.

In the second results chapter the influence of the peptides on hybridisation as a measurement for the structural integrity of nucleic acids is examined. BIAcore surface plasmon resonance, PicoGreen fluorescence and time-resolved FRET were employed to measure the hybridisation levels of oligonucleotide probes.

5. MATERIALS & METHODS

5.1. PEPTIDES

5.1.1. PEPTIDE PREPARATION

Peptides $(HL)_3$ (HLHLHL), $(HL)_5$ (HLHLHLHLHL), $(KL)_3$ (KLKLKL), $(KL)_5$ (KLKLKLKLKL), TVQ (TVQFHMH), $(EL)_3$ (ELELEL) and fluorescein-labelled FITC-$(HL)_3$ were purchased at 95% purity from GL Biochem (PR China) or Peptide 2.0 (USA). Peptides $(KL)_{3.5}$ (KLKLKLK) and $(KL)_4$ (KLKLKLKL) are a kind gift of the lab of Rudolf Allemann (Cardiff University), and some $(KL)_3$ and $(KL)_5$ was synthesised in the lab of Derek M. Woolfson (Bristol University). The chemical structures of the peptides are shown in Figure 5-1 and Figure 5-2. Peptides were usually dissolved in 20 mM HCl and dried twice to remove excess TFA as previously described [197,198], the pH adjusted to 6.0 with NaOH and dialyzed against water (MWCO 100 – 500 cellulose ester membrane; Spectrum Laboratories, UK) to remove residual salt and TFA. Peptide concentrations were verified using an OPA assay for free amine groups (Pierce). The peptide STVIIE was obtained HPLC-purified from Severn Biotech (UK). It was solubilized in 50% Methanol/ water at pH 11, freeze-dried and redissolved in 20 mM glycine pH 10 to create the stock solution. Prior to use it was sonicated for 10 minutes in a bath sonicator and centrifuged for 10 minutes at 4ºC at 16,100 x *g* to remove potential larger aggregates. All peptides were tested by both the Zyggregator [199] or the Waltz [200] algorithm for their amyloid formation potential. The Zyggregator method scanned larger proteins with a 7-residue window to find aggregation-prone and potentially amyloid fibre-forming regions of larger proteins based on several properties of the examined sequence, among them alternating patterns of hydrophilic and hydrophobic residues, secondary structure

propensity, hydrophobicity and charge [199]. Waltz employed a position-specific scoring matrix based a wide range of amino acid residue properties to specifically predict amyloid fibril-forming over non-fibrillar aggregate-forming hexapeptide sequences [200].

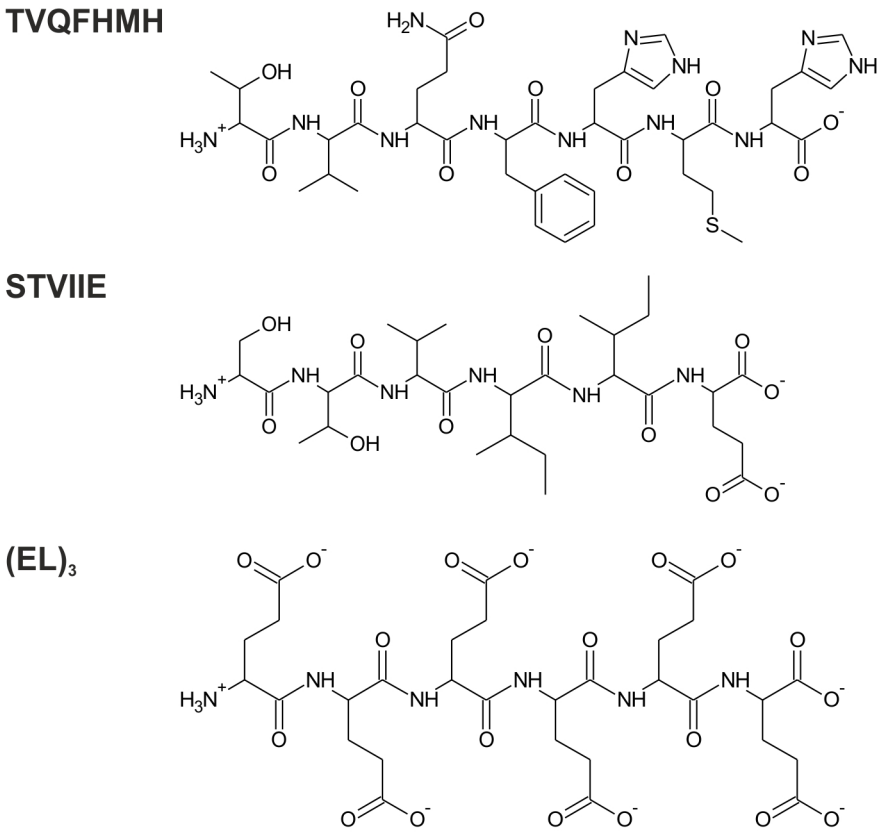

Figure 5-1: Chemical structures of TVQFHMH, STVIIE and $(EL)_3$. Peptides are shown at pH 7 where all amino groups of the N-terminus are expected to be protonated and the carboxyl groups on C-terminus and glutamic acid residues to be deprotonated [201].

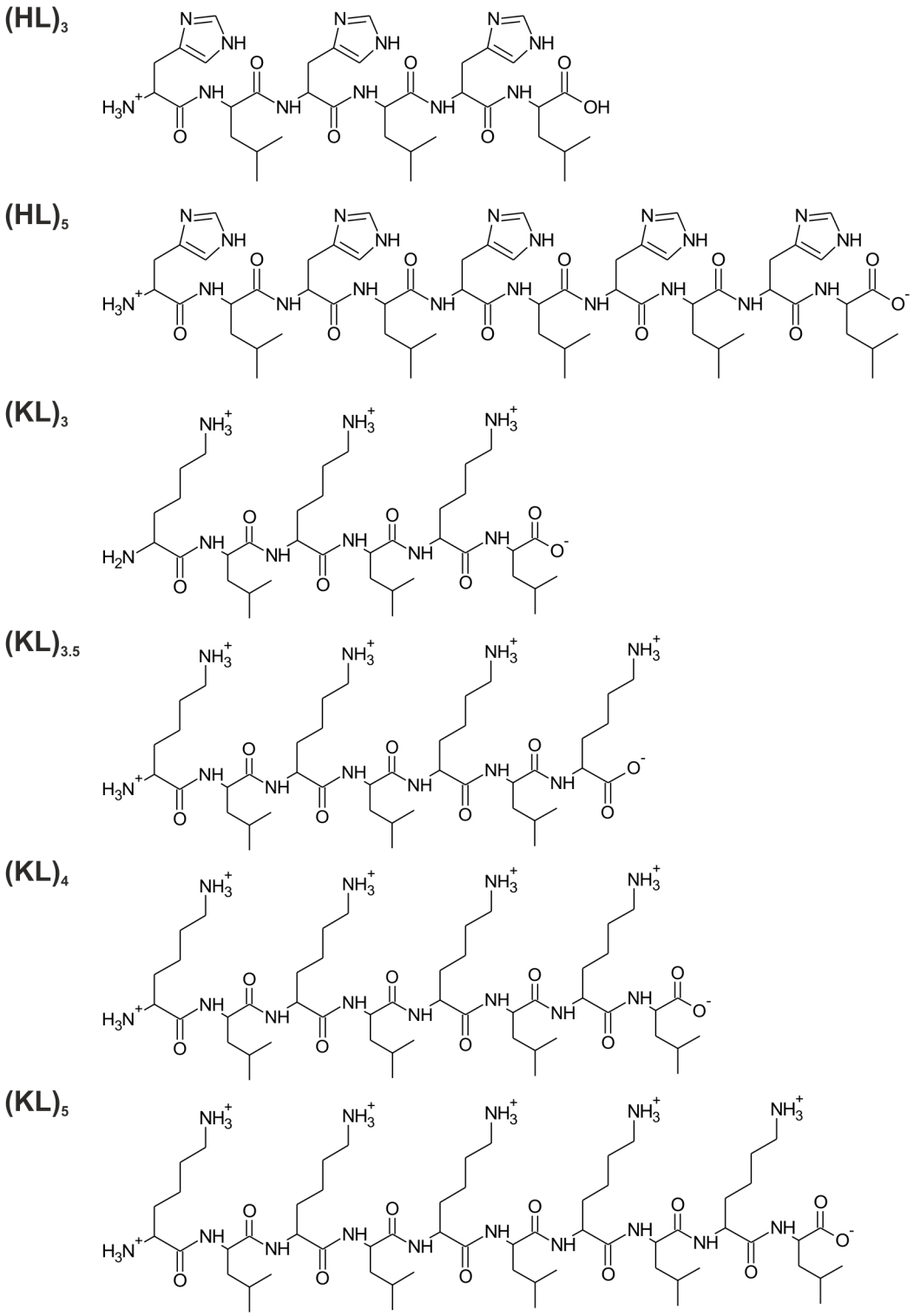

Figure 5-2: Chemical structures of the (HL) and (KL) peptides. Peptides are shown at pH 7 where all amino groups on N-terminus and lysine residues are expected to be protonated and the carboxyl groups of the C-terminus to be deprotonated. The imidazole groups of the

histidine side chains are shown deprotonated according to their theoretical pK_a of 6.04 [201].

5.1.2. PEPTIDE CHARGES

The charges on the peptides were calculated using the Peptide Property Calculator provided by a GenScript website (GenScript UK; www.genscript.com/ssl-bin/site2/peptide_calculation.cgi), resulting in the following net charges (further on referred to as "calculated (net) charges"): $(HL)_3$ has a calculated -0.5 charge at pH 8.5, +1 charge at pH 6.8, +2 charges at pH 6.2, and +3 charges at pH 5.0. $(HL)_5$ has a calculated ±0 charge at pH 8.0, +1 charge at pH 7.0, +2 charges at pH 6.5, +3 charges at pH 6.2, and +4 charges at pH 5.5. $(KL)_3$ is at calculated +3 charges below pH 8.5, and $(KL)_5$ has +5 calculated charges below pH 8.5. TVQFHMH has ±0 charges at pH 7.6, +1 charge at pH 6.5, +2 charges at pH 5.0. The peptide $(EL)_3$ was expected to carry negative calculated net charge in the range of pH 5.0 to 8.5 according to the theoretical pK_a = 4.07 of the γ-carboxyl groups of the glutamic acid residues [201]. This property was used as a negative control for the (calculated) positive charges of the peptides $(HL)_3$, $(HL)_5$, $(KL)_3$, $(KL)_5$, and TVQFHMH, and glutamic acid was a better control than aspartic acid in this context because it was more similar to lysine. The peptide STVIIE was used to study the 'catalytic effects' of what were likely to be charge-based interactions with nucleic acids and has previously been calculated to have a net charge of +1 at pH 2.6 [142]. The fact that the pH was too low for nucleic acid hybridisation was not regarded as being a major issue since a single stranded DNA oligonucleotide was used. Titrations were carried out on several peptides to verify predictions (see Figure 6-1). $(HL)_3$, $(HL)_5$, $(KL)_3$, $(KL)_5$ and TVQFHMH set to pH ~3 with HCl and 1 M NaOH solution was added in 10 or 20 µl steps. $(EL)_3$ was set to pH 13 with NaOH and 1 M HCl was added in 10 µl steps. In both cases

the pH was determined after each addition step. The titrations were designed and carried out by Christine Humphreys (Cardiff University).

5.2. NUCLEIC ACIDS

Salmon testes DNA (ST DNA), herring testes DNA (HT DNA), Baker's yeast RNA (BY RNA) and poly(A) RNA (PA RNA) were obtained from Sigma (UK). All contained nucleic acid (double) strands ranging from few bp to several kbp as confirmed by agarose gel electrophoresis (data not shown). Concentrations were determined via absorption at 260 nm on of a NanoDrop ND-1000 (Thermo Fisher Scientific), using ε(dsDNA) = 0.020 $(\mu g/ml)^{-1}\ cm^{-1}$, ε(ssDNA) = 0.030 $(\mu g/ml)^{-1}\ cm^{-1}$, and ε(ssRNA) = 0.025 $(\mu g/ml)^{-1}\ cm^{-1}$ as extinction coefficients. The resulting concentrations were converted into base concentrations using 309 g mol^{-1} and 325 g mol^{-1} as molecular weights for DNA and RNA, respectively.

The DNA oligonucleotides oligo D, oligo E, and oligo F were custom-made by Invitrogen (UK), while the hybridisation probes for the TR-FRET experiments were purchased from Biomers.net (Germany). See Table 5-1 for sequences and applications.

Diethyl phosphate (Sigma, UK) was used as control for the charges of the phosphate backbone of the nucleic acids in the gel formation tests.

Table 5-1: Oligonucleotide sequences

Name	Application	Sequence (5' -> 3')
Oligo D	BIAcore	Biotin-GAT CTT CGA GTC AGA CAG CT
Oligo E	BIAcore, Congo Red assay on $(KL)_5$, PicoGreen NaCl titration	GGT CGC AAC ACT AGT TTA GCT GTC TGA CTC GAA
Oligo F	BIAcore, PicoGreen NaCl titration	AAC TAG TGT TGC GAC CTT TCG AGT CAG ACA GCT
Probe 1a with 11 bp overlap sequence	FRET assay donor	*TGC TGA AGA GC*T GAA GTT AGC GAT CTT AGA TCA GCT ACA CCC AGT CAC
Probe 1a without overlap sequence		CTC GCT CTA AGC TAG CTC GTA GTC ATT CAC CAG TCA C
Probe 1b	FRET assay donor complementary	CTG GGT GTA GCT GAT CTA AGA TCG CTA ACT TCA
Probe 2a with 11 bp overlap sequence	FRET assay acceptor	GCT CTT CAG CAC TCG CTC TAA GCT AGC TCG TAG TCA TTC ACC AGT CAC
Probe 2a without overlap sequence		CTC GCT CTA AGC TAG CTC GTA GTC ATT CAC CAG TCA C
Probe 2b	FRET assay acceptor complementary	CTG GTG AAT GAC TAC GAG CTA GCT TAG AGC GAG

5.3. PREPARATION OF PEPTIDE-NUCLEIC ACID MIXTURES

ANA complexes were usually formed immediately prior to assay by adding equal volumes of buffered peptides and nucleic acids to generate the final concentrations described. Unless otherwise indicated all DNA was double-stranded and from salmon testes and all nucleic acid concentrations relate to the molarity of the phosphates. The molarity was based on the average molecular weight of the nucleotides integrated into a nucleic acid strand and was calculated as 309 Da per phosphate for DNA and 325 Da per phosphate for RNA. Concentrations were determined by absorbance at 260 nM with help of a NanoDrop ND-1000 (Thermo Fisher Scientific). 10 mM MES was used for assays below pH 7.0 while 10 mM HEPES was used at higher pHs. When necessary, particularly when working with $(HL)_5$- (aggregation), $(HL)_3$- (gel) and TVQFHMH- (gel) ST DNA complexes for preparation of TR-FRET samples (see chapter 5.11.2, page 45), the gels or aggregates were broken down using a pestle, to allow pipetting.

5.4. Fatty Acid Stock Preparation

Stock solutions of myristoleic, palmitoleic and oleic acid were made up to 80 mM fatty acid in 80 mM sodium hydroxide and kept frozen at -20°C.

5.5. Gel Strength Analysis

To evaluate gel strength, 10 µl of peptide-(poly)anion mixture (20 µl total volume) was aspirated several times using a calibrated Gilson P20 pipette over a period of 10 seconds (no filter tip). The introduction of air bubbles was avoided whenever possible. Gel strengths were rated according to 5 classes (see Table 5-2) and compared to the flow behaviour of buffer alone, buffer with peptide and buffer with (poly)anion.

Christine Humphreys (Cardiff University) designed and conducted a preliminary experiment before it was expanded to the format presented in this thesis.

Table 5-2: Gel strength classifications

Strength	Description
Very strong	Gel blob that blocked the pipette tip completely.
Strong	Weaker gel blob that allowed some material to be aspirated, but usually with introduction of air bubbles and not reaching the expected level in the tip.
Medium	Markedly reduced flow; expected level not reached in tip.
Weak	Reduced flow and pronounced meniscus abnormalities.
Very weak	Meniscus abnormalities

5.6. Dye-Binding Assays

5.6.1. Standard Thioflavin T and Congo Red Assays

Enhanced Congo Red absorbance at 544 nm of $(KL)_5$ ANA complexes (0.2 mM $(KL)_5$, 1 mM salmon testes or oligonucleotide DNA, 10 mM HEPES pH 8.0 and 50 μM Congo Red dye) was measured using a BMG FLUOStar OPTIMA plate reader. Values were normalized to the mean of the absorbances at 485 and 450 nm. For an examination of the normalisation please see supplementary chapter 9.1.

Thioflavin T fluorescence of ANA complexes in 10 mM MES buffer containing 150 mM NaCl was measured as previously described [72]. The insulin amyloid positive control was prepared by incubating 1 mM bovine pancreas insulin (Sigma, UK) in 10 mM hydrochloric acid for 3 days at 65ºC followed by neutralization to pH 7 with NaOH. 50 μM pre-formed insulin amyloid was used in assays as positive control to check if the assay worked due to the high variation of the highly aggregated (large, visible aggregates) peptide hormone.

5.6.2. Kinetic Thioflavin T assay

The measurements were taken on a BMG FLUOStar as described above [72]. White clear bottom plates (Costar) were used, and the fluorescence was detected from the bottom in order to avoid issues such as air bubble formation after injection of the DNA solution. The buffer was 150 mM NaCl in 10 mM MES pH 6.5 (+1 calculated net charge on $(HL)_3$, -3 calculated net charge on $(El)_3$). Every solution included 50 μM Thioflavin T and was equilibrated with the dye for 30 minutes before measurement to avoid the observation of dye binding kinetics during the experiment. For the experiment, 100 μl of 1 mM ST DNA was injected at 420 μl/sec to 100 μl 1 mM $(HL)_3$ or $(EL)_3$, yielding final

concentrations of 500 µM for both peptides and nucleic acid in the mixture (1:1 calculated charge ratio). The control was 1 mM ST DNA injected into buffer. The temperature was recorded, but could not be controlled by the instrument, and was in the range of 27 to 30 ºC. The full program consisted of the following steps:

The background level was determined by 25 measurements at 1 measurements/ 5 s, followed by the addition of the salmon testes DNA within 1.7 seconds and a short orbital shaking for mixing (1 s). The ThT fluorescence was followed in 60 measurements at 1 measurement/ 5 s (5 minutes total).

5.6.3. Insulin Amyloid Formation Kinetics

1 mM Bovine insulin in 10 mM hydrochloric acid (pH 2) was incubated at 65ºC in 1.5-ml-tubes in a hot block (no agitation). Every 30 minutes 5 µl samples were taken and transferred to an untreated black 96-well-plate. 195 µl 10 mM MES containing 50 µM Thioflavin T were added and the fluorescence measured using a BMG FLUOStar plate reader (excitation wavelength: 440 nm; emission wavelength: 480 nm).

5.6.4. Thioflavin T on Fatty Acid - Peptide Samples

Samples consisted of 10 mM fatty acid with either 3.33 mM $(KL)_3$, $(HL)_3$ or $(EL)_3$ in 200 mM bicine pH 8.5 mixed directly before the assay and were incubated for 1 hour at room temperature before measurement. Thioflavin T fluorescence and Congo Red absorbance were determined as described above (see Chapter 5.6.1).

5.7. Transmission Electron Microscopy

ANA complex samples were formed as listed in Table 5-3. Following a 1:2 dilution in buffer when necessary the samples were adsorbed onto Pioloform-coated copper 50

meshes or carbon-coated Formvar-coated copper 200/300 meshes and stained with 2% uranyl acetate as previously described [72], and examined on a Philips EM 208 (Cardiff University, School of Biosciences) or Philips CM12 (Cardiff University, Heath Hospital) electron microscope. The images were either scanned from the negatives using a backlit scanner (Philips EM 208) or saved directly as 16-bit TIFF files (Philips CM12). In the latter case a transformation to 8-bit images using ImageJ [202,203] was necessary. All images were then adjusted for brightness and contrast and cropped using Gnu Image Manipulation Program (GIMP; www.gimp.org). Scale bars were added either by using the ones on the negatives (Philips EM 208) or from the overlay of the microscope control software (Philips CM 12). Diameters of the 6 thinnest long fibres were manually determined at 3 points at least ~5 nm apart using ImageJ, i.e. 18 measurements per sample in total [203].

EM grids were partially prepared and imaged by Ant Hann (Cardiff University, School of Biosciences), who also suggested using rotary shadowing to enhance contrast of some of the samples as indicated in Table 5-3. Fibre diameter measurements were taken regardless of potential fibre thickening by rotary shadowing.

Table 5-3: ANA complex samples for electron microscopy.

Peptide	Polyanion	Salt	Buffer	pH	rotary shadowing
0.2 mM $(KL)_5$	1 mM ST DNA	150 mM NaCl	10 mM HEPES	7.0	
1 mM $(KL)_5$	5 mM DNA	150 mM NaCl	10 mM HEPES	7.0	
0.25 mM $(KL)_4$	1 mM poly(A) RNA	-	10 mM HEPES	7.0	+
0.33 mM $(KL)_3$	1 mM poly(A) RNA	-	10 mM HEPES	7.0	+
1 mM $(HL)_5$	1 mM ST DNA	150 mM NaCl	10 mM MES	5.5	+
1 mM $(HL)_3$	1 mM ST DNA	-	10 mM MES	6.2	
5 mM $(HL)_3$	5 mM ST DNA	150 mM NaCl	10 mM MES	5.5	
5 mM TVQFHMH	-	150 mM NaCl	10 mM MES	6.5	
5 mM TVQFHMH	5 mM ST DNA	150 mM NaCl	10 mM MES	6.5	
1 mM TVQFHMH	1 mM ST DNA	150 mM NaCl	10 mM MES	6.5	
5 mM TVQFHMH	5 mM ST DNA	-	10 mM MES	5.0	

Table 5-3 legend: Final sample composition for transmission electron microscopy. Peptide and polyanion (if any) were usually mixed 1:1 to generate the final solution.

5.8. CONFOCAL MICROSCOPY

FITC-$(HL)_3$ was spiked in a 1:20 ratio into $(HL)_3$ to generate a 12 mM $(HL)_3$ working solution. Salmon testes DNA was labelled by incorporating ATTO 550 nucleotides using a nick-translation kit (Jena Biosciences, Germany). Unincorporated nucleotides were removed by gel filtration. ATTO 550-DNA was spiked in a 1:20 ratio into salmon testes DNA yielding a 5 mM (phosphate) working solution. Equal volumes of 5 mM DNA and 12 mM $(HL)_3$ solutions were mixed directly on the slide for imaging. The buffer was 10 mM MES pH 5.0 or pH 6.5 containing 150 mM NaCl. A coverslip was added and the samples sealed with clear nail varnish before imaging. Pictures were taken with a Leica DM6000B upright microscope with a ×63 oil objective using a galvanometer-driven high precision Z-stage. The bleed-through controls were prepared as described above, with either the DNA or the $(HL)_3$ component left unlabelled.

The images were not manipulated for brightness and contrast. The scale bars were taken from screenshots created with the Leica confocal software and scaled accordingly

to fit the original 512 x 512 images extracted from the stacks using GIMP (www.gimp.org). The final overlays were created using ImageJ [204].

This experiment was supported by Anthony Hayes in the Confocal Unit (Cardiff University, School of Bioscience) and partly conducted by Christine Humphreys (Cardiff University).

5.9. X-RAY FIBRE DIFFRACTION

Drops of ANA complex solutions were placed between 2 beeswax-covered capillaries and allowed to dry to align the fibrillar material (see Figure 5-1 for a schematic). Table 5-4 lists the components of the starting gels for sample preparation. The resulting stalks were placed vertically in the x-ray beam of a Rigaku RU-H3R rotating anode x-ray generator (Cu K_α with 1.5418 Å wavelength), and the diffraction pattern was recorded on a Rigaku R-AXIS IV flat plate detector with 180 or 300 mm sample to detector distance and an exposure time of 10 to 20 minutes.

Table 5-4: Composition of samples for X-ray fibre diffraction

Peptide	Polyanion	Salt	Buffer	pH
21.6 mM $(KL)_3$	10.8 mM HT dsDNA	None	None **	pH 6.0
10 mM $(KL)_3$	10 mM ST dsDNA	None	None **	pH 7.0
5 mM $(KL)_3$	5 mM ST dsDNA	150 mM NaCl	10 mM HEPES	pH 7.0
5 mM $(KL)_5$	5 mM ST dsDNA	150 mM NaCl	10 mM HEPES	pH 7.0
5 mM $(KL)_5$	5 mM ST dsDNA	None	10 mM HEPES	pH 7.0
5 mM $(HL)_3$	5 mM ST dsDNA	50 mM NaCl	10 mM MES	pH 6.2
10 mM $(HL)_3$	10 mM ST dsDNA	150 mM NaCl	10 mM MES	pH 6.2
12.6 mM $(HL)_5$	6.3 mM poly(A) RNA	None	5 mM MES	pH 6.0
1.6 mM TVQ	None	None	None	About pH 6
1.6 mM TVQ	1.6 mM ST dsDNA	None	10 mM MES	pH 5.0
17.8 mM TVQ	8.9 mM poly(A) RNA	None	5 mM MES	pH 6.0
1 mM TVQ	1 mM ST dsDNA	None	10 mM MES	pH 5.0
1.6 mM TVQ	1.6 mM ST dsDNA	None	10 mM MES	pH 6.5
20 mM $(HL)_3$	None	None	None	About pH 6
3.33 mM $(HL)_3$	None	None	883 mM bicine	pH 8.5
3.33 mM $(KL)_3$	10 mM MA	None	200 mM bicine	pH 8.5
3.33 mM $(KL)_3$	10 mM PA	None	200 mM bicine	pH 8.5
3.33 mM $(KL)_3$	10 mM OA	None	200 mM bicine	pH 8.5
None	20 mM ST dsDNA	None	None	-
None	10 mM ST dsDNA	150 mM NaCl	None	-
None	20 mM ST ssDNA *	None	None	-

* ST ssDNA was prepared by heating ST dsDNA to 95ºC for 5 minutes before rapid cooling on ice directly before sample preparation.

** Samples were created in sodium carbonate pH 6.0, freeze-dried and reconstituted in water to pH the solutions while avoiding buffer salts.

The diffraction pattern was extracted with ImageJ [204] from the proprietary file format used by the Rigaku CrystalClear software (version 1.40). After import as raw image (16-bit unsigned, 3000 x 3000 pixels, white set to 0), the "Brightness & Contrast" settings were changed to display only the range from 0 - 255 (pixel intensity values). The image was then converted to 8-bit greyscale and saved as TIFF file; this is referred to as 'raw diffraction patterns'. The following modifications were carried out using the Gnu Image Manipulation Program (GIMP; www.gimp.org): Fine-tuning of brightness and contrast, rotation of the diffraction pattern so that the meridional axis was in the vertical, and

cropping to a 2500 x 2500 pixel PNG or JPEG file for display. The Bragg spacings were determined from the originally extracted 8-bit TIFF file using WCEN [205,206] and CLEARER [207].

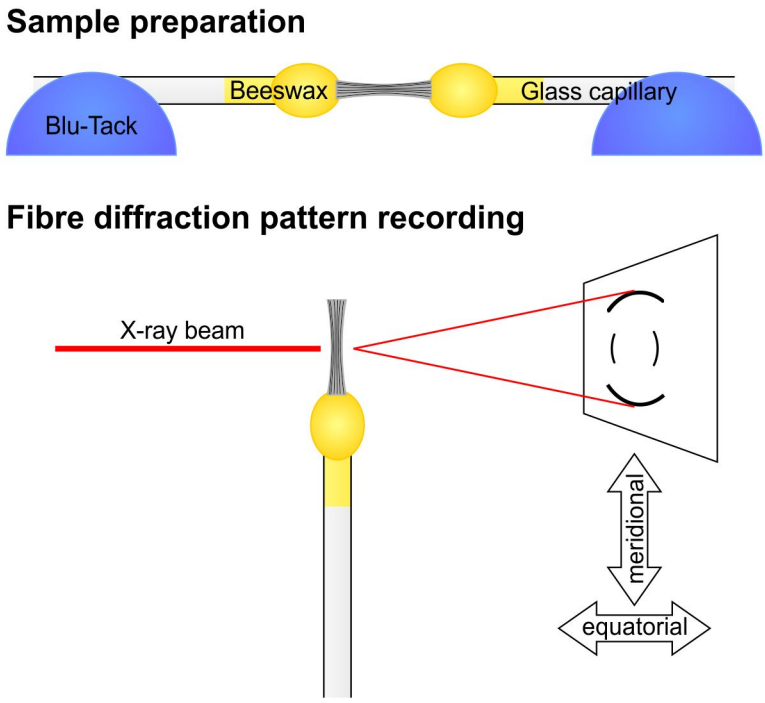

Figure 5-1: Fibre diffraction sample preparation and pattern recording. A drop of sample (about 10 µl, topped up if necessary) was left to dry between the wax-covered ends of two capillaries. The resulting stalk was placed upright in the X-ray beam and the pattern was recorded. The stalk defined the meridional direction as vertical, while the equatorial ones lied horizontally.

For the generation of the overlays the raw diffraction patterns were reduced from 3000x3000 pixels to 1000x1000 pixels using the Gnu Image Manipulation Program (GIMP; www.gimp.org) with cubic interpolation, then centred in CLEARER [207]. The

rotation to bring the meridional axis into the vertical, modification of brightness and contrast and creation of the coloured overlays were carried out using ImageJ [202,203].

5.10. CIRCULAR DICHROISM

20 mM STVIIE in 20 mM glycine pH 10.0 was diluted 1:25 in 20 mM glycine pH 2.6 (carboxyl group buffering) to yield 0.8 mM peptide with a measured pH of 2.6. Where indicated, the 33mer DNA oligonucleotide was premixed with the dilution buffer to yield a final concentration of 242 nM (8 μM with respect to phosphate). Samples with and without oligo E were compared directly and analysed in parallel (5 minutes difference in preparation timing) using the same peptide stock solution in matched cuvettes (1 mm path length; freshly cleaned and dried directly before the experiment). An Applied Photophysics Chirascan Circular Dichroism spectrometer was used to record the CD spectrum from 190 to 260 nm (1 nm step size, 2.5 second integration / step) every 30 minutes for 24 hours at 20ºC. A background spectrum of buffer with or without DNA (3 averaged spectra) was subtracted, and the spectra were set to 0 mdeg ellipticity at 260 nm to remove baseline shift since no signal of the highly diluted (242 nM) single-stranded oligo E could be detected.

5.11. TIME-RESOLVED FÖRSTER RESONANCE ENERGY TRANSFER (TR-FRET)

Time-resolved FRET (TR-FRET) was used to measure hybridisation levels of specifically designed probes. The method follows the description in Perrins *et al.* [208] (it was the same setup), but was carried out in solution without attachment of the probes to a surface. Time-resolved FRET has greater sensitivity than intensity-based FRET, which would be limited by fluorophore bleed-through signal. In addition, the instrument was built within the lab by Paola Borri (Cardiff University) and well validated [209].

5.11.1. FRET PROBES

DNA hybridisation oligonucleotides used for TR-FRET (Donor probe: 5'-CTG GGT GTA GCT GAT CTA AGA TCG CTA AC**6** TCA-3' with 5'-TGC TGA AGA GCT GAA GTT AGC GAT CTT AGA TCA GCT ACA CCC AGT CAC-3' for an 11 bp overlap or 5'-CAC TGA CCA CTT ACT GAT GCT CGA TCG AAT CTC GCT C-3' for a 0 bp overlap; Acceptor probe: 5'-C**7**G GTG AAT GAC TAC GAG CTA GCT TAG AGC GAG-3' with 5'-GCT CTT CAG CAC TCG CTC TAA GCT AGC TCG TAG TCA TTC ACC AGT CAC-3' for an 11 bp overlap or 5'-TGA AGT TAG CGA TCT TAG ATC AGC TAC ACC CAG TCA C-3' for a 0 bp overlap) were synthesized with modified dT bases carrying either ATTO 488 (labelled **6** in the sequence above) and ATTO 550 (labelled **7** in the sequence above) on donor or acceptor oligonucleotides, respectively. The oligonucleotides were cartridge-purified (Biomers.net, Germany) and separately hybridized to form the primarily double-stranded probes in 150 mM NaCl in order to generate 50 µM stock solutions by heating to 95ºC followed by slow cooling (see Figure 5-2).

The samples were prepared in PCR strip tubes in a volume of 10 µl by mixing 5 µl ANA complex/peptide/ST DNA solution with 5 µl of the solution containing the probes. The mixtures were incubated for 30 minutes before measurement. For the measurement, the sample holder was prepared by applying a thin layer of silicone grease to both sides of a 50 x 7 µl chambered coverslip gasket (Grace Bio-Laboratories). The greased gasket was then carefully applied to a glass coverslip to create wells. 4.5 µl of the sample solution were filled into these wells, leaving at least 1 empty well as a spacer between samples to avoid overspill. The wells were sealed with a second coverslip, and the coverslip-gasket-coverslip sandwich was mounted vertically in the setup for fluorescence lifetime measurements.

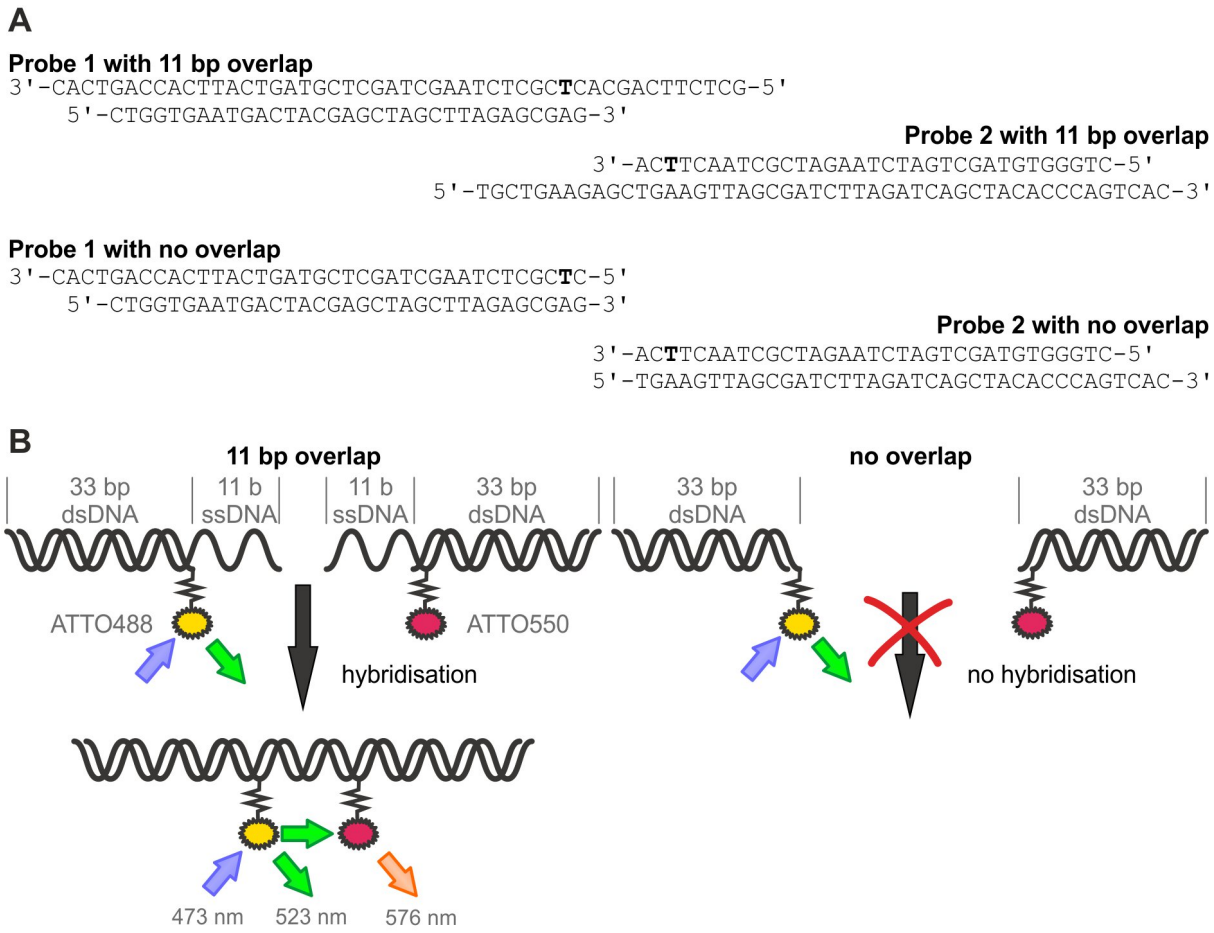

Figure 5-2: Construction of the FRET probes. (**A**) *Sequences of the FRET probes*. The probes were mainly double-stranded as indicated. The residues in bold carried either ATTO 488 (probe 1; donor fluorophore) or ATTO 550 (probe 2; acceptor fluorophore). (B) *Schematic of fluorescence emission of the probe fluorophores.* ATTO 488 attached to the donor probe was the main excited fluorophore by the 473 nm laser light, emitting light at 523 nm. The acceptor was hardly excited by the laser, and only emitted fluorescence at 576 nm with intensity comparable to the donor when FRET occurred and the donor transferred energy to the acceptor. This only happened when the fluorophores were brought within their Förster radius (6.4 nm; Atto-Tec, Germany) upon hybridisation of the 11 bp overlap probes. The 0 bp overlap probes could not give rise to FRET resulting from hybridisation because they lacked the 11 bp complementary sequences.

5.11.2. EXPERIMENTAL SETUP

A diode laser source provided ~50 ps pulses with 20 MHz repetition rate at 473 nm (Becker & Hickl GmbH, Germany; run at 40% power throughout the experiments), exciting the donor fluorophore and to a lesser degree the acceptor fluorophore (see Figure 5-3 B for the excitation spectra). Photon counting electronics (SPC-150, Becker & Hickl GmbH, Germany) were connected to two Hamamatsu H7422P-40 photomultipliers, collecting a band of 502 to 548 nm for the donor channel and 562 to 640 nm for the acceptor channel, which were created by dichroic mirrors and transmission filters (see Figure 5-3 A for a rough schematic): The donor fluorescence emission was separated out by a dichroic beam splitter (Semrock FF555-Di02, cutting at 555 nm), and a 30 nm band pass filter around 520 nm (Newfocus, Clarity filter 5911-B) further defined the wavelength band transmitted into the first PMT by cutting off any scattered or reflected light from the laser source. The light transmitted by the dichroic mirror in front of the first PMT was reflected into the second PMT by a second dichroic beam splitter (Semrock FF650-Di01; cutting at 640). This resulted in light between 562 nm and 640 nm being sent through a long pass colour filter (UQG, SCHOTT OG515; transmission only >515 nm) to remove reflections from the laser source. The time resolution of the system was approximately 250 ps (see Supplementary Figure 5 for the instrument response function). The fluorescence signal was collected over a typical integration time of 30 seconds (minimum 10 s, maximum 300 s).

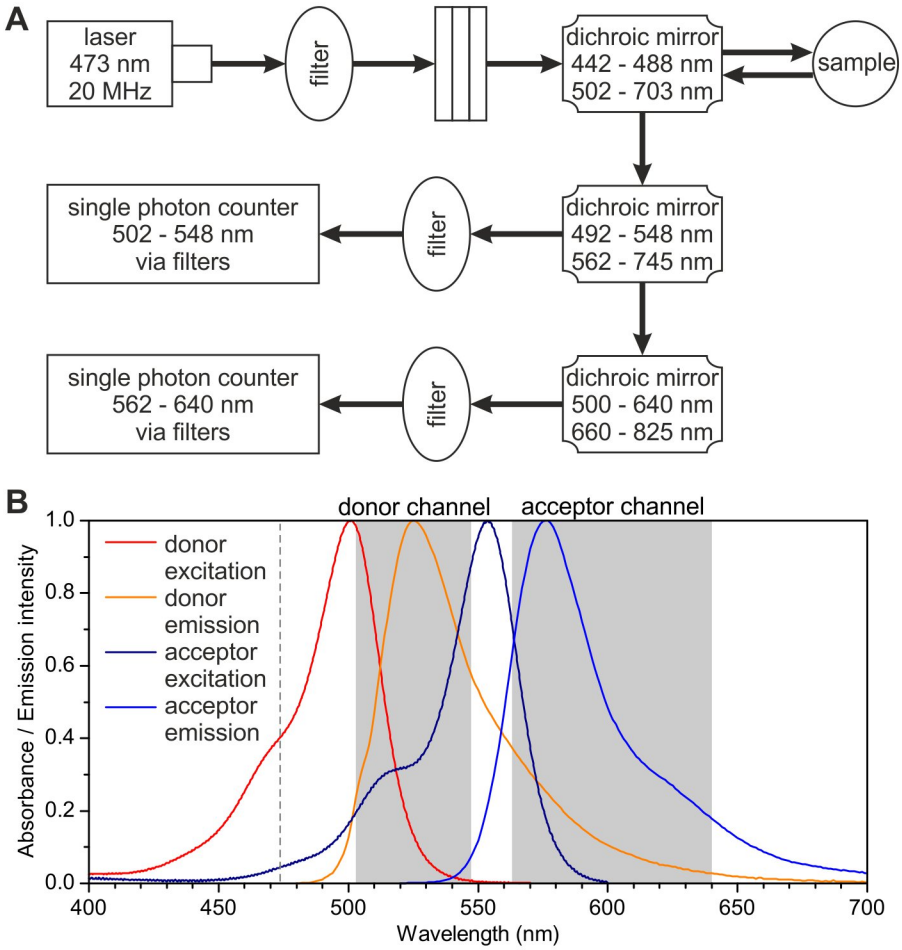

Figure 5-3: FRET fluorophore excitation and emission spectra. (**A**) Schematic of the TR-FRET setup. Arrows indicate the light path. The intensity from the laser was reduced by 3 transmission filters to 1% of the output power before hitting the sample. A system of transmission filters and dichroic mirrors created the donor and acceptor channels whose intensity was measured by two single-photon counters. (**B**) A high spectral overlap of donor emission and acceptor excitation spectra allowed highly efficient FRET to occur. The bands caught by the single photon counters are shown in grey. The grey dashed line marks the excitation wavelength of the blue laser at 473 nm. Note that only a low level of acceptor fluorescence emission was caught by the donor channel, but there was a significant impact of donor fluorescence emission in the acceptor channel that had to be corrected for.

5.11.3. ANALYSIS

FRET occurred when donor fluorophore ATTO 488 and acceptor fluorophore ATTO 550 were brought within their Förster radius (6.4 nm; Atto-Tec, Germany) by hybridisation of the probes (see Figure 5-2). This caused a faster fluorescence decay of the FRET donor probe compared to the FRET time course of the donor probe alone under the same conditions, and a delayed rise and delayed decay of acceptor probe fluorescence compared to the time course of the acceptor probe alone under the same conditions. The donor decay could therefore be used to extract hybridisation levels. The details of the analysis are described below and follow the method given by Perrins *et al*. (which used the same set-up) [209]:

The recorded emitted fluorescence of donor and acceptor fluorophores was corrected for differences in collection time, and the measured background (mainly the coverslip glass with a minor contribution from the buffer and/ or peptides and/ or nucleic acid) was subtracted. The acceptor fluorescence time courses were corrected for the bleed-through of the donor fluorescence using a correction factor α derived from measurements of donor fluorophore in the absence of acceptor fluorophore under the same conditions as the corresponding experiment (see Equation 1). The donor fluorescence was corrected in the same way using a correction factor β by measuring acceptor fluorescence in the absence of donor under experimental conditions, but acceptor bleed-through into the acceptor channel was negligible (<1%; see Equation 2). The correction factor α was determined from background-subtracted intensity measurements from the donor and acceptor channels of a sample containing only donor (D) oligonucleotide under the same conditions as the experiment (buffer, salt, peptide, ST DNA). The ratio of acceptor channel (Ch2) intensity to donor channel (Ch1) intensity

was determined from a region (between time points n and m) that was not too noisy, i.e. where there was actually a signal from the fluorophore and not only background.

$$\alpha = \frac{1}{n-m}\sum_{t=m}^{n}\frac{I_{(t,Ch2,D)}}{I_{(t,Ch1,D)}} \qquad \text{Equation 1}$$

The correction factor β was determined similarly from background-subtracted intensity measurements from the donor and acceptor channels of a sample containing only acceptor (A) oligonucleotide under the same conditions as the experiment (buffer, salt, peptide, ST DNA). The ratio of acceptor channel (Ch2) intensity to donor channel (Ch1) intensity was determined from a region (between time points n and m) that was not too noisy, i.e. where there was actually a signal from the fluorophore and not only background.

$$\beta = \frac{1}{n-m}\sum_{t=m}^{n}\frac{I_{(t,Ch1,A)}}{I_{(t,Ch2,A)}} \qquad \text{Equation 2}$$

The α factors determined on this setup in the course of the experiments were usually about 0.45, while the β factors were <0.01 and negligible.

The corrected donor intensity is described by:

$$I'_{(t,Ch1,DA)} = \frac{I_{(t,Ch1,DA)} - \beta I_{(t,Ch2,DA)}}{1-\beta\alpha} \qquad \text{Equation 3}$$

The corrected acceptor intensity is described by:

$$I'_{(t,Ch2,DA)} = \frac{I_{(t,Ch2,DA)} - \alpha I_{(t,Ch1,DA)}}{1-\beta\alpha} \qquad \text{Equation 4}$$

The signal was smoothed by a rolling average and normalised. The time course of the donor was used to determine the ratio of bound to unbound donor probes. For this, the donor time course of an experimental sample was divided by the time course of a control sample containing only the donor probe under the same conditions (buffer, salt, peptide, ST DNA). The fluorescence intensity of the donor fluorophore followed a single exponential decay when no acceptor fluorophore was present, with τ_{ub} as the fluorescence lifetime in the absence of binding:

$$I_{t,Ch1,D)} = e^{\left(\frac{-t}{\tau_{ub}}\right)} \qquad \text{Equation 5}$$

When donor and acceptor fluorophore were brought within their Förster radius (6.4 nm; Atto-Tec, Germany) FRET could occur between donor and acceptor fluorophore. This provided an additional non-radiative fluorescence decay of the donor fluorophore with a lifetime τ_b. The normalised intensity is given by:

$$I_{(t,Chi1,DA)} = f_{ub}e^{\left(\frac{-t}{\tau_{ub}}\right)} + f_b e^{\left(\frac{-t}{\tau_b}\right)} \qquad \text{Equation 6}$$

Division of equation 6 by equation 5 yields:

$$\frac{I_{(t,Ch1,DA)}}{I_{(t,Ch1,D)}} = f_{ub} + f_b e^{\left(\frac{t}{\tau_{ub}} - \frac{t}{\tau_b}\right)} \qquad \text{Equation 7}$$

As $f_{ub} + f_b = 1$ this can be transformed to:

$$\frac{I_{(t,Ch1,DA)}}{I_{(t,Ch1,D)}} = 1 + f_b\left(e^{\left(\frac{t}{k}\right)} - 1\right) \qquad \text{Equation 8}$$

Where: $k = \frac{\tau_{ub}\tau_b}{\tau_b - \tau_{ub}}$

A plot of $I_{(t)DA}/I_{(t)D}$ vs. time showed the fraction bound f_b in the difference between the line y = 1 and the plateau of the curve. This allowed determination the fraction of binding donor probe without using the absolute intensities that could be affected by instabilities in laser intensity, quenching by the peptides, or sample inhomogeneity (e.g. aggregates of peptide-nucleic acid complexes).

Initially, all steps of the analysis including the data preparation before fitting were carried out in Origin Pro 8 (OriginLab, USA). Later, a Perl script by developed by Richard Perrins (Cardiff University) was used for correction of the starting time of the measurement, subtraction of the background, normalisation of the fluorescence intensity time courses, bleed-through correction and division by the corresponding donor-only time course as outlined above. Only the final non-linear curve fitting was done in Origin Pro 8 (OriginLab, USA).

After background subtraction, starting time correction, normalisation, bleed-through correction and division by the corresponding donor-only time course a nonlinear curve-fitting to the single-exponential decay was carried out in Origin Pro 8 as described in equation 9. This yielded the ratio R of bound to unbound donor probes, which was used to determine the amount of hybridisation f, and the concentration of free donor c_{free} from the starting concentration c_0, via equations 10 and 11.

$$y = U \times (1 + R \times e^{-t/\tau}) \qquad \text{Equation 9}$$

$$f = \frac{1}{1 + 1/R}$$ Equation 10

$$c_{free} = (1 - f) \times c_0$$ Equation 11

The dissociation constant K_d was determined by fitting *f* over the concentration of free donor to a hyperbolic saturation curve (equation 12) with *1* as maximum hybridisation.

$$f = \frac{f_{max} \times c_{free}}{K_d + c_{free}}$$ Equation 12

To determine the NaCl-dependence of hybridisation, the hybridisation probes were used at 500 nM each, a concentration about five times higher than the K_d, thereby ensuring that only the concentration of NaCl was a limiting factor for hybridisation. The NaCl concentration was varied from 1.125 mM to 1 M. Measurements were taken as described above. A Hill curve (Equation 13) was fitted through the data points for visualization purposes.

$$f = \frac{f_{max} \times c_{free}}{k^n + {c_{free}}^n}$$ Equation 13

5.12. TURBIDITY ASSAY

Samples of 10 mM fatty acid with either 1 mM $(KL)_3$, $(HL)_3$ or $(EL)_3$ in 200 mM bicine pH 8.5 were mixed directly before the assay, analogous to experiments previously carried out by Hanczyc *et al.* [210]. Absorbance readings at 450 nm were taken on a

BMG FLUOStar OPTIMA plate reader in white untreated clear-bottom plates every minute for 1 hour as described before [210].

5.13. BIACORE BINDING ASSAY

Streptavidin-coated BIAcore chips (SA chip, BIAcore Sweden) were cleaned before use by injecting 2x 50 mM NaOH at 5 µl/min for 30 seconds. They were functionalised by flowing over 1 µM biotinylated oligo D (see Table 5-1) in 150 mM NaCl and 10 mM HEPES pH 7.0 (HBS) at 5 µl/min for 60 s on a BIAcore 3000 instrument at 25°C. This was repeated until no further increase in response could be detected. Unbound oligonucleotide was removed by injecting 50 mM NaOH at 5 µl/min for 30 sec. Chips were stored in HBS (Hepes Buffered Saline pH 7.4, BIAcore Sweden) at 4°C for up to a week.

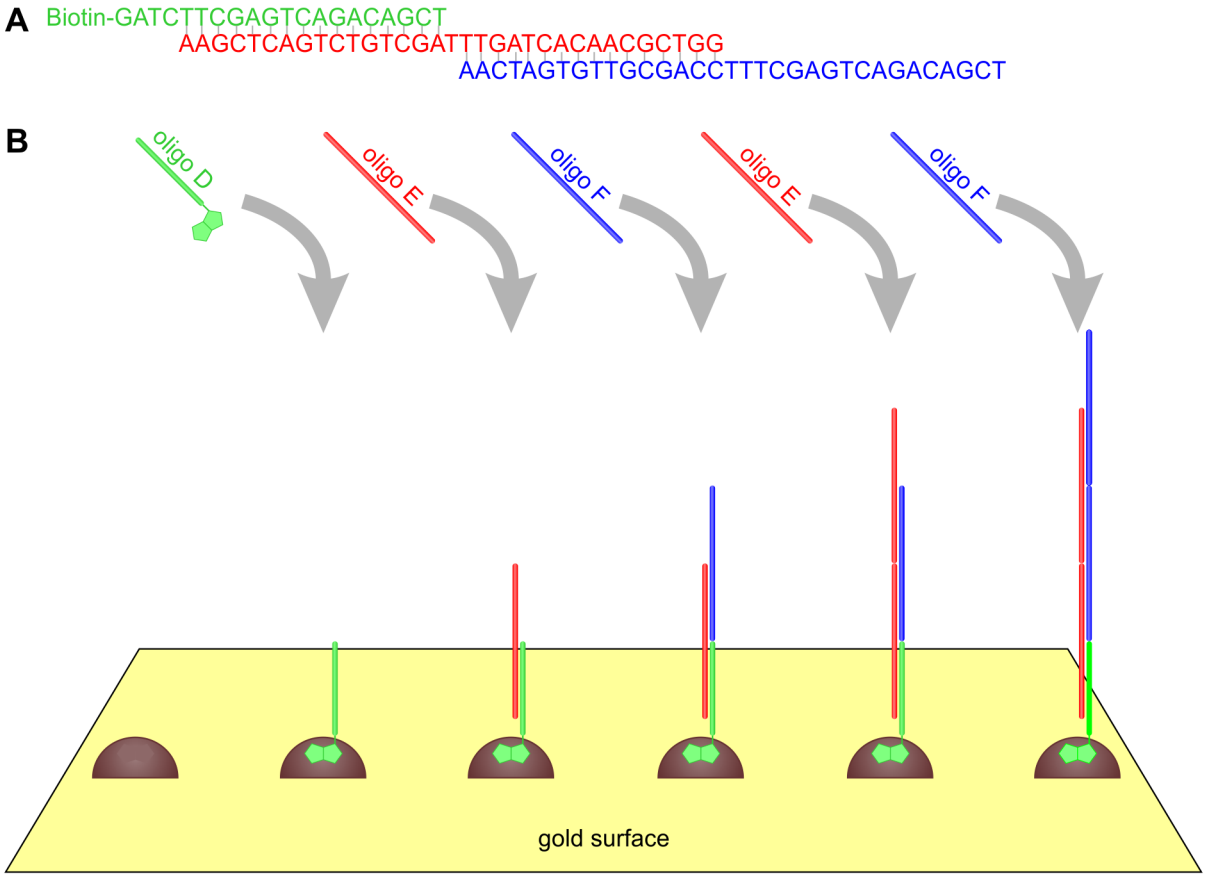

Figure 5-4: Schematic of oligo E and F in the BIAcore build-up experiments. (**A**) Sequences of oligo D (green, 5' to 3'), E (red, 3' to 5'), and F (blue, 5' to 3'), showing their overlap. The free end on oligo F provided a hybridisation site for oligo E. (**B**) Oligo D (green) was captured by streptavidin (brown) immobilised on the gold surface of a BIAcore chip. Successive alternating injections of oligo E (red) and oligo F (blue) created a double-stranded DNA that was linked to the gold surface.

For the build-up of longer DNA strands, 1 µM oligo E and F (see Table 5-1) were alternatingly injected over a chip with immobilised oligo D for 5 minutes each with 7.5 minutes buffer wash intermissions (see Figure 5-4). Bound oligonucleotides were removed with 50 mM NaOH for 30 seconds. Peptides at 10 µM were injected either on

their own or freshly mixed with one of the oligonucleotides for varying injection times and removed by 1 M NaCl and 50 mM NaOH for 30 seconds each.

5.14. PicoGreen Assay

The PicoGreen assay was based on manufacturer's instructions (PicoGreen Broad Range kit, Invitrogen UK). PicoGreen fluorescence was excited at 485 nm (10 nm band-pass filter) and read out at 520 nm (10 nm band-pass filter) on a BMG FLUOStar OPTIMA. For the NaCl titration, 2.5 µM oligo E and 2.5 µM oligo F were incubated for 30 minutes before measurements with 0, 5, 12.5, 25, 100, and 150 mM NaCl concentrations and PicoGreen at a final dilution of 1:200 (stock concentration not disclosed by manufacturer). A logistic curve was fit to the resulting fluorescence for visualisation (see Equation 14; A_2 = minimum, A_1 = maximum, p = potentiation factor, x_0 = transition midpoint).

$$y = A_2 + \frac{A_1 - A_2}{1 + \left(\frac{x}{x_0}\right)^p} \qquad \text{Equation 14}$$

For the $(KL)_5$ titration, , 2.5 µM oligo E and oligo F were incubated with the peptide concentrations ranging from 0 to 10 mM, matching the charges from the NaCl titration. Samples were created by first mixing the oligonucleotides and incubating them at room temperature for 30 minutes before combining them with a same volume solution containing the peptide $(KL)_5$ (10, 1, 0.125, 0.031, 0.016, and 0.001 mM) in buffer. Both oligonucleotide and peptide solutions contained PicoGreen at the final dilution of 1:200 (according to manufacturer's instructions). A logistic curve was fit to the resulting fluorescence for visualisation (see Equation 14).

5.15. LIGHT MICROSCOPY

Liposomes were prepared for use with 1 mM peptide (3.33:1 calculated charge ratio of fatty acid vs. $(KL)_3$)by diluting fatty acid stock solutions into 200 mM bicine pH 8.5 to a final concentration of 10 mM before incubating for 1 hour at room temperature. Either one of the peptides $(EL)_3$, $(HL)_3$, $(KL)_3$ or water was spiked at 1:20 into the liposome solution and mixed by vortexing.

For use with 3.33 mM peptide (1:1 calculated charge ratio of fatty acid vs. $(KL)_3$), liposomes were prepared by diluting fatty acid stocks into 200 mM bicine pH 8.5 to a final concentration of 20 mM and incubating for 1 hour at room temperature. Either one of the peptides $(EL)_3$, $(HL)_3$, $(KL)_3$ at twice the final concentration or water was mixed 1:1 with the liposome solution and mixed by vortexing.

The peptide-liposome complexes were imaged either immediately or after 1 hour incubation at room temperature on an Olympus IX-71 inverted microscope using phase optics via bright field illumination (a 100w Halogen bulb focused through a 0.55 NA long working distance condenser) at 20× magnification. The glass slides used were cleaned with 70% ethanol, sonicated in water for 30min, then sonicated in ethanol for 30 min and left to dry.

6. RESULTS

6.1. ANALYSIS OF COFACTORS DRIVING AMYLOID AGGREGATE FORMATION

The study of the polyanion-mediated amyloid aggregate formation from short peptides has been little researched. An investigation of a multitude of factors that might influence (amorphous) aggregation or (ordered) amyloid fibre formation is the first step towards an understanding the underlying processes, starting with the examination of macroscopic properties like gel or visible clumping, followed by spectrophotometric amyloid aggregation assays and leading to the elucidation of the microscopic structures by electron microscopy and X-ray fibre diffraction. In this work, the main focus has been on amyloid complex formation within peptide-nucleic acid (ANA) complexes, but a system employing fatty acid liposomes as an alternative polyanion has also been studied.

6.1.1. SELECTION AND PROPERTIES OF PEPTIDES USED IN THIS WORK

The main focus of this section was on the study of peptide-nucleic acid interactions using a range of peptides and nucleic acids. The peptides were designed to have an amyloidogenic sequence with alternating hydrophobic/ hydrophilic residues.

Preliminary experiments undertaken by Elizabeth Fraser (School of Biosciences, Cardiff University) indicated that short basic peptides with a repeated (KL) sequence pattern in complex with poly(A) RNA can from gels, suggesting the potential formation of (amyloid) fibres. Based on this observation, I initially focused on highly charged peptides with an alternating pattern of hydrophilic lysine and hydrophobic leucine residues that have previously been shown to form gels with high β-sheet content [211-

213], although the question as to whether this is due to amyloid fibre formation was not investigated by the authors. In order to allow alteration to the charge of the peptides, whilst allowing nucleic acid hybridisation, alternating peptides were designed in which the hydrophilic lysine residues were replaced with histidine residues that were protonated at physiological pH values [201]. The ability to carry a positive charge that could be influenced by pH changes was the main reason to choose histidine, although it had other properties that differed from the replaced lysine residues, e.g. hydropathy and shape [201]. Charge modulation by pH change would be expected to occur at pH values close to the pK_a of the imidazole group (pK_a = 6.04; [201]), a range at which most amyloidosis-related polypeptides form amyloid aggregates *in vivo*. In contrast, the high pK_a of 10.54 of the ε-amino group was not compatible with nucleic acid hybridisation [201], and RNA would generally not be stable under these conditions due to hydrolysis of the phosphate backbone[201]. The 7mer peptide TVQFHMH originated from a previous study of amyloidogenic protein design in which the sequence EVQFHMH was suggested to drive amyloid fibre formation. This sequence was chosen as it offered the ability to modulate pH (via the histidine residues) and included an aromatic residue that might prove useful for future biophysical spectroscopic studies. To maximise the potential for interactions with nucleic acids, the negatively charged glutamate residue was replaced with a threonine residue [138]. The negatively charged peptide $(EL)_3$ was used as control for the basic, positively charged peptides mentioned above, although its glutamate residues differed greatly from the lysine or histidine residues of $(HL)_3$ or $(KL)_3$, respectively. Within the pH range used in this work (pH 5.0 to pH 8.0) the glutamate side chains would be mainly deprotonated (pK_a = 4.07 for the γ-carboxyl group; [201]).

In contrast with the alternating hydrophilic/ hydrophobic peptides described above, STVIIE was synthesised to allow a study of the kinetics of amyloid formation (see chapter 6.1.4 and chapter 6.1.9). This peptide was described before as carrying a positive charge at pH 2.6 allowing for interaction with nucleic acids and was able to form amyloid on its own [143]. TVQFHMH formed amyloid on its own, but the required concentration was incompatible with CD spectroscopy, the method chosen to follow the conformational conformation (see chapter 6.1.9). The other peptides might also have formed amyloid on their own at higher concentrations (not tested), as this was likely to be a generic property of all polypeptide sequences [139].

All peptides were readily water-soluble up to 20 mM (which was set as the normal peptide stock solution concentration) with the exception of $(HL)_5$ which required warming to 37°C to allow stock solutions of 10 mM to be generated. The peptides were found to act as weak surfactants as indicated by froth formation if solutions were vortexted or pipetted vigorously. Because of these properties, care was taken to avoid bubble formation immediately prior to use in the assays. None of the peptides were identified as being prone to amyloid formation using the Zyggregator algorithm [199], most likely because this algorithm predicts aggregating (not necessarily amyloid-forming) sequences within larger polypeptide chains. The Waltz algorithm predicted amyloid aggregation only for STVIIE, but not for any other peptide used in this work [200].

6.1.2. PEPTIDE CHARGES

Theoretical peptide charges were calculated using the 'Peptide Property Calculator' from the Genscript website (https://www.genscript.com/ssl-

bin/site2/peptide_calculation.cgi) and were listed for the pH values explored in this work in Table 6-1. This calculation of the peptide charges did not take into account any neighbour effects that might influence the pK_a of functional groups. All residues had the same pK_a regardless of their position within the peptide, which was an unlikely scenario. For example, the central lysine residue of $(KL)_3$ in β-sheet conformation would be close to two neighbouring lysine residues, which, by charge repulsion of the positively charged ε-amino groups, would induce a reduced pK_a of the central ε-amino group with resulting easier deprotonation in order to reduce this repulsion. Additionally, the neighbour effects would be expected to change depending on the peptide conformation, e.g. on how close the relevant groups would get to each other.

Table 6-1: Theoretical peptide charges

Peptide	pH									
	2.6	5.0	5.5	6.0	6.2	6.5	6.8	7.0	8.0	8.5
$(KL)_5$	+6	+5	+5	+5	+5	+5	+5	+5	+5	+5
$(KL)_4$	+5	+4	+4	+4	+4	+4	+4	+4	+4	+4
$(KL)_{3.5}$	+5	+4	+4	+4	+4	+4	+4	+4	+4	+4
$(KL)_3$	+4	+3	+3	+3	+3	+3	+3	+3	+3	+3
$(HL)_5$	+6	+5	+4.5	+4	+3	+2	+1.5	+1	0	-0.25
$(HL)_3$	+4	+3	+3	+2.5	+2	+1.5	+1	+0.5	0	-0.5
TVQFHMH	+3	+2	+2	+1.5	+1.25	+1	+0.5	+0.25	0	-0.5
STVIIE	+1	-1	-1	-1	-1	-1	-1	-1	-1	-1.5

Table 6-1 legend: The charges of the individual peptides were calculated by the Peptide Property Calculator' from the Genscript website (https://www.genscript.com/ssl-bin/site2/peptide_calculation.cgi). The charges were extracted from the output Net Charge vs. pH graphs. All charges were estimates only.

The sequence-dependent pK_a values were reflected in the titrations carried out on some of the peptides used for this work (see Figure 6-1). The titration curves were more complex than expected from the theoretical calculations with more (de)protonation steps. As a consequence the transitions appeared less clear than the calculated titration curves, and equivalence points were difficult to determine. This suggested, as mentioned above, the presence of several functional groups with very similar pK_a values that were (de)protonated sequentially. Nevertheless, the calculated peptide charges were useful approximations for the charge state of the peptides.

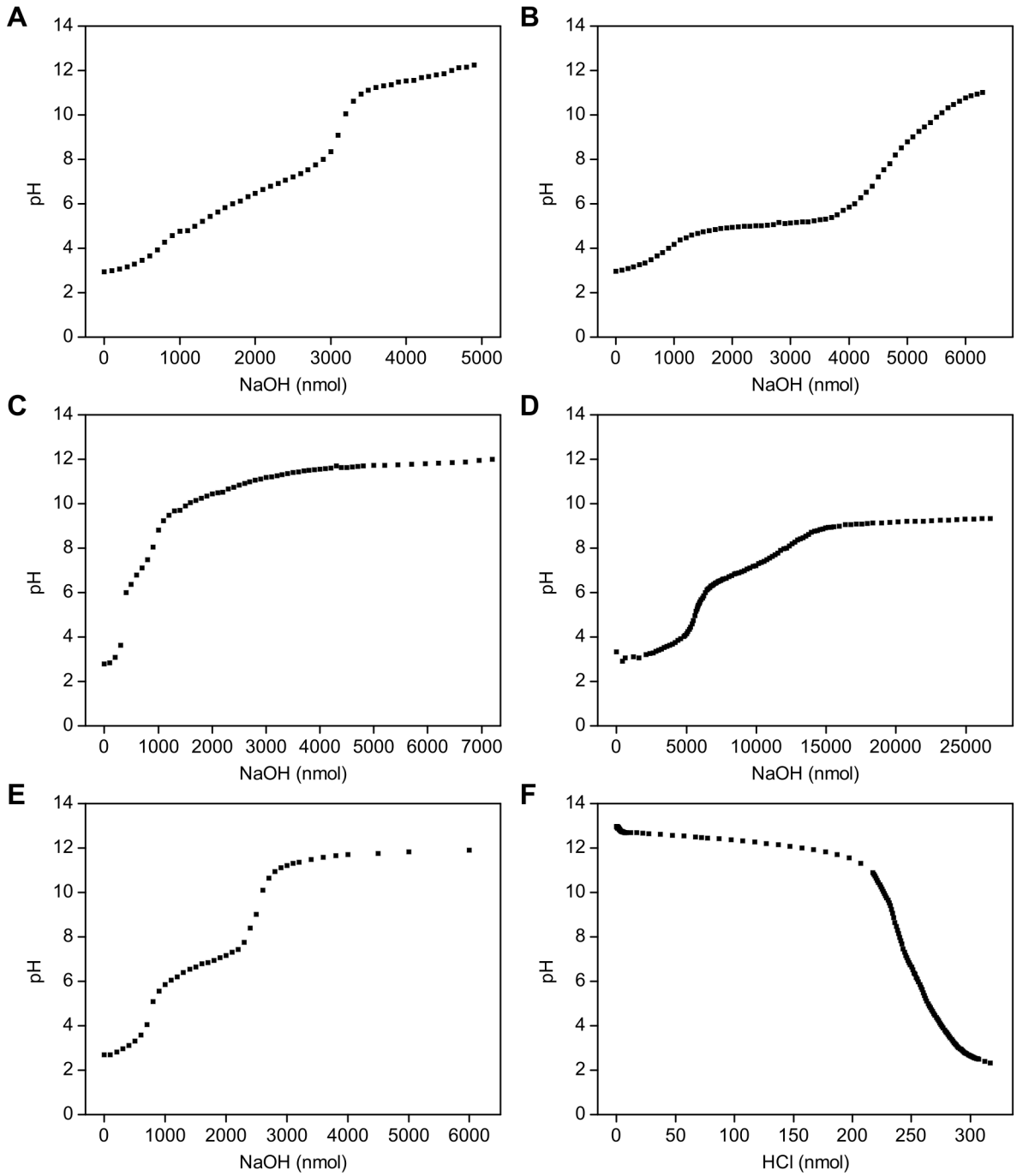

Figure 6-1: Peptide titration curves. The peptides $(HL)_3$ (**A**), $(HL)_5$ (**B**), $(KL)_3$ (**C**), $(KL)_5$ (**D**) and TVQFHMH (**E**) were set to pH ~3 with HCl and subsequently titrated with NaOH, and the peptide $(EL)_3$ was set to pH ~13 with NaOH and subsequently titrated with HCl (**F**).

6.1.3. GEL FORMATION BY PEPTIDE-NUCLEIC ACID MIXTURES

The formation of amyloid complexes by proteins and peptides can be accompanied by the formation of gels over time when the proteinaceous fibres form and create entangled nets, or the appearance of aggregates consisting of densely packed amyloid fibrils. Although a rather weak indicator of amyloid fibre formation, potential gel and aggregate formation would indicate complex formation or polymerisation [72], so I initially examined mixtures of positively charged peptides (at least according to the theoretical calculations) and negatively charged nucleic acids for gel formation to find a suitable range for further studies. I looked at various aspects that might have affected amyloid formation like pH (5.0 to 8.0), salt concentration (0 to 150 mM NaCl), and ratio of peptide to nucleic acid.

Gel formation by nucleic acid solutions

The ST DNA stock solution at 20 mM concentration in water formed gels whose strength was dependent on temperature. At room temperature only a weak gel was present, which at 0ºC (stock solution usually kept on ice) increased to a medium strength gel. At higher concentrations generated to produce the 20 mM stock solutions the gel strength increased further, but the solution could always be pipetted. At 10 mM, the highest concentration of ST DNA used for the gel formation assays (see Table 6-2 and Table 6-7), no gel could be detected at room temperature. Most of the gel strength was lost after heat-denaturation of the double-stranded ST-DNA, which then showed like PA RNA and BY RNA only very weak gels at 20 mM concentration at 0ºC. At lower concentrations no gel could be detected with any of the single-stranded nucleic acids. The addition of NaCl did not give rise to any changes in gel strength. The oligonucleotides oligo D, oligo E, oligo F, and the TR-FRET probes did not gel at any concentration.

The gelation of DNA in the presence of cations has been described before, albeit with short fragments (200 +/- 30 bp) of sonicated calf thymus DNA. Fried and Bloomfield used sonicated calf thymus DNA (fragments of about 200 ± 30 bp), which showed gelation from about 100 μM concentration on [214]. This molar concentration would correspond to about a 20 mM concentrations with respect to charges/ bases as used in this work, and indeed a weak gel was seen. The gels of ST DNA used here quickly became weaker at lower concentrations.

Gel formation by $(HL)_3$-anion mixtures

Mixtures of $(HL)_3$ with double-stranded salmon testes (ST DNA) formed gels within 10 seconds that decreased in strength with increasing NaCl concentrations (see Table 6-2), suggesting that gel formation may be dependent on ionic interactions. In the absence of NaCl the strongest gels were observed at lower pH values, corresponding to the most protonated states of the $(HL)_3$ peptide. Note that HEPES had to be used in place of MES to maintain pH 8.0 and effects at this pH my therefore be dependent on buffer-peptide interactions rather than alterations to the protonation state of the peptide. However, trends in gel formation in the presence of MES at lower pHs were consistent with results at pH 8.0, suggesting that effects were most likely due to peptide-mediated charge interactions. At 75 mM NaCl $(HL)_3$ gels were formed at pH 6.5 and pH 6.8, and strengthened over a period of 1 hour. At 150 mM NaCl, gels were generally very weak and did not show a clear dependence on pH. Mixtures of $(HL)_3$ with poly(A) RNA (PA RNA) mostly formed weaker gels than $(HL)_3$-ST DNA mixtures and showed both gel formation and evidence of aggregation in the form of visible aggregates and turbidity at pH 6.2 to pH 8.0. For PA RNA mixtures in the absence of NaCl, weak gels were observed at pH 5.0 and pH 6.2, while at higher pHs aggregation dominated. At 75 mM NaCl, the

same pattern emerged, but the gels were barely detectable. Interestingly, at 150 mM NaCl slightly stronger gels (up to medium) formed while mixing peptide and RNA, but they seemed to convert to visible aggregates and turbidity within 1 hour except at pH 5.0, where a very weak gel was maintained.

To examine the effect of non-polymerised phosphate on gel formation, diethyl phosphate was added at concentrations that matched the charges present within the nucleic acids. Diethyl phosphate under all NaCl concentrations and at all pHs failed to induce gel formation. However, aggregation in the form of visible aggregates or turbidity appeared at pH 8.0 at all NaCl concentrations. Further supporting the suggestion that gel formation required polymerised phosphate, no gels were observed with 5 mM $(HL)_3$ and an equimolar concentration of $NaPO_4$.

The gels of $(HL)_3$-ST DNA at pH 6.2 in the absence of NaCl were the strongest ones observed for this peptide (see Table 6-2). These conditions were chosen to carry out a titration with varying ST DNA concentrations in order to examine if the ratio of peptide to anion had an effect on gel formation, albeit with a lowered peptide concentration of 2.5 mM $(HL)_3$ to allow a wider concentration range to be explored (from 4:1 to 1:4 ST DNA to $(HL)_3$). The strongest gels appeared close to a 1:1 charge ratio at 2.5 mM and 1.3 mM ST DNA (see Table 6.2). Gels became weaker towards higher and lower ST DNA concentrations. No gels were detected at the same peptide concentration when varying concentrations of diethyl phosphate were added.

Table 6-2: Gel formation and visible aggregation by $(HL)_3$ in mixture with (poly)anions.

NaCl	$(HL)_3$	anion	buffer	gel 10 s	agg. 10 s	gel 1 hour	agg. 1 hour?
150 mM	5 mM $(HL)_3$	none	10 mM MES pH 5.0	-		-	
150 mM	5 mM $(HL)_3$	none	10 mM MES pH 6.2	-		-	
150 mM	5 mM $(HL)_3$	none	10 mM MES pH 6.5	-		-	
150 mM	5 mM $(HL)_3$	none	10 mM MES pH 6.8	-		-	
150 mM	5 mM $(HL)_3$	none	10 mM HEPES pH 8.0	-	T	-	T
150 mM	5 mM $(HL)_3$	5 mM ST DNA	10 mM MES pH 5.0	-		*	
150 mM	5 mM $(HL)_3$	5 mM ST DNA	10 mM MES pH 6.2	*		**	
150 mM	5 mM $(HL)_3$	5 mM ST DNA	10 mM MES pH 6.5	*		*	
150 mM	5 mM $(HL)_3$	5 mM ST DNA	10 mM MES pH 6.8	*		**	
150 mM	5 mM $(HL)_3$	5 mM ST DNA	10 mM HEPES pH 8.0	**	A	*	A
150 mM	5 mM $(HL)_3$	5 mM PA RNA	10 mM MES pH 5.0	**		*	
150 mM	5 mM $(HL)_3$	5 mM PA RNA	10 mM MES pH 6.2	**		-	AT
150 mM	5 mM $(HL)_3$	5 mM PA RNA	10 mM MES pH 6.5	*	T	-	AT
150 mM	5 mM $(HL)_3$	5 mM PA RNA	10 mM MES pH 6.8	**	A	-	AT
150 mM	5 mM $(HL)_3$	5 mM PA RNA	10 mM HEPES pH 8.0	***	T	-	AT
150 mM	5 mM $(HL)_3$	5 mM DEP	10 mM MES pH 5.0	-		-	
150 mM	5 mM $(HL)_3$	5 mM DEP	10 mM MES pH 6.2	-		-	
150 mM	5 mM $(HL)_3$	5 mM DEP	10 mM MES pH 6.5	-		-	
150 mM	5 mM $(HL)_3$	5 mM DEP	10 mM MES pH 6.8	-		-	
150 mM	5 mM $(HL)_3$	5 mM DEP	10 mM HEPES pH 8.0	-	T	-	T
150 mM	5 mM $(HL)_3$	none	10 mM MES pH 5.0	-		-	
150 mM	5 mM $(HL)_3$	none	10 mM MES pH 6.2	-		-	
150 mM	5 mM $(HL)_3$	none	10 mM MES pH 6.5	-		-	
150 mM	5 mM $(HL)_3$	none	10 mM MES pH 6.8	-		-	
150 mM	5 mM $(HL)_3$	none	10 mM HEPES pH 8.0	-	T	-	T
75 mM	5 mM $(HL)_3$	none	10 mM MES pH 5.0	-		-	
75 mM	5 mM $(HL)_3$	none	10 mM MES pH 6.2	-		-	
75 mM	5 mM $(HL)_3$	none	10 mM MES pH 6.5	-		-	
75 mM	5 mM $(HL)_3$	none	10 mM MES pH 6.8	-		-	
75 mM	5 mM $(HL)_3$	none	10 mM HEPES pH 8.0	-	T	-	T
75 mM	5 mM $(HL)_3$	5 mM ST DNA	10 mM MES pH 5.0	-		*	
75 mM	5 mM $(HL)_3$	5 mM ST DNA	10 mM MES pH 6.2	**		***	
75 mM	5 mM $(HL)_3$	5 mM ST DNA	10 mM MES pH 6.5	**		***	
75 mM	5 mM $(HL)_3$	5 mM ST DNA	10 mM MES pH 6.8	**		****	
75 mM	5 mM $(HL)_3$	5 mM ST DNA	10 mM HEPES pH 8.0	*	AT	*	AT
75 mM	5 mM $(HL)_3$	5 mM PA RNA	10 mM MES pH 5.0	-		*	
75 mM	5 mM $(HL)_3$	5 mM PA RNA	10 mM MES pH 6.2	*	A	-	A
75 mM	5 mM $(HL)_3$	5 mM PA RNA	10 mM MES pH 6.5	-	AT	-	A
75 mM	5 mM $(HL)_3$	5 mM PA RNA	10 mM MES pH 6.8	-	AT	-	AT
75 mM	5 mM $(HL)_3$	5 mM PA RNA	10 mM HEPES pH 8.0	-	AT	-	AT
75 mM	5 mM $(HL)_3$	5 mM DEP	10 mM MES pH 5.0	-		-	
75 mM	5 mM $(HL)_3$	5 mM DEP	10 mM MES pH 6.2	-		-	
75 mM	5 mM $(HL)_3$	5 mM DEP	10 mM MES pH 6.5	-		-	
75 mM	5 mM $(HL)_3$	5 mM DEP	10 mM MES pH 6.8	-		-	
75 mM	5 mM $(HL)_3$	5 mM DEP	10 mM HEPES pH 8.0	-	T	-	T

NaCl	$(HL)_3$	anion	buffer	gel 10 s	agg. 10 s	gel 1 hour	agg. 1 hour?
0 mM	5 mM $(HL)_3$	none	10 mM MES pH 5.0	-		-	
0 mM	5 mM $(HL)_3$	none	10 mM MES pH 6.2	-		-	
0 mM	5 mM $(HL)_3$	none	10 mM MES pH 6.5	-		-	
0 mM	5 mM $(HL)_3$	none	10 mM MES pH 6.8	-		-	
0 mM	5 mM $(HL)_3$	none	10 mM HEPES pH 8.0	-	T	-	T
0 mM	5 mM $(HL)_3$	5 mM ST DNA	10 mM MES pH 5.0	****		*****	
0 mM	5 mM $(HL)_3$	5 mM ST DNA	10 mM MES pH 6.2	****		*****	
0 mM	5 mM $(HL)_3$	5 mM ST DNA	10 mM MES pH 6.5	***		**	
0 mM	5 mM $(HL)_3$	5 mM ST DNA	10 mM MES pH 6.8	***		***	
0 mM	5 mM $(HL)_3$	5 mM ST DNA	10 mM HEPES pH 8.0	**	A	***	A
0 mM	5 mM $(HL)_3$	5 mM PA RNA	10 mM MES pH 5.0	**		**	
0 mM	5 mM $(HL)_3$	5 mM PA RNA	10 mM MES pH 6.2	**	T	*	A
0 mM	5 mM $(HL)_3$	5 mM PA RNA	10 mM MES pH 6.5	-	AT	-	A
0 mM	5 mM $(HL)_3$	5 mM PA RNA	10 mM MES pH 6.8	-	AT	-	A
0 mM	5 mM $(HL)_3$	5 mM PA RNA	10 mM HEPES pH 8.0	*	T	-	A
0 mM	5 mM $(HL)_3$	5 mM DEP	10 mM MES pH 5.0	-		-	
0 mM	5 mM $(HL)_3$	5 mM DEP	10 mM MES pH 6.2	-		-	
0 mM	5 mM $(HL)_3$	5 mM DEP	10 mM MES pH 6.5	-		-	
0 mM	5 mM $(HL)_3$	5 mM DEP	10 mM MES pH 6.8	-		-	
0 mM	5 mM $(HL)_3$	5 mM DEP	10 mM HEPES pH 8.0	-	T	-	T
0 mM	2.5 mM $(HL)_3$	10 mM ST DNA	10 mM MES pH 6.2	*		*	
0 mM	2.5 mM $(HL)_3$	7.5 mM ST DNA	10 mM MES pH 6.2	**		**	
0 mM	2.5 mM $(HL)_3$	5.0 mM ST DNA	10 mM MES pH 6.2	**		**	
0 mM	2.5 mM $(HL)_3$	2.5 mM ST DNA	10 mM MES pH 6.2	***		****	
0 mM	2.5 mM $(HL)_3$	1.3 mM ST DNA	10 mM MES pH 6.2	***		****	
0 mM	2.5 mM $(HL)_3$	0.8 mM ST DNA	10 mM MES pH 6.2	**		**	
0 mM	2.5 mM $(HL)_3$	0.6 mM ST DNA	10 mM MES pH 6.2	*		*	
150 mM	2.5 mM $(HL)_3$	10 mM DEP	10 mM MES pH 6.2	-		-	
150 mM	2.5 mM $(HL)_3$	7.5 mM DEP	10 mM MES pH 6.2	-		-	
150 mM	2.5 mM $(HL)_3$	5.0 mM DEP	10 mM MES pH 6.2	-		-	
150 mM	2.5 mM $(HL)_3$	2.5 mM DEP	10 mM MES pH 6.2	-		-	
150 mM	2.5 mM $(HL)_3$	1.3 mM DEP	10 mM MES pH 6.2	-		-	
150 mM	2.5 mM $(HL)_3$	0.8 mM DEP	10 mM MES pH 6.2	-		-	
150 mM	2.5 mM $(HL)_3$	0.6 mM DEP	10 mM MES pH 6.2	-		-	
150 mM	500 µM $(HL)_3$	none	10 mM MES pH 6.5	-		-	
150 mM	500 µM $(HL)_3$	50 µM ST DNA	10 mM MES pH 6.5	-		-	
150 mM	6 mM $(HL)_3$ + 0.3 mM FITC-$(HL)_3$	2.5 mM ST DNA + 0.125 mM ATTO550-DNA	10 mM MES pH 5.0	*		*	
150 mM	6 mM $(HL)_3$	2.5 mM ST DNA	10 mM MES pH 6.5	*		*	
150 mM	6 mM $(HL)_3$ + 0.3 mM FITC-$(HL)_3$	2.5 mM ST DNA + 0.125 mM ATTO550-DNA	10 mM MES pH 6.5	*		*	
150 mM	50 µM $(HL)_3$	50 µM ST DNA	10 mM MES pH 5.5	-		-	
150 mM	50 µM $(HL)_3$	50 µM ST DNA	10 mM MES pH 6.0	-		-	
150 mM	50 µM $(HL)_3$	50 µM ST DNA	10 mM MES pH 6.5	-		-	
150 mM	50 µM $(HL)_3$	50 µM ST DNA	10 mM MES pH 8.0	-		-	
150 mM	1 mM $(HL)_3$	1 mM ST DNA	10 mM MES pH 6.2	-		*	
150 mM	6 mM $(HL)_3$	2.5 mM ST DNA	10 mM MES pH 5.0	*		*	
150 mM	5 mM $(HL)_3$	5 mM ST DNA	10 mM MES pH 5.5	-		*	
150 mM	10 mM $(HL)_3$	10 mM ST DNA	10 mM MES pH 6.2	**		***	
75 mM	10 mM $(HL)_3$	none	10 mM MES pH 8.0	-	T	-	T

NaCl	$(HL)_3$	anion	buffer	gel 10 s	agg. 10 s	gel 1 hour	agg. 1 hour?
50 mM	5 mM $(HL)_3$	5 mM ST DNA	10 mM MES pH 6.2	*		*	
0 mM	1 mM $(HL)_3$	none	200 mM bicine pH 8.5	-		-	
0 mM	3.33 mM $(HL)_3$	none	200 mM bicine pH 8.5	-		-	
0 mM	3.33 mM $(HL)_3$	none	883 mM bicine pH 8.5	-	T	-	T
0 mM	1 mM $(HL)_3$	1 mM ST DNA	10 mM MES pH 6.2	**		**	
0 mM	20 mM $(HL)_3$	none	none (pH ~6)	*		n.d.	
0 mM	10 µM (HL)3	0.5 µM oligo E	10 mM MES pH 6.2	-		-	
150 mM	1 mM $(HL)_3$	9 mM ST DNA	10 mM MES pH 6.8	-		n.d.	
150 mM	2 mM $(HL)_3$	8 mM ST DNA	10 mM MES pH 6.8	-		n.d.	
150 mM	3 mM $(HL)_3$	7 mM ST DNA	10 mM MES pH 6.8	-		n.d.	
150 mM	4 mM $(HL)_3$	6 mM ST DNA	10 mM MES pH 6.8	-		n.d.	
150 mM	5 mM $(HL)_3$	5 mM ST DNA	10 mM MES pH 6.8	-		n.d.	
150 mM	6 mM $(HL)_3$	4 mM ST DNA	10 mM MES pH 6.8	*		n.d.	
150 mM	7 mM $(HL)_3$	3 mM ST DNA	10 mM MES pH 6.8	*		n.d.	
150 mM	8 mM $(HL)_3$	2 mM ST DNA	10 mM MES pH 6.8	*		n.d.	
150 mM	9 mM $(HL)_3$	1 mM ST DNA	10 mM MES pH 6.8	*		n.d.	
150 mM	10 mM $(HL)_3$	none	10 mM MES pH 6.8	-		n.d.	
150 mM	10 mM $(HL)_3$	10 mM ST DNA	10 mM MES pH 6.8	**		n.d.	
150 mM	5 mM $(HL)_3$	5 mM $NaPO_4$	10 mM MES pH 6.8	-		n.d.	
150 mM	5 mM $(HL)_3$	5 mM PA RNA	10 mM MES pH 6.8	-		n.d.	
75 mM	12 mM $(HL)_3$	5 mM ST DNA	10 mM MES pH 5.0	-		n.d.	
75 mM	12 mM $(HL)_3$	5 mM ST DNA	10 mM MES pH 6.2	****		n.d.	
75 mM	12 mM $(HL)_3$	5 mM ST DNA	10 mM MES pH 6.5	****		n.d.	
75 mM	12 mM $(HL)_3$	100 mM $NaPO_4$	10 mM MES pH 5.0	-		n.d.	
75 mM	12 mM $(HL)_3$	100 mM $NaPO_4$	10 mM MES pH 6.2	-		n.d.	
75 mM	12 mM $(HL)_3$	100 mM $NaPO_4$	10 mM MES pH 6.5	-		n.d.	
75 mM	2.4 mM (HL)3	5 mM ST DNA	10 mM MES pH 5.0	-		n.d.	
75 mM	2.4 mM (HL)3	5 mM ST DNA	10 mM MES pH 6.2	*		n.d.	
75 mM	2.4 mM (HL)3	5 mM ST DNA	10 mM MES pH 6.5	*		n.d.	
50 mM	10 µM (HL)3	0.5 mM oligo E	10 mM MES pH 6.2	-		-	
150 mM	5 mM (HL)3	100 mM $NaPO_4$	10 mM MES pH 5.0	-		n.d.	
150 mM	5 mM (HL)3	100 mM $NaPO_4$	10 mM MES pH 6.2	-		n.d.	
150 mM	5 mM (HL)3	100 mM $NaPO_4$	10 mM MES pH 6.5	-		n.d.	
150 mM	10 µM (HL)3	0.5 mM oligo E	10 mM MES pH 6.2	-		-	

Table 6-2 legend: The peptide $(HL)_3$ was mixed with equal volumes (poly)anion solutions (ST DNA = salmon testes DNA, PA RNA = poly(A) RNA, DEP = diethyl phosphate, buffer) to give the indicated concentration in the indicated buffers with 0, 75, or 150 mM NaCl. Mixtures were monitored for strength and speed (within 10 seconds during mixing/ 1 hour) of gel formation. Absence of gel was denoted by "-"; n.d. = not determined. Gels were denoted as very strong (*****), strong (****), medium (***), weak (**), or very weak (*), following the classification given in Table 5-2. Aggregation was denoted by A (larger aggregates in clear solution), T (turbidity), and AT (aggregates in turbid solution).

This data was collected in collaboration with Christine Humphreys (Cardiff University).

Some conditions described in Table 6-2above were replicated in subsequent experiments (see sections 6.1.4, 6.1.5, 6.1.6, 6.1.7, and 6.2.3). Where assay-specific requirements dictated, non-standard conditions were occasionally examined and these conditions have been included in Table 6-2 shown. For example, lower concentrations of peptide and DNA had to be used in ThT assays to avoid saturating detector responses. In the case of the ThT assays, the 50 μM and 500 μM peptide concentration failed to form gels. This may have either been a result of a lower ratio of interaction between nucleic acid and peptide or may have resulted from the presence of weaker gels that did not register as being viscous in the assay format (see chapter 6.1.4, Figure 6-4 and Figure 6-5). Similarly, under the conditions used for confocal microscopy (chapter 6.1.6; 6 mM $(HL)_3$ with 2.5 mM ST DNA, pH 6.2 and pH 5.0, 150 mM NaCl) a weak gel appeared, as well as for the same concentrations with 1:20 FITC-$(HL)_3$ and 1:20 ATTO550-ST DNA (used for confocal microscopy; chapter 5.8, Figure 6-13). The solutions used for the TR-FRET studies (1 mM $(HL)_3$ with 1 mM ST DNA in 150 mM NaCl at pH 6.2; chapter 6.2.3, Figure 6-41, Figure 6-44, Figure 6-46) were barely detectable as gels. The fibre diffraction samples (see also Table 5-4 for their composition) formed weak gels with 5 mM $(HL)_3$ with 5 mM ST DNA in 50 mM NaCl at pH 6.2, up to medium gels with 10 mM $(HL)_3$ with 10 mM ST DNA in 150 mM NaCl at pH 6.2 (Chapter 6.1.7, Figure 6-14), and small aggregates became visible as turbidity with 3.33 mM $(HL)_3$ in 883 mM bicine pH 8.5 or (see Chapter 6.1.8, Figure 6-25). The 20 mM $(HL)_3$ stock solution (~pH 6) showed neither gels nor aggregates before it was used to create a fibre diffraction stalk. The samples for electron microscopy (see also chapter 5.7, Table 5-3) showed weak (5 mM

$(HL)_3$, 5 mM ST DNA, 150 mM NaCl, pH 5.5) to medium (1 mM $(HL)_3$, 1 mM ST DNA, pH 6.2) gels (chapter 6.1.5, Figure 6-9).

Gel formation by $(KL)_3$-anion mixtures

$(KL)_3$ formed relatively weak gels, which only appeared in mixtures of the peptide with ST DNA or PA RNA (see Table 6-3). No gel formation could be detected with $(KL)_3$ alone or in mixture with diethyl phosphate. Interestingly, there was some turbidity and gel formation seen at pH 6.2 in the absence of NaCl with $(KL)_3$-ST DNA and $(KL)_3$-PA RNA, suggesting the presence of small aggregates.

Table 6-3: Gel formation and visible aggregation by $(KL)_3$ in mixture with (poly)anions.

NaCl	$(KL)_3$	anion	buffer	gel 10 s	agg. 10 s	gel 1 hour	agg. 1 hour?
150 mM	5 mM $(KL)_3$	none	10 mM MES pH 5.0	-		-	
150 mM	5 mM $(KL)_3$	none	10 mM MES pH 6.2	-		-	
150 mM	5 mM $(KL)_3$	none	10 mM MES pH 6.5	-		-	
150 mM	5 mM $(KL)_3$	none	10 mM MES pH 6.8	-		-	
150 mM	5 mM $(KL)_3$	none	10 mM HEPES pH 8.0	-		-	
150 mM	5 mM $(KL)_3$	5 mM ST DNA	10 mM MES pH 5.0	-		-	
150 mM	5 mM $(KL)_3$	5 mM ST DNA	10 mM MES pH 6.2	-		*	
150 mM	5 mM $(KL)_3$	5 mM ST DNA	10 mM MES pH 6.5	-		*	
150 mM	5 mM $(KL)_3$	5 mM ST DNA	10 mM MES pH 6.8	*		*	
150 mM	5 mM $(KL)_3$	5 mM ST DNA	10 mM HEPES pH 8.0	*		-	
150 mM	50 µM $(KL)_3$	50 µM ST DNA	10 mM HEPES pH 7.0	-		-	
150 mM	5 mM $(KL)_3$	5 mM PA RNA	10 mM MES pH 5.0	*		-	
150 mM	5 mM $(KL)_3$	5 mM PA RNA	10 mM MES pH 6.2	*		*	
150 mM	5 mM $(KL)_3$	5 mM PA RNA	10 mM MES pH 6.5	-		-	
150 mM	5 mM $(KL)_3$	5 mM PA RNA	10 mM MES pH 6.8	-		-	
150 mM	5 mM $(KL)_3$	5 mM PA RNA	10 mM HEPES pH 8.0	-		-	
150 mM	5 mM $(KL)_3$	5 mM DEP	10 mM MES pH 5.0	-		-	
150 mM	5 mM $(KL)_3$	5 mM DEP	10 mM MES pH 6.2	-		-	
150 mM	5 mM $(KL)_3$	5 mM DEP	10 mM MES pH 6.5	-		-	
150 mM	5 mM $(KL)_3$	5 mM DEP	10 mM MES pH 6.8	-		-	
150 mM	5 mM $(KL)_3$	5 mM DEP	10 mM HEPES pH 8.0	-		-	
75 mM	5 mM $(KL)_3$	none	10 mM MES pH 5.0	-		-	
75 mM	5 mM $(KL)_3$	none	10 mM MES pH 6.2	-		-	

NaCl	$(KL)_3$	anion	buffer	gel 10 s	agg. 10 s	gel 1 hour	agg. 1 hour?
75 mM	5 mM $(KL)_3$	none	10 mM MES pH 6.5	-		-	
75 mM	5 mM $(KL)_3$	none	10 mM MES pH 6.8	-		-	
75 mM	5 mM $(KL)_3$	none	10 mM HEPES pH 8.0	-		-	
75 mM	5 mM $(KL)_3$	5 mM ST DNA	10 mM MES pH 5.0	*		*	
75 mM	5 mM $(KL)_3$	5 mM ST DNA	10 mM MES pH 6.2	*		*	
75 mM	5 mM $(KL)_3$	5 mM ST DNA	10 mM MES pH 6.5	-		*	
75 mM	5 mM $(KL)_3$	5 mM ST DNA	10 mM MES pH 6.8	-		*	
75 mM	5 mM $(KL)_3$	5 mM ST DNA	10 mM HEPES pH 8.0	-		*	
75 mM	5 mM $(KL)_3$	5 mM PA RNA	10 mM MES pH 5.0	***		**	
75 mM	5 mM $(KL)_3$	5 mM PA RNA	10 mM MES pH 6.2	*		*	
75 mM	5 mM $(KL)_3$	5 mM PA RNA	10 mM MES pH 6.5	-		*	
75 mM	5 mM $(KL)_3$	5 mM PA RNA	10 mM MES pH 6.8	-		-	
75 mM	5 mM $(KL)_3$	5 mM PA RNA	10 mM HEPES pH 8.0	-		-	
75 mM	5 mM $(KL)_3$	5 mM DEP	10 mM MES pH 5.0	-		-	
75 mM	5 mM $(KL)_3$	5 mM DEP	10 mM MES pH 6.2	-		-	
75 mM	5 mM $(KL)_3$	5 mM DEP	10 mM MES pH 6.5	-		-	
75 mM	5 mM $(KL)_3$	5 mM DEP	10 mM MES pH 6.8	-		-	
75 mM	5 mM $(KL)_3$	5 mM DEP	10 mM HEPES pH 8.0	-		-	
0 mM	5 mM $(KL)_3$	none	10 mM MES pH 5.0	-		-	
0 mM	5 mM $(KL)_3$	none	10 mM MES pH 6.2	-		-	
0 mM	5 mM $(KL)_3$	none	10 mM MES pH 6.5	-		-	
0 mM	5 mM $(KL)_3$	none	10 mM MES pH 6.8	-		-	
0 mM	5 mM $(KL)_3$	none	10 mM HEPES pH 8.0	-		-	
0 mM	5 mM $(KL)_3$	5 mM ST DNA	10 mM MES pH 5.0	*		*	
0 mM	5 mM $(KL)_3$	5 mM ST DNA	10 mM MES pH 6.2	*	T	*	T
0 mM	5 mM $(KL)_3$	5 mM ST DNA	10 mM MES pH 6.5	**		**	
0 mM	5 mM $(KL)_3$	5 mM ST DNA	10 mM MES pH 6.8	*		*	
0 mM	5 mM $(KL)_3$	5 mM ST DNA	10 mM HEPES pH 8.0	-		*	
0 mM	5 mM $(KL)_3$	5 mM PA RNA	10 mM MES pH 5.0	*		*	
0 mM	5 mM $(KL)_3$	5 mM PA RNA	10 mM MES pH 6.2	*	T	*	T
0 mM	5 mM $(KL)_3$	5 mM PA RNA	10 mM MES pH 6.5	-		*	
0 mM	5 mM $(KL)_3$	5 mM PA RNA	10 mM MES pH 6.8	-		-	
0 mM	5 mM $(KL)_3$	5 mM PA RNA	10 mM HEPES pH 8.0	-		-	
0 mM	5 mM $(KL)_3$	5 mM DEP	10 mM MES pH 5.0	-		-	
0 mM	5 mM $(KL)_3$	5 mM DEP	10 mM MES pH 6.2	-		-	
0 mM	5 mM $(KL)_3$	5 mM DEP	10 mM MES pH 6.5	-		-	
0 mM	5 mM $(KL)_3$	5 mM DEP	10 mM MES pH 6.8	-		-	
0 mM	5 mM $(KL)_3$	5 mM DEP	10 mM HEPES pH 8.0	-		-	
0 mM	5 mM $(KL)_3$	none	10 mM MES pH 5.0	-		-	
0 mM	5 mM $(KL)_3$	none	10 mM MES pH 6.2	-		-	
0 mM	5 mM $(KL)_3$	none	10 mM MES pH 6.5	-		-	
0 mM	5 mM $(KL)_3$	none	10 mM MES pH 6.8	-		-	
0 mM	5 mM $(KL)_3$	none	10 mM HEPES pH 8.0	-		-	
150 mM	17 µM $(KL)_3$	50 µM ST DNA	10 mM HEPES pH 8.0	-		-	
0 mM	1 mM $(KL)_3$	none	200 mM bicine pH 8.5	-		-	
0 mM	3.33 mM $(KL)_3$	none	200 mM bicine pH 8.5	-		-	
0 mM	0.33 mM $(KL)_3$	1 mM PA RNA	10 mM HEPES pH 7.0	*		*	
0 mM	21.6 mM $(KL)_3$	10.8 mM HT DNA	pH 6.0	****	A	****	A
0 mM	10 mM $(KL)_3$	10 mM ST DNA	10 mM HEPES pH 7.0	***		***	

Table 6-3 legend: The peptide $(KL)_3$ was mixed with equal volumes of (poly)anion solutions (ST DNA = salmon testes DNA, PA RNA = poly(A) RNA, DEP = diethyl phosphate, buffer) to

give the indicated concentration in the indicated buffers with 0, 75, or 150 mM NaCl. Mixtures were monitored for strength and speed (within 10 seconds during mixing/ 1 hour) of gel formation. Absence of gel is denoted by "-". Gels were denoted as very strong (*****), strong (****), medium (***), weak (**), or very weak (*), following the classification given in Table 5-2. Aggregation was denoted by A (larger aggregates in clear solution), T (turbidity), and AT (aggregates in turbid solution).

This data was collected in collaboration with Christine Humphreys (Cardiff University).

Regarding the concentrations and conditions used in other experiments (see Table 6-3 at the bottom), the $(KL)_3$-PA RNA sample for electron microscopy (0.33 mM $(KL)_3$, 1 mM PA RNA, pH 7; chapter 6.1.5, Figure 6-10) formed a very weak gel. No gel could be detected at the conditions used for the Thioflavin T assay (17 μM $(KL)_3$, 50 μM ST DNA, 150 mM NaCl, pH 8; chapter 6.1.4, Figure 6-4). At the very high concentrations (21.6 mM $(KL)_3$ with 10.8 mM HT DNA at pH 6, and 10 mM $(KL)_3$ with 10 mM ST DNA at pH 7) used to create the fibre diffraction samples (chapter 5.9, Table 5-4; chapter 6.1.7, Figure 6-15, Table 6-12) medium to strong gels appeared.

Gel formation by $(EL)_3$-anion mixtures

The peptide $(EL)_3$ showed no gel formation under the conditions explored (0, 75, and 150 mM NaCl; pH 5.0, 6.2, 6.5, 6.8, and 8.0) with ST DNA, PA RNA, diethyl phosphate, or on its own. It could form a gel at about pH 2 (in 20 mM HCl) during purification (strength not determined due to unknown concentration).

Table 6-4: Gel formation and visible aggregation by $(EL)_3$ in mixture with (poly)anions.

NaCl	$(EL)_3$	anion	buffer	gel 10 s	agg. 10 s	gel 1 hour	agg. 1 hour?
150 mM	5 mM $(EL)_3$	none	10 mM MES pH 5.0	-		-	
150 mM	5 mM $(EL)_3$	none	10 mM MES pH 6.2	-		-	
150 mM	5 mM $(EL)_3$	none	10 mM MES pH 6.5	-		-	
150 mM	5 mM $(EL)_3$	none	10 mM MES pH 6.8	-		-	
150 mM	5 mM $(EL)_3$	none	10 mM HEPES pH 8.0	-		-	
150 mM	5 mM $(EL)_3$	5 mM ST DNA	10 mM MES pH 5.0	-		-	
150 mM	5 mM $(EL)_3$	5 mM ST DNA	10 mM MES pH 6.2	-		-	
150 mM	5 mM $(EL)_3$	5 mM ST DNA	10 mM MES pH 6.5	-		-	
150 mM	5 mM $(EL)_3$	5 mM ST DNA	10 mM MES pH 6.8	-		-	
150 mM	5 mM $(EL)_3$	5 mM ST DNA	10 mM HEPES pH 8.0	-		-	
150 mM	5 mM $(EL)_3$	5 mM PA RNA	10 mM MES pH 5.0	-		-	
150 mM	5 mM $(EL)_3$	5 mM PA RNA	10 mM MES pH 6.2	-		-	
150 mM	5 mM $(EL)_3$	5 mM PA RNA	10 mM MES pH 6.5	-		-	
150 mM	5 mM $(EL)_3$	5 mM PA RNA	10 mM MES pH 6.8	-		-	
150 mM	5 mM $(EL)_3$	5 mM PA RNA	10 mM HEPES pH 8.0	-		-	
150 mM	5 mM $(EL)_3$	5 mM DEP	10 mM MES pH 5.0	-		-	
150 mM	5 mM $(EL)_3$	5 mM DEP	10 mM MES pH 6.2	-		-	
150 mM	5 mM $(EL)_3$	5 mM DEP	10 mM MES pH 6.5	-		-	
150 mM	5 mM $(EL)_3$	5 mM DEP	10 mM MES pH 6.8	-		-	
150 mM	5 mM $(EL)_3$	5 mM DEP	10 mM HEPES pH 8.0	-		-	
75 mM	5 mM $(EL)_3$	none	10 mM MES pH 5.0	-		-	
75 mM	5 mM $(EL)_3$	none	10 mM MES pH 6.2	-		-	
75 mM	5 mM $(EL)_3$	none	10 mM MES pH 6.5	-		-	
75 mM	5 mM $(EL)_3$	none	10 mM MES pH 6.8	-		-	
75 mM	5 mM $(EL)_3$	none	10 mM HEPES pH 8.0	-		-	
75 mM	5 mM $(EL)_3$	5 mM ST DNA	10 mM MES pH 5.0	-		-	
75 mM	5 mM $(EL)_3$	5 mM ST DNA	10 mM MES pH 6.2	-		-	
75 mM	5 mM $(EL)_3$	5 mM ST DNA	10 mM MES pH 6.5	-		-	
75 mM	5 mM $(EL)_3$	5 mM ST DNA	10 mM MES pH 6.8	-		-	
75 mM	5 mM $(EL)_3$	5 mM ST DNA	10 mM HEPES pH 8.0	-		-	
75 mM	5 mM $(EL)_3$	5 mM PA RNA	10 mM MES pH 5.0	-		-	
75 mM	5 mM $(EL)_3$	5 mM PA RNA	10 mM MES pH 6.2	-		-	
75 mM	5 mM $(EL)_3$	5 mM PA RNA	10 mM MES pH 6.5	-		-	
75 mM	5 mM $(EL)_3$	5 mM PA RNA	10 mM MES pH 6.8	-		-	
75 mM	5 mM $(EL)_3$	5 mM PA RNA	10 mM HEPES pH 8.0	-		-	
75 mM	5 mM $(EL)_3$	5 mM DEP	10 mM MES pH 5.0	-		-	
75 mM	5 mM $(EL)_3$	5 mM DEP	10 mM MES pH 6.2	-		-	
75 mM	5 mM $(EL)_3$	5 mM DEP	10 mM MES pH 6.5	-		-	
75 mM	5 mM $(EL)_3$	5 mM DEP	10 mM MES pH 6.8	-		-	
75 mM	5 mM $(EL)_3$	5 mM DEP	10 mM HEPES pH 8.0	-		-	
0 mM	5 mM $(EL)_3$	none	10 mM MES pH 5.0	-		-	
0 mM	5 mM $(EL)_3$	none	10 mM MES pH 6.2	-		-	
0 mM	5 mM $(EL)_3$	none	10 mM MES pH 6.5	-		-	
0 mM	5 mM $(EL)_3$	none	10 mM MES pH 6.8	-		-	
0 mM	5 mM $(EL)_3$	none	10 mM HEPES pH 8.0	-		-	
0 mM	5 mM $(EL)_3$	5 mM ST DNA	10 mM MES pH 5.0	-		-	
0 mM	5 mM $(EL)_3$	5 mM ST DNA	10 mM MES pH 6.2	-		-	
0 mM	5 mM $(EL)_3$	5 mM ST DNA	10 mM MES pH 6.5	-		-	
0 mM	5 mM $(EL)_3$	5 mM ST DNA	10 mM MES pH 6.8	-		-	
0 mM	5 mM $(EL)_3$	5 mM ST DNA	10 mM HEPES pH 8.0	-		-	
0 mM	5 mM $(EL)_3$	5 mM PA RNA	10 mM MES pH 5.0	-		-	
0 mM	5 mM $(EL)_3$	5 mM PA RNA	10 mM MES pH 6.2	-		-	
0 mM	5 mM $(EL)_3$	5 mM PA RNA	10 mM MES pH 6.5	-		-	
0 mM	5 mM $(EL)_3$	5 mM PA RNA	10 mM MES pH 6.8	-		-	

NaCl	$(EL)_3$	anion	buffer	gel 10 s	agg. 10 s	gel 1 hour	agg. 1 hour?
0 mM	5 mM $(EL)_3$	5 mM PA RNA	10 mM HEPES pH 8.0	-		-	
0 mM	5 mM $(EL)_3$	5 mM DEP	10 mM MES pH 5.0	-		-	
0 mM	5 mM $(EL)_3$	5 mM DEP	10 mM MES pH 6.2	-		-	
0 mM	5 mM $(EL)_3$	5 mM DEP	10 mM MES pH 6.5	-		-	
0 mM	5 mM $(EL)_3$	5 mM DEP	10 mM MES pH 6.8	-		-	
0 mM	5 mM $(EL)_3$	5 mM DEP	10 mM HEPES pH 8.0	-		-	
150 mM	500 µM $(EL)_3$	none	10 mM MES pH 6.5	-		-	
150 mM	500 µM $(EL)_3$	500 µM ST DNA	10 mM MES pH 6.5	-		-	
0 mM	1 mM $(EL)_3$	none	200 mM bicine pH 8.5	-		-	
0 mM	3.33 mM $(EL)_3$	none	200 mM bicine pH 8.5	-		-	

Table 6-4 legend: The peptide $(EL)_3$ was mixed with equal of volumes (poly)anion solutions (ST DNA = salmon testes DNA, PA RNA = poly(A) RNA, DEP = diethyl phosphate, buffer) to give the indicated concentration in the indicated buffers with 0, 75, or 150 mM NaCl. Mixtures were monitored for strength and speed (within 10 seconds during mixing/ 1 hour) of gel formation. Absence of gel is denoted by "-". Gels were denoted as very strong (*****), strong (****), medium (***), weak (**), or very weak (*), following the classification given in Table 5-2. No gel formation of $(EL)_3$ alone or in mixtures with anions was observed under the explored conditions.

No gels or aggregates could be found in the $(EL)_3$-anion samples prepared as control for the (calculated) positively charged peptide, for example at 500 µM $(EL)_3$ with and without 500 µM ST DNA used for the kinetic Thioflavin T assay (chapter 6.1.4, Figure 6-5), or with 1 mM or 3.33 mM in 200 mM bicine pH 8.5 (chapter 6.1.8, Figure 6-20, Figure 6-21, Figure 6-22, and Figure 6-23).

Gel formation by $(KL)_5$-anion mixtures

Within the 10 seconds of mixing $(KL)_5$-ST DNA mixtures formed very strong gels at all pHs and NaCl concentrations examined (see Table 6-5). These did not increase in strength within 1 hour, but large, white and partially translucent aggregates became

visible. Mixtures of $(KL)_5$ with PA RNA showed mainly aggregates at 0 and 75 mM NaCl. At 150 mM NaCl $(KL)_5$-PA RNA showed gels at pH 6.5 to 8.0 and aggregation at pH 5.0 to 6.5. Neither gel formation nor visible aggregates appeared in $(KL)_5$-DEP mixtures or $(KL)_5$ alone.

Table 6-5: Gel formation and visible aggregation by $(KL)_5$ in mixture with (poly)anions.

NaCl	$(KL)_5$	anion	buffer	gel 10 s	agg. 10 s	gel 1 hour	agg. 1 hour?
150 mM	5 mM $(KL)_5$	none	10 mM MES pH 5.0	-		-	
150 mM	5 mM $(KL)_5$	none	10 mM MES pH 6.2	-		-	
150 mM	5 mM $(KL)_5$	none	10 mM MES pH 6.5	-		-	
150 mM	5 mM $(KL)_5$	none	10 mM MES pH 6.8	-		-	
150 mM	5 mM $(KL)_5$	none	10 mM HEPES pH 8.0	-		-	
150 mM	5 mM $(KL)_5$	5 mM ST DNA	10 mM MES pH 5.0	****		*****	A
150 mM	5 mM $(KL)_5$	5 mM ST DNA	10 mM MES pH 6.2	****		****	A
150 mM	5 mM $(KL)_5$	5 mM ST DNA	10 mM MES pH 6.5	****		****	A
150 mM	5 mM $(KL)_5$	5 mM ST DNA	10 mM MES pH 6.8	****		****	A
150 mM	5 mM $(KL)_5$	5 mM ST DNA	10 mM HEPES pH 8.0	*****		*****	A
150 mM	5 mM $(KL)_5$	5 mM PA RNA	10 mM MES pH 5.0	-	A	-	A
150 mM	5 mM $(KL)_5$	5 mM PA RNA	10 mM MES pH 6.2	-	A	-	A
150 mM	5 mM $(KL)_5$	5 mM PA RNA	10 mM MES pH 6.5	**	A	**	A
150 mM	5 mM $(KL)_5$	5 mM PA RNA	10 mM MES pH 6.8	***		***	
150 mM	5 mM $(KL)_5$	5 mM PA RNA	10 mM HEPES pH 8.0	***		***	
150 mM	5 mM $(KL)_3$	5 mM DEP	10 mM MES pH 5.0	-		-	
150 mM	5 mM $(KL)_5$	5 mM DEP	10 mM MES pH 6.2	-		-	
150 mM	5 mM $(KL)_5$	5 mM DEP	10 mM MES pH 6.5	-		-	
150 mM	5 mM $(KL)_5$	5 mM DEP	10 mM MES pH 6.8	-		-	
150 mM	5 mM $(KL)_5$	5 mM DEP	10 mM HEPES pH 8.0	-		-	
75 mM	5 mM $(KL)_5$	none	10 mM MES pH 5.0	-		-	
75 mM	5 mM $(KL)_5$	none	10 mM MES pH 6.2	-		-	
75 mM	5 mM $(KL)_5$	none	10 mM MES pH 6.5	-		-	
75 mM	5 mM $(KL)_5$	none	10 mM MES pH 6.8	-		-	
75 mM	5 mM $(KL)_5$	none	10 mM HEPES pH 8.0	-		-	
75 mM	5 mM $(KL)_5$	5 mM ST DNA	10 mM MES pH 5.0	*****		*****	A
75 mM	5 mM $(KL)_5$	5 mM ST DNA	10 mM MES pH 6.2	*****		*****	A
75 mM	5 mM $(KL)_5$	5 mM ST DNA	10 mM MES pH 6.5	*****		*****	A
75 mM	5 mM $(KL)_5$	5 mM ST DNA	10 mM MES pH 6.8	*****		*****	A
75 mM	5 mM $(KL)_5$	5 mM ST DNA	10 mM HEPES pH 8.0	*****		*****	A
75 mM	5 mM $(KL)_5$	5 mM PA RNA	10 mM MES pH 5.0	-	A	-	A
75 mM	5 mM $(KL)_5$	5 mM PA RNA	10 mM MES pH 6.2	-	A	-	A
75 mM	5 mM $(KL)_5$	5 mM PA RNA	10 mM MES pH 6.5	-	A	-	A
75 mM	5 mM $(KL)_5$	5 mM PA RNA	10 mM MES pH 6.8	-	A	-	A
75 mM	5 mM $(KL)_5$	5 mM PA RNA	10 mM HEPES pH 8.0	-	A	-	A
75 mM	5 mM $(KL)_5$	5 mM DEP	10 mM MES pH 5.0	-		-	
75 mM	5 mM $(KL)_5$	5 mM DEP	10 mM MES pH 6.2	-		-	
75 mM	5 mM $(KL)_5$	5 mM DEP	10 mM MES pH 6.5	-		-	
75 mM	5 mM $(KL)_5$	5 mM DEP	10 mM MES pH 6.8	-		-	

NaCl	$(KL)_5$	anion	buffer	gel 10 s	agg. 10 s	gel 1 hour	agg. 1 hour?
75 mM	5 mM $(KL)_5$	5 mM DEP	10 mM HEPES pH 8.0	-		-	
0 mM	5 mM $(KL)_5$	none	10 mM MES pH 5.0	-		-	
0 mM	5 mM $(KL)_5$	none	10 mM MES pH 6.2	-		-	
0 mM	5 mM $(KL)_5$	none	10 mM MES pH 6.5	-		-	
0 mM	5 mM $(KL)_5$	none	10 mM MES pH 6.8	-		-	
0 mM	5 mM $(KL)_5$	none	10 mM HEPES pH 8.0	-		-	
0 mM	5 mM $(KL)_5$	5 mM ST DNA	10 mM MES pH 5.0	*****		*****	A
0 mM	5 mM $(KL)_5$	5 mM ST DNA	10 mM MES pH 6.2	*****		*****	A
0 mM	5 mM $(KL)_5$	5 mM ST DNA	10 mM MES pH 6.5	*****		*****	A
0 mM	5 mM $(KL)_5$	5 mM ST DNA	10 mM MES pH 6.8	*****		*****	A
0 mM	5 mM $(KL)_5$	5 mM ST DNA	10 mM HEPES pH 8.0	*****		*****	A
0 mM	5 mM $(KL)_5$	5 mM PA RNA	10 mM MES pH 5.0	-	A	-	A
0 mM	5 mM $(KL)_5$	5 mM PA RNA	10 mM MES pH 6.2	-	T	-	A
0 mM	5 mM $(KL)_5$	5 mM PA RNA	10 mM MES pH 6.5	-	A	-	A
0 mM	5 mM $(KL)_5$	5 mM PA RNA	10 mM MES pH 6.8	-	A	-	A
0 mM	5 mM $(KL)_5$	5 mM PA RNA	10 mM HEPES pH 8.0	-	A	-	A
0 mM	5 mM $(KL)_5$	5 mM DEP	10 mM MES pH 5.0	-		-	
0 mM	5 mM $(KL)_5$	5 mM DEP	10 mM MES pH 6.2	-		-	
0 mM	5 mM $(KL)_5$	5 mM DEP	10 mM MES pH 6.5	-		-	
0 mM	5 mM $(KL)_5$	5 mM DEP	10 mM MES pH 6.8	-		-	
0 mM	5 mM $(KL)_5$	5 mM DEP	10 mM HEPES pH 8.0	-		-	
150 mM	0.2 mM $(KL)_5$	1 mM ST DNA	10 mM HEPES pH 7.0	**		**	
150 mM	1 mM $(KL)_5$	5 mM ST DNA	10 mM HEPES pH 7.0	***		***	
150 mM	5 mM $(KL)_5$	5 mM ST DNA	10 mM HEPES pH 7.0	****		****	
150 mM	5 mM $(KL)_5$	5 mM ST DNA	10 mM HEPES pH 7.0	*****		*****	
150 mM	1 mM $(KL)_5$	9 mM ST DNA	10 mM MES pH 6.8	-		n.d.	
150 mM	2 mM $(KL)_5$	8 mM ST DNA	10 mM MES pH 6.8	**		n.d.	
150 mM	3 mM $(KL)_5$	7 mM ST DNA	10 mM MES pH 6.8	***		n.d.	
150 mM	4 mM $(KL)_5$	6 mM ST DNA	10 mM MES pH 6.8	***		n.d.	
150 mM	5 mM $(KL)_5$	5 mM ST DNA	10 mM MES pH 6.8	***		n.d.	
150 mM	6 mM $(KL)_5$	4 mM ST DNA	10 mM MES pH 6.8	****		n.d.	
150 mM	7 mM $(KL)_5$	3 mM ST DNA	10 mM MES pH 6.8	****		n.d.	
150 mM	8 mM $(KL)_5$	2 mM ST DNA	10 mM MES pH 6.8	****		n.d.	
150 mM	9 mM $(KL)_5$	1 mM ST DNA	10 mM MES pH 6.8	****		n.d.	
150 mM	10 mM $(KL)_5$	none	10 mM MES pH 6.8	-		n.d.	
150 mM	10 mM $(KL)_5$	10 mM ST DNA	10 mM MES pH 6.8	****		n.d.	
150 mM	1 mM $(KL)_5$	5 mM $NaPO_4$	10 mM MES pH 6.8	-		n.d.	
150 mM	9 mM $(KL)_5$	45 mM $NaPO_4$	10 mM MES pH 6.8	-		n.d.	
150 mM	5 mM $(KL)_5$	100 mM $NaPO_4$	10 mM MES pH 6.2	-		n.d.	

Table 6-5 legend: The peptide $(KL)_5$ was mixed with equal volumes of (poly)anion solutions (ST DNA = salmon testes DNA, PA RNA = poly(A) RNA, DEP = diethyl phosphate, buffer) to give the indicated concentration in the indicated buffers with 0, 75, or 150 mM NaCl. Mixtures were monitored for strength and speed (within 10 seconds during mixing/ 1 hour) of gel formation. Absence of gel is denoted by "-"; n.d. = not determined. Gels were denoted as very strong (*****), strong (****), medium (***), weak (**), or very weak (*), following

the classification given in Table 5-2. Aggregation was denoted by A (larger aggregates in clear solution), T (turbidity), and AT (aggregates in turbid solution).

This data was collected in collaboration with Christine Humphreys (Cardiff University).

Regarding the concentrations and conditions used in other experiments (see Table 6-5 at the bottom), the $(KL)_5$-ST DNA samples for X-ray fibre diffraction (5 mM $(KL)_5$ with 5 mM ST DNA with and without 150 mM NaCl in 10 mM HEPES pH 7; see chapter 5.9, Table 5-4, and chapter 6.1.7, Figure 6-15) formed weak to strong gels, similar to the electron microscopy samples (0.2 mM $(KL)_5$ with 1 mM ST DNA or 1 mM $(KL)_5$ with 5 mM ST DNA in 10 mM HEPES pH 7.0 with 150 mM NaCl (see chapter 5.7, Table 5-3, and chapter 6.1.5, RNA sample for electron microscopy (0.33 mM $(KL)_3$, 1 mM PA RNA, pH 7; chapter 6.1.5, Figure 6-10) formed a very weak gel. No gel could be detected at the conditions used for the Thioflavin T assay (17 μM $(KL)_3$, 50 μM ST DNA, 150 mM NaCl, pH 8; chapter 6.1.4.1.4, Figure 6-4). At the very high concentrations (21.6 mM $(KL)_3$ with 10.8 mM HT DNA at pH 6, and 10 mM $(KL)_3$ with 10 mM ST DNA at pH 7) used to create the fibre diffraction samples (chapter 5.9, Table 5-4; chapter 6.1.7, Figure 6-15, Table 6-12) medium to strong gels appeared.

Gel formation by $(HL)_5$-anion mixtures

The peptide $(HL)_5$, was not soluble in water at 20 mM like $(HL)_3$, $(KL)_3$, $(KL)_5$, $(EL)_3$ or TVQFHMH but formed a turbid solution containing small aggregates. A clear 10 mM stock solution could be achieved by mild heating to 42°C for about 30 minutes, but this limited the concentrations that could be explored for gel formation so only mixtures of 1

mM $(HL)_5$ with various anions were examined (see Table 6-6, middle). A smaller series of gel formation examinations (only pH 5.0, 6.5 and 8.0) were carried out with a final concentration of 5 mM $(HL)_5$ generated from a turbid 20 mM $(HL)_5$ stock solution that contained visible aggregates (see Table 6-6, top).

At 1 mM $(HL)_5$ final concentration, hardly any gels could be detected (see Table 6-6, middle). While no aggregation appeared, only very weak gels could be seen. They appeared at 150 mM NaCl throughout all pH values with ST DNA, but were sporadic in 75 mM and 0 mM NaCl, where they could mainly be detected in $(HL)_5$-PA RNA mixtures. Interestingly, some very weak gels developed within 1 hour at 150 mM NaCl with the peptide alone.

At 5 mM $(HL)_5$, aggregation and turbidity were dominant, partially due to their presence in the 20 mM stock solution (Table 6-6, top). Solutions of $(HL)_5$ alone or with diethyl phosphate showed aggregates and turbidity at all pHs independent of NaCl concentration. In the absence of NaCl the turbidity of $(HL)_5$-ST DNA and $(HL)_5$-PA RNA mixtures disappeared within 1 hour and larger aggregates formed. Only very weak gels formed at the lower pH values. At 75 mM NaCl, very weak gels formed only at pH 5.0 in $(HL)_5$-ST DNA and $(HL)_5$-PA RNA mixtures. Turbidity and aggregates were usually maintained, with $(HL)_5$-PA RNA at pH 8.0 lacking turbidity and $(HL)_5$-ST DNA losing turbidity within 1 hour. In 150 mM NaCl weak and medium gels developed in $(HL)_5$-PA RNA solutions within 1 hour at pH 6.5 and pH 5.0, respectively. $(HL)_5$-ST DNA showed very weak gels at pH 5.0, but not at any other pH in 150 mM NaCl.

Table 6-6: Gel formation and visible aggregation by $(HL)_5$ in mixture with (poly)anions

NaCl	$(HL)_5$	anion	buffer	gel 10 s	agg. 10 s	gel 1 hour	agg. 1 hour?
150 mM	5 mM $(HL)_5$	none	10 mM MES pH 5.0	-	AT	-	AT
150 mM	5 mM $(HL)_5$	none	10 mM MES pH 6.5	-	AT	-	AT
150 mM	5 mM $(HL)_5$	none	10 mM MES pH 8.0	-	AT	-	AT
150 mM	5 mM $(HL)_5$	5 mM ST DNA	10 mM MES pH 5.0	*	AT	*	AT
150 mM	5 mM $(HL)_5$	5 mM ST DNA	10 mM MES pH 6.5	-	AT	-	AT
150 mM	5 mM $(HL)_5$	5 mM ST DNA	10 mM MES pH 8.0	-	AT	-	AT
150 mM	5 mM $(HL)_5$	5 mM PA RNA	10 mM MES pH 5.0	-	AT	***	A
150 mM	5 mM $(HL)_5$	5 mM PA RNA	10 mM MES pH 6.5	-	AT	**	T
150 mM	5 mM $(HL)_5$	5 mM PA RNA	10 mM MES pH 8.0	-	AT	-	AT
150 mM	5 mM $(HL)_5$	5 mM DEP	10 mM MES pH 5.0	-	AT	-	AT
150 mM	5 mM $(HL)_5$	5 mM DEP	10 mM MES pH 6.5	-	AT	-	AT
150 mM	5 mM $(HL)_5$	5 mM DEP	10 mM MES pH 8.0	-	AT	-	AT
75 mM	5 mM $(HL)_5$	none	10 mM MES pH 5.0	-	AT	-	AT
75 mM	5 mM $(HL)_5$	none	10 mM MES pH 6.5	-	AT	-	AT
75 mM	5 mM $(HL)_5$	none	10 mM MES pH 8.0	-	AT	-	AT
75 mM	5 mM $(HL)_5$	5 mM ST DNA	10 mM MES pH 5.0	*	AT	*	A
75 mM	5 mM $(HL)_5$	5 mM ST DNA	10 mM MES pH 6.5	-	AT	-	AT
75 mM	5 mM $(HL)_5$	5 mM ST DNA	10 mM MES pH 8.0	-	AT	-	AT
75 mM	5 mM $(HL)_5$	5 mM PA RNA	10 mM MES pH 5.0	-	AT	*	AT
75 mM	5 mM $(HL)_5$	5 mM PA RNA	10 mM MES pH 6.5	-	AT	-	AT
75 mM	5 mM $(HL)_5$	5 mM PA RNA	10 mM MES pH 8.0	-	A	-	A
75 mM	5 mM $(HL)_5$	5 mM DEP	10 mM MES pH 5.0	-	AT	-	AT
75 mM	5 mM $(HL)_5$	5 mM DEP	10 mM MES pH 6.5	-	AT	-	AT
75 mM	5 mM $(HL)_5$	5 mM DEP	10 mM MES pH 8.0	-	AT	-	AT
0 mM	5 mM $(HL)_5$	none	10 mM MES pH 5.0	-	AT	-	AT
0 mM	5 mM $(HL)_5$	none	10 mM MES pH 6.5	-	AT	-	AT
0 mM	5 mM $(HL)_5$	none	10 mM MES pH 8.0	-	AT	-	AT
0 mM	5 mM $(HL)_5$	5 mM ST DNA	10 mM MES pH 5.0	-	A	*	A
0 mM	5 mM $(HL)_5$	5 mM ST DNA	10 mM MES pH 6.5	-	AT	*	A
0 mM	5 mM $(HL)_5$	5 mM ST DNA	10 mM MES pH 8.0	-	AT	-	A
0 mM	5 mM $(HL)_5$	5 mM PA RNA	10 mM MES pH 5.0	-	AT	*	A
0 mM	5 mM $(HL)_5$	5 mM PA RNA	10 mM MES pH 6.5	-	AT	-	A
0 mM	5 mM $(HL)_5$	5 mM PA RNA	10 mM MES pH 8.0	-	A	-	A
0 mM	5 mM $(HL)_5$	5 mM DEP	10 mM MES pH 5.0	-	AT	-	AT
0 mM	5 mM $(HL)_5$	5 mM DEP	10 mM MES pH 6.5	-	AT	-	AT
0 mM	5 mM $(HL)_5$	5 mM DEP	10 mM MES pH 8.0	-	AT	-	AT
150 mM	1 mM $(HL)_5$	none	10 mM MES pH 5.0	-		-	
150 mM	1 mM $(HL)_5$	none	10 mM MES pH 6.2	-		*	
150 mM	1 mM $(HL)_5$	none	10 mM MES pH 6.5	-		-	
150 mM	1 mM $(HL)_5$	none	10 mM MES pH 6.8	-		*	
150 mM	1 mM $(HL)_5$	none	10 mM HEPES pH 8.0	-		-	
150 mM	1 mM $(HL)_5$	5 mM ST DNA	10 mM MES pH 5.0	*		*	
150 mM	1 mM $(HL)_5$	5 mM ST DNA	10 mM MES pH 6.2	*		*	
150 mM	1 mM $(HL)_5$	5 mM ST DNA	10 mM MES pH 6.5	*		*	
150 mM	1 mM $(HL)_5$	5 mM ST DNA	10 mM MES pH 6.8	*		*	
150 mM	1 mM $(HL)_5$	5 mM ST DNA	10 mM HEPES pH 8.0	*		*	
150 mM	1 mM $(HL)_5$	1 mM ST DNA	10 mM MES pH 5.5	*		*	
150 mM	1 mM $(HL)_5$	5 mM PA RNA	10 mM MES pH 5.0	-		-	
150 mM	1 mM $(HL)_5$	5 mM PA RNA	10 mM MES pH 6.2	-		-	
150 mM	1 mM $(HL)_5$	5 mM PA RNA	10 mM MES pH 6.5	-		-	
150 mM	1 mM $(HL)_5$	5 mM PA RNA	10 mM MES pH 6.8	-		-	
150 mM	1 mM $(HL)_5$	5 mM PA RNA	10 mM HEPES pH 8.0	-		-	
150 mM	1 mM $(HL)_5$	5 mM DEP	10 mM MES pH 5.0	-		-	

NaCl	$(HL)_5$	anion	buffer	gel 10 s	agg. 10 s	gel 1 hour	agg. 1 hour?
150 mM	1 mM $(HL)_5$	5 mM DEP	10 mM MES pH 6.2	-		-	
150 mM	1 mM $(HL)_5$	5 mM DEP	10 mM MES pH 6.5	-		-	
150 mM	1 mM $(HL)_5$	5 mM DEP	10 mM MES pH 6.8	-		-	
150 mM	1 mM $(HL)_5$	5 mM DEP	10 mM HEPES pH 8.0	-		-	
75 mM	1 mM $(HL)_5$	none	10 mM MES pH 5.0	-		-	
75 mM	1 mM $(HL)_5$	none	10 mM MES pH 6.2	-		-	
75 mM	1 mM $(HL)_5$	none	10 mM MES pH 6.5	-		-	
75 mM	1 mM $(HL)_5$	none	10 mM MES pH 6.8	-		-	
75 mM	1 mM $(HL)_5$	none	10 mM HEPES pH 8.0	-		-	
75 mM	1 mM $(HL)_5$	5 mM ST DNA	10 mM MES pH 5.0	-		-	
75 mM	1 mM $(HL)_5$	5 mM ST DNA	10 mM MES pH 6.2	-		*	
75 mM	1 mM $(HL)_5$	5 mM ST DNA	10 mM MES pH 6.5	-		-	
75 mM	1 mM $(HL)_5$	5 mM ST DNA	10 mM MES pH 6.8	-		-	
75 mM	1 mM $(HL)_5$	5 mM ST DNA	10 mM HEPES pH 8.0	-		-	
75 mM	1 mM $(HL)_5$	5 mM PA RNA	10 mM MES pH 5.0	-		-	
75 mM	1 mM $(HL)_5$	5 mM PA RNA	10 mM MES pH 6.2	*		*	
75 mM	1 mM $(HL)_5$	5 mM PA RNA	10 mM MES pH 6.5	-		*	
75 mM	1 mM $(HL)_5$	5 mM PA RNA	10 mM MES pH 6.8	*		-	
75 mM	1 mM $(HL)_5$	5 mM PA RNA	10 mM HEPES pH 8.0	-		-	
75 mM	1 mM $(HL)_5$	5 mM DEP	10 mM MES pH 5.0	-		-	
75 mM	1 mM $(HL)_5$	5 mM DEP	10 mM MES pH 6.2	-		-	
75 mM	1 mM $(HL)_5$	5 mM DEP	10 mM MES pH 6.5	-		-	
75 mM	1 mM $(HL)_5$	5 mM DEP	10 mM MES pH 6.8	-		-	
75 mM	1 mM $(HL)_5$	5 mM DEP	10 mM HEPES pH 8.0	-		-	
0 mM	1 mM $(HL)_5$	none	10 mM MES pH 5.0	-		-	
0 mM	1 mM $(HL)_5$	none	10 mM MES pH 6.2	-		-	
0 mM	1 mM $(HL)_5$	none	10 mM MES pH 6.5	-		-	
0 mM	1 mM $(HL)_5$	none	10 mM MES pH 6.8	-		-	
0 mM	1 mM $(HL)_5$	none	10 mM HEPES pH 8.0	-		-	
0 mM	1 mM $(HL)_5$	5 mM ST DNA	10 mM MES pH 5.0	-		-	
0 mM	1 mM $(HL)_5$	5 mM ST DNA	10 mM MES pH 6.2	-		-	
0 mM	1 mM $(HL)_5$	5 mM ST DNA	10 mM MES pH 6.5	-		-	
0 mM	1 mM $(HL)_5$	5 mM ST DNA	10 mM MES pH 6.8	-		-	
0 mM	1 mM $(HL)_5$	5 mM ST DNA	10 mM HEPES pH 8.0	-		-	
0 mM	1 mM $(HL)_5$	5 mM PA RNA	10 mM MES pH 5.0	-		-	
0 mM	1 mM $(HL)_5$	5 mM PA RNA	10 mM MES pH 6.2	*		-	
0 mM	1 mM $(HL)_5$	5 mM PA RNA	10 mM MES pH 6.5	-		*	
0 mM	1 mM $(HL)_5$	5 mM PA RNA	10 mM MES pH 6.8	-		*	
0 mM	1 mM $(HL)_5$	5 mM PA RNA	10 mM HEPES pH 8.0	*		*	
0 mM	1 mM $(HL)_5$	5 mM DEP	10 mM MES pH 5.0	-		-	
0 mM	1 mM $(HL)_5$	5 mM DEP	10 mM MES pH 6.2	-		-	
0 mM	1 mM $(HL)_5$	5 mM DEP	10 mM MES pH 6.5	-		-	
0 mM	1 mM $(HL)_5$	5 mM DEP	10 mM MES pH 6.8	-		-	
0 mM	1 mM $(HL)_5$	5 mM DEP	10 mM HEPES pH 8.0	-		-	
150 mM	1 mM $(HL)_5$	1 mM ST DNA	10 mM MES pH 5.5	*		*	
0 mM	12.6 mM $(HL)_5$	6.3 mM PA RNA	5 mM MES pH 6.0	****	A	n.d.	n.d.

Table 6-6 legend: The peptide $(HL)_5$ was mixed with equal volumes of (poly)anion solutions (ST DNA = salmon testes DNA, PA RNA = poly(A) RNA, DEP = diethyl phosphate, buffer) to give the indicated concentration in the indicated buffers with 0, 75, or 150 mM NaCl.

Mixtures were monitored for strength and speed (within 10 seconds during mixing/ 1 hour) of gel formation. Absence of gel is denoted by "-"; n.d. = not determined. Gels were denoted as very strong (*****), strong (****), medium (***), weak (**), or very weak (*), following the classification given in Table 5-2. Aggregation was denoted by A (larger aggregates in clear solution).

This data was collected in collaboration with Christine Humphreys (Cardiff University).

Regarding the concentrations and conditions used in other experiments (see Table 6-3 at the bottom), the $(HL)_5$-PA RNA sample for X-ray fibre diffraction (12.6 mM $(HL)_5$, 6.3 mM PA RNA, 5 mM MES pH 6.0; chapter 6.1.7, Figure 6-14) formed a strong gel containing some aggregates that appeared to mainly originate from not-fully-dissolved $(HL)_5$ in the stock solution. The sample created for electron microscopy (1 mM $(HL)_5$, 1 mM ST DNA, 150 mM NaCl, 10 mM MES pH 5.5; chapter 6.1.5, Figure 6-9) showed a very weak gel and no visible aggregates.

Gel formation by TVQFHMH-anion mixtures

TVQFHMH was very prone to form gels, either with PA RNA or ST DNA or on its own, but did not form visible aggregates (see Table 6-7). Like STVIIE (see Table 6-9) it was able to form gels on its own, especially at higher pH values when the level of histidine protonation was reduced. These gels appeared primarily at pH 6.8 and pH 8.0 in the absence of NaCl, but the gel formation expanded down to pH 6.2 in the presence of 75 or 150 mM NaCl. Nucleic acid-independent gel formation seemed to be slightly enhanced by the presence of diethyl phosphate.

TVQFHMH and ST DNA mixtures immediately formed medium to very strong gels upon mixing in the absence of NaCl. The gel at pH 5.0 was a bit weaker than at the higher pHs, a pattern that also became apparent with 75 and 150 mM NaCl, where no or only very weak gels appeared at pH 5.0. Initially, the strongest gels appeared at pH 6.2 to pH 6.8 throughout, but within 1 hour strong to very strong gels developed in all samples. Right after mixing there seemed to be a preference for stronger gels at pH 6.2 to 6.8, but within 1 hour strong and very strong gels developed in the samples (with exception of pH 5.0). TVQFHMH-PA RNA mixtures showed a stronger dependence on time than ST DNA: While initially weak to medium strong gels formed during mixing, after 1 hour the strength of the gels usually increased to strong and very strong. In the presence of NaCl the gels were generally weaker at pH 5.0 than at higher pH. Immediately during mixing there seemed to be a preference for about pH 6.5. Within 1 hour all samples formed very strong gels. At 75 mM NaCl and 150 mM NaCl, a similar pattern was observed. Interestingly, at 75 mM NaCl at pH 5.0 stronger gels developed than under the same conditions with ST DNA.

TVQFHMH was also able to form gels on its own. Without NaCl these gels appeared during mixing at pH 8.0, and within 1 hour at pH 6.5 to 8.0. At 75 mM NaCl, gels developed immediately from pH 6.5 to 8.0 with a maximum at pH 6.8, and also at pH 6.2 after 1 hour incubation. Diethyl phosphate increased gel strength in the presence of 75 or 150 mM NaCl at higher pHs, but did not have a big effect.

The gels of TVQFHMH-ST DNA at pH 6.5 in 150 mM NaCl were among the strongest ones observed for this peptide. These conditions were chosen to carry out a titration with varying ST DNA concentrations in order to examine if the ratio of peptide to anion had

an effect on gel formation, albeit with a lowered peptide concentration of 2.5 mM TVQFHMH to allow a wider concentration range to be explored (from 4:1 to 1:4 ST DNA to TVQFHMH). The strongest gels appeared at 2.5 mM and 1.3 mM ST DNA (see Table 6-7). Gels became weaker towards higher and lower ST DNA concentrations.

The gels of TVQFHMH-ST DNA and TVQFHMH-PA RNA were generally very sticky and clung to pipette tips.

Table 6-7: Gel formation and visible aggregation by TVQFHMH in mixture with (poly)anions

NaCl	TVQFHMH	anion	buffer	gel 10 s	agg. 10 s	gel 1 hour	agg. 1 hour?
150 mM	5 mM TVQ	none	10 mM MES pH 5.0	-		-	
150 mM	5 mM TVQ	none	10 mM MES pH 6.2	-		*	
150 mM	5 mM TVQ	none	10 mM MES pH 6.5	**		***	
150 mM	5 mM TVQ	none	10 mM MES pH 6.8	*		***	
150 mM	5 mM TVQ	none	10 mM HEPES pH 8.0	*		*	
150 mM	5 mM TVQ	5 mM ST DNA	10 mM MES pH 5.0	*		-	
150 mM	5 mM TVQ	5 mM ST DNA	10 mM MES pH 6.2	***		*****	
150 mM	5 mM TVQ	5 mM ST DNA	10 mM MES pH 6.5	****		*****	
150 mM	5 mM TVQ	5 mM ST DNA	10 mM MES pH 6.8	****		*****	
150 mM	5 mM TVQ	5 mM ST DNA	10 mM HEPES pH 8.0	**		****	
150 mM	5 mM TVQ	5 mM PA RNA	10 mM MES pH 5.0	-		*	
150 mM	5 mM TVQ	5 mM PA RNA	10 mM MES pH 6.2	**		***	
150 mM	5 mM TVQ	5 mM PA RNA	10 mM MES pH 6.5	**		****	
150 mM	5 mM TVQ	5 mM PA RNA	10 mM MES pH 6.8	***		****	
150 mM	5 mM TVQ	5 mM PA RNA	10 mM HEPES pH 8.0	*		***	
150 mM	5 mM TVQ	5 mM DEP	10 mM MES pH 5.0	-		-	
150 mM	5 mM TVQ	5 mM DEP	10 mM MES pH 6.2	-		*	
150 mM	5 mM TVQ	5 mM DEP	10 mM MES pH 6.5	**		***	
150 mM	5 mM TVQ	5 mM DEP	10 mM MES pH 6.8	**		****	
150 mM	5 mM TVQ	5 mM DEP	10 mM HEPES pH 8.0	***		**	
75 mM	5 mM TVQ	none	10 mM MES pH 5.0	-		-	
75 mM	5 mM TVQ	none	10 mM MES pH 6.2	-		*	
75 mM	5 mM TVQ	none	10 mM MES pH 6.5	**		**	
75 mM	5 mM TVQ	none	10 mM MES pH 6.8	***		****	
75 mM	5 mM TVQ	none	10 mM HEPES pH 8.0	*		**	
75 mM	5 mM TVQ	5 mM ST DNA	10 mM MES pH 5.0	*		-	
75 mM	5 mM TVQ	5 mM ST DNA	10 mM MES pH 6.2	***		*****	
75 mM	5 mM TVQ	5 mM ST DNA	10 mM MES pH 6.5	***		*****	
75 mM	5 mM TVQ	5 mM ST DNA	10 mM MES pH 6.8	**		*****	
75 mM	5 mM TVQ	5 mM ST DNA	10 mM HEPES pH 8.0	*		*****	
75 mM	5 mM TVQ	5 mM PA RNA	10 mM MES pH 5.0	*		***	
75 mM	5 mM TVQ	5 mM PA RNA	10 mM MES pH 6.2	**		****	

NaCl	TVQFHMH	anion	buffer	gel 10 s	agg. 10 s	gel 1 hour	agg. 1 hour?
75 mM	5 mM TVQ	5 mM PA RNA	10 mM MES pH 6.5	**		*****	
75 mM	5 mM TVQ	5 mM PA RNA	10 mM MES pH 6.8	*		****	
75 mM	5 mM TVQ	5 mM PA RNA	10 mM HEPES pH 8.0	*		***	
75 mM	5 mM TVQ	5 mM DEP	10 mM MES pH 5.0	-		-	
75 mM	5 mM TVQ	5 mM DEP	10 mM MES pH 6.2	-		**	
75 mM	5 mM TVQ	5 mM DEP	10 mM MES pH 6.5	**		**	
75 mM	5 mM TVQ	5 mM DEP	10 mM MES pH 6.8	***		****	
75 mM	5 mM TVQ	5 mM DEP	10 mM HEPES pH 8.0	***		***	
0 mM	5 mM TVQ	none	10 mM MES pH 5.0	-		-	
0 mM	5 mM TVQ	none	10 mM MES pH 6.2	-		-	
0 mM	5 mM TVQ	none	10 mM MES pH 6.5	-		*	
0 mM	5 mM TVQ	none	10 mM MES pH 6.8	-		*	
0 mM	5 mM TVQ	none	10 mM HEPES pH 8.0	*		**	
0 mM	5 mM TVQ	5 mM ST DNA	10 mM MES pH 5.0	***		*****	
0 mM	5 mM TVQ	5 mM ST DNA	10 mM MES pH 6.2	****		*****	
0 mM	5 mM TVQ	5 mM ST DNA	10 mM MES pH 6.5	*****		*****	
0 mM	5 mM TVQ	5 mM ST DNA	10 mM MES pH 6.8	*****		*****	
0 mM	5 mM TVQ	5 mM ST DNA	10 mM HEPES pH 8.0	*****		*****	
0 mM	5 mM TVQ	5 mM PA RNA	10 mM MES pH 5.0	**		*****	
0 mM	5 mM TVQ	5 mM PA RNA	10 mM MES pH 6.2	**		*****	
0 mM	5 mM TVQ	5 mM PA RNA	10 mM MES pH 6.5	***		*****	
0 mM	5 mM TVQ	5 mM PA RNA	10 mM MES pH 6.8	**		*****	
0 mM	5 mM TVQ	5 mM PA RNA	10 mM HEPES pH 8.0	**		*****	
0 mM	5 mM TVQ	5 mM DEP	10 mM MES pH 5.0	-		-	
0 mM	5 mM TVQ	5 mM DEP	10 mM MES pH 6.2	-		-	
0 mM	5 mM TVQ	5 mM DEP	10 mM MES pH 6.5	-		-	
0 mM	5 mM TVQ	5 mM DEP	10 mM MES pH 6.8	-		*	
0 mM	5 mM TVQ	5 mM DEP	10 mM HEPES pH 8.0	*		**	
150 mM	2.5 mM TVQ	10 mM ST DNA	10 mM MES pH 6.5	*		*****	
150 mM	2.5 mM TVQ	7.5 mM ST DNA	10 mM MES pH 6.5	*		*****	
150 mM	2.5 mM TVQ	5.0 mM ST DNA	10 mM MES pH 6.5	**		*****	
150 mM	2.5 mM TVQ	2.5 mM ST DNA	10 mM MES pH 6.5	***		*****	
150 mM	2.5 mM TVQ	1.3 mM ST DNA	10 mM MES pH 6.5	**		****	
150 mM	2.5 mM TVQ	0.8 mM ST DNA	10 mM MES pH 6.5	**		****	
150 mM	2.5 mM TVQ	0.6 mM ST DNA	10 mM MES pH 6.5	*		***	
150 mM	2.5 mM TVQ	10 mM DEP	10 mM MES pH 6.5	*		*	
150 mM	2.5 mM TVQ	7.5 mM DEP	10 mM MES pH 6.5	*		*	
150 mM	2.5 mM TVQ	5.0 mM DEP	10 mM MES pH 6.5	*		*	
150 mM	2.5 mM TVQ	2.5 mM DEP	10 mM MES pH 6.5	*		*	
150 mM	2.5 mM TVQ	1.3 mM DEP	10 mM MES pH 6.5	*		*	
150 mM	2.5 mM TVQ	0.8 mM DEP	10 mM MES pH 6.5	*		*	
150 mM	2.5 mM TVQ	0.6 mM DEP	10 mM MES pH 6.5	*		*	
150 mM	1 mM TVQ	none	10 mM MES pH 6.5	-		*	
150 mM	0.5 mM TVQ	none	10 mM MES pH 6.5	-		-	
150 mM	2.5 mM TVQ	none	10 mM MES pH 6.5	*		*	
150 mM	5 mM TVQ	5 mM ST DNA	10 mM MES pH 5.5	**		***	
150 mM	1 mM TVQ	9 mM ST DNA	10 mM MES pH 6.8	-		n.d.	
150 mM	2 mM TVQ	8 mM ST DNA	10 mM MES pH 6.8	***		n.d.	
150 mM	3 mM TVQ	7 mM ST DNA	10 mM MES pH 6.8	***		n.d.	
150 mM	4 mM TVQ	6 mM ST DNA	10 mM MES pH 6.8	***		n.d.	
150 mM	5 mM TVQ	5 mM ST DNA	10 mM MES pH 6.8	***		n.d.	
150 mM	6 mM TVQ	4 mM ST DNA	10 mM MES pH 6.8	****		n.d.	
150 mM	7 mM TVQ	3 mM ST DNA	10 mM MES pH 6.8	****		n.d.	
150 mM	8 mM TVQ	2 mM ST DNA	10 mM MES pH 6.8	***		n.d.	
150 mM	9 mM TVQ	1 mM ST DNA	10 mM MES pH 6.8	***		n.d.	
150 mM	10 mM TVQ	10 mM ST DNA	10 mM MES pH 6.8	****		n.d.	

NaCl	TVQFHMH	anion	buffer	gel 10 s	agg. 10 s	gel 1 hour	agg. 1 hour?
150 mM	1 mM TVQ	9 mM PA RNA	10 mM MES pH 6.8	-		n.d.	
150 mM	2 mM TVQ	8 mM PA RNA	10 mM MES pH 6.8	-		n.d.	
150 mM	3 mM TVQ	7 mM PA RNA	10 mM MES pH 6.8	-		n.d.	
150 mM	4 mM TVQ	6 mM PA RNA	10 mM MES pH 6.8	(**)		n.d.	
150 mM	5 mM TVQ	5 mM PA RNA	10 mM MES pH 6.8	(**)		n.d.	
150 mM	6 mM TVQ	4 mM PA RNA	10 mM MES pH 6.8	(**)		n.d.	
150 mM	7 mM TVQ	3 mM PA RNA	10 mM MES pH 6.8	(**)		n.d.	
150 mM	8 mM TVQ	2 mM PA RNA	10 mM MES pH 6.8	(**)		n.d.	
150 mM	9 mM TVQ	1 mM PA RNA	10 mM MES pH 6.8	(**)		n.d.	
150 mM	10 mM TVQ	10 mM PA DNA	10 mM MES pH 6.8	(**)		n.d.	
150 mM	5 mM TVQ	5 mM $NaPO_4$	10 mM MES pH 6.8	-		n.d.	
75 mM	28.3 mM TVQ	5 mM ST DNA	10 mM MES pH 5.0	***		n.d.	
75 mM	28.3 mM TVQ	5 mM ST DNA	10 mM MES pH 6.2	****		n.d.	
75 mM	28.3 mM TVQ	5 mM ST DNA	10 mM MES pH 6.5	*****		n.d.	
75 mM	28.3 mM TVQ	100 mM $NaPO_4$	10 mM MES pH 6.2	-		n.d.	
75 mM	28.3 mM TVQ	100 mM $NaPO_4$	10 mM MES pH 6.5	-		n.d.	
0 mM	1.6 mM TVQ	none	none (pH 6)	-		*	
0 mM	1.6 mM TVQ	1.6 mM ST DNA	10 mM MES pH 5.0	***		*****	
0 mM	17.8 mM TVQ	8.9 mM PA RNA	5 mM MES pH 6.0	*****	A		
0 mM	1 mM TVQ	1 mM ST DNA	10 mM MES pH 5.0	**		*****	
0 mM	1.6 mM TVQ	1.6 mM ST DNA	10 mM MES pH 6.5	***		*****	

Table 6-7 legend: The peptide TVQFHMH was mixed with equal volumes of (poly)anion solutions (ST DNA = salmon testes DNA, PA RNA = poly(A) RNA, DEP = diethyl phosphate, buffer) to give the indicated concentration in the indicated buffers with 0, 75, or 150 mM NaCl. Mixtures were monitored for strength and speed (within 10 seconds during mixing/ 1 hour) of gel formation. Absence of gel is denoted by "-"; n.d. = not determined. Gels were denoted as very strong (*****), strong (****), medium (***), weak (**), or very weak (*), following the classification given in Table 5-2. No aggregation could be seen. Gel formation appeared to be faster for ST DNA than for PA RNA independent of salt concentration. Gel strength seemed to reduce slightly with increasing NaCl concentration, and was lower for TVQFHMH alone or with DEP.

This data was collected in collaboration with Christine Humphreys (Cardiff University).

Regarding the concentrations and conditions used in other experiments (see Table 6-3 at the bottom), the $(KL)_3$-PA RNA sample for electron microscopy (0.33 mM $(KL)_3$, 1 mM PA RNA, pH 7; chapter 6.1.5, Figure 6-10) formed a very weak gel.

Gel formation by various length (KL)-peptides with PA and BY RNA

A quick series of gelation experiments were carried out to get an idea about the effect of peptide chain length on gelation or aggregation. Some of these experiments were carried out with baker's yeast RNA which, at the time when the studies were initiated, was observed to induce gel formation in the same way as PA RNA. Later experiments were standardised to PA RNA.

Table 6-8: Gel formation and visible aggregation by various length KL-peptides

peptide	anion	buffer	gel 10 s	agg. 10 s	gel 1 hour	agg. 1 hour?
5 mM $(KL)_3$	none	10 mM MES pH 6.8	-		-	
	5 mM ST DNA	10 mM MES pH 6.8	*		*	
	5 mM PA RNA	10 mM MES pH 6.8	*		*	
	5 mM BY RNA	10 mM MES pH 6.8	-		-	
	5 mM DEP	10 mM MES pH 6.8	-		-	
5 mM $(KL)_{3.5}$	none	10 mM MES pH 6.8	-		-	
	5 mM ST DNA	10 mM MES pH 6.8	**		**	
	5 mM PA RNA	10 mM MES pH 6.8	*		*	
	5 mM BY RNA	10 mM MES pH 6.8	-		-	
	5 mM DEP	10 mM MES pH 6.8	-		-	
5 mM $(KL)_4$	none	10 mM MES pH 6.8	-		-	
	5 mM ST DNA	10 mM MES pH 6.8	**		***	
	5 mM PA RNA	10 mM MES pH 6.8	*		*	
	5 mM BY RNA	10 mM MES pH 6.8	*		*	
	5 mM DEP	10 mM MES pH 6.8	-		-	

Table 6-8 legend: The peptides were mixed with equal volumes of (poly)anion solutions (ST DNA = salmon testes DNA, PA RNA = poly(A) RNA, BY RNA = Baker's Yeast RNA, DEP = diethyl phosphate, or buffer) to give the indicated final concentrations in the indicated buffers. Mixtures were monitored for strength and speed (within 10 seconds during mixing/ 1 hour)

of gel formation. Absence of gel is denoted by "-". Gels were denoted as very strong (*****), strong (****), medium (***), weak (**), or very weak (*), following the classification given in Table 5-2. No aggregation could be seen. This data was collected in collaboration with Christine Humphreys (Cardiff University).

$(KL)_3$ was here included for easier comparison; for the full $(KL)_3$ gel formation and aggregation see Table 6-3. It showed very weak gels with ST DNA and PA RNA, but not with BY RNA, DEP or on its own. The gels of $(KL)_{3.5}$ (KLKLKLK) were slightly stronger with ST DNA than with PA RNA; no gels could be detected with BY RNA, DEP or peptide alone. $(KL)_3$ developed a medium strength gel within 1 hour with ST DNA, while PA RNA and BY RNA induced only very weak gels. No gels appeared with DEP or peptide alone. None of the samples with either $(KL)_3$, $(KL)_{3.5}$, or $(KL)_4$ showed any visible aggregation or turbidity. Overall, a trend towards stronger gel formation was observed with longer peptides.

Gel formation by STVIIE

STVIIE was able to form amyloid on its own as described before [142], and formed within a day (>16 hours; exact time not recorded) a quite weak gel containing visible small aggregates at 0.8 mM peptide concentration at pH 2.6 (see Table 6-9). This concentration was lower than the ones used to test for gel formation of the other peptides (see Figure 6-2, Table 6-3, Table 6-4, Table 6-5, Table 6-6, and Table 6-7, and Table 6-8) to keep it compatible with CD spectroscopy (see chapter 6.1.9, Figure 6-26, Figure 6-28, Figure 6-29, and Figure 6-30; Supplementary Figure 6). Also, the formation

of amyloid aggregates of STVIIE has been shown before [142], so it was not strictly necessary to include STVIIE in this range-finding exercise for following experiments like X-ray fibre diffraction. This gel was not sticky, i.e. it did not cling to pipette tips. Its gel formation abilities in the presence of long nucleic acids like salmon testes DNA or poly(A) RNA were not investigated.

Table 6-9: Gel formation and visible aggregation by STVIIE

NaCl	STVIIE	anion	buffer	gel 10 s	agg. 10 s	gel 24 hours	agg. 24 hours
0 mM	20 mM STVIIE	none	20 mM glycine pH 10	-		-	
0 mM	0.8 mM STVIIE	none	20 mM glycine pH 2.6	-		*	A
0 mM	0.8 mM STVIIE	242 nM oligo E	20 mM glycine pH 2.6	-		*	A

Table 6-9 legend: A solution of 20 mM STVIIE in 20 mM glycine pH 10 was diluted with 20 mM glycine pH 2.6 with or without oligo E to give the final concentrations given in the table. Gels were denoted as very strong (*****), strong (****), medium (***), weak (**), or very weak (*), following the classification given in Table 5-2. Neither gel nor aggregates could be detected in the peptide stock solution. With 0.8 mM STVIIE at pH 2.6 a very weak gel and some aggregates appeared within 24 h.

Summary

Gel strength was generally dependent on the concentration of peptide-DNA complexes, which would influence the number of entangled and/or cross-linked fibres that gave rise to the gel. Inorganic phosphate ($NaPO_4$) or diethyl phosphate did not seem to increase gel formation or aggregation above background level with the exception of TVQFHMH where gel formation was slightly increased in the presence of DEP (see Table 6-7). This

suggested that either the number of polymerised negative charges of the phosphate groups were important for creation of gels and aggregates by the peptides, or that longer nucleic acid strands were required to be cross-linked by the peptides. Gel formation appeared to be dependent on NaCl concentration with increasing gel strength and/or formation speed at lower salt concentrations for $(HL)_3$ and TVQFHMH (see Table 6-2 and Table 6-7). This would suggest that charge interactions that could be screened by NaCl between these peptides and nucleic acids were important for the formation of gels or aggregates.

6.1.4. SPECTROPHOTOMETRIC ASSAYS

Gel formation alone cannot demonstrate amyloid fibre formation because a gel can arise from either formation of an entangled net of amyloid fibres, or from electrostatic cross-linking of the longer nucleic acid strands by positively-charged peptides such as $(HL)_3$, $(HL)_5$, $(KL)_3$, $(KL)_5$ and TVQFHMH in the absence of amyloid. Also, amyloid complexes might not form an extended network of fibrils, but compact aggregates. Alternatively, the observed aggregates (see Table 6-2, Table 6-3, Table 6-5, Table 6-6, and Table 6-9) might be amorphous aggregates and not based on amyloid fibres. In order to gather information about the possible formation of amyloid aggregates, spectrophotometric assays using Thioflavin T or Congo Red were employed to examine the peptide-nucleic acid mixtures. A 1:1 charge ratio was chosen because there was a trend to stronger gels and potentially larger amount of amyloid fibres under this condition, at least for $(HL)_3$ without NaCl (see Table 6-2) and for TVQFHMH with 150 mM NaCl (see Table 6-7). This in both cases was close to a calculated +2 net charge of the peptides, resulting at a 1:1 ratio of peptide to nucleic acid backbone phosphate in a theoretical +1 net charge per peptide; a +1 or -1 net charge was previously described as being ideal for ordered amyloid aggregation and fibre formation [142].

Thioflavin T

A Thioflavin T plate reader assay (excitation at 440 nm, emission detection at 480 nm; both with 10 nm bandwidth) suggested the presence of amyloid aggregates for the $(KL)_3$- and $(HL)_3$-DNA complexes (see Figure 6-2 and Figure 6-3). A low concentration of 50 μM was chosen for the peptide-nucleic acid complexes in order to avoid the gel formation at higher concentrations, which might have interfered with both the dye accessing potential amyloid complexes in the sample and with sufficient mixing of the

sample. The assay was carried out in 10 mM MES pH 6.2 with 150 mM NaCl, where the peptide was expected to carry a +2 calculated net charge. $(HL)_3$ on its own showed no increased Thioflavin T fluorescence, but $(HL)_3$-ST DNA mixtures significantly exceeded the fluorescence of ST DNA on its own (see Figure 6-2). The binding of Thioflavin T by peptide and/or nucleic acid was much lower than the insulin amyloid positive control at the same concentration.

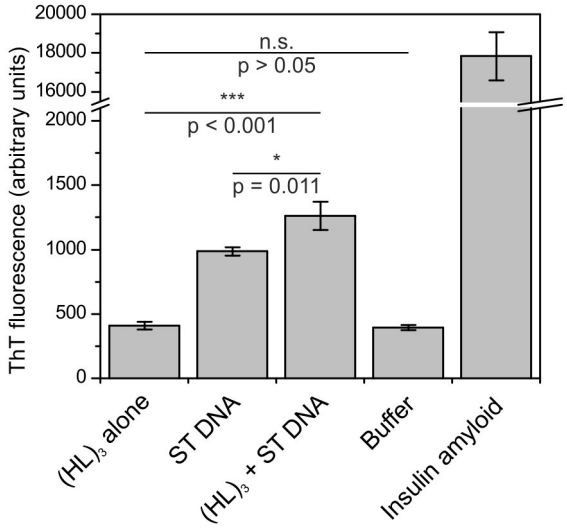

Figure 6-2: Thioflavin T assay on $(HL)_3$-ST DNA mixtures. 50 µM $(HL)_3$ and 50 µM ST DNA were prepared in 10 mM MES pH 6.2 (+2 calculated net charge) with 150 mM NaCl. The insulin amyloid (50 µM) in the same buffer was used as a positive control for the whole assay. The peptide-nucleic acid mixture showed a slight increase over the ST DNA signal, while the peptide on its own displayed no increased fluorescence. The samples were prepared directly in untreated black plates and the fluorescence measured in a BMG FLUOStar plate reader (excitation: 440 nm; emission: 480 nm; 10 nm band pass filters). All samples were quadruplicates. ThT fluorescence is in arbitrary units. A Student's unpaired 2-

sample *t*-test with n = 4 was carried out using R to compare the means as indicated (* = $p < 0.05$; ** = $p < 0.01$; *** = $p < 0.001$) [215] (see Appendix 9.2 for a full list of the statistical parameters).

$(KL)_3$ on its own showed no increased Thioflavin T fluorescence, but $(KL)_3$-ST DNA mixtures exceeded the fluorescence of ST DNA on its own (see Figure 6-3). The assay was carried out in 10 mM HEPES pH 7 with 150 mM NaCl, where the peptide was expected to carry a +3 calculated net charge. The risk of strong gel formation was not as high as for $(HL)_3$-ST DNA mixtures (Table 6-2 and Table 6-3), but the issue of the DNA-caused ThT fluorescence going out of range of the instrument remained. The use of the same instrument settings allowed a comparison to $(HL)_3$-ST DNA complexes, which showed a very similar result (see Figure 6-3). Again, the binding of Thioflavin T by peptide and/or nucleic acid was much lower than the insulin amyloid positive control at the same concentration.

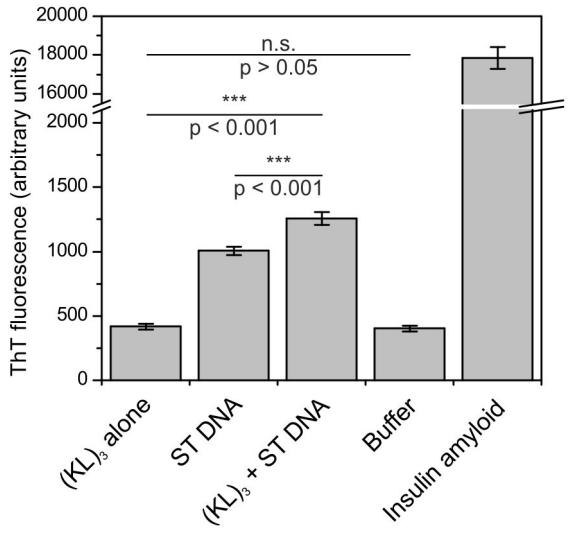

Figure 6-3: Thioflavin T assay on $(KL)_3$-ST DNA mixtures. 50 µM $(KL)_3$ and 50 µM ST DNA were prepared alone or in mixture with each other in 10 mM HEPES pH 7.0 (+3 calculated net charge) with 150 mM NaCl. The insulin amyloid (50 µM) in the same buffer was used as a positive control for the whole assay. The peptide-nucleic acid mixture showed a slight increase over the ST DNA signal, while the peptide on its own displayed no increased fluorescence. The samples were prepared directly in untreated black plates and the fluorescence measured in a BMG FLUOStar plate reader (excitation: 440 nm; emission: 480 nm; 10 nm band pass filters). All samples were quadruplicates. ThT fluorescence is in arbitrary units. A Student's unpaired 2-sample *t*-test with n = 4 was carried out using R to compare the means as indicated (* = $p < 0.05$; ** = $p < 0.01$; *** = $p < 0.001$) [215] (see Appendix 9.2 for a full list of the statistical parameters).

The fluorescence of complexes of $(KL)_3$ or $(HL)_3$ with salmon testes DNA exceeded the background fluorescence of ST DNA alone under the same conditions (see Figure 6-2 and Figure 6-3). The cause of the small signal increase remained unclear because of the

non-specificity of Thioflavin T binding [216]. It might have been the formation of amyloid aggregates that led to an increase in ThT fluorescence, or that the peptide influenced the structure of the ST DNA without formation of amyloid so the nucleic acid would bind more ThT. The peptides on their own did not give rise to Thioflavin T fluorescence, suggesting that either they did not bind the dye, or that they could not form amyloid on their own under the tested conditions (pH 7 for $(KL)_3$, pH 6.2 for $(HL)_3$; both in 150 mM NaCl). The ThT fluorescence of the peptide-nucleic acid mixtures was smaller than that of the insulin amyloid positive control, especially regarding the fluorescence signal above the DNA background, which was probably partly due to the smaller size of the peptides compared to the larger peptide hormone (742 Da of $(KL)_3$ and 769 Da of $(HL)_3$ vs. 5734 Da) at the same molecular concentration. The larger peptide hormone would probably provide more ThT binding sites than the smaller $(HL)_3$ and $(KL)_3$.

The strength of peptide-nucleic acid mixture gels seemed to be dependent on pH (see Table 6-2, Table 6-5, Table 6-7), which might be related to the presence of amyloid fibres. To examine the effect of potentially different charge densities (see Table 6-1) on the ThT binding of $(HL)_3$-ST DNA complexes the pH was varied from 5.5 to 8.0 while peptide and DNA concentrations were kept constant (see Figure 6-4). The ThT fluorescence of the ANA complexes was stable, but the DNA-induced fluorescence decreased with decreasing pH for the corresponding DNA-only control. This made interpretation of the results difficult. At pH 8 there was no net ThT fluorescence of the $(HL)_3$-ST DNA complex above the ThT fluorescence caused by ST DNA alone. With lower pH a net signal appeared although the fluorescence of DNA alone was also reduced. The increasing difference between the ANA complex and the DNA alone control of the same

pH might be due to the formation of amyloid aggregates, but alternatively the presence of the peptides could have modified the conformation of the DNA, which allowed binding and excitation of more Thioflavin T. A dependence of Thioflavin T fluorescence on pH was described before [217], and low non-physiological pH conditions (pH 0.8 to 2.8) were suggested by Kelenyi (1967) to be used in fluorescence assays to avoid the ThT fluorescence induced by DNA and RNA [217,218]. It could be expected that under these conditions the (partial) protonation of the DNA phosphate backbone would reduce charge-based attraction of nucleic acids and Thioflavin T, thereby reducing the amount of fluorescence resulting from these interactions [219]. Intercalation-caused fluorescence of ThT would probably not be affected by pH changes within the physiological range where no DNA denaturation would occur [219]. Outside the physiological range at least partial denaturation of the salmon testes DNA would occur, which made the suggested low range of pH 0.8 to pH 2.8 seem unsuitable for the examination of the effects of peptides or potential amyloid fibres on the nucleic acid (as shown in chapter 6.2).

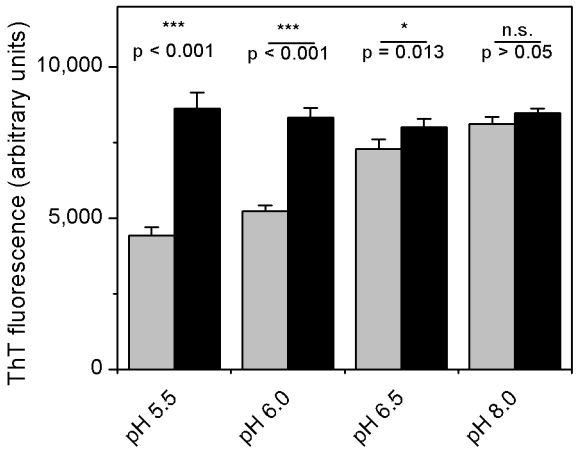

Figure 6-4: Thioflavin T assay on $(HL)_3$-ST DNA mixtures at different pH values. 50 µM $(HL)_3$ were mixed with 50 µM salmon testes in 150 mM NaCl at pH 5.5, 6.0, 6.5, or 8.0. The buffer consisted of 10 mM MES (pH 5.5, 6.0, and 6.5) or 10 mM HEPES (8.0). The samples were prepared directly in untreated black plates and the fluorescence measured in a BMG FLUOStar plate reader (excitation: 440 nm; emission: 480 nm; 10 nm band pass filters). All samples were quadruplicates; ThT fluorescence is in arbitrary units after buffer background subtraction. A Student's unpaired 2-sample *t*-test with n = 4 was carried out using R to compare the means as indicated (* = $p < 0.05$; ** = $p < 0.01$; *** = $p < 0.001$) [215] (see Appendix 9.2 for a full list of the statistical parameters).

Since gel formation occurred rapidly (often within seconds; see gel formation tables Table 6-2, Table 6-3, Table 6-5, Table 6-6, Table 6-7, and Table 6-8) I was interested in whether this was accompanied by amyloid formation. A kinetic ThT assay was carried out on $(HL)_3$ in mixture with salmon testes DNA. The negatively charged peptide $(EL)_3$ provided a negative control. The increase in ThT fluorescence occurred rapidly after mixing of $(HL)_3$ and salmon testes DNA (see Figure 6-5), in a similar time scale to gel formation at higher concentrations (usually 5 mM $(HL)_3$ with 5 mM ST DNA; see Table

6-2). The process reached a saturation plateau of maximal ThT fluorescence after about 4 minutes. No ThT fluorescence was observed with the negatively charged $(EL)_3$ peptide. This would suggest that charge interactions might be important for the peptide-DNA interactions. The negatively charged $(EL)_3$ would be excluded from interactions with nucleic acids due to charge repulsion. There was no lag phase as seen with most other amyloid-forming peptides and proteins [72], like during the formation of insulin amyloid used as our positive control (see Figure 6-6; also [23,220]). This was even more pronounced with $(KL)_3$-ST DNA, where the ThT fluorescence immediately reached the plateau level without the gradual increase shown by $(HL)_3$-ST DNA (data not shown). This could suggest a very rapid nucleation so that the typical sigmoidal curve shape would not appear, or it might be that the presence of the peptide $(HL)_3$ increased binding to ThT to DNA.

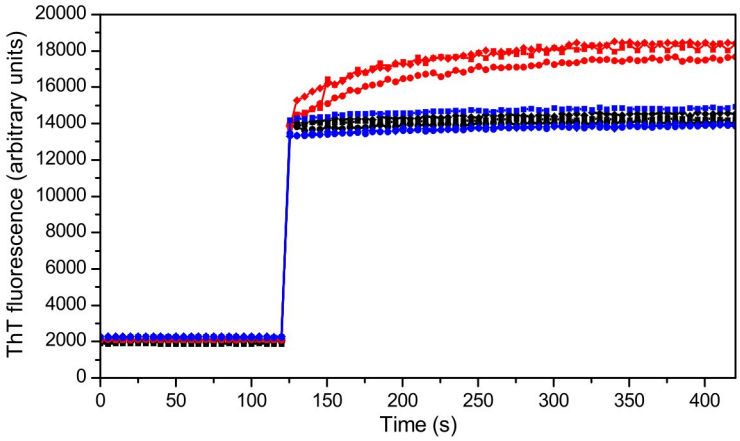

Figure 6-5: Kinetics of Thioflavin T binding by $(HL)_3$- and $(EL)_3$-ST DNA mixtures. 500 µM ST DNA was injected to either buffer alone (black traces), 500 µM $(EL)_3$ (blue traces) or 500 µM $(HL)_3$ (red traces). The major jump in ThT fluorescence from about 2000 (background level) to about 14000 at 120 s was due to ThT binding to ST DNA. Only the $(HL)_3$-ST DNA mixture

showed a further gradual increase, but not buffer alone or $(EL)_3$-ST DNA. The buffer was 10 mM MES pH 6.2 with 150 mM NaCl. All solutions contained 50 µM Thioflavin T and were incubated on their own for 30 minutes before the assay. All samples were run in triplicates. Background scattering (same setup without addition of ThT) resulted in <500 arbitrary fluorescence units.

Summary Thioflavin T

The use of Thioflavin T with ANA complexes presented a number of problems: DNA gave rise to a high background signal of Thioflavin T fluorescence, which appeared to be pH-dependent [218] (Figure 6-4). It has been described before by Ilanchelian *et al*. that both groove binding and electrostatic interactions were observed for interactions of ThT with DNA, and that high (1.0 M) NaCl concentrations could abolish the electrostatic interactions that were responsible for the increased Thioflavin T fluorescence [219]. The NaCl concentration of 150 mM used here (see Figure 6-2, Figure 6-3, Figure 6-4, and Figure 6-5) might not have been sufficient to shield all electrostatic interactions between dye and nucleic acid, but might have removed most of the unwanted DNA-cause fluorescence. Also, not all peptides and/ or peptide-nucleic acid mixtures used in these experiments showed signal in the presence of Thioflavin T. TVQFHMH, $(HL)_5$, $(KL)_5$, $(EL)_3$ and STVIIE did not show a reliable signal above background. Differences between the dye-binding behaviour of protein-based amyloids and amyloids generated from short peptides have been observed before (Louise Serpell, personal communication) and may be based on the differential ability of fibres to incorporate dyes in such a way as to alter their fluorescence.

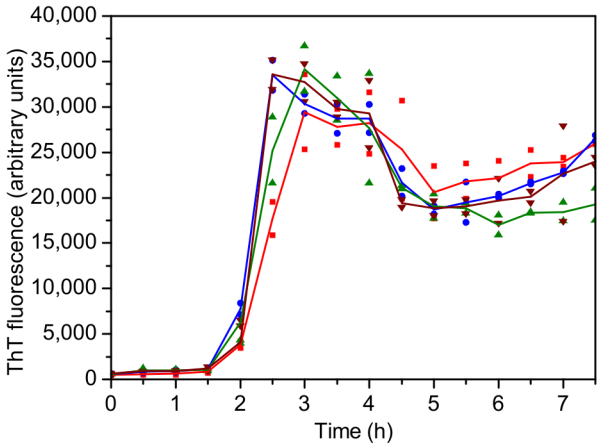

Figure 6-6: Insulin amyloid formation kinetics. 1 mM Bovine insulin in 10 mM hydrochloric acid (pH 2) was incubated at 65ºC in 1.5-ml-tubes (no agitation). Samples (5 µl) were taken every 30 minutes and transferred to an untreated black 96-well-plate. 195 µl 10 mM MES containing 50 µM Thioflavin T was added and the fluorescence measured using a BMG FLUOStar plate reader (excitation wavelength: 440 nm; emission wavelength: 480 nm). After a lag phase of 1.5 hours a maximum was reached after 2.5 to 3.0 hours, indicating amyloid formation. Dots denote the duplicate values, lines follow the mean. The big spread between the duplicates probably resulted from strong aggregation within the samples which coincided with the end of the lag phase at about 2 hours.

Congo Red

Congo Red is a dye mainly used to stain "congophilic" amyloid deposits in histology [73]. It exhibited a red-shift in its absorbance spectrum, resulting initially in a shoulder on the main absorbance spectrum near 544 nm [72]. Peptide and nucleic acid complexes were assessed for Congo Red binding by measuring absorbance at 544 nm. Only $(KL)_5$ out of all peptide-nucleic acid complexes tested showed a nucleic acid-induced increase in Congo Red absorbances (see Supplementary Table 2). The correlation between Congo

Red binding and amyloid formation was not absolute (for example, see Klunk *et al*. (1989) [70] and Khurana *et al*. (2001) [221]) and it was therefore not surprising to find that some peptide-nucleic acid complexes did not show increased Congo Red absorbance that could indicate amyloid complex formation. Alternatively, the lower peptide concentration (50 μM to 0.2 mM) used in these assays to allow mixing and pipetting may have been too low for amyloid complex formation for some peptides. To study $(KL)_5$ in greater detail, it was tested for Congo Red binding in 10 mM HEPES pH 7 with 150 mM NaCl where the peptide was expected to carry a +5 net charge. Following the suggestion that a 1:1 charge ratio might be ideal for peptide-nucleic acid interactions, I used 0.2 mM $(KL)_5$ with 1 mM ST DNA or oligo E (see Table 6-2 and Table 6-7). The Congo Red absorbance increase indicated significant binding of the dye by $(KL)_5$-oligo E and $(KL)_5$-ST DNA complexes, which in turn suggested amyloid aggregate formation. There seemed to be no difference between the shorter oligo E (33 bp) and longer ST DNA (smear of about 100 bp to >4000 bp on an agarose gel; data not shown). The absorbance increase of $(KL)_5$ alone against the buffer background was not significant. This was accompanied by strong aggregation visible by eye with larger aggregates than the insulin amyloid positive control. The $(KL)_5$-DNA mixtures showed a colour change but no change in aggregation as assessed by eye. To control for scattering by large aggregates a scattering control of all samples in the absence of Congo Red was carried out and did not show significantly increased absorbance (data not shown). No aggregates were observed in the $(KL)_5$ alone sample in the absence of the dye.

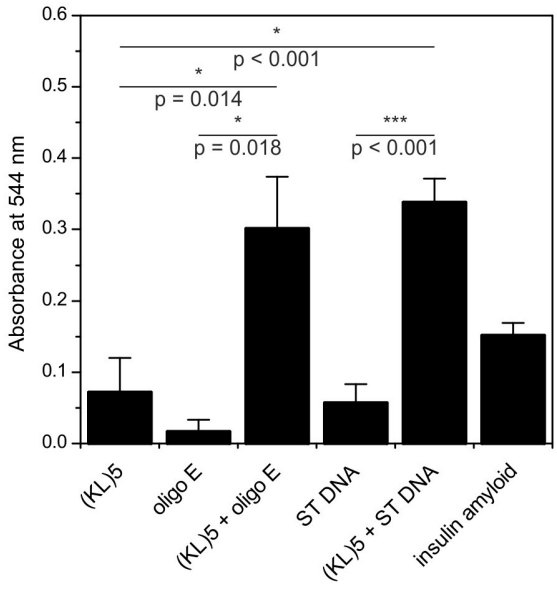

Figure 6-7: Congo Red absorbance assay on $(KL)_5$-DNA complexes. The absorbance at 544 nm of 0.2 mM $(KL)_5$ with 1 mM salmon testes DNA or 1 mM oligo E in 10 mM HEPES pH 7 with 150 mM NaCl was normalised as described in the methods section. The background absorbance of Congo Red alone in buffer was subtracted for all samples. $(KL)_5$-ST DNA and $(KL)_5$-oligo E showed a significant increase in absorbance compared to the peptide alone or the corresponding nucleic acid alone, exceeding the 50 µM insulin amyloid positive control. All samples were run in quadruplicates with exception of $(KL)_5$-oligo E, where 1 measurement had to be discarded due to air bubble formation. A Student's unpaired 2-sample t-test (n = 4 except for $(KL)_5$-oligo E, where it was n =3) was carried using R out to compare the means as indicated (* = $p < 0.05$; ** = $p < 0.01$; *** = $p < 0.001$) [215] (see Appendix 9.2 for a full list of the statistical parameters).

Summary

Both ThT and Congo red binding assays showed increased signals upon mixing of selected peptides with nucleic acids. ThT and Congo red signals were usually interpreted

as evidence for amyloid complex formation. In the assays shown here, there was a lack of signal for some peptide-nucleic acid combinations /conditions. This might be taken as evidence against the formation of amyloid complexes and it could be argued that the ThT and Congo red signals could result from peptide-induced changes to dye-interaction with the nucleic acids. However, the binding of dyes into on the surface of amyloid fibrils was likely to be highly dependent on the sequence of the amyloidogenic peptides [70,75,222,223]. Taken together, the increased signals observed with both ThT and Congo red assays in combination with the gel formation assays suggested that the peptide nucleic acid mixtures contain amyloid complexes.

Taken together, the spectrophotometric assays showing increased Thioflavin T binding by $(KL)_3$-ST DNA and $(HL)_3$-ST DNA mixtures and Congo Red binding by $(KL)_5$-ST DNA and $(KL)_5$-oligo E mixtures supported the idea that amyloid aggregates are formed following the interaction of nucleic acids with short basic peptides.. This could suggest the formation of amyloid aggregates in these mixtures. Some of the peptides did not show any positive results with either Congo Red or Thioflavin T, probably due to their small size or low dye-binding capacity. An overview of the Thioflavin T and Congo Red results is listed in Supplementary Table 2.

6.1.5. Electron Microscopy Showed Fibres in Peptide-Nucleic Acid Mixtures

The observed gel formation of peptide-nucleic acid mixtures (by all peptides except $(EL)_3$; see Table 6-2, Table 6-3, Table 6-5, Table 6-6, Table 6-7, Table 6-8, and Table 6-9) suggested the presence of fibrous, entangled material; the visible aggregates formed by some peptides might be of fibrous nature, too. Alternatively, the gels could have arisen from a network of chemically or physically conjugated smaller molecules. The dye-binding assays (see Figure 6-4, Figure 6-5, and Figure 6-7) suggested the presence of amyloid in $(HL)_3$-DNA, $(KL)_3$-DNA, and $(KL)_5$-DNA complexes. I used transmission electron microscopy (TEM) to examine the complexes formed by $(HL)_3$, $(HL)_5$, $(KL)_3$, $(KL)_3$, $(KL)_5$, and TVQFHMH with nucleic acids or on their own. This was not a complete survey of all possible conditions under which peptide-nucleic acid complexes could form, but I was interested to see if such complexes were associated with fibrous material.

Most peptide-nucleic acid complexes appeared as linear, unbranched fibres or fibrillar complexes on electron micrographs. They displayed a wide variety of morphologies including occasional helical twists and tape formations (see Figure 6-9, Figure 6-10, Figure 6-11 and Figure 6-12). The majority of the fibres had diameters ranging from 5 to 20 nm (see Table 6-10), agreeing with descriptions of amyloid fibres in the literature [2,31,139].

Controls

EM samples consisting only of buffer (here: 150 mM NaCl/ 20 mM HEPES pH 7; see Figure 6-8 A to C) showed background changes (light to dark; see Figure 6-8 B) and occasionally white aggregates on dark background (Figure 6-8 B) or dark aggregates on

lighter background (Figure 6-8 A). Similar results were obtained from peptide alone controls in buffer, but not always recorded; representative images of $(HL)_3$ and $(HL)_5$ alone were included in Figure 6-8, panel D and E. Note that the $(HL)_5$ sample was created from a fully dissolved stock solution which showed no aggregation as recorded in Table 6-6. The different staining properties of the Formvar or Pioloform-covered grids might have originated from unequally drying buffer solution during the sample preparation process. ST DNA in 150 mM NaCl/ 20 mM HEPES pH 7 displayed small aggregates with short fibrillar extensions. Similar images were obtained in the other buffers used for electron microscopy (data not shown). Such aggregation behaviour of DNA on unmodified EM grids without a spreading agent like cytochrome c for the nucleic acid has been observed before [224-228]. PA RNA in 150 mM NaCl/ 20 mM HEPES pH 7 formed fibrillar aggregates of varying size. No aggregates of this type were found in sample of $(KL)_3$- or $(KL)_4$-PA RNA mixtures (see Figure 6-10, top row).

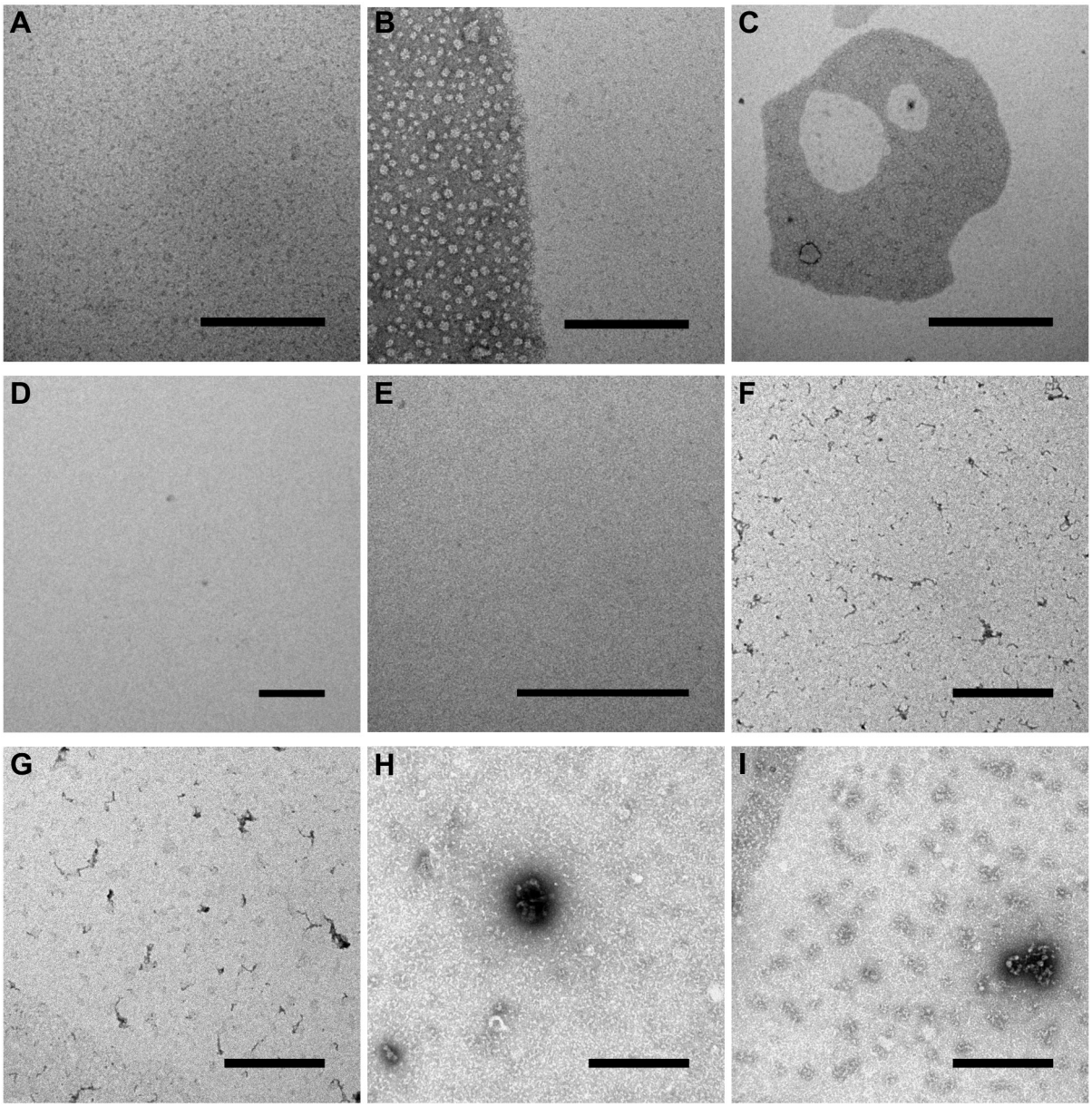

Figure 6-8: EM control images. (**A** to **C**) *Buffer control*. The grids showed a variety of circular structures and background changes (light <-> dark) that might originate from crystallisation of the 20 mM HEPES buffer containing 150 mM NaCl at pH 7. Similar images were observed with all buffers used for electron microscopy. (**D**) *$(HL)_5$ alone.* 1 mM $(HL)_5$ in 10 mM MES pH 5.5 with 150 mM NaCl showed no aggregates or fibres (note: these samples were prepared from a fully dissolved 10 mM peptide stock solution). (**E**) $(HL)_3$ alone. 1 mM $(HL)_3$ in 10 mM MES pH 6.2 with 150 mM NaCl showed no aggregates or fibres. (**F** and **G**) *Salmon testes DNA control*. 1 mM ST DNA in 150 mM NaCl/ 20 mM HEPES pH 7 displayed small aggregates with

short fibrillar extensions. Similar images were obtained in the other buffers used for electron microscopy (data not shown). (**H** and **I**) *Poly(A) RNA control*. 1 mM PA RNA in 150 mM NaCl/ 20 mM HEPES pH 7 showed aggregates consisting of short fibres. Similar images were obtained in the other buffers used for electron microscopy (data not shown). Scale bars were 500 nm.

$(HL)_n$-based complexes

$(HL)_3$-DNA complexes displayed several different fibre morphologies (Figure 6-9, bottom row). At pH 6.2 in the absence of NaCl (Figure 6-9, bottom left and centre) thick fibres (minimal diameters of about 12 nm; see Table 6-10) with a helical twist could be seen; background material consisting of thinner (minimal diameters of about 2.6 nm; see Table 6-10) and shorter fibres could be detected in the background. The morphology of the thicker fibres appeared to agree with the presence of amyloid fibrils, while the shorter, thinner fibres might have been protofibrils. At pH 5.5 in 150 mM NaCl (Figure 6-9, bottom right) very thin and not well-defined fibres appeared with minimal fibre diameters of 3.0 nm (see also Table 6-10). They would be very thin for amyloid fibrils, and they might have been DNA strands (about 2 nm diameter; [229]) decorated with peptides that did not form amyloid. It might be possible that the peptide only spread the DNA which usually formed aggregated clumps on EM grids, similar to the spreading effect of cytochrome c and other techniques used for DNA visualisation by electron microscopy [226-228]. On the other hand, the fibres were a bit too thick for single DNA strands (2.0 nm diameter of double-stranded DNA vs. 3.0 nm diameter of the detected fibres).

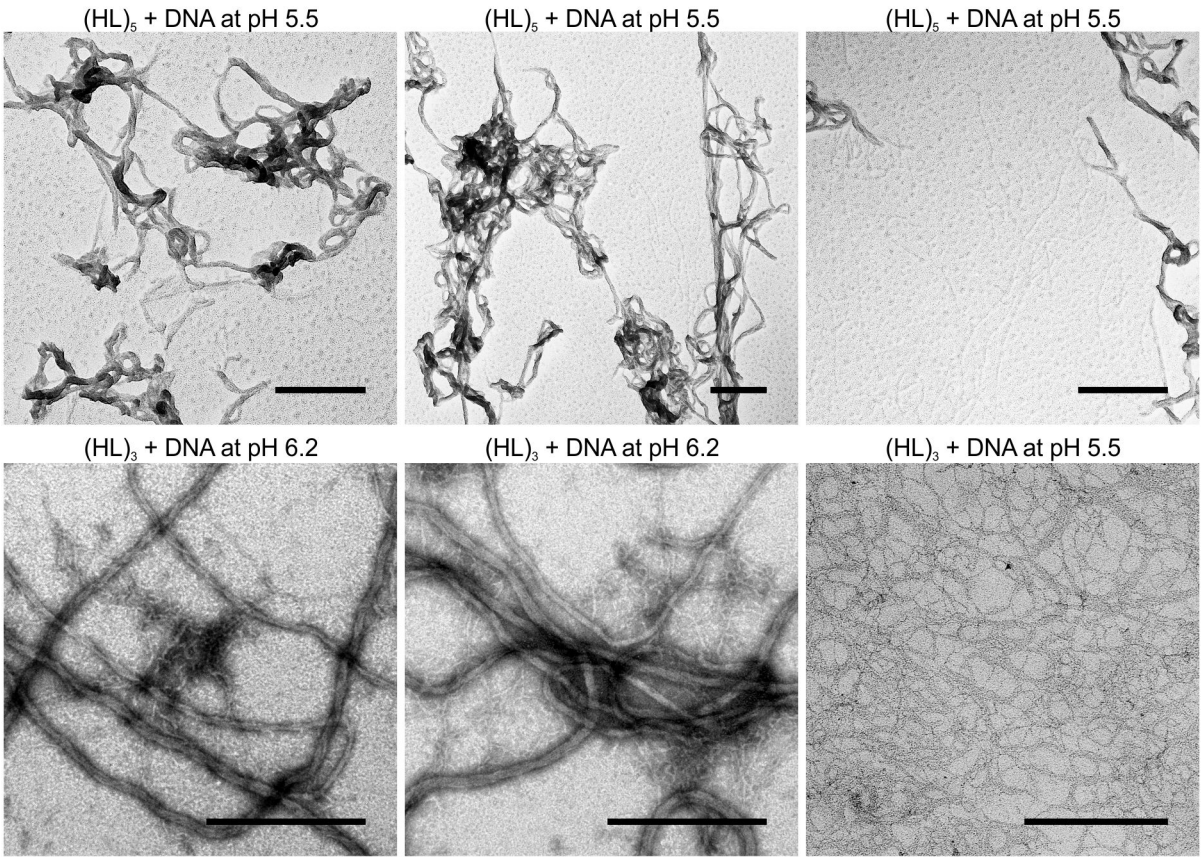

Figure 6-9: Electron micrographs showing fibres of $(HL)_3$- and $(HL)_5$-nucleic acid complexes. $(HL)_5$-DNA complexes (1 mM peptide, 1 mM ST DNA, 150 mM NaCl, 10 mM MES pH 5.5) showed fibres of varying thickness with a morphology not typical for amyloid fibrils, and some aggregates in the background (top row; rotary shadowed). At pH 6.2 attachment of $(HL)_3$-ANA complexes to the grid for imaging could only be achieved in the absence of salt, (1 mM $(HL)_3$, 1 mM ST DNA, 10 mM MES pH 6.2). They appeared as twisted fibres of varying thickness, with background material of thinner and shorter fibres (bottom left and centre). At pH 5.5 (1 mM $(HL)_3$, 1 mM ST DNA, 10 mM MES pH 5.5, 150 mM NaCl), very thin fibres could be seen. Scale bars were 300 nm. Rotary shadowing was done to increase the contrast of the images.

Although $(HL)_5$ only had two additional (HL) units more than $(HL)_3$, its peptide-DNA complexes exhibited a very different morphology. $(HL)_5$-ST DNA at pH 5.5 with 150 mM NaCl appeared as entangled fibres of varying thickness, which might be branching (see Figure 6-9, top row). There were at least two populations of fibres: Barely visible thin and relatively straight fibres (minimum diameter 5.8 nm (Table 6-10; Figure 6-9, top centre and right), and thicker, highly curved and maybe branched fibres (minimum diameter 14 nm (Table 6-10; Figure 6-9, top row). The appearance of fibres was a bit surprising given its poor gel formation abilities and bad stability in aqueous solution (only a very weak gel in the EM sample (1 mM $(HL)_5$ with 1 mM ST DNA at pH 5.5) and a general propensity to aggregate at higher (5 mM) concentrations; see Table 6-6), but it seemed that these entangled fibres represented a type of aggregate that gave rise to these properties. The morphology of these $(HL)_5$-ST DNA fibres would be very unusual for amyloid fibres, and the negative outcome of the Thioflavin T and Congo Red assays would suggest that these complexes may not represent amyloid fibrils.

$(KL)_n$-based complexes

All $(KL)_n$-based nucleic acid complexes tested showed fibrous structures by EM. The various (KL)-based complexes displayed varied fibril morphologies although they were based on the same amino acid repeat. $(KL)_3$-RNA complexes showed needle-like straight fibres (Figure 6-10, upper left panel), and $(KL)_4$-RNA complexes had a shorter and more curvaceous appearance (Figure 6-10, upper right panel). The complexes of $(KL)_5$ with DNA showed longer fibres that in some cases took on a ribbon morphology (see Figure 6-10, bottom left), but also some ring-like structures and amorphous aggregates (see Figure 6-10, bottom row). Although $(KL)_5$ alone was able to bind Congo Red suggesting

the presence of amyloid aggregates (Figure 6-7), no structures were observed when this peptide was examined at the EM (data not shown).

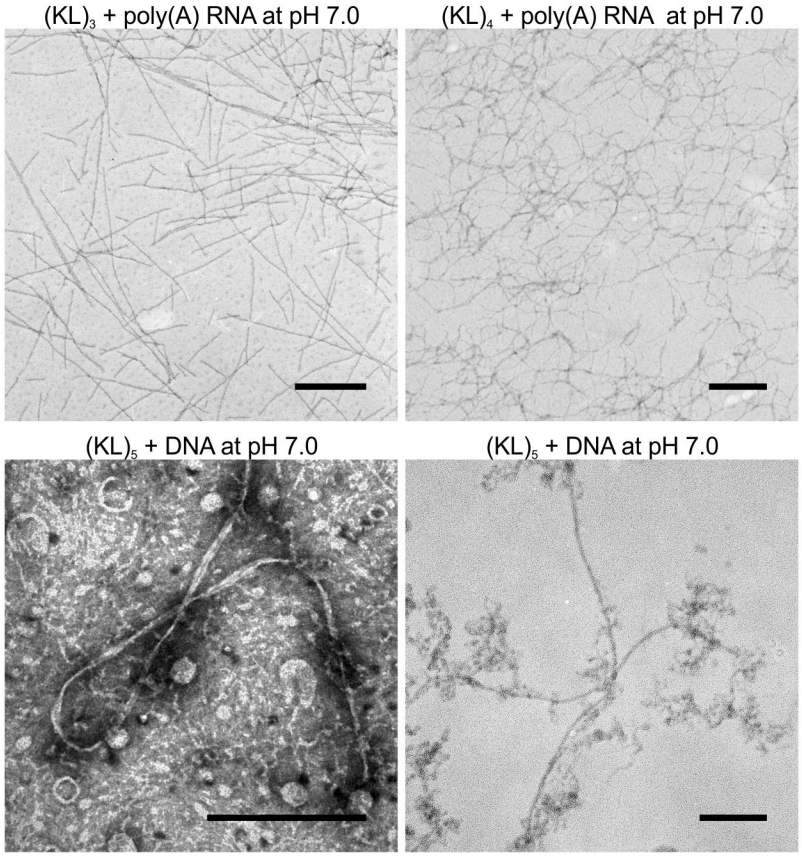

Figure 6-10: Electron micrographs showing fibres of KL-peptide-nucleic acid complexes. $(KL)_3$-RNA, $(KL)_4$-RNA and $(KL)_5$-ST DNA displayed fibres with amyloid morphology. $(KL)_3$-RNA complexes (0.33 mM peptide, 1 mM PA RNA, 10 mM HEPES pH 7.0) show very straight fibres (top left), while $(KL)_4$-RNA complexes (0.25 mM peptide, 1 mM PA RNA, 10 mM HEPES pH 7.0) appeared much more flexible and bendable (top right). $(KL)_5$-DNA complexes showed diverse morphologies at different concentrations: In the bottom left panel (1 mM peptide, 5 mM ST DNA, 150 mM NaCl, 10 mM HEPES pH 7) wide tapes in a strong background of round as well as circular and short thinner fibrous material, while in the bottom right panel (0.2

mM peptide, 5 mM ST DNA, 150 mM NaCl, 10 mM HEPES pH 7.0) fibres in contact with amorphous aggregates appeared. The latter morphology is similar to TVQFHMH-DNA complexes (see Figure 6-11). The top row was rotary shadowed to enhance the contrast of the fibres. Scale bars were 300 nm.

TVQFHMH-based complexes

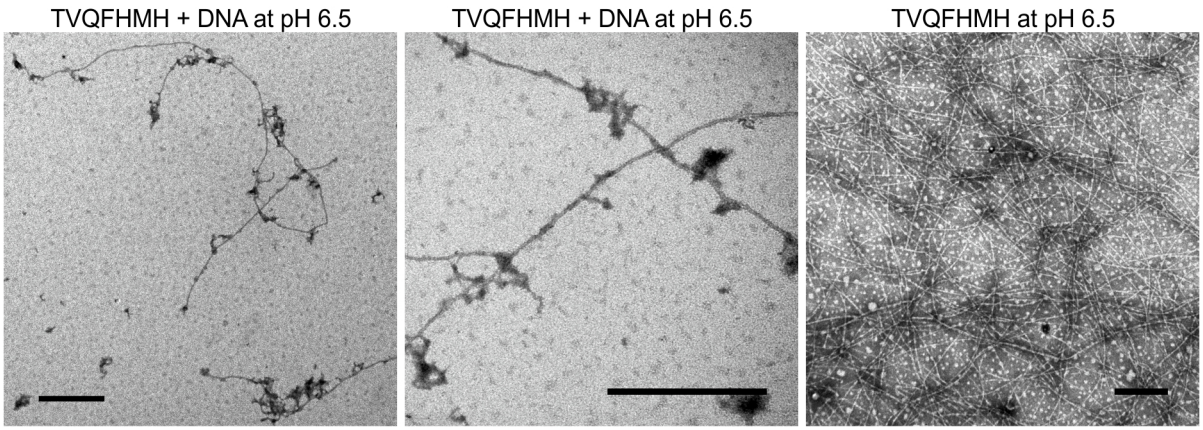

Figure 6-11: Electron micrographs showing fibres of TVQFHMH with or without DNA. *Left and centre panel:* The complexes of 5 mM TVQFHMH-ST DNA mixtures at pH 6.5 and in 150 mM NaCl appeared as fibres as well as large fibre-associated aggregates. Not many fibres were observed because the complexes were difficult to attach to the EM grids, although the samples formed strong gels indicating the presence large amounts of fibres. *Right panel:* 5 mM TVQFHMH alone in 150 mM NaCl/ 10 mM MES pH 6.5 (right panel) showed fibres and round aggregates of varying size. Scale bars were 300 nm.

A limited exploration of the effects of pH and NaCl on TVQFHMH-ST DNA fibres showed low fibre densities in the presence of 150 mM NaCl at pH 6.5 (see Figure 6-11 left and centre), but more fibres at pH 5.0 without NaCl (see Figure 6-12). The fibres had a

minimum diameter of about 10 nm (Table 6-10) and were associated with amorphous aggregates in 150 mM NaCl, and there seemed to be a background of round small aggregates (see Figure 6-11 left centre). In the absence of NaCl at pH 5.0 the fibres sometimes appeared to change diameter as shown in Figure 6-12.

Interestingly, TVQFHMH could be induced to form gels in the absence of nucleic acids (see Table 6-7). These gels were weaker than those of TVQFHMH-ST DNA or TVQFHMH-PA RNA complexes and were pipettable even at peptide concentrations up to 5 mM, while the TVQFHMH ANA gels were generally very sticky and stiff. Examination of such nucleic acid-free TVQFHMH gels by electron microscopy revealed large numbers of fibres, which could only be composed of TVQFHMH amyloid (see Figure 6-11 right). The fibres of TVQFHMH alone were generally thinner than the ones of TVQFHMH-DNA complexes (minimum diameter of about 6.4 nm; see Table 6-10), suggesting a different lateral association of the fibres (see Table 6-10). The presence of the charge-neutralising nucleic acid might have allowed closer interactions of the otherwise self-repelling fibrils, assuming that TVQFHMH was positively charged at pH 6.5 according to the peptide charge calculations. All in all, TVQFHMH fibres (with and without ST DNA) displayed amyloid morphology. It remained unclear what gave rise to the TVQFHMH-only fibres, but a change of properties by methionine oxidation might be a possibility. This reaction would convert methionine to methionine sulfoxide, which would reduce the hydrophobicity of the residue compared to methionine. It might be possible that this change would enhance fibre formation by TVQFHMH by an unknown mechanism. On the other hand, methionine sulfoxide would be expected to be found in the hydrophobic

core of a β-sheet sandwich, and the introduction of a polar functional group might interfere with the formation of amyloid fibres [137,138]. Future studies could resolve this issue by careful control of the oxidation potential of the system.

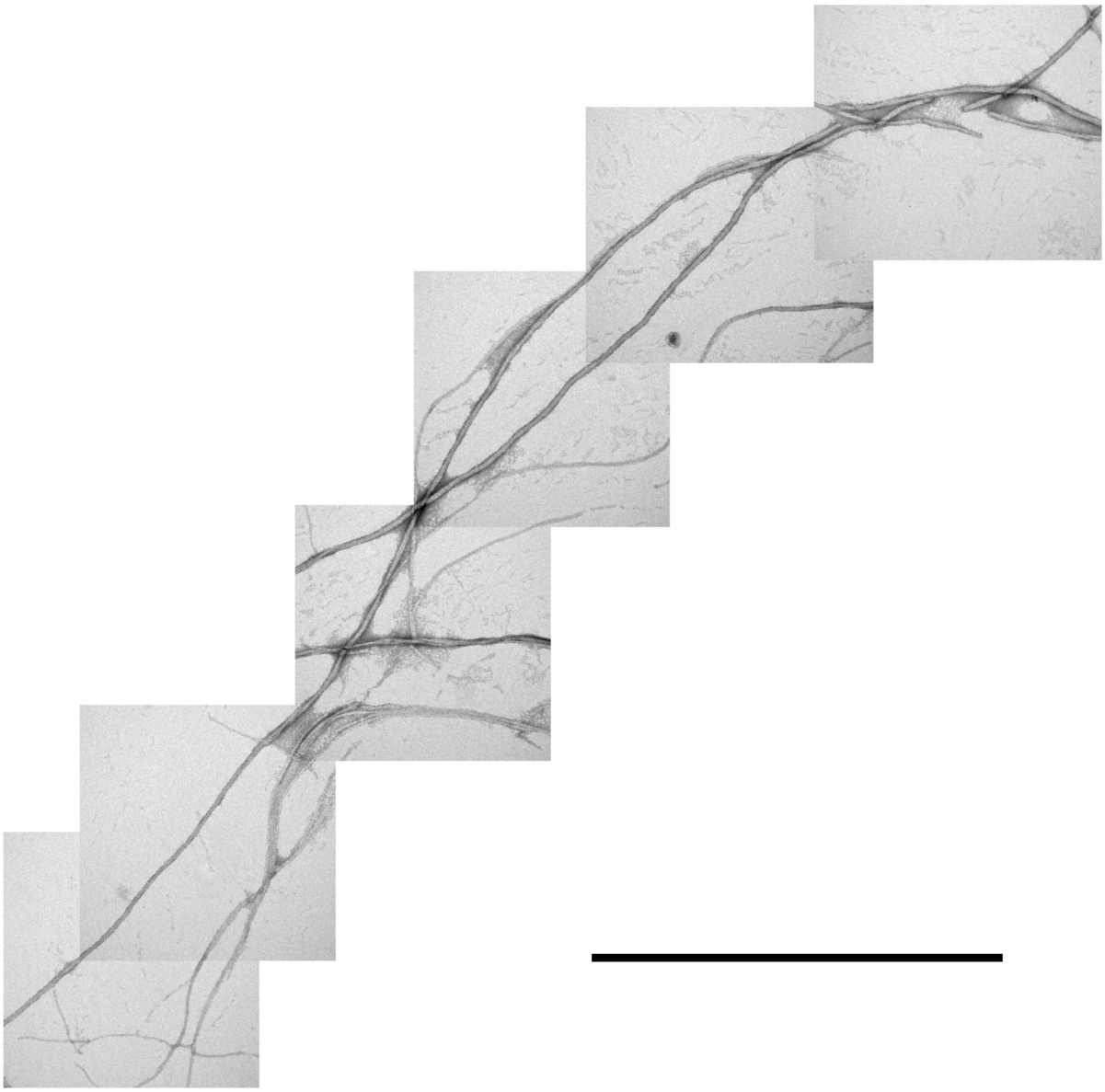

Figure 6-12: Composite TEM image of a TVQFHMH-DNA fibre. The sample was prepared from 5 mM TVQFHMH with 5 mM DNA in 10 mM MES at pH 5.0 and directly imaged without dilution. The fibre showed changes in diameter and was fragmented during sample preparation (see top right). Scale bar was 1 µm x 10 nm.

Fibre Diameters

The fibre diameters determined from these images largely agreed with the nucleic acid strand running collinearly with the amyloid fibres. For example, a B-DNA strand would have a diameter of 2 nm, while a $(KL)_5$-β-sheet would be about 3.1 x 2.6 nm (along the peptide backbone and across the β-sheet sandwich). This would result in a minimal fibre diameter of about 6.5 nm (DNA-β-sheet sandwich-DNA), at least for the highly charged $(KL)_5$ that would probably depend on nucleic acids on both lysine faces of the fibre for charge neutralisation. This was matched or exceeded by most ANA fibres as listed in Table 6-10. The only fibres that undercut this were from $(HL)_3$-DNA complexes which exhibited diameters of down to 3 nm diameter. As mentioned above, this might be due to potential fibrous complexes not attaching to EM grids in 150 mM NaCl-containing buffers.

Table 6-10: Diameters of the peptide-nucleic acid fibres

insulin amyloid pH 2.0	$(KL)_5$ + DNA pH 5.5	$(KL)_4$ + RNA pH 7.0	$(KL)_3$ + RNA pH 7.0	$(HL)_5$ + DNA pH 5.5 thick	$(HL)_5$ + DNA pH 5.5 thin
7.5 ± 0.9	8.1 ± 1.1	5.9 ± 1.2 *	4.4 ± 0.4 *	5.8 ± 0.3 *	14.0 ± 2.8 *
7.6 ± 0.9	11.6 ± 0.9	7.0 ± 0.7 *	5.4 ± 0.4 *	6.3 ± 0.3 *	14.5 ± 3.8 *
9.1 ± 0.4	11.7 ± 0.7	7.1 ± 0.4 *	5.4 ± 0.4 *	6.7 ± 0.3 *	14.5 ± 3.6 *
9.4 ± 0.9	15.0 ± 3.0	7.6 ± 0.6 *	5.5 ± 0.5 *	9.4 ± 2.1 *	17.5 ± 2.9 *
10.1 ± 1.5	16.1 ± 2.6	8.3 ± 0.9 *	5.7 ± 0.8 *	9.8 ± 1.3 *	18.3 ± 2.4 *
11.1 ± 1.6	18.5 ± 3.4	9.0 ± 2.2 *	5.9 ± 0.9 *	9.8 ± 0.7 *	19.8 ± 0.8 *
$(HL)_3$ + DNA pH 5.5	**$(HL)_3$ + DNA pH 6.2 thin**	**$(HL)_3$ + DNA pH 6.2 thick**	**TVQ + DNA pH 6.5**	**TVQ pH 6.5**	
3.0 ± 0.3	2.6 ± 0.3	11.9 ± 1.8	9.9 ± 1.0	6.4 ± 0.5	
3.3 ± 0.3	3.0 ± 0.8	12.5 ± 1.0	15.4 ± 1.8	8.2 ± 1.0	
3.3 ± 0.6	3.5 ± 0.3	15.8 ± 0.7	18.2 ± 1.1	8.4 ± 0.9	
3.6 ± 0.1	3.6 ± 0.4	17.4 ± 1.9	19.5 ± 1.6	8.8 ± 0.3	
4.0 ± 0.8	4.6 ± 1.1	17.5 ± 2.4	19.8 ± 2.6	9.2 ± 1.7	
4.1 ± 0.3	6.7 ± 1.8	17.8 ± 0.4	20.2 ± 1.5	9.7 ± 1.5	

Table 6-10 legend: Fibre diameters were determined using ImageJ from the fibres shown in Figure 6-9, Figure 6-10 and Figure 6-11 [204]. Three measurements were taken on 6 well-defined fibres with a distance of at least twice the diameter between measurement sites, i.e. 18 measurements in total for each sample. The focus was on the determination of minimal fibre diameters of longer fibres. In case of $(HL)_3$-ST DNA and $(HL)_5$-ST DNA the diameters of the thicker and thinner fibres were treated separately as indicated. Diameters are in nm ± standard deviation. *, rotary shadowed sample; diameters of fibres might be slightly smaller.

Summary

All complexes of peptide-nucleic acid complexes showed fibres with varying morphology. Taken together, TEM imaging further strengthened the idea that simple positively charged peptides with an alternating pattern of hydrophobic and hydrophilic amino acid residues could form amyloid fibres because all peptide-nucleic acid complexes examined here ($(KL)_3$, $(KL)_4$, $(KL)_5$, $(HL)_3$, $(HL)_5$, and TVQFHMH with ST DNA or PA RNA; TVQFHMH on its own) showed fibre morphologies compatible with amyloid formation. The attachment of the peptide-nucleic acid fibres to the EM grids presented a challenge, particularly for $(HL)_3$-ST DNA and TVQFHMH-ST DNA mixtures.

6.1.6. CONFOCAL MICROSCOPY OF ANA COMPLEXES

This experiment was designed by Christine Humphreys (Cardiff University) with support from me for gel formation and sample mounting on the confocal microscope. We set imaging parameters, acquired and analysed the data together. Further support was provided by Anthony Hayes (Cardiff University).

Since it was possible that the peptides required nucleic acids only for amyloid nucleation and the fibres in the micrographs contained no nucleic acids, we looked at $(HL)_3$-DNA ANA complexes by confocal microscopy under near-physiological conditions in 150 mM NaCl-containing buffer (see Figure 6-13). $(HL)_3$ was chosen because its charges could be modulated by pH changes, and we wanted to examine the effect of charge density on the peptide on complex formation between $(HL)_3$ and ST DNA. $(HL)_3$ was expected to carry a calculated +3 net charge at pH 5.0, and a +1.5 net charge at pH 6.5 (see Table 6-1). Salmon testes DNA was labelled by nick-translation with ATTO 550 and spiked at a 1:20 ratio into unlabelled ST DNA, and the peptide $(HL)_3$ was spiked at a 1:20 ratio with N-terminally fluorescein-labelled $(HL)_3$. Neither labelling should affect the primary attributes of DNA (negatively-charged phosphate backbone) or peptide (alternating pattern of hydrophilic/ hydrophobic amino acid residues with theoretical positive charges) necessary for peptide-nucleic acid complex formation. The low ratio of the labelled tracers made it unlikely that they were the primary interaction partners, while still highlighting the spatial distribution of DNA or peptide as a whole. The presence of the tracers had no effect on gel formation (see Table 6-2), but it might be possible that local dye/ peptide/ nucleic acid interactions could be distinct from the bulk material. The dyes had little overlap in their absorption spectra, so their fluorescence could be

excited and detected separately, allowing examination of the spatial distribution of DNA and peptide in the sample independently.

Intimate association of peptide and DNA was seen in large, fibrous structures that were the basis for the peptide-nucleic acid gels (orange/ yellow areas in Figure 6-13 A and B, right panels), while there was no detectable bleed-through (Figure 6-13 C and D, right panels). No such complexes could be seen when ATTO550-DNA-spiked ST DNA or FITC-$(HL)_3$-spiked $(HL)_3$ were imaged on their own (data not shown); only dirt and scratches of object slide and coverslip could be detected. Unlike the gel samples, diffusion of the sample may have prevented the imaging of individual fibres. Interestingly, the complexes formed at pH 5 showed finer structures, perhaps made from thinner fibres. The complexes might consist of DNA in complex with amyloid fibres, or alternatively of DNA strands decorated by peptide molecules not in amyloid conformation. In the former case the fibres displayed in Figure 6-13 would consist of colinear DNA and amyloid fibrils because no pattern of DNA strands crossing peptide fibrils could be resolved, in the latter case the DNA fibres would be decorated by peptide. Taken together, confocal microscopy suggested that $(HL)_3$ and ST DNA were closely associated in large fibrous complexes.

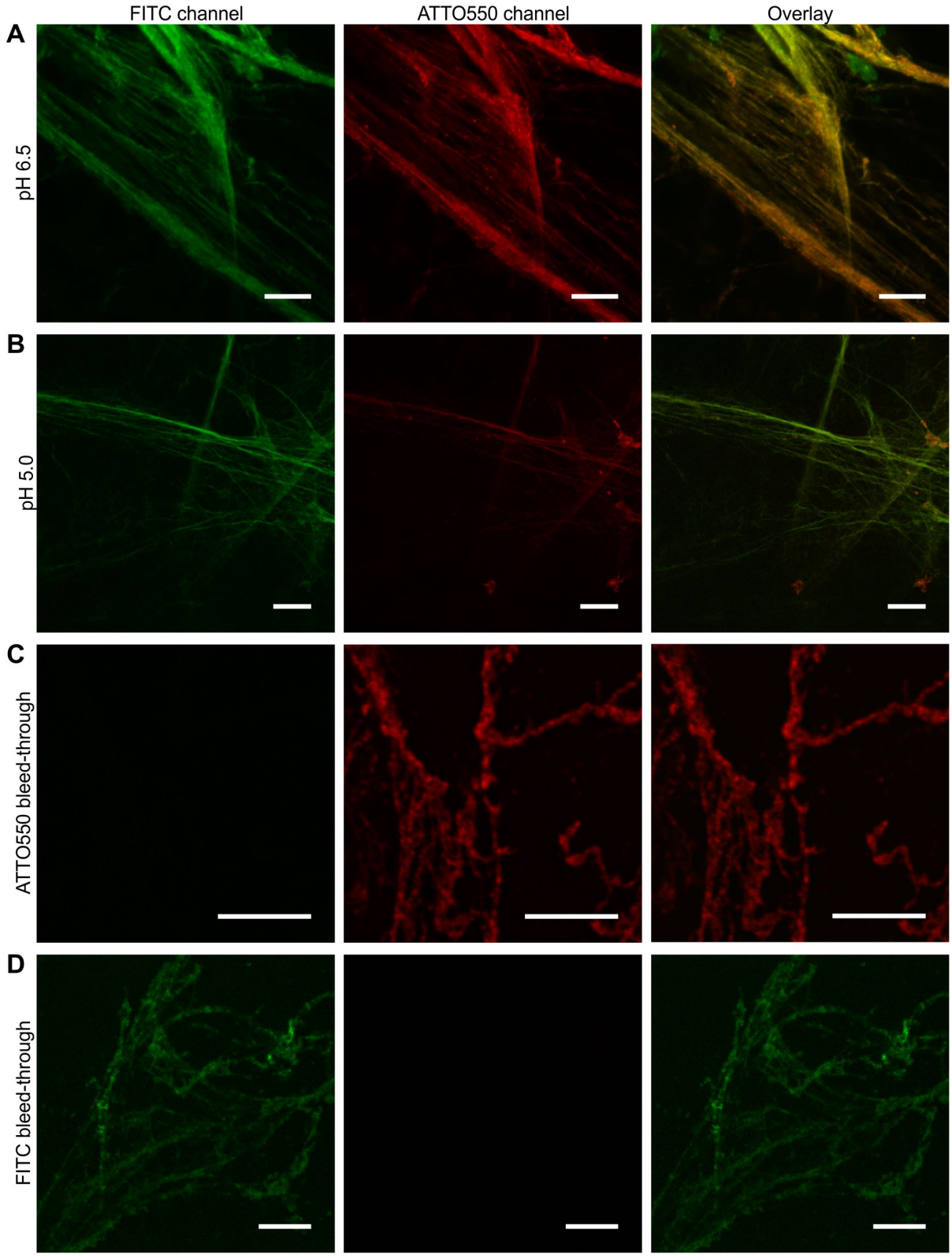

Figure 6-13: Confocal microscopy. (**A, B**) Representative confocal images of $(HL)_3$-DNA ANA complexes where peptide and DNA samples had previously been spiked with fluorescently labelled variants in 10 mM MES buffers containing 150 mM NaCl. 6 mM $(HL)_3$ spiked 1:20

with FITC-$(HL)_3$; 2.5 mM ST DNA spiked 1:20 with nick-translated ATTO 550-ST DNA. The structures at pH 5.0 (**B**) are generally finer than the ones at pH 6.5 (**A**). (**C, D**) No bleed-through was detected between fluorescence channels. (**C**) Unlabelled $(HL)_3$ mixed with labelled ATTO 550-DNA-spiked salmon testes DNA. (**D**) FITC-$(HL)_3$-spiked $(HL)_3$ with unlabelled salmon testes DNA. No aggregates or fibres could be detected in peptide-only or ST-DNA only controls (data not shown). Scale bars were 10 µm.

These images were taken by Christine Humphreys with support from Anthony Hayes of the Confocal Microscopy Unit (Cardiff University, School of Biosciences).

6.1.7. Cross-β Patterns of ANA Complexes Shown by X-ray Fibre Diffraction

Fibre diffraction was the most robust test for amyloid because it allowed the detection of the characteristic cross-β pattern. The method was independent of dyes like Thioflavin T or Congo Red having access to their binding sites, and was free of the interfering DNA-binding-capacity of Thioflavin T or aggregation enhancement of Congo Red (see above).

Complexes of most examined peptide-nucleic acid complexes gave rise to clear cross-β patterns in X-ray fibre diffraction, indicating that they contained amyloid (see Figure 6-14, Figure 6-15 and Figure 6-17). The patterns were dominated by a strong meridional reflection at 4.6 to 4.8 Å, which originated from the spacing between the β–strand peptide backbones that lay perpendicular to the fibre axis (see Figure 4-3 for a schematic, and Table 6-11, Table 6-12 and Table 6-13 for the Bragg spacings of the reflections); this agreed with previously analysed amyloid diffraction patterns [2,41,79,142,230]. Due to the quasi-crystalline order along the fibre axis this reflection was very strong with high intensities. Equatorial reflections in the range of 10 to 12 Å were consistent with inter-sheet spacings, which were determined by the van-der-Waals-radii of the amino acid residues [24,130,139]. The diffraction patterns of the individual ANA complexes are described and discussed below in detail.

$(HL)_n$-based complexes

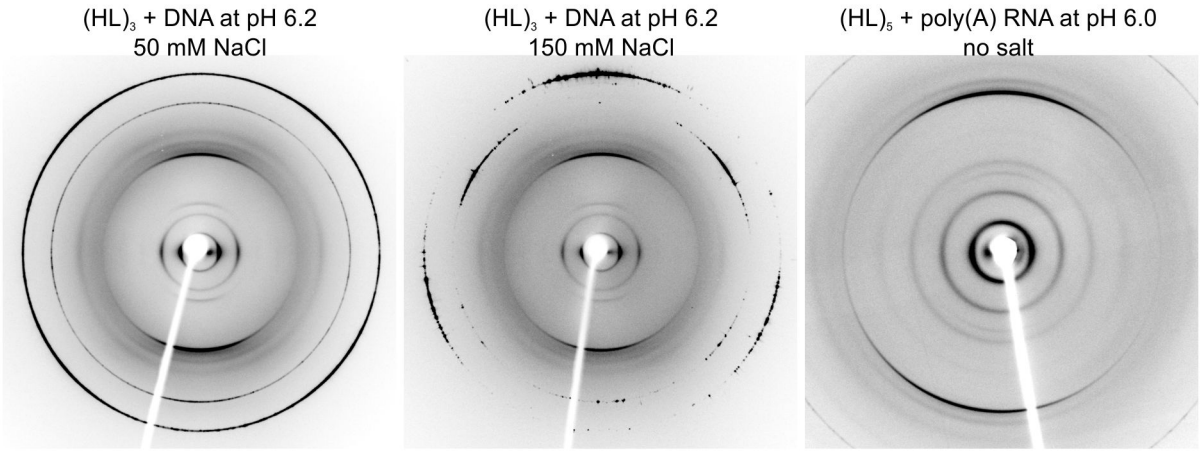

Figure 6-14: Fibre diffraction of HL-based peptides. $(HL)_3$ with ST DNA and $(HL)_5$ with poly(A) RNA showed clear cross-β patterns. The samples consisted of 5 mM $(HL)_3$ with 5 mM ST DNA in 10 mM MES pH 6.2/ 50 mM NaCl (left), 10 mM $(HL)_3$ with 10 mM ST DNA in 10 mM MES pH 6.2/ 150 mM NaCl (middle), and 12.6 mM $(HL)_5$ with 6.3 mM PA RNA in 5 mM MES pH 6.0 (right). Sample-detector distance was 180 mm for $(HL)_3$ samples and 300 mm for the $(HL)_5$ sample.

$(HL)_3$-ST DNA readily formed relatively weak gels at pH 6.2 in the presence of NaCl, and they did not easily yield stalks suitable for X-ray fibre diffraction analysis. Several conditions were explored to initiate stalk formation, among them varying NaCl concentration (0, 50, and 150 mM) and peptide concentration (1 mM to 10 mM). The pH was kept at pH 6.2 with 10 mM MES in order to maintain a calculated +2 net charge per peptide. This was supposed to generate a net +1 charge per peptide (+2 chargers per peptide at pH 6.2, -1 charge per base of ST DNA) which was previously described as favourable for ordered amyloid formation [142]. Eventually stalks could be generated from 5 mM $(HL)_3$ with 5 mM ST DNA in 50 mM NaCl and 10 mM $(HL)_3$ with 10 mM ST

DNA in 150 mM NaCl showing cross-β patterns (see Figure 6-14). $(HL)_5$ with its general propensity to form aggregates and precipitate (see Table 6-6) formed stalks easily in the absence of NaCl and displayed a surprisingly clear cross-β pattern (see Figure 6-14, right).

Table 6-11: Bragg spacings of $(HL)_n$-based peptides in X-ray fibre diffraction

$(HL)_3$ ST DNA 50 mM NaCl pH 6.2			$(HL)_3$ ST DNA 150 mM NaCl pH 6.2			$(HL)_5$ poly(A) RNA pH 6.0		
22.9	e	(vs)	23.3	e	(s)	24.31	e	(vs)
11.6	**e**	**s**	**11.7**	**e**	**m**	**12.25**	**e**	**s**
9.20	m	w	9.21	m	w	9.35	m	w
						8.23	e +	m
						6.08	e	vw
4.72	**m**	**vs**	**4.72**	**m**	**s**	**4.78**	**m**	**s**
4.25	m	w	4.26	m	vw			
						4.47	m	m
						(4.12)	m	(vw)
3.91	m (+?)	vw	3.94	ring?	vw			
						3.54	ring	vw
3.25	salt		3.25	salt				
2.82	salt		2.82	salt				

Table 6-11 legend: Bragg spacings were determined using WCEN and CLEARER from the diffraction patterns shown in Figure 6-14. The strong meridional reflections at 4.7 Å for $(HL)_3$-DNA or 4.8 Å for $(HL)_5$-RNA in combination with the equatorial reflections at 11.6 Å for $(HL)_3$-DNA or 12.3 Å $(HL)_5$-RNA comprised a cross-β pattern (marked in bold print). Abbreviations: e, equatorial; m, meridional; vs, very strong; s, strong; m, medium; w, weak; vw, very weak; +, equatorial and meridional; ?, uncertainty about anisotropy. Reflections in brackets were diffuse (4.12 Å reflection of $(HL)_5$-PA RNA) or partially covered by the beam stop (reflections >20 Å) and could not be determined with much confidence.

As the reflections of $(HL)_3$-ST DNA determined from these patterns showed (see Figure 6-14 left and centre; Table 6-11), the difference in salt concentration between 50 mM and 150 mM NaCl did not affect the diffraction pattern. It was highly consistent between the two samples and virtually identical apart from rings and spots caused by enclosed buffer and NaCl salt crystals (see also Supplementary Figure 9 for an overlay of the two patterns). A meridional reflection at 9.2 Å most likely originated from a repeat unit within the fibril every two peptides, suggesting the presence of anti-parallel β-sheet [231]. The pattern of $(HL)_5$-PA RNA was very similar to the $(HL)_3$-ST DNA patterns (see Table 6-11). The meridional 9.35 Å reflection might, similar to the $(HL)_3$-ST DNA patterns, suggested the presence of anti-parallel β-sheet [231]. The 'additional' equatorial reflections compared to the $(HL)_3$-ST DNA patterns at 8.23 Å and 6.08 Å might be caused by well-ordered lateral packing of fibrils; alternatively they may be caused by the presence of protofilaments within the amyloid fibril, similar to the β-helix structure suggested by Blake and Serpell for TTR amyloid fibrils [79,230,232]. In such a structure the individual β-sheets would be twisted with respect to its neighbours, generating a helical twist in the β-sheets around an axis parallel to the protofilaments axis. The beta-helix has also been suggested to be a generic structure of amyloid fibrils [79], among others [134].

$(KL)_n$-based complexes

$(KL)_3$-DNA complexes readily formed stalks in the absence of NaCl and diffracted well (see Figure 6-15, top row). Herring testes DNA was used for one sample because stock of salmon testes DNA had run out; no difference in gel formation could be detected (data

not shown). The patterns showed a multitude of well-defined reflections which in one case displayed an unusual triplet of reflections at about 4.7 Å (4.50 Å, 4.77 Å, and 5.03 Å; see Table 6-12) instead of a single strong one (see Figure 6-15, top left). This deviated from the 'canonical' cross-β pattern with only a single strong reflection at 4.7 to 4.8 Å as described in the literature [2,79,135,230], maybe indicating an unusual packing polymorphism in direction of the fibre axis. The meridional 5.03 Å reflection was not found in any other sample examined here, and was not previously described in the literature [79,230]. This suggested that the fibres formed by $(KL)_3$ with HT DNA at pH 6.0 might not represent amyloid fibrils. The pattern of $(KL)_3$-ST DNA at pH 7 showed, similar to $(HL)_5$-PA RNA at pH 6, additional equatorial reflections that suggested the presence of protofilaments within the amyloid fibril [79,230,232].

The $(KL)_5$-DNA complexes did not easily form a stalk in the absence of NaCl, although they presented as very strong gels (see Table 6-5). This resulted in only partially aligned material with a diffuse cross-β pattern (see Figure 6-15, bottom left; Table 6-12). However, more and sharper reflections appeared in the presence of 150 mM NaCl (see Figure 6-15, bottom right; Table 6-12). There might have been a charge-screening effect of the salt that modulated the otherwise very strong interactions of peptide and nucleic acid to allow for proper adoption of the amyloid conformation. The pattern of $(KL)_5$-ST DNA at pH 7 with 150 mM NaCl showed, similar to $(HL)_5$-PA RNA at pH 6 and $(KL)_3$-ST DNA at pH 7, additional equatorial reflections that suggested the presence of protofilaments within the amyloid fibril [79,230,232].

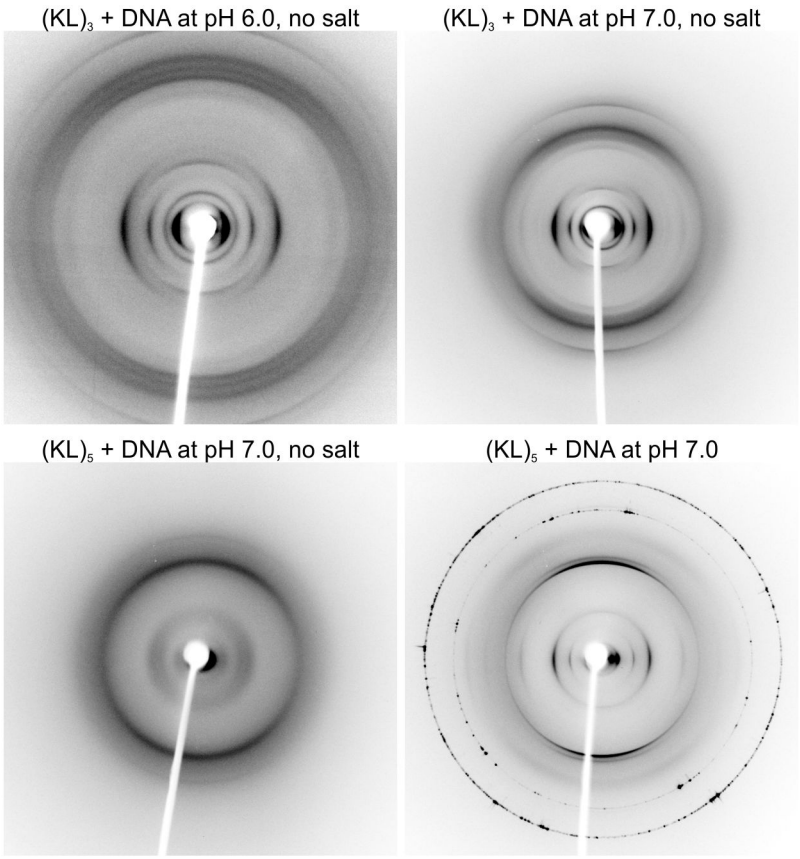

Figure 6-15: Fibre diffraction of KL-based peptide. Both $(KL)_3$ and $(KL)_5$ exhibit clear cross-β patterns, but $(KL)_5$-DNA complexes exhibited higher order structures solely in the presence of NaCl. Samples consisted of 21.6 mM $(KL)_3$ with 10.8 mM HT DNA at pH 6.0 (top left), 10 mM $(KL)_3$ with 10 mM ST DNA at pH 7.0 (top right), 5 mM $(KL)_5$ with 5 mM ST DNA in 10 mM HEPES pH 7.0 (bottom left), and 5 mM $(KL)_5$ with 5 mM ST DNA in 10 mM HEPES pH 7.0/ 150 mM NaCl (bottom right). The top-left pattern was recorded at 300 mm sample-detector distance, the others at 180 mm. A larger version of the $(KL)_3$-DNA pattern shown in Figure 6-15 top right with all reflections annotated can be found in Figure 6-16.

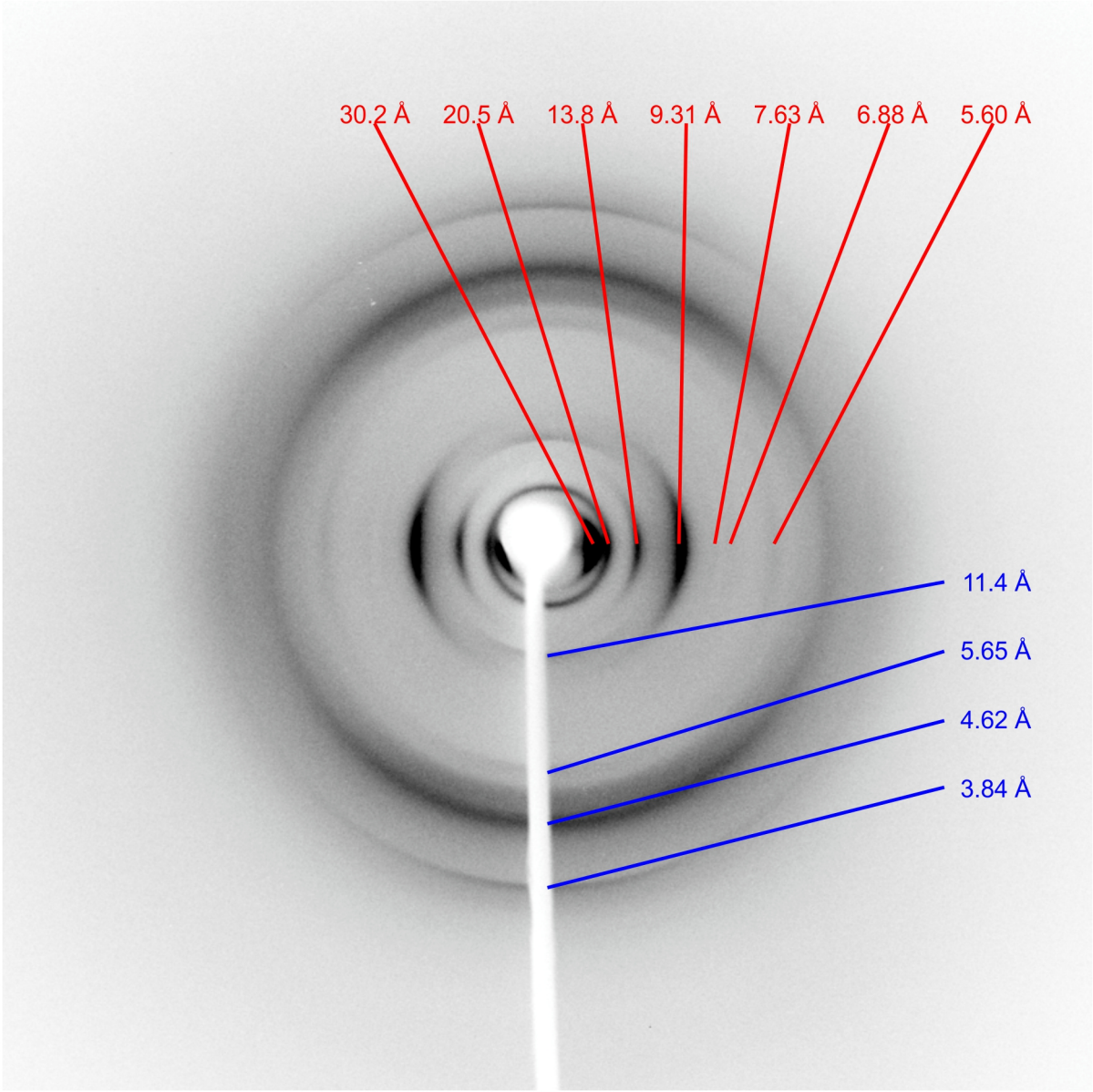

Figure 6-16: Annotated diffraction pattern of $(KL)_3$-DNA. The Bragg spacings listed in Table 6-12 for the pattern of $(KL)_3$-DNA (10 mM peptide with 10 mM ST DNA at pH 7.0) also shown in Figure 6-15 (top right) are annotated for equatorial reflections in red (top row) and for meridional reflections in blue (right column).

$(KL)_3$-ST DNA at pH 7 and $(KL)_5$-ST DNA with 150 mM NaCl at pH 7 exhibited very similar diffraction patterns (see Figure 6-15, top right and bottom right; Table 6-12 and

Supplementary Figure 8 with an overlay of the patterns). The main equatorial reflection was nearly identical, as would be expected because it represented the distance of the two beta-sheets facing each other. This spacing would be influenced by the side chain volumes, which were identical in this case. The equatorial reflections suggested a similar organisation of protofilaments and/ or lateral fibril packing, i.e. the additional reflections of $(KL)_3$-ST DNA at pH 7 compared to $(KL)_5$-ST DNA at pH 7 with 150 mM NaCl might indicate a better order fibrillar complex [79,230,232]. But while $(KL)_5$-ST DNA exhibited canonical reflections in the meridional direction, the $(KL)_3$- DNA patterns were quite unusual. $(KL)_3$-ST DNA at pH 6 showed relatively small (4.6 Å) inter-strand spacing of the peptide backbones with salmon testes DNA at pH 6, and triple meridional reflections around 4.8 Å with herring testes DNA at pH 7. This made unlikely that in the latter case the structure of the fibre diffraction sample constituted an amyloid fibre.

The $(HL)_n$ and $(KL)_n$ peptides used here showed quite similar diffraction patterns (see Figure 6-14, Figure 6-15, Table 6-11, Table 6-12, Supplementary Figure 8, and Supplementary Figure 9), with the exception of the triple-meridional reflection at about 4.7 A of $(KL)_3$-HT DNA at pH 6. There were only very small differences in meridional direction, as expected from the very low potential variation in β-strand packing and the quasi-crystalline order along the fibril axis [79]. Several factors might have influenced the equatorial reflections: Different lateral packing of fibrils, different arrangement of protofibrils, and different sizes and Van-der-Waals volumes of the histidine and lysine side chains for the $(HL)_n$ and $(KL)_n$ peptides that determined the separation of the beta-sheets [79,230,232].

Table 6-12: Bragg spacings of (KL)-based peptides in X-ray fibre diffraction

$(KL)_3$ HT DNA pH 6.0			**$(KL)_3$ ST DNA pH 7.0**			**$(KL)_5$ ST DNA pH 7.0**			**$(KL)_5$ ST DNA 150 mM NaCl pH 7.0**		
(28.5)	(e)	(vs)	(30.2)	(e)	(vs)				(30.2)	(e)	(vs)
(20.5)	(e (ring?))	(s)	(20.5)	(e)	(s)						
14.3	e	s	13.8	e	s				14.0	e	m
11.1	m	w	(11.4)	m	(w)						
9.56	**e**	**vs**	**9.31**	**e**	**vs**	**10.1**	**e**	**(w)**	**9.30**	**e**	**s**
			7.63	e	vw						
			6.88	e	vw						
(5.66)	e (+)	(vw)	5.60	e	w				5.63	e	w
			5.65	m	w						
5.03	m	s									
4.77	**m**	**s**				**4.7**	**m**	**w**	**4.78**	**m**	**vs**
4.50	m	s	**4.62**	**m**	**s**				4.53	m	m
3.84	m	s	3.84	m	m	3.8	m	w	(3.82)	m (x)	(m)
									3.26	salt	
									2.82	salt	

Table 6-12 legend: Bragg spacings were determined using WCEN and CLEARER from the diffraction patterns shown in Figure 6-15. The strong meridional reflections at 4.6 Å to 4.8 Å in combination with the equatorial reflections at 9 to 10 Å comprised a cross-β pattern. There were more reflections visible with $(KL)_3$ than with $(KL)_5$. $(KL)_3$-DNA complexes showed some unusual diffractions at the expected 4.8 Å meridional with either a triple reflection ($(KL)_3$ with HT DNA at pH 6) or a relatively small reflection at 4.62 Å ($(KL)_3$ with ST DNA at pH 7). Abbreviations: e, equatorial; m, meridional; vs, very strong; s, strong; m, medium; w, weak; vw, very weak; +, equatorial and meridional; reflections in brackets were diffuse or partially covered by the beam stop (>20 Å) and could not be determined with much confidence.

TVQFHMH-based complexes

The strong and sticky TVQFHMH-DNA gels (see Table 6-7) and the very weak gels of TVQFHMH alone (see Table 6-7) readily produced stalks that diffracted well. The diffraction patterns of TVQFHMH alone and TVQFHMH-ST DNA complexes were remarkably similar (see Figure 6-17 and Supplementary Figure 10 for some overlays). The core reflections comprising the cross-β pattern appeared to be independent of pH (5.0, 6.0, and 6.5) and nucleic acid (poly(A) RNA, salmon testes DNA) changes. In one case, a multitude of additional reflections indicated the presence of microcrystals that were embedded into the stalk (Figure 6-17, bottom left). The cross-β pattern suggested amyloid formation, but the overlay of the three different diffraction patterns of amyloid fibres, buffer and salt rings, and the microcrystal powder pattern made an in-depth analysis unfeasible.

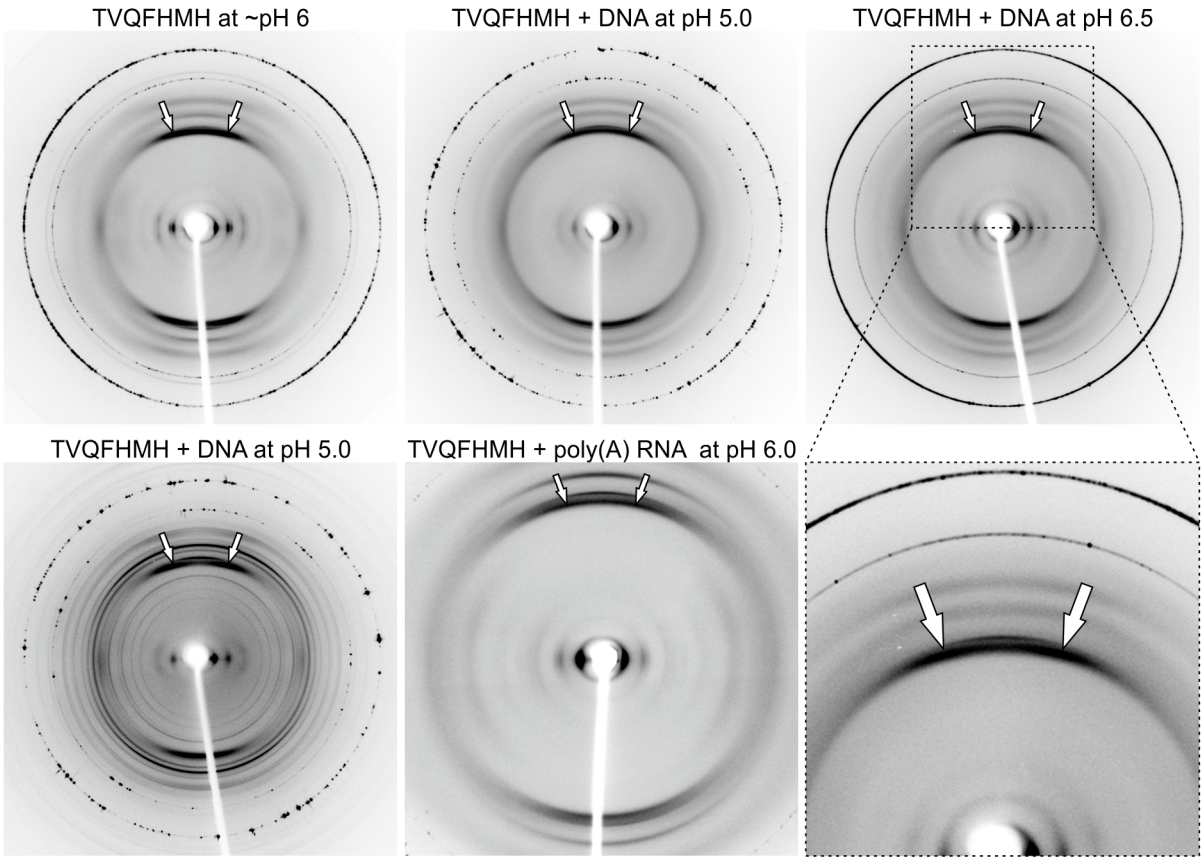

Figure 6-17: Fibre diffraction of TVQFHMH. All TVQFHMH samples showed clear cross-β patterns, even in the absence of nucleic acid (top left). Arrows point to the split maxima in the ~4.7 Å reflection in the top arc, which has been enlarged for the top right pattern (TVQFHMH + ST DNA at pH 6.5) at the bottom right. Similar reflections appeared in all TVQFHMH-based diffraction patterns, and they were also visible in the bottom arc but less clear due to the beam stop. The bottom left pattern had additional reflections due to enclosed microcrystals. The samples were created with 1.6 mM TVQFHMH (top left), 1.0 mM TVQFHMH + 1.0 mM ST DNA in 10 mM MES pH 5.0 (top middle), 1.6 mM TVQFHMH + 1.6 mM ST DNA in 10 mM MES pH 6.5 (top right), 1.6 mM TVQFHMH + 1.6 mM ST DNA in 10 mM MES pH 5.0 (bottom left), and 17.8 mM TVQFMH + 8.9 mM poly(A) RNA in 5 mM MES pH 6.0 (bottom middle). Patterns were recorded at 180 mm sample-detector distance, except for the bottom centre one, which was done at 300 mm.

Table 6-13: Bragg spacings of TVQFHMH in X-ray fibre diffraction

TVQFHMH ~ pH 6			TVQFHMH ST DNA pH 5.0			TVQFHMH ST DNA pH 6.5			TVQFHMH Poly(A) RNA pH 6.0		
(31.9)	(e)	(vs)	(35.6)	(e)	(vs)	(34.9)	(e)	(vs)	(31.9)	(e)	(vs)
16.3	e	vs	16.0	e	(m)	16.3	e	s	17.8	e	s
14.5	e	s									
									11.4	e	w
10.5	**e x**	**m**	**(10.5)**	**e**	**(w)**	**(10.4)**	**e (x?)**	**(w)**	**(10.3)**	**e**	**(vw)**
(7.59)	e	(vw)	(7.65)	e	(vw)	(7.56)	e (x?)	(vw)	7.39	e x	w
(5.63)	e x	(vw)	5.60	e	w				5.66	e (x?)	vs
4.70	**m (x?)**	**vs**	**4.73**	**m**	**vs**	**4.72**	**m**	**vs**	**4.81**	**m**	**vs**
4.59	e +	(w)	4.60	m	s	4.59	m	s	4.59	m	s
4.14	m	m	4.07	m	w	4.07	m	w	4.17	m	m
3.70	m (x?)	w	3.72	m	(w)	3.72	m	w	3.67	m	w
3.25	salt		3.25	salt		3.25	salt				
3.14	ring? +?	vw									
2.82	salt		2.81	salt		2.82	salt				

Table 6-13 legend: Bragg spacings in Å were determined using WCEN and CLEARER from the diffraction patterns shown in Figure 6-17. The strong meridional reflection at 4.7 Å (TVQFHMH alone or with ST DNA) or 4.8 Å (with poly(A) RNA) in combination with the equatorial reflection at about 10.5 Å comprised a cross-β pattern. There were no striking differences between the individual diffraction patterns. Abbreviations: e, equatorial; m, meridional; vs, very strong; s, strong; m, medium; w, weak; vw, very weak; +, equatorial and meridional; reflections in brackets were diffuse or partially covered by the beam stop (>20 Å) and could not be determined with much confidence.

All diffraction patterns based on TVQFHMH displayed very similar reflections (see Figure 6-17 and Table 6-13), indicating that they were primarily due to the peptide and largely independent of the identity of nucleic acid and pH. This was maintained over

different peptide batches, purifications and stock solutions. This suggested that nucleic acids were not necessary to induce the cross-β structure in TVQFHMH. The 4.7 Å reflections of all TVQFHMH diffraction patterns were quite unusual. They displayed a split reflection with two maxima in the main arc, suggesting some helical symmetry, which normally did not show up in other amyloid diffraction patterns (Matthias Bochtler, Louise Serpell, personal communication) [233,234]. Again, the equatorial reflections might indicate the presence of a β-helix structure similar to TTR amyloid fibrils [230], but the weakness of these reflections could also suggested the formation of a β-solenoid. Such a structure would be an alternative to the β-sheet sandwich [134] and have been described as having parallel β-sheets perpendicular to the fibre axis that wound around a water-filled [235,236] or hydrophobic core [237]. Diffraction patterns of β-solenoids were very similar to β-sheet sandwiches with a strong meridional reflection at 4.7 to 4.8 Å, but lacking or having only a weak characteristic equatorial reflection at around 10 Å. This reflection resulted in the β-sandwich from the spacing between the two β-sheets facing each other and would be absent in a cylindrical or triangular tube [235,237,238]. On the other hand, the peptide TVQFHMH would have a very short sequence compared to the peptides and proteins involved in the formation of β-solenoids [134]. It would probably not be sufficiently long to form a full turn around the core, and β-solenoids with a discontinuous polypeptide turns have not been previously described [235-239].

DNA Diffraction Patterns

While the peptides diffracted well and gave rise to clear amyloid cross-β patterns, no reflections of any DNA diffraction pattern could be found in the peptide-DNA complex patterns. This was even more remarkable since fibre diffraction samples consisting only

of salmon testes DNA with or without 150 mM NaCl yielded clear A-DNA diffraction patterns as expected from dried crystallised DNA (Figure 6-18) [233]. The presence of salt seemed to push the intensity of the DNA reflections to the background, obscuring some of the finer details (compare Figure 6-18 left and centre; Table 6-14). This could present a general issue when working with physiological salt concentrations if the crystallisation of NaCl or other salts could not be prevented. Single-stranded heat-denatured DNA exhibited only a strong meridional reflection at about 3.4 Å that corresponded with the distance of stacked bases of double-stranded DNA, indicating that not all structural features of the double-helix were lost during the heat denaturation (see Figure 6-18 left and also Supplementary Figure 7; Table 6-14). Also some rings with weak of off-meridional anisotropy suggested partial formation of double-strands from the denatured DNA, but the fuzziness of the reflections indicated that the majority of the material was single-stranded and not well aligned. It remained unclear what the conformation of DNA in peptide-DNA complexes might be, and potential conformational changes (e.g. A-DNA <-> B-DNA) induced by the peptides or denaturation might change the diffraction pattern drastically.

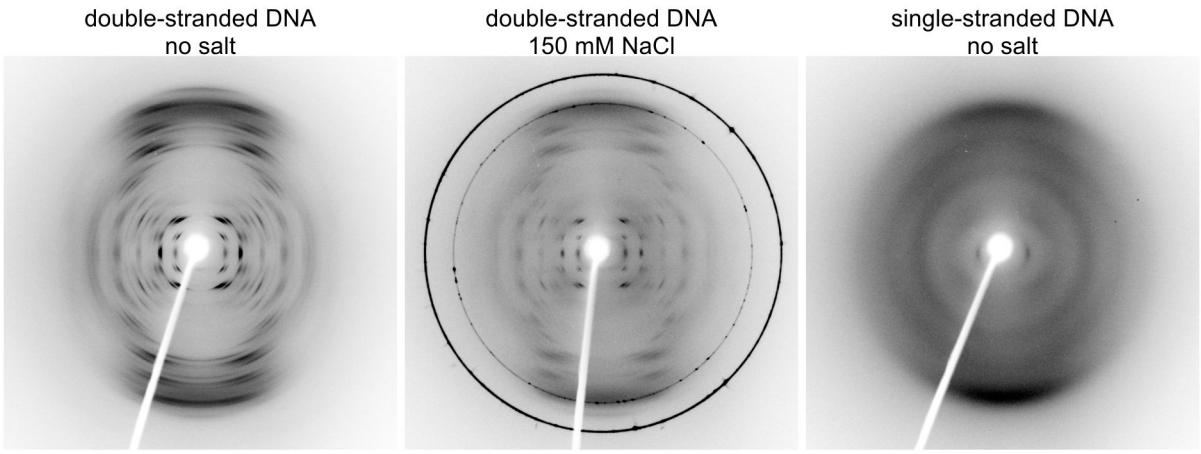

Figure 6-18: Fibre diffraction patterns of DNA. Double-stranded DNA with (10 mM ST DNA, middle) or without (20 mM ST DNA; left) 150 mM NaCl showed a clear A-DNA diffraction pattern [233], while heat-denatured single-stranded DNA (20 mM heat-denatured ST DNA, right) lost most of these features but retained a strong meridional reflection at 3.4 Å. All patterns were recorded at 180 mm sample-detector distance.

Table 6-14: Bragg spacings of DNA diffraction patterns

ST DNA			ST DNA 150 mM NaCl			heat-denatured ST-DNA		
			18.8	e	m			
17.8	e	m				17.8	e	(w)
			16.5	xe	m			
16.1	xe	m						
14.8	xe	w						
11.8	xm	vs	11.7	xm	m			
11.3	xm	vs	11.3	e	m			
11.3	e	vs						
10.7	xe	m	10.8	xe	w			
10.5	xm	s	10.7	xm	w			
9.50	xe	w						
						9.10	xm	(vw)
8.14	xe	w	8.21	xe	(vw)			
7.39	e	vw	7.42	e	(vw)			
7.38	xe	w						
6.68	xe	m	6.73	xe	w			

ST DNA			ST DNA 150 mM NaCl			heat-denatured ST-DNA		
5.96	xe	w						
5.47	e	(w)	5.51	e	(vw)	5.50	xm	(vw)
5.29	xe	(w)	5.32	xe	(vw)			
5.18	xe	(w)						
4.96	xm	w	4.94	xm	vw			
4.78	xm	m						
4.64	xm	w	4.62	xm	vw			
4.54	xm	w	4.57	xm	vw			
4.33	xm	m	4.35	xm	vw			
4.32	e	(vw)						
						4.27	xm	(vw)
4.15	e	(vw)						
4.14	xm	(s)	4.19	xm	vw			
			4.07	xm	vw			
3.94	xm	m						
3.79	xm	w	3.80	xm	vw			
3.63	xm	(s)	3.63	xm	vw			
3.53	xm	(s)						
						3.38	m	(m)
3.24	xm	(s)						
			3.25	salt	s			
3.01	m	w						
			2.81	salt	vs			

Table 6-14 legend: Bragg spacings in Å were determined using WCEN from the diffraction patterns shown in Figure 6-18. The diffraction pattern of ST DNA with 150 mM NaCl (Figure 6-18, centre) was mostly identical to the diffraction pattern of ST DNA alone (Figure 6-18, left); the main differences were the 2 salt rings and intensity differences (mainly weaker DNA reflections in the presence of NaCl). After heat denaturation only few and diffuse reflections could be detected (see also Figure 6-18, right). Abbreviations: e, equatorial; m, meridional, xe, off-equatorial; xm, off-meridional; salt, salt ring; vs, very strong; s, strong; m, medium; w, weak; vw, very weak; reflections in brackets are diffuse and their Bragg spacings could not be determined with much confidence.

In conclusion, nearly all peptide-nucleic acid complexes examined here with X-ray fibre diffraction displayed a cross-β pattern indicative of amyloid formation. In some cases there were suggestions of higher order aggregates like beta-helix formation. Interestingly, no signature of the involved nucleic acids could be detected.

6.1.8. Interactions of Fatty Acids with $(KL)_3$, $(HL)_3$, and $(EL)_3$

Mutual interactions between amyloidogenic polypeptides and membranes have been shown in some cases to lead to membrane disruption and amyloid fibrillisation [112], but were usually studied only for larger polypeptides with rather specific interactions with certain lipids like gangliosides [112,119,240] and/ or specific membrane-anchoring peptide sequences [112,120]. Here we concentrated on interactions between artificial fatty acid vesicles and our short amyloidogenic peptides to elucidate mutual interaction effects of polyanionic membrane surfaces and short amyloidogenic peptides which would also be of interest in the context of prebiotic evolution.

Fatty acid liposomes as model membranes were easy to prepare from homogeneous micelle solutions. Vesicles readily formed when fatty acid stock solutions were brought from pH 11 to pH 8.5 where the fatty acid micelles converted into liposomes [241]. A general issue during the work with fatty acids was their high surface activity, making pipetting difficult due to air bubble formation and reduced surface tension.

Turbidity assay

The formation of liposomes from fatty acid micelles at pH 8.5 was explored by measuring the turbidity as previously described [210]. This was based on the better light scattering of large liposomes (100 nm to several µm diameters), which formed from small fatty acid micelles (about 2 nm diameter) at this wavelength [210,242]. The liposome formation could be accelerated by the addition of the clay montmorillonite, which was said to enhance assembly of the fatty acids via its positively charged surface [210]. This was thought to be an important process in prebiotic development [210]. Here we used the theoretically positively charged $(KL)_3$, the theoretically net neutral

$(HL)_3$ and the theoretically negatively charged $(EL)_3$ to examine the possible effect of mutual interactions of peptides and fatty acids on the formation of amyloid fibres and fatty acid vesicles. The turbidity measurements were adapted for use in a BMG plate reader by using 96-well clear-bottom plates and a 450 nm absorbance filter. Spectra were taken of 1-hour-old fatty acid liposomes on a NanoDrop instrument in 200 mM bicine pH 8.5, which suggested that 450 nm was a suitable wavelength for the turbidity assay, although scattering was higher at 400 nm as used by Hanczyc *et al.* [210] (see Supplementary Figure 11).

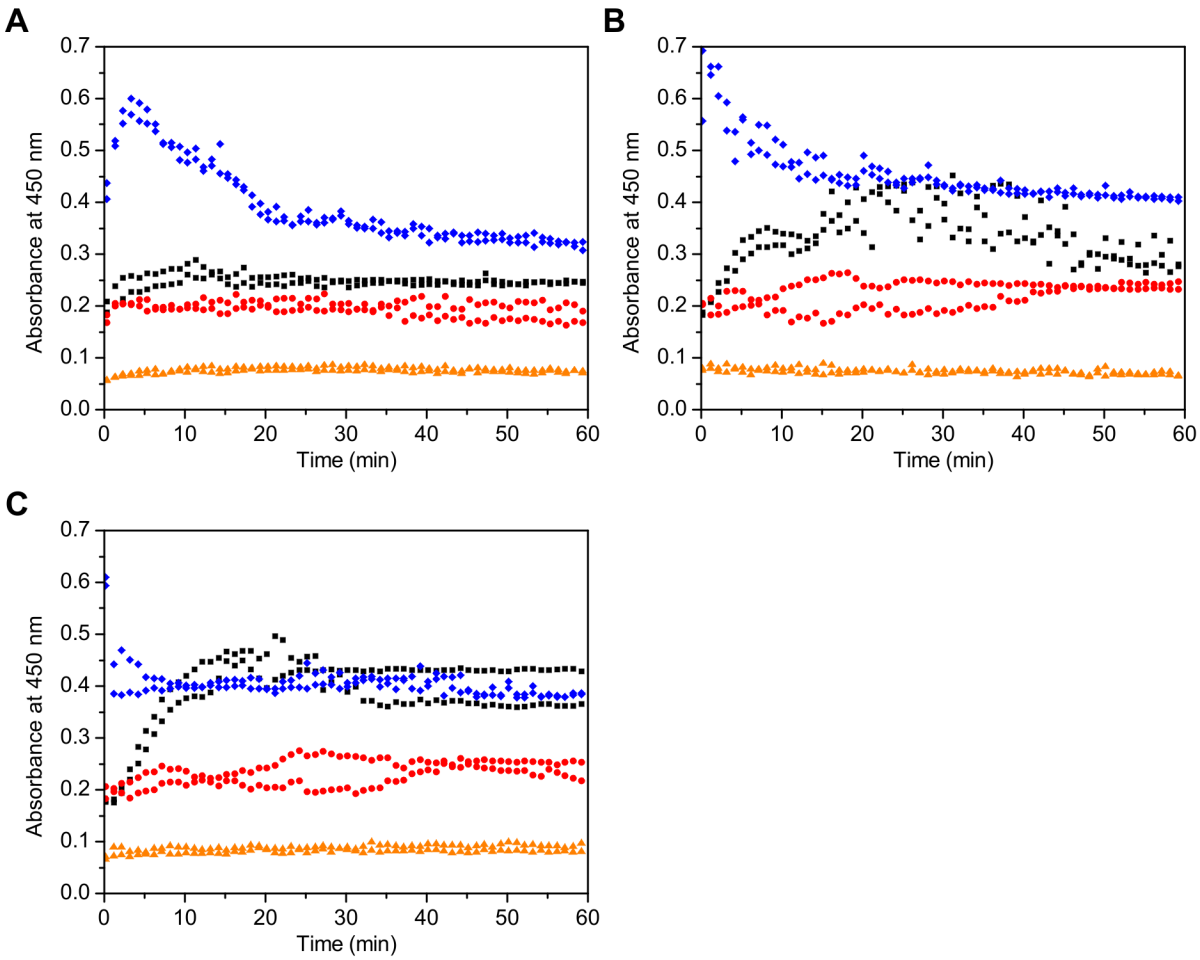

Figure 6-19: $(KL)_3$ enhanced vesicle formation. A time course of turbidity as assessed by measuring the absorbance at 450 nm was recorded over 60 minutes for fatty acid alone (black), $(KL)_3$ alone (**red**), fatty acid-(KL)3 mixtures (**blue**), and buffer background (**orange**). 1 mM $(KL)_3$ was added directly prior to measurement to 10 mM myristoleic (**A**), palmitoleic (**B**) or oleic (**C**) acid in 200 mM bicine pH 8.5 or buffer. A possible reason for the late increase in noise may have been the formation of oil droplets since these were observed in samples at the end of the experiments.

Initially, we explored the effect of our peptides on liposome formation by adding the peptide to a liposome formation reaction. The read-out was the absorbance caused by

increasing levels of turbidity (see Figure 6-19). Of the fatty acids alone (black curves in Figure 6-19), oleic acid showed a larger maximum turbidity level (about 0.4 a.u.) than palmitoleic acid (about 0.35 a.u.), which again was larger than myristoleic acid (about 0.25 a.u.). This suggested that either more liposomes were formed or the size distribution of the vesicles maximised the scattering effect. The kinetics were similar for all fatty acids on their own and potentially followed a sigmoidal or maybe hyperbolic curve (black curves in Figure 6-19). The effect of $(KL)_3$ was examined by mixing the peptide with the lipids at a 1:10 molar ratio of peptide to fatty acid prior to the start of the turbidity assay. The focus was on the formation of fatty acid liposomes, and we wanted to avoid potential strong effects that might occur if the net positive charges on the peptide exceeded the net charges of the fatty acids. Interestingly, the peptide alone (red curves in Figure 6-19) had an intermediate absorbance of about 0.20 AU, which was higher than the buffer background of about 0.07 AU (orange curves in Figure 6-19). It remained unclear what gave rise to this turbidity or absorbance because $(KL)_3$ was expected to be fully soluble under these conditions due to its high charge density (calculated +3 net charge). Myristoleic acid alone (black) showed only a low increase in turbidity over time, but in the presence of the peptide (blue) turbidity peaked after about 3 minutes before falling to about 0.4 a.u. after 20 minutes, when turbidity decreased more slowly down to about 0.3 a.u. by 60 minutes (see Figure 6-19 A). A similar result was obtained with palmitoleic acid-$(KL)_3$ (blue; see Figure 6-19 B), but the peak appeared right at the beginning of the measurement. There was considerable noise after the plateau turbidity was reached by palmitoleic acid alone (blue). A potential peak of oleic acid-$(KL)_3$ (blue; see Figure 6-19 C) occurred within the dead time of the experiment prior to the first measurement and rapidly decreased over time to a stable plateau so that only the first time point appeared above plateau level. The turbidity of

the $(KL)_3$-oleic acid mixture (blue) did not exceed the plateau level reached by the fatty acid alone (black). By the end of the measurement after 60 minutes the $(KL)_3$-fatty acid mixtures showed no difference to the fatty acid control (oleic acid, Figure 6-19 C) or were slightly above and approaching control level (myristoleic and palmitoleic acid, Figure 6-19 A and B). The palmitoleic acid alone and oleic acid alone showed a few small oil droplets by the end of measurements. This was also seen in all $(KL)_3$-fatty acid samples, which exceeded the size and number of oil droplets in the fatty acid alone samples. The initial peak in signal at the onset of the time course was not seen before [210] and could not simply be the result of the addition of the peptide and fatty acid signals. This might indicate the formation of larger, maybe non-vesicular complexes that either fell apart again or quickly rose to sizes that no longer scattered efficiently at 450 nm anymore.

Light microscopy

From the turbidity assay it became clear that mixing $(KL)_3$ with fatty acids had a marked effect on the formation of scattering/ absorbing aggregates. To visualise these structures, light microscopy was used to observe macroscopic structures. The formation of potential liposome-peptide complexes at pH 8.5 from these vesicles and either $(KL)_3$, $(HL)_3$ and $(EL)_3$ was examined by light microscopy (see Figure 6-20 and Figure 6-21). The 200 mM bicine pH 8.5 buffer has been used before to examine the formation of liposomes from fatty acids without and with additional binding partners like clay or RNA by Hanczyc *et al.* [210,243]. The peptides were carrying a theoretical net charge of +3 for $(KL)_3$, +/- 0 for $(HL)_3$, and -3 for $(EL)_3$ as calculated (see chapters 5.1.2 and 6.1.2). The fatty acids on their own formed liposomes of varying sizes, apparently increasing in size and density from myristoleic acid over palmitoleic acid to oleic acid (Figure 6-20 and

Figure 6-21, first column). $(EL)_3$ had no detectable effect on the liposomes (Figure 6-20 and Figure 6-21, second column). $(HL)_3$ mainly gave rise to some large aggregates of possibly fibrous origin, but there were still some liposomes visible (see Figure 6-20 and Figure 6-21, third column). The nature of the aggregates was unknown, but since the peptide on its own showed no aggregates (data not shown) and the fatty acids alone were found to form only circular liposomes, an interaction seemed to be likely. The picture was more differentiated for the $(KL)_3$. At lower concentrations (see Figure 6-20, right column) fibrous aggregates could be made out while the number of liposomes was reduced for myristoleic and palmitoleic acid. The aggregates looked similar to aggregates formed during insulin amyloid formation detected by Manno *et al.* using phase contrast light microscopy [89,244]. Oleic acid predominantly showed large aggregates and reduced numbers of liposomes, but the aggregates seemed to consist of fibrous material. This behaviour changed at higher concentrations (1:1 concentration ratio to liposomes) where only large amorphous aggregates were formed (see Figure 6-21, right column). The peptides on their own showed no visible complexes or aggregates (data not shown).

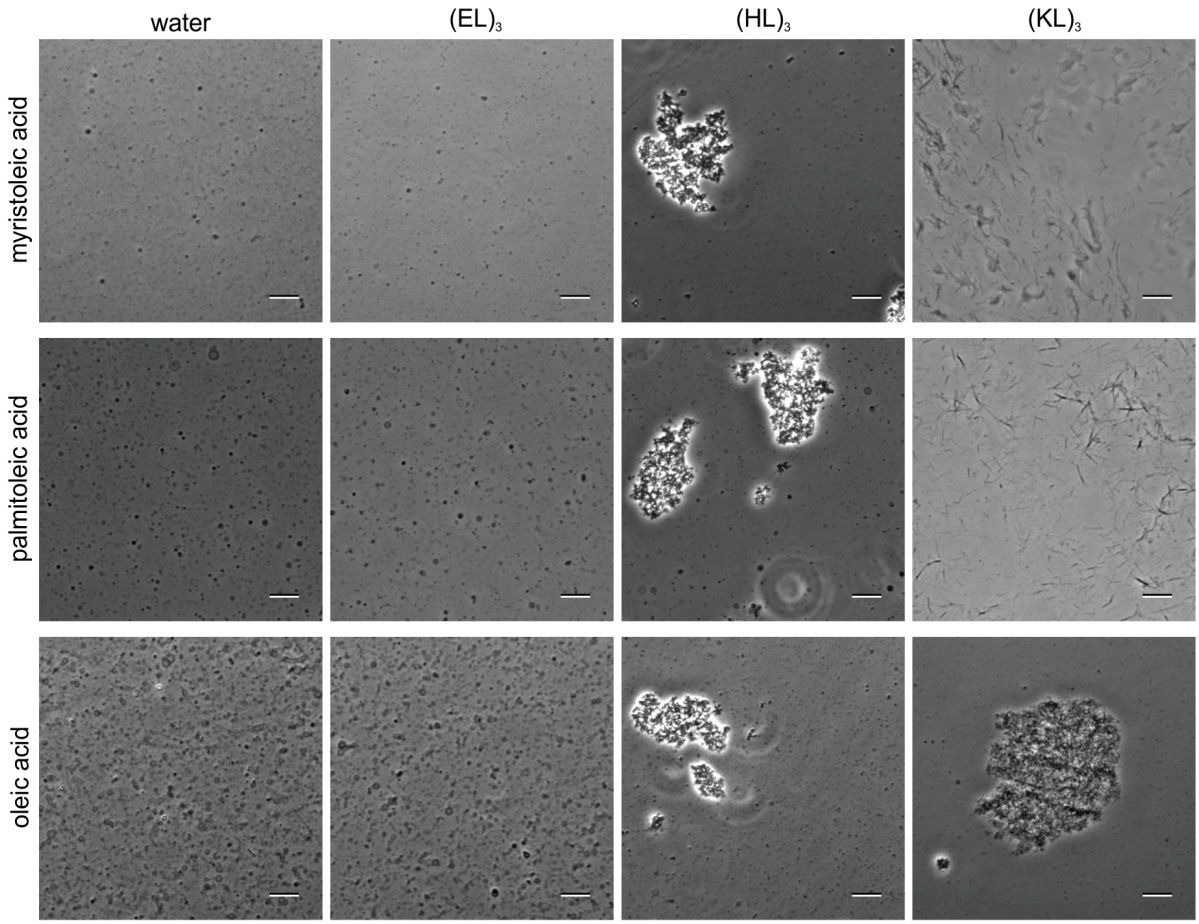

Figure 6-20: Light microscopy on fatty acid liposomes (from 3.33 mM fatty acid) in complex with 1 mM peptide. Peptide or the same volume of water was spiked (1:20) into pre-formed, 1 hour old fatty acid liposomes, incubated for 1 hour at room temperature and then imaged. $(EL)_3$ had no effect on the liposomes compared to the water control, but in the presence of $(HL)_3$ amorphous aggregates appeared. $(KL)_3$ gave rise to fibres, or fibrous aggregates that in general were larger than the $(HL)_3$ aggregates; the number of liposomes seemed to be reduced. Scale bars are 10 µm.

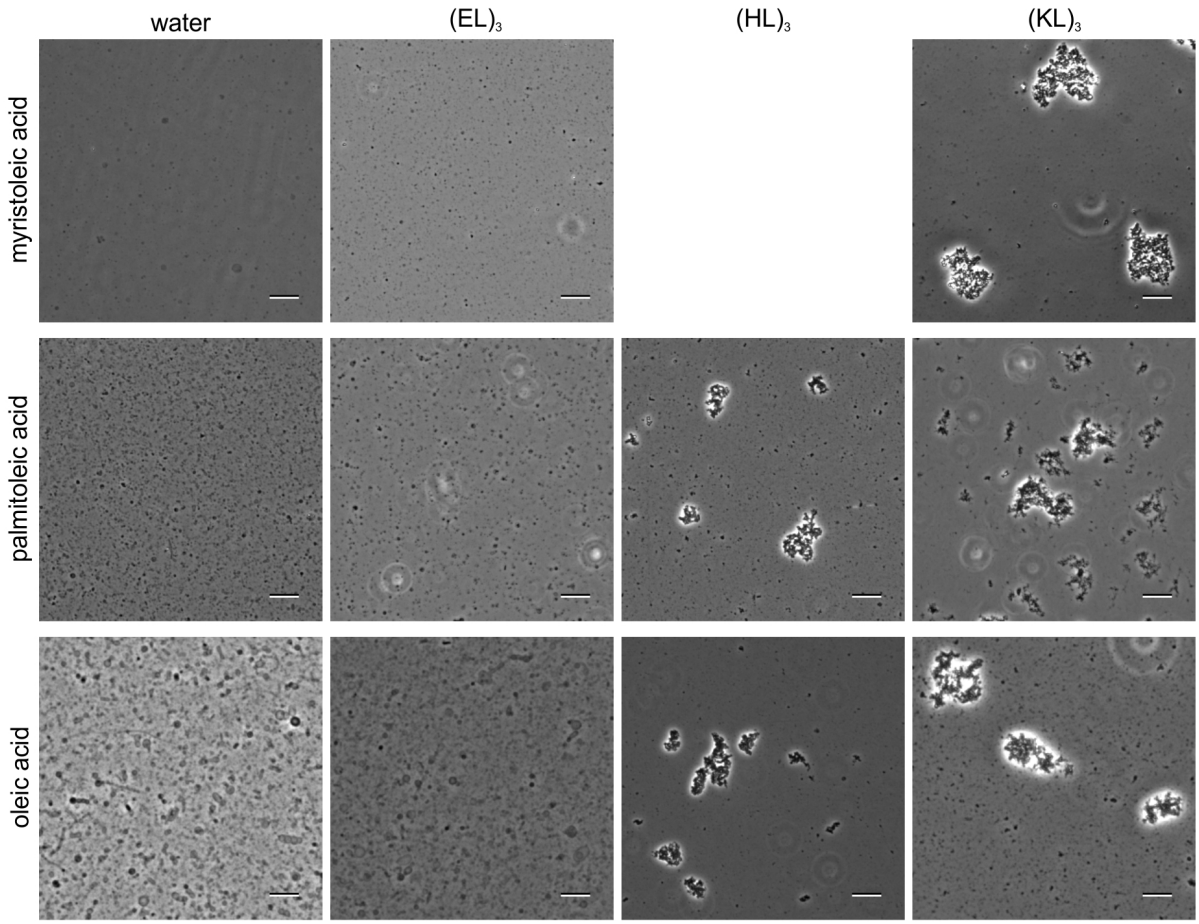

Figure 6-21: Light microscopy on fatty acid liposomes (3.33 mM fatty acid) in complex with 3.33 mM peptide. Peptide or the same volume of water was spiked (1:6) into pre-formed, 1 hour old fatty acid liposomes, incubated for 1 hour at room temperature and then imaged. $(EL)_3$ had no visible effect on the liposomes compared to the water control, but in the presence of $(HL)_3$ amorphous aggregates appeared. $(KL)_3$ gave rise to aggregates that were in general larger than the $(HL)_3$ aggregates. Scale bars were 10 µm.

Dye-binding assays

The next step was to find out if the liposomes and peptides did more than just aggregate and to find out whether they interacted to from amyloid structures. The fibrous material

seen in the $(KL)_3$-liposome samples encouraged us to examine the samples using Thioflavin T fluorescence and Congo Red absorbance as this might indicate the formation of amyloid (see Figure 6-22 and Figure 6-23).

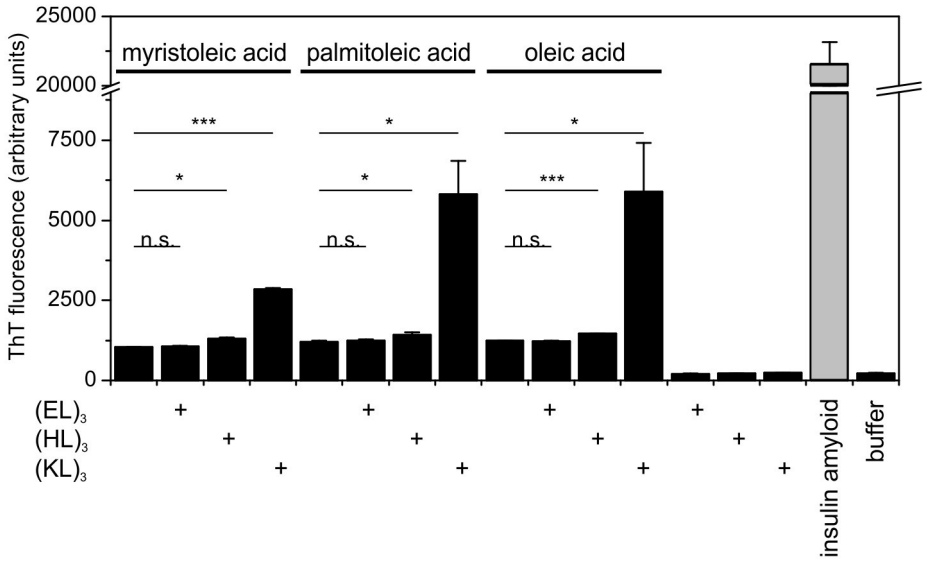

Figure 6-22: ThT assay on peptide-fatty acid complexes. 3.33 mM peptides were incubated with 10 mM pre-formed fatty acid vesicles or buffer (200 mM bicine pH 8.5) in the presence of 50 µM ThT as indicated. $(KL)_3$ greatly increased ThT fluorescence in the presence of fatty acids. $(HL)_3$ only slightly increased ThT fluorescence, while $(EL)_3$ had no apparent effect. All samples were run in triplicate (mean + s.d.). 50 µM Insulin amyloid positive control in grey, buffer background fluorescence shown on the right. ThT fluorescence in arbitrary units. A scattering control without dye showed no increase in signal. A Student's unpaired 2-sample *t*-test with n = 3 was carried out using R to compare the means as indicated (* = $p < 0.05$; ** = $p < 0.01$; *** = $p < 0.001$) [215] (see Appendix 9.2 for a full list of the statistical parameters). The peptides alone showed no significant increase above the buffer background.

$(KL)_3$-fatty acid complexes showed a significant interaction with Thioflavin T. This suggested that fatty acid liposomes might promote amyloid aggregate formation by this peptide (see Figure 6-22). The ThT fluorescence was highest for oleic and palmitoleic acid and about half as high for myristoleic acid. The signal obtained from fatty acid-$(KL)_3$ mixtures was considerably higher than from $(KL)_3$-ST DNA mixtures (compare to Figure 6-3). Interestingly, there also was a significantly increased ThT fluorescence showed by $(HL)_3$-fatty acid complexes, suggesting that this peptide might form amyloid under these conditions. There was no significant increase of $(EL)_3$, and none of the peptides alone significantly exceeded the buffer background. The fatty acids caused some amyloid-independent ThT fluorescence, probably because they provided a hydrophobic phase for the dye that enhanced excitation of its fluorescence. A control assay run under the same conditions in the absence of the dye showed no scattering contribution to the fluorescence signal. Also, no significant differences between peptide-fatty acid mixtures and fatty acid alone due to scattering could be detected when the scattering at the excitation (440 nm) or emission (480 nm) wavelengths was examined separately.

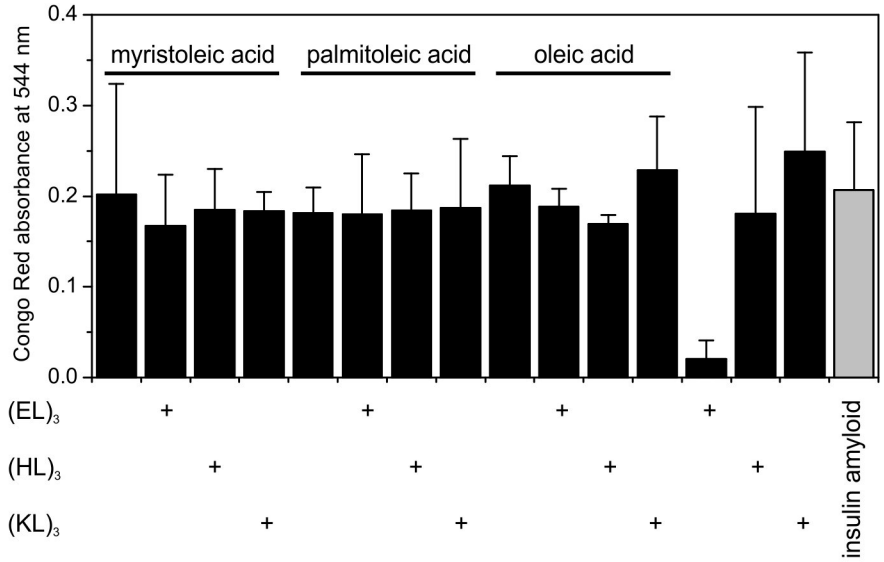

Figure 6-23: Congo Red assay on peptide-fatty acid complexes. 3.33 mM $(EL)_3$, $(HL)_3$ or $(KL)_3$ were incubated with 10 mM pre-formed fatty acid (1 hour old) vesicles in 200 mM bicine pH 8.5 in the presence 50 µM Congo Red as indicated. All samples with exception of $(EL)_3$ alone reached the level of the insulin amyloid positive control (50 µM; grey), although there was considerable noise. All samples were run in duplicate (mean + s.d.).

Generally, Congo Red seemed not to be suitable to investigate amyloid formation in the presence of fatty acids because all fatty acids showed high Congo Red binding preventing any analysis of fatty acid-induced amyloid formation, maybe because of high background absorbance of the turbid fatty acid solutions (compare to turbidity assay in Figure 6-19). Although the Congo Red assay was set up to assess lipid complex formation, the peptide-only controls that were performed at pH 8.5 added to the body of data on the behaviour of peptides alone. $(HL)_3$ and $(KL)_3$ alone showed increased Congo Red binding at pH 8.5 (see Figure 6-23), which might suggest that both peptides could form amyloid aggregates under these conditions (200 mM bicine pH 8.5, resulting in a theoretical 0 to -0.5 net charge for $(HL)_3$, and +3 net charge for $(KL)_3$; see Table 6-1).

However, the increase was probably not significant (the samples were run only in duplicate preventing statistical analysis), and $(HL)_3$ showed no ThT binding under the same conditions (see Figure 6-22).

X-ray Fibre Diffraction

Although the Congo Red assay gave only a weak suggestion of amyloid formation by $(KL)_3$ with pre-formed fatty acid liposomes, we were encouraged by the result to examine such complexes by X-ray fibre diffraction. Stalk preparation with these complexes was complicated by the reduced surface tension due to the fatty acids, but eventually yielded milky-white stalks for all samples. The resulting patterns displayed many salt rings and spots, maybe due to the high concentration of buffer ions (200 mM bicine) and the fatty acids compared to the peptides (see Figure 6-24 and Table 6-15). These might obscure a potential underlying peptide pattern. Some rings showed some anisotropy agreeing with a cross-β pattern, which might suggest the presence of amyloid fibres (bold print in Table 6-15). There were anisotropic rings that could not be assigned to either meridional or equatorial direction, and that seemed to show only a single maximum in contrast to the two opposing maxima mainly along or perpendicular to the amyloid fibre axis of the amyloid-related reflections. There was no recognisable trend whether the different fatty acids influenced the weak cross-β pattern of potential $(KL)_3$-fatty acid amyloid fibrils; the 3 recorded patterns showed different potential main equatorial reflections (8.43 Å with myristoleic acid, 7.88 Å with palmitoleic acid, and 8.95 Å with oleic acid). Interestingly, the equatorial reflections of the potential $(KL)_3$ cross-β pattern seemed to be smaller than in the $(KL)_3$-ST DNA pattern at pH 7 (see Figure 6-15 and Table 6-12). Further analysis under altered conditions would be necessary to prove amyloid formation, possibly recording patterns before the stalks are

fully dried and the salt not yet crystallised, or trying to wash off the salt crystals on the stalk surface.

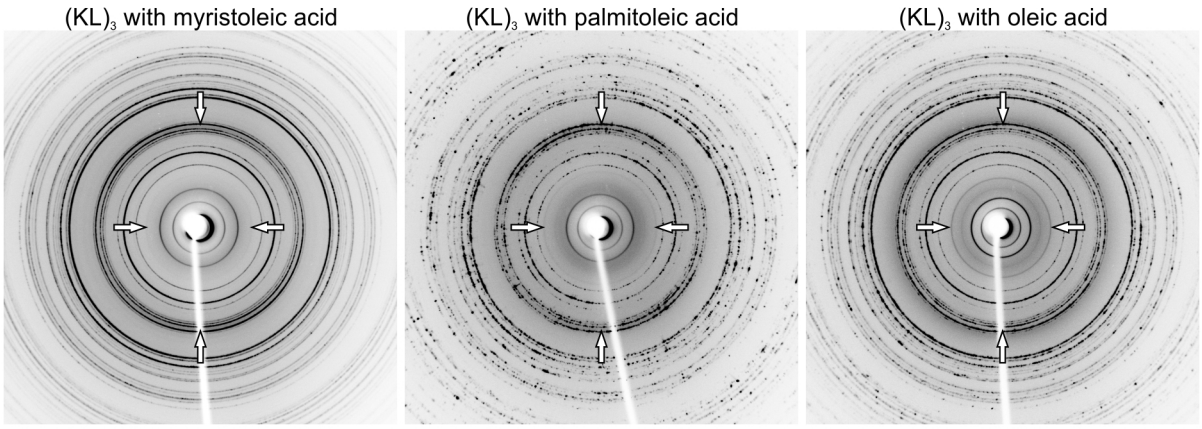

Figure 6-24: Fibre diffraction on $(KL)_3$-fatty acid fibres. Samples were created from $(KL)_3$ in 200 mM bicine pH 8.5 with fatty acid vesicles as indicated. The patterns show anisotropy on some reflections that might be associated with amyloid formation, but were overlaid by strong diffraction of fatty acids and buffer salt. The reflections most were likely to be due to an very weak underlying cross-β pattern of the $(KL)_3$ peptide marked by arrows (labelled bold in Table 6-15).

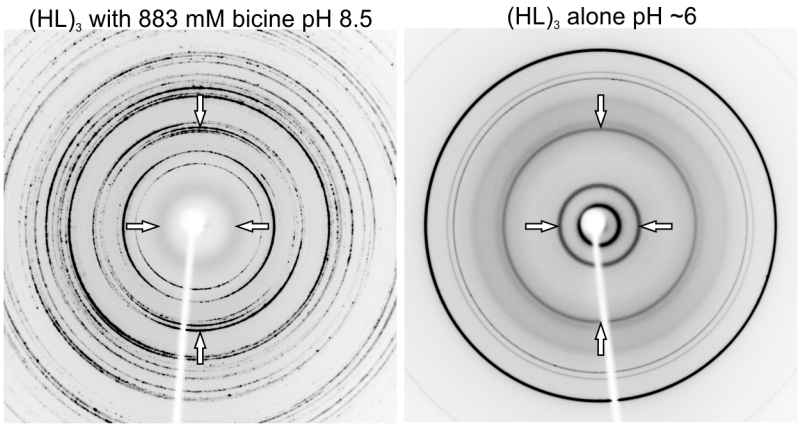

Figure 6-25: Fibre diffraction on non-crystalline $(HL)_3$ aggregates. Samples were composed of 3.33 mM $(HL)_3$ in 200 mM bicine pH 8.5 (**left**) and 20 mM $(HL)_3$ at about pH 6 (**right**). The patterns showed anisotropy on some reflections that were compatible with a cross-β pattern (indicated by arrows; about 4.7 Å meridional and 11 Å equatorial). The left pattern showed mainly salt rings and spots that were probably due to buffer salt crystallisation, sometimes with anisotropy not in the equatorial or meridional direction (i.e. bottom left of the recorded pattern). The right pattern displayed only very weak anisotropy.

An interesting side-effect of the treatment of $(HL)_3$ with 200 mM bicine pH 8.5 was an increased Congo Red binding which might suggest the formation of amyloid aggregates by this peptide on its own, although the high turbidity of the solution might have been responsible for this response (see Figure 6-23). $(HL)_3$ alone in 883 mM bicine pH 8.5 (concentration created by accident) did not create a gel, but gave rise to aggregates as indicated by visible turbidity (see Table 6-2). This material was used to make up stalks for X-ray fibre diffraction and compared to a stalk prepared from a gloopy $(HL)_3$ stock solution in water before dialysis (very weak gel; see Table 6-2). Both gave rise to stalks with opaque appearance suggesting either the presence of salt crystals on the surface or of primarily unordered aggregates.

Table 6-15: Reflections of $(HL)_3$- and $(KL)_3$-fatty acid complexes and $(HL)_3$ alone

$(HL)_3$ no fatty acid 883 mM bicine pH 8.5			**$(HL)_3$ no fatty acid unbuffered pH ~6**			**$(KL)_3$ myristoleic acid 200 mM bicine pH8 8.5**			**$(KL)_3$ palmitoleic acid 200 mM bicine pH 8.5**			**$(KL)_3$ oleic acid 200 mM bicine pH 8.5**		
						17.02	e	m	19.82	e	m	22.45	e	s
									13.11	e	s	14.94	e	vs
11.27	**e**	**(vw)**	**11.05**	**(e)**	**vs**	11.31	e	s				11.15	ring	w
						8.43	**e**	**vw**	**7.88**	**e**	**w**	**8.95**	**e**	**w**
7.05	m	m				7.08	ring	m	7.07	ring	m	7.07	ring	m
5.96	e	vs				5.96	ring	vs	5.93	ring	s	5.95	ring	vs
5.51	ring	w				5.51	ring	m	5.50	ring	m	5.50	ring	m
4.79	**m**	**w**				**4.83**	**m**	**w**	**4.77**	**m**	**s**	**4.83**	**m**	**w**
4.70	**m**	**s**	**4.73**	**(m)**	**m**	**4.73**	**m**	**s**	**4.67**	**m**	**s**	**4.72**	**m**	**s**
4.57	m	vs				4.62	m	vs				4.60	m	s
4.52	m	vs	4.47	ring	(w)	4.43	m	vs	4.51	m	vs	4.41	m	vs
4.33	e	s				4.34	ring	w	4.37	m	vs	4.33	ring	m
			3.72	ring	(vw)									
3.61	ring	vs				3.60	m	vs	3.61	ring	s	3.60	ring	vs
3.54	m	s				3.53	m	m	3.54	ring	m	3.53	ring	m
3.41	ring	s				3.41	m	vs	3.41	ring	vw	3.40	ring	s
3.34	ring	m				3.30	m	w	3.34	ring	vw	3.33	ring	vw
3.25	ring	w	3.25	ring	m	3.24	m	w	3.26	ring	vw	3.28	ring	vw
3.10	ring	vs	3.14	ring	weak	3.22	m	w	3.15	ring	w	3.21	ring	m
						3.15	m	w				3.15	ring	m
2.96	ring	w				3.01	ring	w	2.96	ring	vw	3.05	ring	m
2.90	ring	vw				2.92	m	vw	2.92	ring	w	2.92	ring	w
2.86	ring	vw				2.87	m	m	2.87	ring	vw			
2.83	ring	w	2.82	ring	vs	2.84	m	w				2.82	ring	w
2.76	ring	vw				2.77	ring	vw	2.75	ring	vw			
2.56	ring	w				2.60	ring	vw	2.54	ring	w	2.66	ring	vw
2.50	ring	vw				2.48	ring	vw	2.50	ring	vw	2.52	ring	w
2.44	ring	vw							2.46	ring	vw	2.48	ring	w
						2.43	ring	vw	2.41	ring	vw	2.43	ring	vw
2.35	ring	vw				2.36	ring	vw	2.36	ring	vw	2.37	ring	vw
									2.31	ring	vw	2.33	ring	vw

Table 6-15 legend: Bragg spacings were determined using WCEN from the diffraction patterns shown in Figure 6-24 and Figure 6-25. Abbreviations: e, equatorial; m, meridional; vs, very strong; s, strong; m, medium; w, weak; vw, very weak; reflections in brackets are diffuse and their Bragg spacings cannot be determined with much confidence or anisotropy is not very strong and difficult to spot. Bold reflections most likely represent an underlying

cross-beta pattern of amyloid fibril-forming peptide-fatty acid complexes. Interestingly, the equatorial reflections are smaller than the ones shown by $(HL)_3$ or $(KL)_3$-DNA complexes, suggesting a different mode of lateral association (see Table 6-5 and Table 6-6).

The liposome buffer sample primarily exhibited salt rings and spots. But the weak anisotropy on some of the rings suggested the presence of an underlying cross-β pattern, which might indicate that $(HL)_3$ formed amyloid. The strongest equatorial reflection was at 5.9 Å, which was not seen with the other $(HL)_3$-DNA complexes (see Figure 6-14 and Table 6-11). A more likely candidate for the reflection representing the spacing between the β-sheets of would be a fuzzy ring at about 11 Å, which agreed better with the previous fibre diffraction experiments (see Figure 6-14 and Table 6-11) and would indicate either rather poor lateral association of maybe quite short fibrils or a low degree of order within the stalk. A similar effect was seen with a sample of $(HL)_3$ alone at about pH 6 (unbuffered), but the even weaker anisotropy suggested that primarily amorphous aggregates were present (see Figure 6-25). All in all, $(HL)_3$ in liposome formation buffer might have formed amyloid fibrils, but further analysis would be necessary to confirm this finding. The fibre diffraction pattern as a whole was not conclusive because of the overlaying salt rings.

Summary

Taken together, light microscopy revealed aggregation of $(HL)_3$ and $(KL)_3$ in the presence of fatty acid, which in the latter case took on an appearance similar to insulin amyloid aggregates (see Figure 6-20 and Figure 6-21; ref [89,244]). The results from a Congo Red assay were inconclusive because of a high background probably due to

turbidity (see Figure 6-22), but the Thioflavin T assay showed increased binding to $(KL)_3$-fatty acid complexes; Figure 6-22). While the fibre diffraction patterns were not very convincing they provided a hint at amyloid formation in $(KL)_3$-fatty acid complexes (Figure 6-24). This would support the suggestion that $(KL)_3$ formed amyloid fibres in the presence of fatty acids. Additionally, Congo Red binding (see Figure 6-23) and a weak hint in fibre diffraction (see Figure 6-25 and Table 6-15) might suggest that $(HL)_3$ could form amyloid aggregates at pH 8.5 in a high-ionic strength (>200 mM) bicine buffer.

The effect of the peptides $(HL)_3$ and $(KL)_3$ on fatty acid liposome formation seemed to be disruptive, as the aggregates seen by light microscopy (see Figure 6-20 and Figure 6-21) and the oil droplet formation during the turbidity assay (see Figure 6-19) indicated. This would suggest that they did not act like the clay montmorillonite [210], but they might act similarly to other basic and amyloidogenic or cell-penetrating peptides that interfere with membrane function [112,245].

6.1.9. NUCLEIC ACIDS PROMOTED STVIIE CONFORMATIONAL CHANGES

So far I mainly used long DNA or RNA molecules and concentrations compatible with a charge-neutralisation of the calculated positive net charges on the peptides by the negatively-charged phosphate backbone close to a 1:1 charge ratio. This was thought to create conditions favourable for amyloid aggregation by peptides that were not expected to undergo this process so due to their high charge. I was interested to see if nucleic acids could also have a catalytic role and could enhance amyloid formation kinetics. To study a 'catalytic effect', the experiments needed to be conducted with limited amount of DNA that could then be assessed for the ability to initiate amyloid aggregation without necessarily being present as a structural component of the final aggregate. The relatively fast amyloid formation, assuming it followed gel formation within a few seconds (see Table 6-2, Table 6-3, Table 6-5, Table 6-6, Table 6-7, and Table 6-8) or the dye-binding assays within a few minutes (see ThT assays in Figure 6-5), made it difficult to examine the kinetics of this process in ANA complexes. Additionally, I wanted to avoid probes like the dyes Thioflavin T or Congo Red that might interfere with the samples during amyloid formation. Therefore a decision was taken to follow amyloid formation in the presence of trace amounts of DNA by circular dichroism (CD) spectroscopy based on the well-characterised changes in CD spectra of peptides due to conformational changes that have previously been shown to accompany amyloid formation [139,142].

Our first choice was TVQFHMH, the peptide that formed amyloid on its own (cross-β pattern shown in Figure 6-17; gel formation in Table 6-7). It would have allowed the examination of amyloid formation in the time frame of up to an hour based on gel formation observation (Table 6-7), but its CD spectra did not agree with the established

standard spectra [139,246-248] and were not reproducible even within the same experiment when taken from the same sample (see Supplementary Figure 12). Some of the observed problems may have been due to the high peptide concentrations (1 mM) that were necessary to cause detectable gelation of TVQFHMH on its own (1 mM and more; see Table 6-7), and the HT values of the CD spectrophotometer exceeded 800 V, indicating that the generated spectra were out of range of the photomultiplier. This phenomenon could have additionally been influenced by lack of tumbling of the molecules in the cuvette due to fibre and gel formation, thereby violating a requirement for circular dichroism spectroscopy (personal communication with Matthias Bochtler, and ref. [249]).

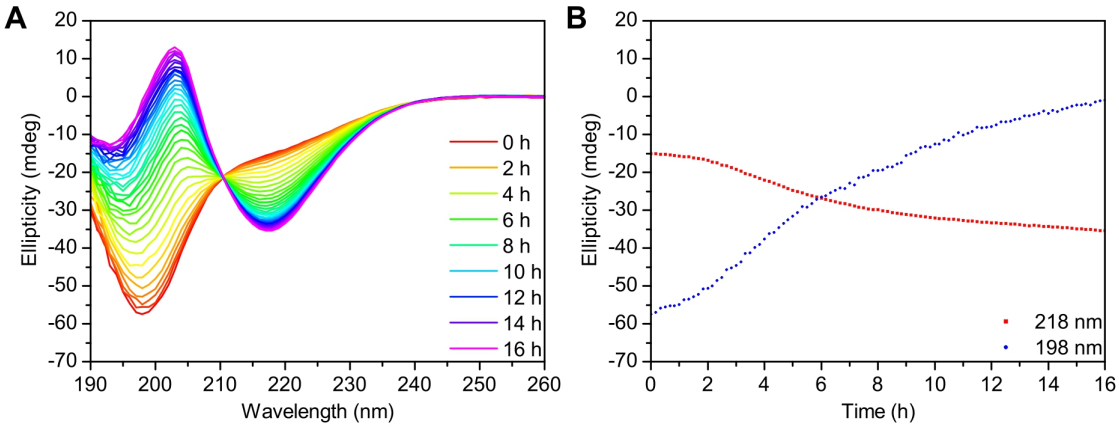

Figure 6-26: Time course of STVIIE forming amyloid on its own. The conformational change of 0.8 mM STVIIE in 20 mM glycine pH 2.6 was followed by CD as previously described [142]. (**A**) CD spectra showing the transition from random coil (minimum at 198 nm) to β-sheet (minimum at 218 nm). (**B**) Time courses of the ellipticity at 198 nm (blue; random coil) and 218 nm (red; β-sheet).

The literature was then surveyed to identify basic peptides that had been characterised by CD and that might therefore interact with DNA. We were unable to find a peptide which had the necessary properties close to neutral pH and decided to focus on the peptide STVIIE from Lopez de la Paz *et al.* [142] which was shown to display clear CD time course spectra at pH 2.6. This offered the opportunity to analyse interactions with single-stranded oligonucleotide DNA which would be stable at this pH. We then focussed our attention on STVIIE that could form amyloid fibrils on its own within 24 hours (see Figure 6-26; [142]). While this peptide was negative in ThT assays, probably because it is too small to properly interact with the dye (personal communication with Louise Serpell), it had a clear CD spectrum that was used before to follow the conformational transition from random coil (minimum at 198 nm) to β-sheet (minimum at 218 nm), which in combination with evidence of fibre formation seen by electron microscopy was described as indicative for amyloid formation [142]. I were able to reproduce the published results by recording a time course over 16 hours, showing a gradual transition from the initial random coil spectrum to β-sheet (Figure 6-26). The main changes were visible at the disappearing minimum at 198 nm (random coil peak) and the appearing minimum at 218 nm (β-sheet peak). These peaks were used to monitor the progress of the conversion to amyloid conformation. Additionally, a peak at 204 nm belonging to the β-sheet signature developed. During the time course some particles appeared in the cuvette, showing that amyloid aggregates formed by STVIIE were not stable in solution. An isosbestic point at about 210.5 nm (between the recorded 210 and 211 nm steps) indicated a direct transition between two distinct conformations.

Throughout subsequent CD studies the control (peptide-only) spectra varied both for the time of onset of measurable changes and for the profile of the curve at the final time

point. (For example, compare Figure 6-26, Figure 6-28, Figure 6-29, and Supplementary Figure 6). Because the kinetics of aggregate formation and the conformation of the amyloid aggregates may have been dependent on the starting state, great care was taken to analyse samples in parallel since control samples analysed simultaneously showed very similar spectral changes and time of onset (data not shown). The samples were prepared using the same peptide stock solution, buffer stock solution and freshly cleaned cuvettes, and were examined simultaneously. Care was taken to minimise differences in sample mixing during analysis by careful handling of the cuvettes during the experiments.

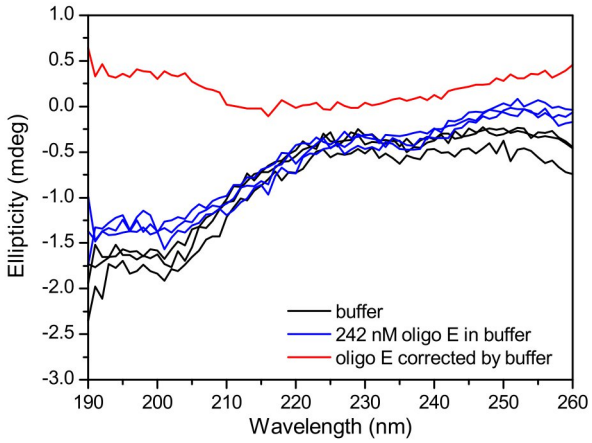

Figure 6-27: Oligo E control CD spectrum. CD spectra of 20 mM glycine pH 6 with (**blue**) and without (**black**) 242 nM oligo E (8 µM with respect to charge) were recorded in three repeats from 190 to 260 nm. After averaging and subtraction of the buffer spectra mean from the oligo E spectra mean a virtually featureless spectrum (**red**) remained.

Matched side-by-side comparison of samples with and without oligo E revealed a conformational switch from random coil (minimum at 198 nm) to β structure (minimum at 218 nm), but the final spectra were influenced by the presence of DNA (see Figure 6-28 and Figure 6-30). There were also changes in the time course (see next paragraph). The oligonucleotide did not have a big contribution to the CD spectra because of its low concentration (242 nM), which resulted in a relatively featureless spectrum (see Figure 6-27). The absence of a DNA spectrum allowed the examination of peptide conformational changes without interference. The spectra of STVIIE alone shown in Figure 6-28 B and Figure 6-29 B indicated that not all random coil conformation was lost in contrast to Figure 6-26 A as indicated by the trough of signal at 198 nm. However, similar spectra were regularly encountered as the endpoint of the conformational change both with and without oligo E (see Supplementary Figure 6). In one case (see Figure 6-28 B) the presence of an isosbestic point at 214 nm suggested a direct transition between two distinct conformations. The presence of 242 nM oligo E seemed to influence the conformation adopted after 24 h as shown in Figure 6-28 A and Figure 6-30 A. The trough in signal at 218 nm became wider and deeper in comparison to the matched STVIIE only sample. A shoulder at 198 nm suggested that not all random coil conformation was lost. The absence of isosbestic points suggested that the conformational transition did not occur directly between two distinct conformations, but might have involved alternative trajectories.

The onset of conformational change of STVIIE as shown by the loss of the random coil signal at 198 nm was greatly enhanced by the presence of 1:100 charge ratio oligo E (1:3300 molar ratio, i.e. 242 nM) (see Figure 6-28 and Figure 6-29). There was variation in the time of onset of the conformational change between different preparation of

samples of STVIIE without oligo E (compare Figure 6-26, Figure 6-28 B/D and Figure 6-29 B/D) and STVIIE with oligo E (compare Figure 6-28 A/C, Figure 6-29 A/C, and Supplementary Figure 6). The peak at 204 nm did not develop after the experiment shown in Figure 6-26 which matched the published spectrum [142]. Additional batches of STVIIE were prepared to try to 'regain' the first observed spectrum, but a range of spectra were obtained in which the most consistent feature was the loss of the random coil signal at 198 nm. The conformational switch was accompanied by the appearance of white deposits on the walls of the glass cuvettes both with and without oligo E. These aggregates initially had a web-like appearance, grew in size and visibility with larger clumps emerging before disappearing again. The aggregates appeared to be immobile during cuvette switches in the course of the experiments. The cleaning of the cuvettes afterwards revealed that they were held in place due to gel formation.

The ellipticity increase at 198 nm was more robust and stronger than the decrease at 218 nm, indicating that the major process is the loss of random coil conformation and not the adoption of beta-sheet conformation by the peptide. Logistic curves were fitted to the time courses to determine the transition midpoints. The loss of the random coil conformation occurred earlier with DNA (4.1 ± 0.2 and 3.3 ± 0.1 hours vs. 7.3 ± 0.1, 13.2 ± 0.3 and 10.0 ± 0.1 hours), while the temporal differences in β-sheet formation were less pronounced (9.3 ± 0.2 and 7.5 ± 0.1 hours vs. 5.7 ± 0.0 and 8.8 ± 1.7 hours). In the absence of DNA the formation of β-sheet started before a loss of random coil could be detected, while in the presence of DNA this was reversed. This suggested a different conformational route for the transition to β-sheet in each case.

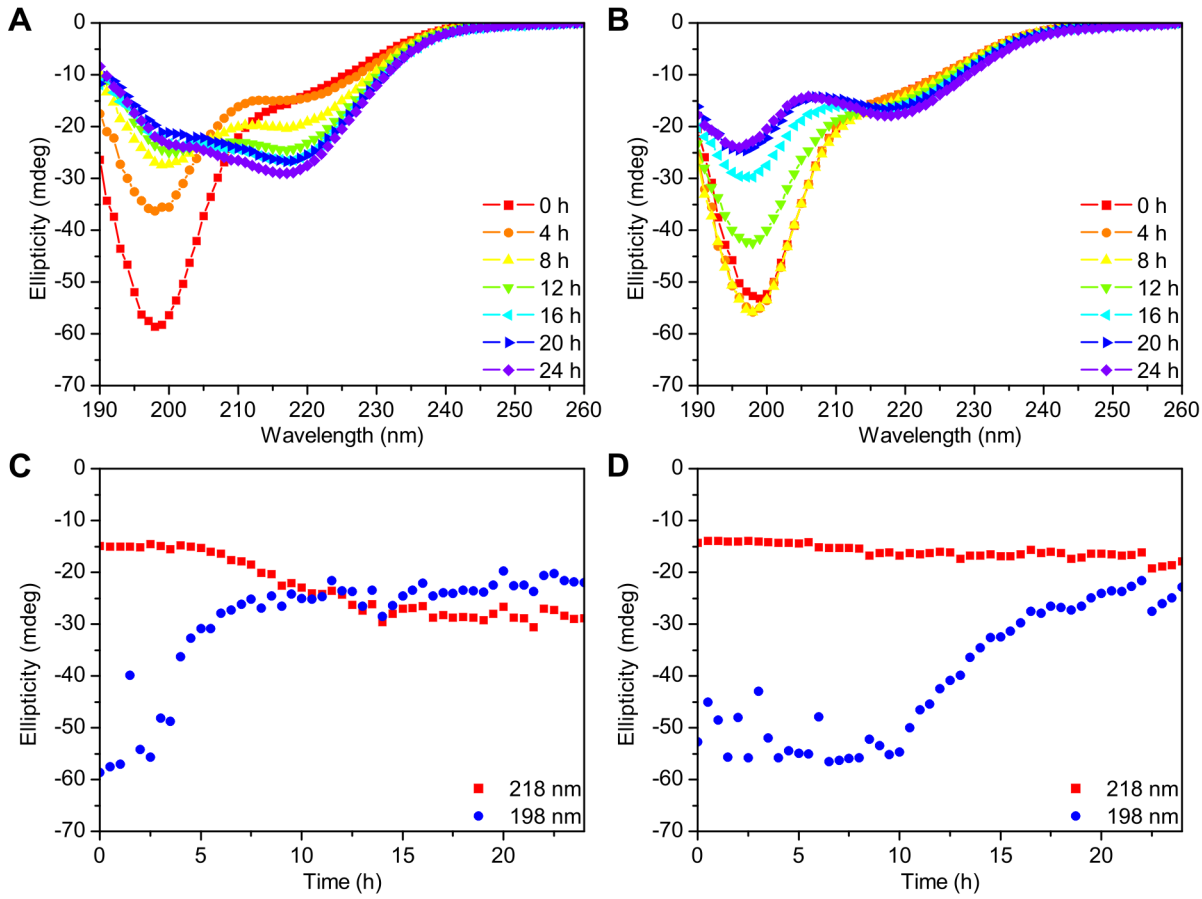

Figure 6-28: DNA oligonucleotides promoted loss of random coil conformation, repeat 1. A time course of the conformational change of 0.8 mM STVIIE in 20 mM glycine pH 2.6 without (**B**, **D**) or with (**A**, **C**) 242 nM oligo E (33mer; 1:100 charge ratio) was followed over 24 h by CD spectroscopy. (**A** and **B**) A buffer background spectrum was subtracted from the spectra of the time course (0 - 24 hours as indicated) shown in panel A (with oligo E) and B (without oligo E). The initial spectra showed a minimum at 198 nm and a shoulder at about 215 nm. The final spectra displayed minima about 201 nm and 218 nm (A) or at about 197 and 218 nm (B). (**C** and **D**) The ellipticity at 198 nm (blue) and at 218 nm (red) was chosen to follow the conformational changes of STVIIE with (**C**) and without (**D**) oligo E.

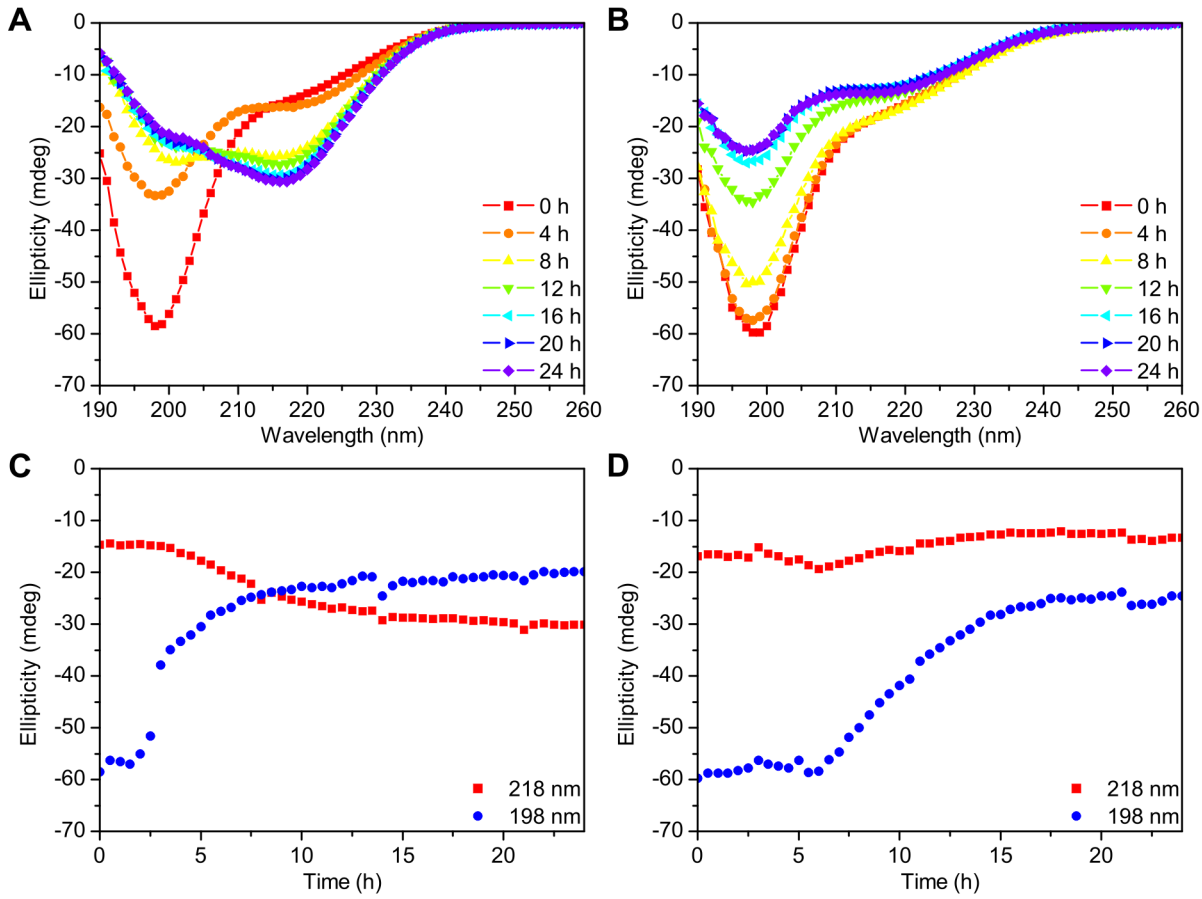

Figure 6-29: DNA oligonucleotides promoted loss of random coil conformation, repeat 2. A time course of the conformational change of 0.8 mM STVIIE in 20 mM glycine pH 2.6 without (**B**, **D**) or with (**A**, **C**) 242 nM oligo E (33mer; 1:100 charge ratio) was followed over 24 h by CD spectroscopy. (**A** and **B**) A buffer background spectrum was subtracted from the spectra of the time course (0 - 24 hours as indicated) shown in panel A (with oligo E) and B (without oligo E). The initial spectra showed a minimum at 198 nm and a shoulder at about 215 nm. The final spectra displayed minima about 201 nm and 218 nm (A) or at about 197 and 218 nm (B). (**C** and **D**) The ellipticity at 198 nm (blue) and at 218 nm (red) was chosen to follow the conformational changes of STVIIE with (**C**) and without (**D**) oligo E.

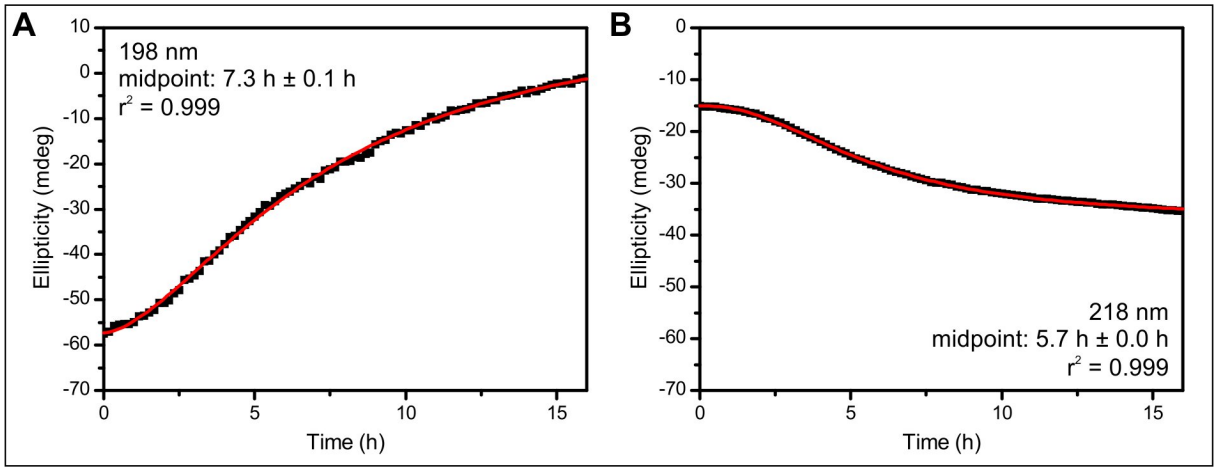

Figure 6-30: Logistic fits to STVIIE conformational change to determine the midpoints of the conformational transition. Logistic curves (red lines; Equation 7) were fit to time courses (black squares) at 198 nm (**A**) and 218 (**B**) shown in Figure 6-26 B. Results of the fits are shown in the graphs.

$$y = A_2 + \frac{A_1 - A_2}{1 + \left(\frac{x}{x_0}\right)^p}$$ **Equation 7**

In summary, the studies suggested that samples with DNA lost the random coil conformation at an earlier time point than peptide-only samples. This observation supports the idea that DNA may be able to catalyse the loss of random coil conformation of STVIIE. The identity of the peptide conformations at 24 h after the start of the assay was less clear based on the variations in the final spectra observed. However, these samples were observed to contain fibrils (see next section), suggesting that amyloid formation had occurred.

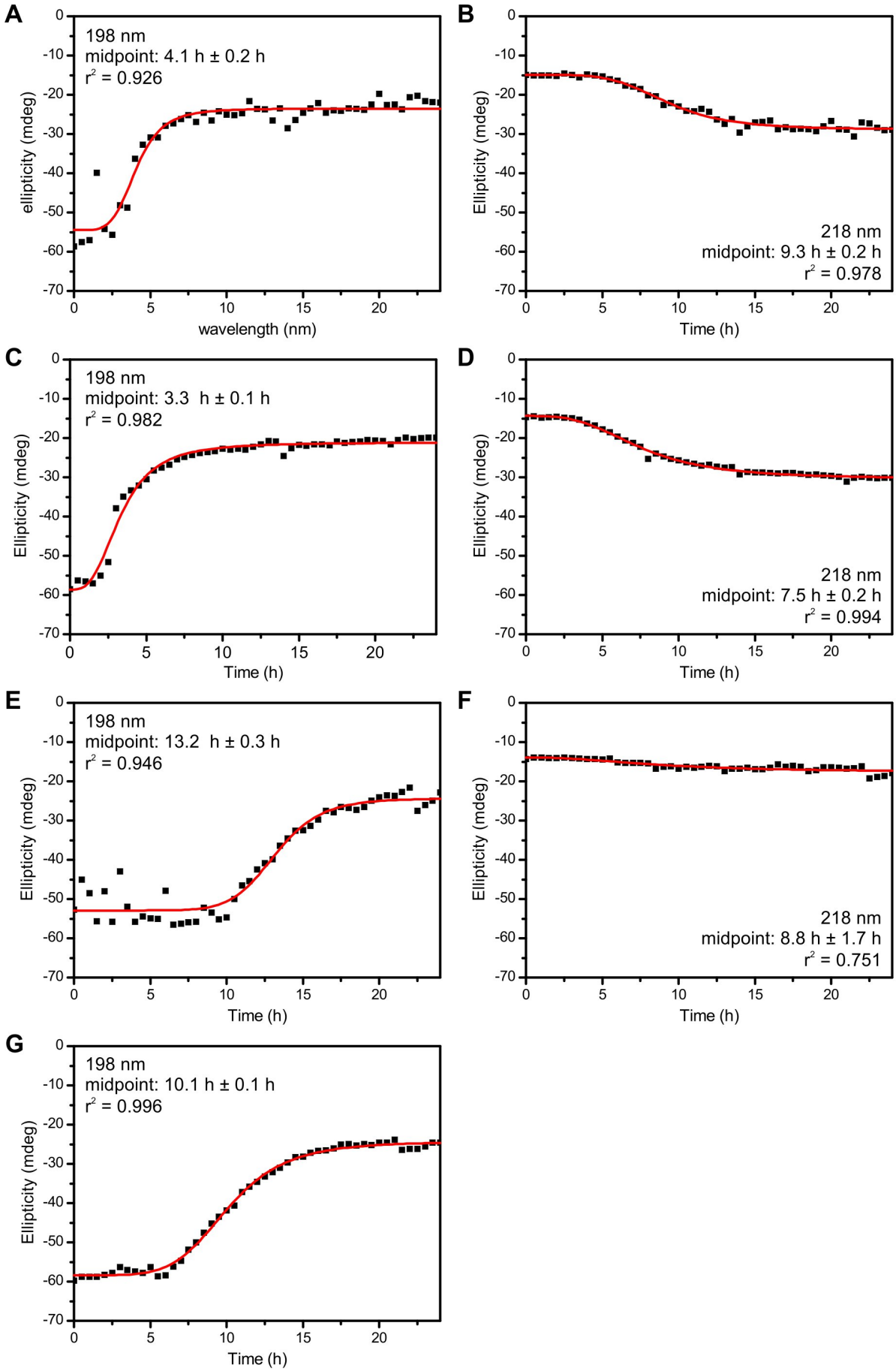
A
198 nm
midpoint: 4.1 h ± 0.2 h
r² = 0.926
ellipticity (mdeg)
wavelength (nm)
B
218 nm
midpoint: 9.3 h ± 0.2 h
r² = 0.978
Ellipticity (mdeg)
Time (h)
C
198 nm
midpoint: 3.3 h ± 0.1 h
r² = 0.982
Ellipticity (mdeg)
Time (h)
D
218 nm
midpoint: 7.5 h ± 0.2 h
r² = 0.994
Ellipticity (mdeg)
Time (h)
E
198 nm
midpoint: 13.2 h ± 0.3 h
r² = 0.946
Ellipticity (mdeg)
Time (h)
F
218 nm
midpoint: 8.8 h ± 1.7 h
r² = 0.751
Ellipticity (mdeg)
Time (h)
G
198 nm
midpoint: 10.1 h ± 0.1 h
r² = 0.996
Ellipticity (mdeg)
Time (h)

Figure 6-31: Logistic fits to STVIIE conformational change with or without oligo E to determine the midpoints of the conformational transition. Logistic curves (red lines; Equation 7) were fit to time courses (black squares) at 198 nm (**A**, **C**, **E**, **G**) and 218 nm (**B**, **D**, **F**) shown in Figure 6-28 C and D (A, B, E, F) and Figure 6-29 C and D (C, D, G). No curve was fit to the time course at 218 nm shown in Figure 6-29 D because it was not clearly sigmoidal.

$$y = A_2 + \frac{A_1 - A_2}{1 + \left(\frac{x}{x_0}\right)^p}$$ **Equation 7**

Table 6-16: Midpoints and lag times for random coil to β-sheet transition of STVIIE ± DNA

Sample	lag phase 198 nm	midpoint 198 nm	r^2	lag phase 218 nm	midpoint 218 nm	r^2	Figure
STVIIE without oligo E	n.a.	7.3 h ± 0.1 h	0.999	2 h	5.7 h ± 0.0 h	0.999	Figure 6-26 B
STVIIE without oligo E	6 h	13.2 h ± 0.3 h	0.946	10 h	8.8 h ± 1.7 h	0.751	Figure 6-28 D
STVIIE without oligo E	6 h	10.1 h ± 0.1 h	0.996	n.a.	not determined	n/a	Figure 6-29 D
STVIIE with oligo E	3 h	4.1 h ± 0.2 h	0.926	6 h	9.3 h ± 0.2 h	0.978	Figure 6-28 C
STVIIE with oligo E	2 h	3.3 h ± 0.1 h	0.982	6 h	7.5 h ± 0.1 h	0.994	Figure 6-29 C

Table 6-17 legend: Midpoints were determined by fitting a logistic curve using Origin Pro 8 to the time courses shown in Figure 6-26 B, Figure 6-28 C and D, and Figure 6-29 C and D. The fits are shown in Figure 6-30 and Figure 6-31. The lag phases were determined visually from the same graphs. The data indicated that the presence of 1:100 charge ratio oligo E promoted loss of random coil conformation (transition at 198 nm), while the gain of β-sheet was not as clear (transition at 218 nm).

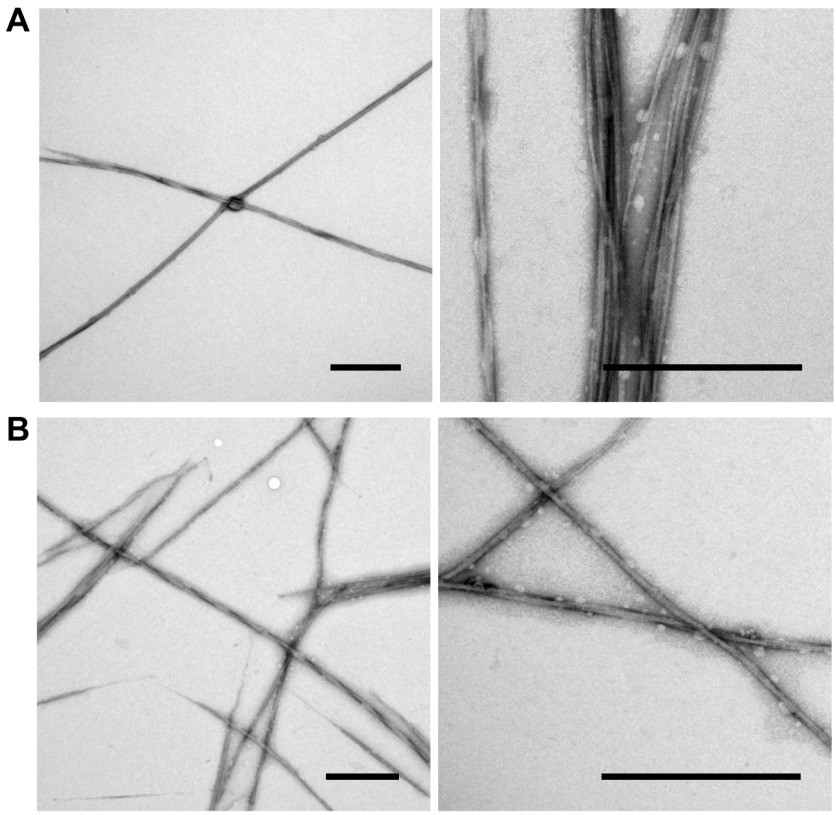

Figure 6-32: Electron micrographs of STVIIE amyloid fibres. The samples created during the first CD time course experiment (shown in Figure 6-28) from 0.8 mM STVIIE in 20 mM glycine pH 2.6 without (**A**) and with (**B**) 1:100 (calculated charge ratio) DNA oligonucleotide showed no clear difference in fibre morphology. Both showed long, relatively straight fibres, of which some were twisted, with diameters of about 9 nm. Oligo E seemed to have no apparent effect on the formation of larger fibre bundles or aggregates. Scale bars are 500 nm.

No striking morphological difference of STVIIE fibres formed either with or without oligo E could be detected by EM analysis. Both appeared as amyloid fibrils with long, relatively straight, occasionally twisted fibres with a minimal diameter of about 9 nm (see Figure 6-32 and Table 6-17). No difference in aggregation either toward fibres or

amorphous aggregates could be detected between STVIIE +/- oligo E, although this survey was not exhaustive. This suggested that the presence of the oligonucleotide did not induce macroscopic morphological changes detectable by TEM (see Figure 6-32), but the differing spectra for the samples with and without oligo E suggested different final conformations (see Figure 6-28). However, it might also be possible that material giving rise to the CD signal did not attach to EM grids. The lack of an isosbestic point in the presence of oligo E furthermore suggested that different pathways were followed by the peptide when adopting its final conformation. Fibre diffraction experiments did not yield usable results because the glycine buffer gave rise to surprisingly strong salt rings and spots, completely masking the STVIIE diffraction pattern (data not shown). As mentioned before for the fatty acid-peptide stalks, washing the stalks or using them when still moist for diffraction might reduce this problem, but it would not be guaranteed that this would allow picking up the potentially subtle differences between STVIIE fibres with or without oligo E.

Table 6-17: STVIIE fibre diameters

STVIIE alone	STVIIE + oligo E
9.6 ± 0.3	9.5 ± 0.1
9.2 ± 0.8	10.4 ± 1.4
10.1 ± 0.7	11.9 ± 1.8
10.5 ± 0.7	12.3 ± 0.1
10.5 ± 0.8	12.4 ± 0.6
11.2 ± 0.9	13.0 ± 0.8
11.3 ± 2.0	14.5 ± 1.9
11.5 ± 0.9	14.9 ± 2.6
13.7 ± 0.4	15.1 ± 1.1
13.7 ± 0.9	15.5 ± 2.1

Table 6-17 legend: Fibre diameters were determined using ImageJ [204]. Three measurements were taken on clearly defined fibres with a distance of at least twice the diameter between measurement sites. Measurements were not taken of large diameter fibres/aggregates in order to determine minimum fibre diameters. No striking difference between STVIIE fibres with and without oligo E could be made out. Diameters are in nm ± standard deviation of the three measurements of the same fibre.

In conclusion, we have shown that even very small amounts of nucleic acid could greatly promote conformational changes of STVIIE, specifically the loss of random coil conformation, by reducing the lag phase. The resulting fibres had the same appearance on TEM images with or with support from the oligonucleotide, but the CD spectra suggested different conformational polymorphisms and folding pathways to reach them.

6.2. Analysis of Hybridisation in the Presence of ANA Complexes

From our studies it became clear that nucleic acids had a marked effect on simple basic peptides with alternating polar and apolar amino acid residues by enhancing their amyloid formation potential. These interactions were probably based on peptide and nucleic acid charges as suggested by the gel formation (see chapter 6.1.3). Additionally, the absence of a DNA signature in the fibre diffraction experiments cast doubt on the structural integrity of DNA and made it seem worthwhile to examine DNA hybridisation in the context of peptide-nucleic acid complexes. The ability of DNA to hybridise is directly related to its ability to form base pairs and its double-helical structure.

6.2.1. PicoGreen Analysis of Hybridisation

PicoGreen is an asymmetric cyanine dye that shows increased fluorescence upon binding double-stranded, but not single-stranded DNA or RNA [250-252]. Initially I concentrated on the hybridisation of oligo E and oligo F that at least theoretically would form double-stranded DNA strands of indefinite length (see Figure 5-4; also used for BIAcore experiments, see Chapter 6.2.2). The effect of salt was examined with a NaCl titration from 0 to 150 mM (see Figure 6-33). Even the quite low NaCl concentration of 10 mM was sufficient to give rise to half-maximal hybridisation, with a hybridisation plateau reached at about 40 mM NaCl. This was a very low concentration compared to what was used for hybridisation experiments like Northern and Southern blots or microarrays [253-255].

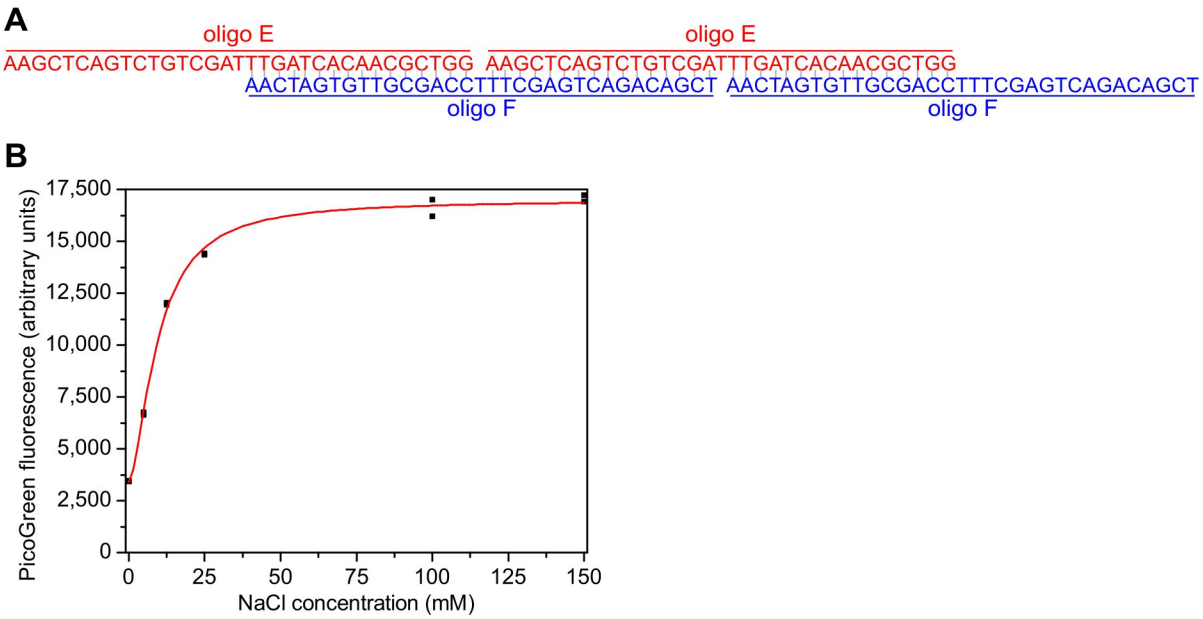

Figure 6-33: Hybridisation promotion of oligo E and F by NaCl measured by PicoGreen fluorescence. (**A**) *Schematic of oligo E and F hybridising to each other.* The 16 bp overlap sequences with a thymidine as a spacer would theoretically allow the creation of nicked DNA double-strands of indefinite length. (**B**) *PicoGreen assay of oligo E with oligo F.* 2.5 µM of the oligonucleotides were incubated with 0 to 150 NaCl at room temperature for 30 minutes before measurement. Hybridisation of oligo E and F reached a saturation plateau at about 40 mM NaCl. A logistic curve was fit using Origin (A_1 = 3390 ± 242, A_2 = 16993 ± 205, x_0 = 9.6 ± 0.5 mM NaCl and p = 1.7 ± 0.1 through the n = 12 points (r^2 = 0.98);see Equation 6).

$$y = A_2 + \frac{A_1 - A_2}{1 + \left(\frac{x}{x_0}\right)^p}$$ **Equation 6**

In the next step I wanted to study the effect of $(KL)_5$ on hybridisation of oligo E and oligo F. It had the highest charge density of the peptides used in this study (see Table 6-1), and it was felt that it might be able to denature DNA. A BIAcore assay (see Figure 6-37) showed that $(KL)_5$ might interfere with hybridisation and denature DNA.

The presence of even very low concentrations of $(KL)_5$ resulted in a reduction of PicoGreen fluorescence. The half-maximal fluorescence was reached at about 35 μM, and at 100 μM all fluorescence it was reduced to background level (see Figure 6-34). This was a low peptide concentration compared to the range explored before, for example for gel formation (0.2 to 5 mM peptide; Table 6-5) and the Congo Red assay (0.2 mM peptide; Figure 6-7).

The reduction of PicoGreen fluorescence might have been caused by the peptide interfering with binding of the dye to double-stranded DNA, which is required for its fluorescence. PicoGreen has been reported to most likely intercalate between the base pairs [250-252], but its structural similarity to SybrGreen has also led to the suggestion that it exhibits minor groove binding [256]. Independent of the exact PicoGreen binding mode, the lack of binding may result from the distortion/ denaturation of the DNA structure by $(KL)_5$, thereby preventing dye binding. Alternatively, the peptide may have quenched the fluorophore, resulting in a reduced fluorescence. The results of the BIAcore assay (see Figure 6-37) suggested that $(KL)_5$ might interfere with hybridisation of DNA strands to each other, making denaturation of DNA a more likely explanation for the reduced PicoGreen binding.

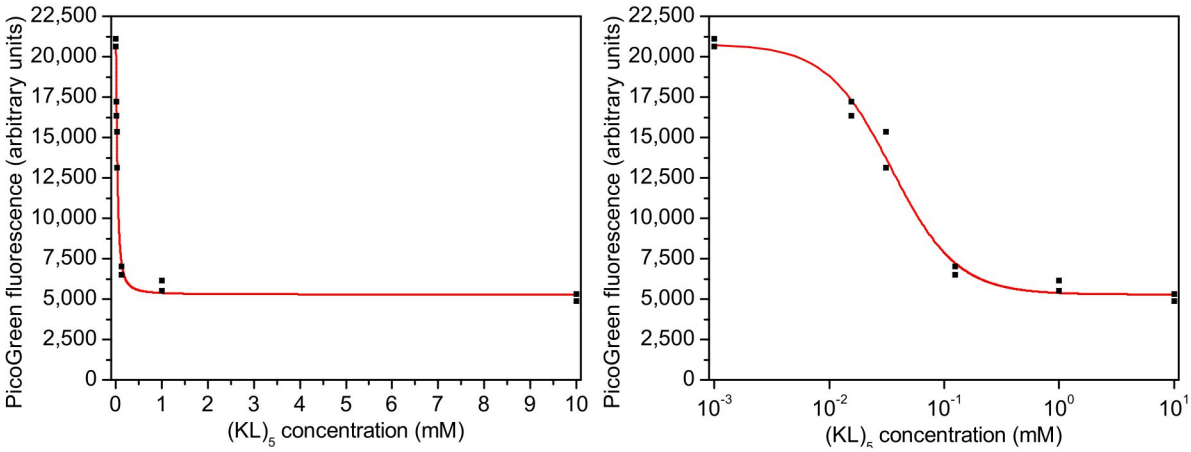

Figure 6-34: Signal reduction of PicoGreen by $(KL)_5$. Very low concentrations of $(KL)_5$ (from about 10 µM on) reduced fluorescence of PicoGreen, reaching the basal level at about 100 µM peptide. 2.5 µM oligo E and F were incubated with 0 to 10 mM $(KL)_5$ and 50 mM NaCl at room temperature for 30 minutes before measurement, reaching maximum quenching to background levels (about 5000 fluorescence units) at about 100 µM. A logistic curve was fit using Origin (A_1 = 20784 ± 602, A_2 = 4286 ± 426, x_0 = 0.035 ± 003 mM $(KL)_5$ and p = 1.53 ± 0.23 through the n = 12 points (r^2 = 0.98); see Equation 6).

$$y = A_2 + \frac{A_1 - A_2}{1 + \left(\frac{x}{x_0}\right)^p} \qquad \textbf{Equation 6}$$

Taken together, PicoGreen appeared to be able to detect the hybridisation from single-stranded oligonucleotides, but the loss of fluorescence signal at concentrations lower than previously used to explore the interactions of $(KL)_5$ with nucleic acids (gel formation: Table 6-5, Congo Red binding: Figure 6-7, electron microscopy: Figure 6-10) made this assay unsuitable for further experiments. The difficulties in distinguishing between the effects of the peptide on DNA hybridisation and potential quenching led us to switch to use the FRET setup, which allowed us to interpret possible effects on

hybridisation or on the fluorophores by comparison of the 11 bp overlap and 0 bp overlap probes. (see section 6.2.3 (page179) and Figure 6-39).

6.2.2. BIAcore Analysis of the Mutual Interactions of Peptides and Oligonucleotides

Interactions between biomolecules are frequently studied using surface plasmon resonance (SPR; BIAcore) [257,258]. A system of multiple overlapping oligonucleotides was designed to examine the effect of peptides and peptide-nucleic acid complexes on nucleic acid hybridisation and of nucleic acid length on peptide aggregation [259-261]. For these studies, DNA oligonucleotides were immobilised on a gold chip, while peptides were flowed over the surface. Local changes in refractivity result from changes in mass at the surface and were expressed as response units (RU).

Initially a biotinylated anchor oligo D was bound to a streptavidin-covered gold BIAcore chip (SA chip: carboxymethylated dextran pre-immobilized with streptavidin; BIAcore, Sweden) (see Figure 6-35 for a schematic). Overlapping complementary sequences (16 bp with equal use of each base) were hybridised to allow the sequential generation of a stepwise increase in DNA of defined length with an increase in length of 17 b per injection cycle (16 bp hybridising to each other with 1 base as a spacer). Importantly, the DNA formed would have contained nucleic acid nicks at regular intervals as shown in the diagram (see Figure 6-35 for a schematic).

Flowing oligo E over the chip led to an increase in response in the experimental flow cell modified with oligo D on its surface and a control flow cell (see Figure 6-36 A, first oligo E injection). The resulting curve after subtraction of the background of the control flow cell showed that the response increased until a plateau was reached. This increase in RU was interpreted as material associated with the chip surface, in this case oligo E. The

response did not drop markedly during the buffer wash, indicating that the oligonucleotide remained bound to the surface. Hybridisation of oligo E to oligo D was seen as the cause for this response curve; without such stable interactions oligo E would have been washed away. The plateau would suggest that all free binding sites were occupied by the oligonucleotide. The following injection of oligo F resulted in a similar curve shape, but the net increase from plateau to plateau was smaller (see Figure 6-36 A, first oligo F injection). This pattern was repeated for the following injections of oligo E and F, with oligo E reaching a stronger net response than oligo F. After the third injection of oligo E no net increase in response was seen.

The apparent reduction in net response with each alternating flowing of oligonucleotide over the chip might be due to the intensity decrease of the plasmon resonance field with increasing distance from the chip surface. But the material accumulated on the chip would create DNA strands of 30 nm length (based on 0.34 nm rise per base; 88 bp long DNA), while the SPR-efficient field extended to about 200 nm above the surface (BIAcore 3000 manual). So it appeared as though the hybridisation of the oligonucleotides to each other was not to 100% efficient, maybe due to some undetected secondary structure formation. Hybridisation as a cause for the response increase was also supported by the reduced association of the oligonucleotides with the surface in 50 mM NaCl, and no binding could be observed in the absence of NaCl (data not shown); hybridisation would require NaCl for charge shielding of the phosphate backbone [201]. Oligo E usually seemed to hybridise with about 70 to 80% efficiency, while oligo F reached only about 30% efficiency (see Figure 6-36 B). It remained unclear why no net response increase could be seen after the 5th injection cycle. However, this pattern was reproducible, and I thought that this system provided an assay suitable for the examination of peptides on

DNA hybridisation. It should be noted that the final products in the control DNA experiments would be predicted in the range of 20 b ssDNA to a nicked partial duplex of maximum of 88 b (30 nm).

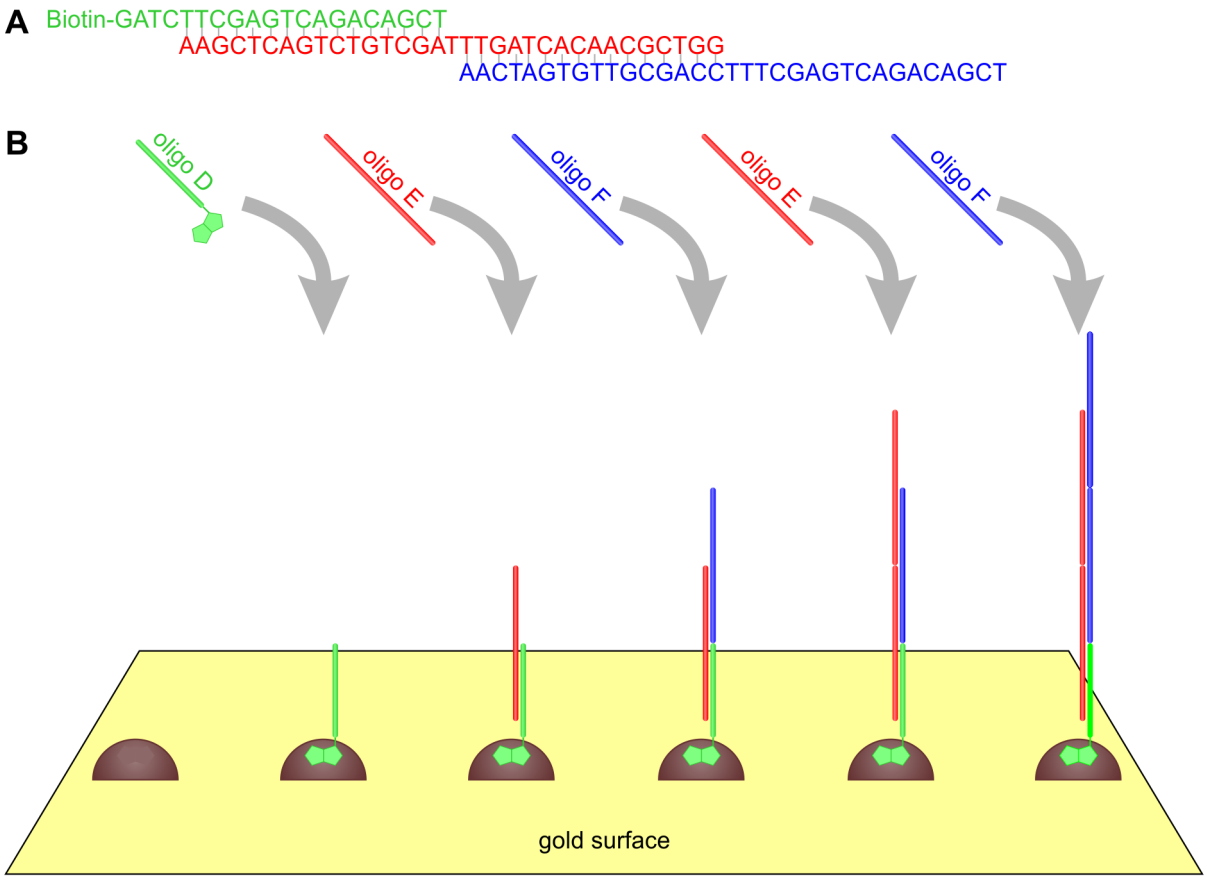

Figure 6-35: Schematic of oligo E and F in the BIAcore build-up experiments. (**A**) Sequences of oligo D (green, 5' to 3'), E (red, 3' to 5'), and F (blue, 5' to 3'), showing their overlap. The free end on oligo F provides a hybridisation site for oligo E. (**B**) Oligo D (green) is captured by streptavidin (brown) immobilised on the gold surface of a BIAcore chip. Successive alternating injections of oligo E (red) and oligo F (blue) build up a double-stranded DNA that is linked to the gold surface.

In the next step I wanted to examine the effects of the peptide on DNA hybridisation. To avoid forming gels in the delicate liquid handling system of the BIAcore instrument 10 µM $(KL)_5$ was used in initial assays. This peptide concentration was lower than those previously used to show gel formation (see Table 6-5) and that which was used in the Congo Red assay (see Figure 6-7). However, it was thought that if positive interaction data was obtained, the presence of fibrous aggregates could be determined on the BIAcore chip surface using AFM as previously described [262]. In addition, the concentration of peptide 10 µM was previously shown to be sufficient for amyloid aggregate formation by $A\beta_{1\text{-}40}$ [157]. $(KL)_5$ was used for initial assays as it had the highest charge density and was amongst the largest of the peptides, thus most likely to give a good signal.

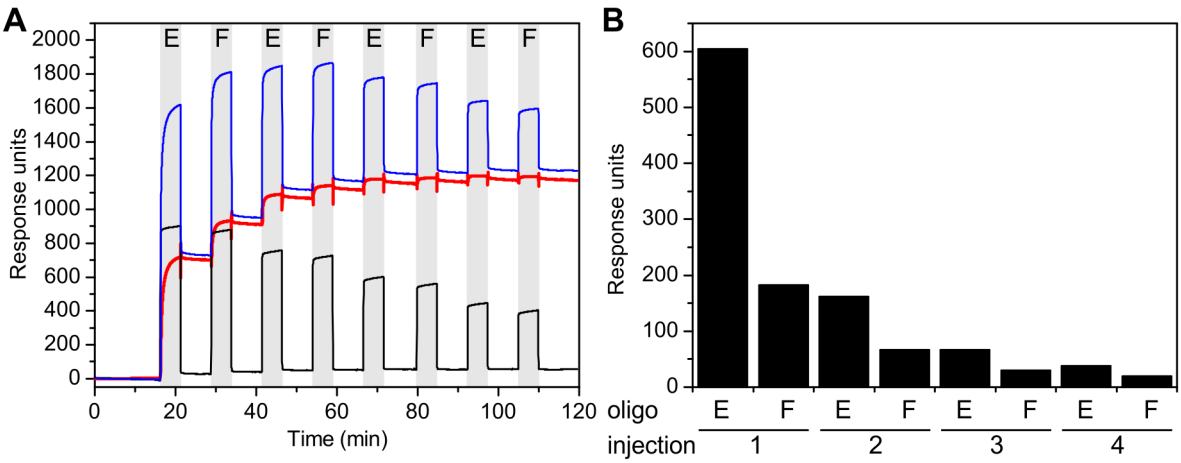

Figure 6-36: Hybridisation of oligo E and F on the BIAcore. (**A**) Oligo E and F were injected (grey areas as indicated; E and F indicated on the top) over a chip functionalised with oligo D (blue curve). A reference flow cell (black) was used to subtract the buffer/ unbound background. This allowed the response curve (red) to be calculated. (**B**) Changes in response

with each injection (plateau level of red curve in panel A). Oligo F reached only about a third of the response of oligo E, which seemed to saturate nearly all available binding sites on oligo D and oligo F. After 3 injection cycles only very low levels of new binding were detected.

I wanted to explore the binding of $(KL)_5$ to longer DNA strands and its effect on hybridisation (see Figure 6-37). The DNA build-up showed the expected pattern of good oligo E binding and weaker oligo F binding (compare to Figure 6-36). The addition of $(KL)_5$ to the running buffer (10 mM HEPES pH 7) resulted in a large response which quickly dropped at the end of the peptide injection, reaching a response level lower than the plateau before the peptide injection. The response increase during peptide injection would suggest that $(KL)_5$ associated only transiently with the surface in the experimental flow cell. The response was lower in the control flow cell, which presented a lower density of negative charges (oligonucleotide-modified streptavidin surface vs. unmodified streptavidin surface). The decreased plateau level after dissociation of the transiently bound peptide would suggest that some of the oligonucleotide was removed from the chip surface, too. This might be due to either $(KL)_5$ interfering with hybridisation, or to the peptide causing the release of the biotinylated anchor from streptavidin. The reduction in PicoGreen fluorescence (see Figure 6-34) might support the idea that the peptide interfered with hybridisation by denaturing the DNA.

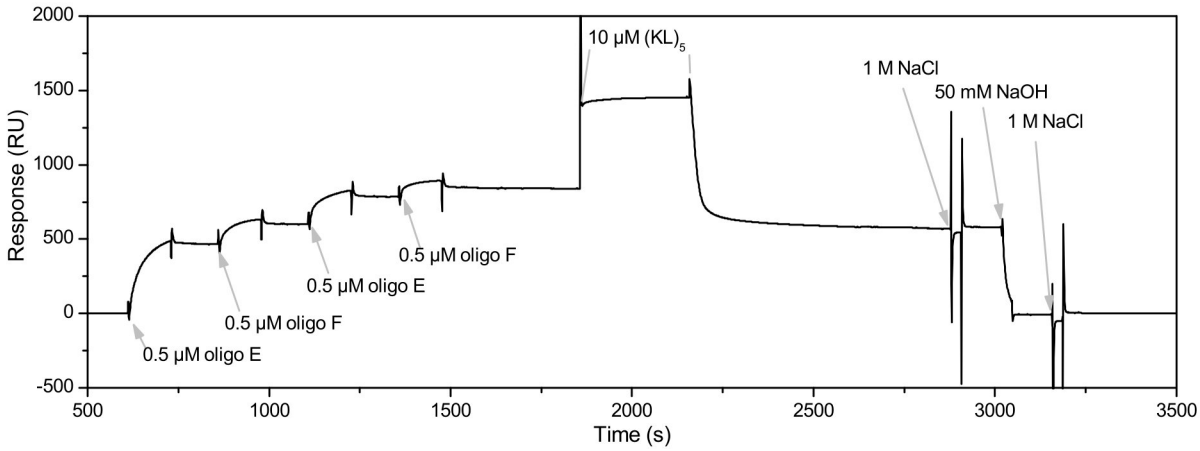

Figure 6-37: Binding of $(KL)_5$ to oligo E/F on the BIAcore chip. Running buffer was 10 mM HEPES pH 7.0 with 150 mM NaCl at 20 µl/min. Dissolved in the same buffer, 0.5 µM of oligo E or oligo F were alternatingly injected for 30 seconds as indicated in order to build nicked double-stranded DNA of defined length on the chip surface before 10 µM $(KL)_5$ was injected for 2 minutes. During the injection of the peptide the response increased because of a change in buffer refractivity. The following response decrease fell below the response level of the oligonucleotides on their own. The chip surface consisted of oligo D immobilised on streptavidin and was regenerated by injection of 50 mM NaOH for 30 seconds to remove the oligonucleotides and 1 M NaCl for 30 seconds to wash off any peptides sticking by charge-interactions as indicated. The shown traces were buffer subtracted from a control flow cell containing an unmodified streptavidin surface.

After $(KL)_5$ appeared to interfere with hybridisation and native DNA structure I examined the direct effect of $(HL)_3$ during oligo E binding to a BIAcore chip. The peptide was mixed with the oligonucleotides directly before injection (no gel detectable; see Table 6-2). There was virtually no difference in response between $(HL)_3$-oligo E

mixtures and oligo E alone (see Figure 6-38). While the oligonucleotide in both cases seemed to hybridise as usual, no additional response that might have been due to the peptides could be seen. This would suggest that the peptide did not associate with the chip surface, and that it also did not interfere with hybridisation. A change in NaCl concentration (0, 50, 150 mM) had no effect; no additional binding above the oligonucleotide associating with the chip surfaces could be detected.

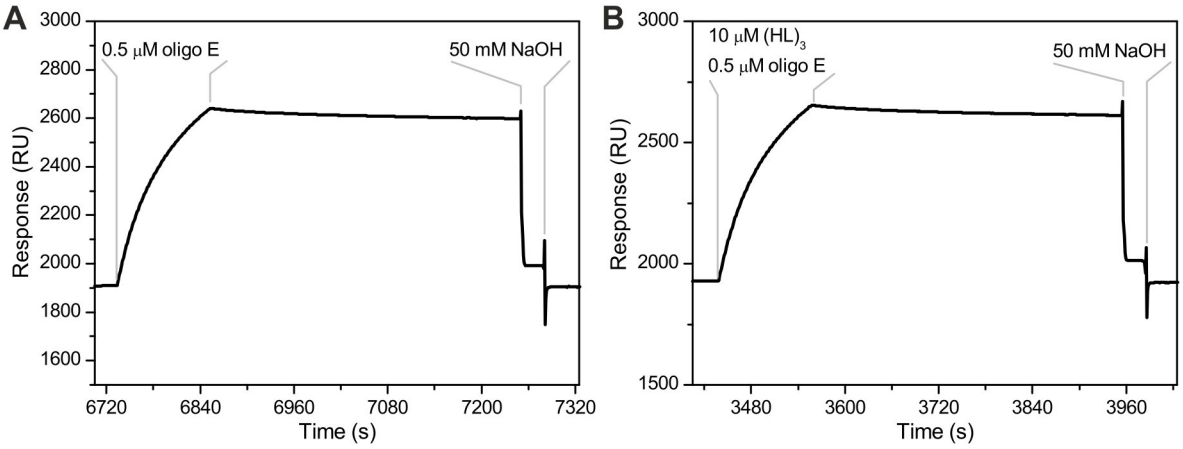

Figure 6-38: Binding of $(HL)_3$-oligo E mixtures to an oligo D BIAcore chip surface. 0.5 µM oligo E (A) or 10 µM $(HL)_3$ with 0.5 µM oligo E were flowed for 2 minutes over a chip surface modified with oligo D. The chip was washed with buffer for 6.5 minutes before it was regenerated by injection of 50 mM NaOH for 30 seconds. Running buffer was 10 mM MES pH 6.2 with 150 mM NaCl at 20 µl/min.

Taken together, the BIAcore binding assays suggested that $(KL)_5$ may have denatured double-stranded DNA because it seemed to be able to reduce the amount of oligonucleotides bound to the chip surface (see Figure 6-37). $(HL)_3$ on the other hand

did not appear to interfere with hybridisation (see Figure 6-38). Since no aggregate formation by the peptide could be detected, the work with this assay was stopped.

6.2.3. Enhancement of Hybridisation by ANA Complexes Shown by TR-FRET

To study the effects of positively charged ANA complexes on hybridisation of oligonucleotides, time-resolved FRET (TR-FRET) was used to follow the binding of two oligonucleotides to each other. These probes carried either a donor (ATTO 488) or acceptor (ATTO 550) fluorophore that showed only fluorescence energy transfer when brought within the Förster radius (6.4 nm; Atto-Tec, Germany) of the fluorophore pair. This was most likely to occur when the DNA probes hybridised with each other via their complementary single-stranded 11-bp-overlap sequences. The existence of hybridisation-independent processes that could bring the probes within the Förster radius was controlled by the use of sequence-matched 0 bp controls (see schematic in Figure 6-39). Additionally, samples without any peptide but with higher levels of salmon testes DNA (3.5 mM ST DNA) were used to control for potential crowding effects (for an example see Figure 6-45). It was thought that ST DNA would be a suitable, though not ideal, control since the peptides used here would be expected to form amyloid fibres and would not be available as monomers. The negatively charged peptide $(EL)_3$ was used as a control for the positively charged peptides since it showed no evidence for amyloid complex formation under these conditions (see Figure 6-46).

The use of TR-FRET had several advantages over DNA-binding dyes like PicoGreen: The fluorophores were covalently attached to probe oligonucleotides via a linker and did not have to bind to DNA, avoiding access issues by aggregate or gel formation. Also, TR-FRET was largely independent of the absolute fluorescence signal since measurements

were not altered by minor changes to probe concentrations. In addition, the technique was potentially more sensitive to lower levels of binding than intensity-based measurements as fluorophore 'bleed-through' did not set a lower limit to the detection range. Bleed through varies with the spectra of the fluorophore pairs used. I used the time-resolved FRET set-up built and maintained for a different application by the lab of Paola Borri [209].

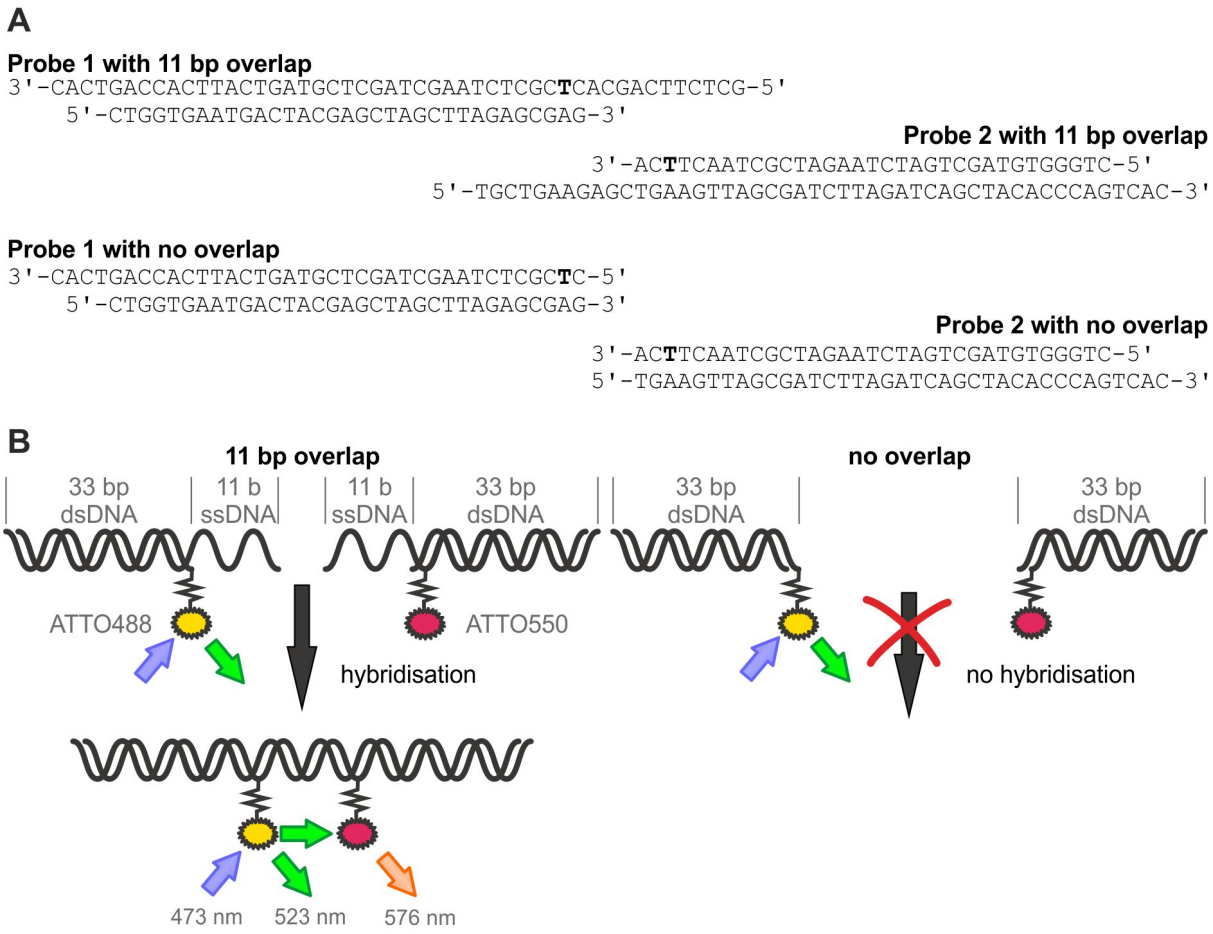

Figure 6-39: Construction of the FRET probes. (**A**) *Sequences of the FRET probes*. The probes were mainly double-stranded as indicated. The residues in bold carried either ATTO 488 (probe 1; donor fluorophore) or ATTO 550 (probe 2; acceptor fluorophore). (B) *Schematic of*

fluorescence emission of the probe fluorophores. ATTO 488 attached to the donor probe was the main excited fluorophore by the 473 nm laser light, emitting light at 523 nm. The acceptor was minimally excited by the laser, and only emitted fluorescence at 576 nm with intensity comparable to the donor when FRET occurred and the donor transferred energy to the acceptor. This only happened when the fluorophores were brought within their Förster radius (6.4 nm; Atto-Tec, Germany) upon hybridisation of the 11 bp overlap probes. The 0 bp overlap probes could not give rise to FRET resulting from hybridisation because they lacked the 11 bp complementary sequences.

Initially, I explored the ability of the system to detect hybridisation in a salt titration ranging from 1.125 mM to 1 M NaCl in the presence of 500 nM hybridisation probes. The probes were used at a concentration where near maximal saturation could be expected at about 5x K_d (K_d of approximately 100 nM as determined by BIAcore analysis; personal communication with Amal Kasry (Cardiff University); see also Figure 6-44). The fluorescence decay of the donor fluorophore became faster with increasing NaCl concentrations, while the fluorescence decay acceptor fluorophore showed a delayed rise with a shift and broadening of the maximum (see Figure 6-40). FRET could be safely detected from 20 mM NaCl to 1 M NaCl as indicated by a delayed rise and decay in the acceptor channel (see Figure 6-40). At 5 and 10 mM NaCl there was only a weak FRET signal, and at 1.125 mM NaCl no changes in donor or acceptor fluorescence decay could be observed. NaCl did not affect the fluorescence decay of donor probe or acceptor probe alone. Hybridisation levels could be calculated from the donor decay curves, showing that a plateau was reached in the presence of 500 nM hybridisation probes at about 150 mM NaCl. A Hill curve was fitted to the data in order to determine the NaCl

concentration required for half-maximal hybridisation as c_{free} = 53 mM NaCl. The NaCl concentration required for half-maximal hybridisation was higher than the one determined for oligo E and oligo F using the PicoGreen assay (9.6 mM NaCl; see Figure 6-33). This might be at least partially due to the shorter hybridisation sequence of the FRET probes (11 bp) compared to the oligo E/F system (16 bp).

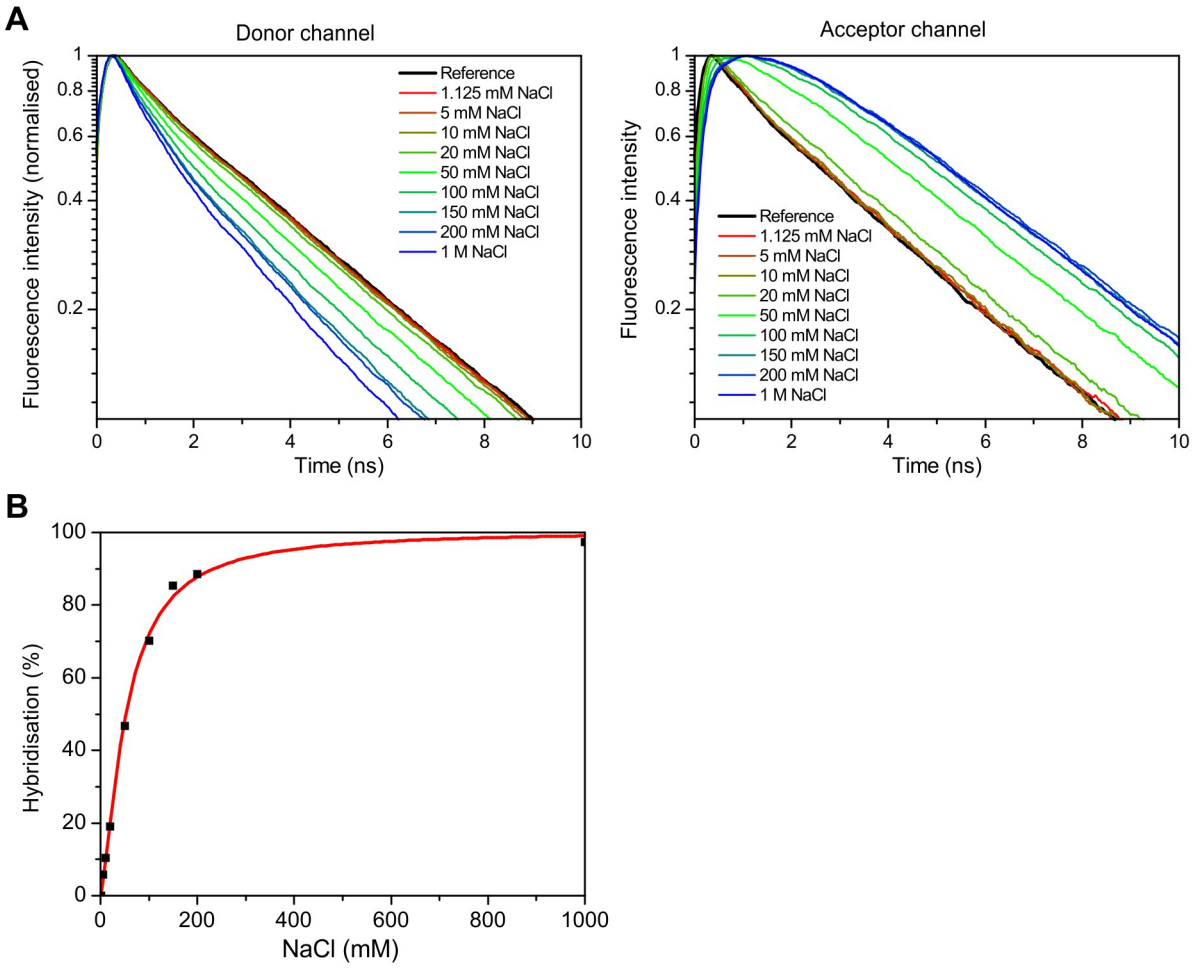

Figure 6-40: Hybridisation promotion by NaCl measured by TR-FRET. (**A**) *Fluorescence decay time courses at varying NaCl concentrations.* 500 nM of donor and acceptor hybridisation probes were incubated with 1.125 mM to 1 M NaCl at room temperature for 30 minutes before measurement. The reference was 500 nM donor or acceptor in 150 mM NaCl,

respectively. (**B**) *Hill fit to hybridisation levels.* Hybridisation levels were calculated from the fluorescence decay time courses shown in panel A as detailed in the methods section. A Hill curve (red; Equation 13) with a Hill coefficient of n = 1.4 ± 0.1 s.d. and a dissociation constant k = 53 mM ± 3 mM s.d. NaCl was fitted to the 9 data points (r^2 = 0.996), indicating half-maximal saturation at 53 mM NaCl.

$$f = \frac{f_{max} \times c_{free}}{k^n + {c_{free}}^n} \qquad \text{Equation 13}$$

The next step was to examine the effect of peptide-nucleic acid complexes on the hybridisation of the probes in order to detect potential effects of the amyloid state of the peptides. The presence of ST DNA seemed to be necessary to induce amyloid formation from $(HL)_3$, $(KL)_5$, $(HL)_5$, and TVQFHMH. Complexes of $(HL)_3$ and TVQFHMH were chosen under their strongest gel-formation conditions (see Table 6-2 and Table 6-7), i.e. with +2 calculated net charge per peptide at pH 6.2 or pH 5.0, respectively (see Table 6-1). The peptides were mixed with the same concentration of ST DNA, resulting in a +1 overall net charge. The concentration of 150 mM NaCl was chosen because this condition was previously used to form ANA complexes, and it induced near-maximal hybridisation of the probes in solution (see Figure 6-40). The TR-FRET hybridisation probes were spiked into the pre-formed peptide-nucleic acid complexes. Exemplar fluorescence time courses of donor and acceptor fluorophores with or without the hybridising 11 bp overlap in the presence of 1 mM $(HL)_3$-ST DNA gel are shown in Figure 6-41. The donor fluorophore of the 11-bp-overlap probe exhibited a faster decay, while the acceptor showed a delayed rise and decay of fluorescence, which was indicative for FRET. None of these effects were detected with probes lacking the complementary overlap sequences, which closely followed the reference curves of donor

or acceptor alone. This indicated that the 11 bp overlap sequences were necessary to give rise to the FRET signal in the presence of the ANA complexes. The lack of FRET from the 0 bp control in the presence of $(HL)_3$-ST DNA complex contrasted with the observation of low level FRET in samples with peptide alone (see Figure 6-42 A). Similar curves were obtained in the presence of TVQFHMH-DNA complexes (data not shown).

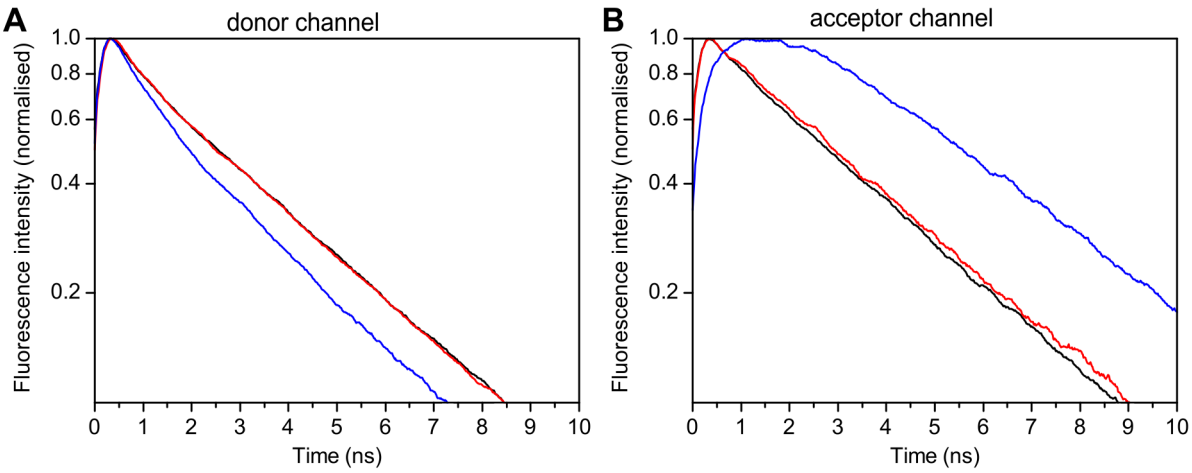

Figure 6-41: FRET example time courses. A faster fluorescence decay in the donor channel (**A**) and a delayed rise and decay of fluorescence in the acceptor channel (**B**) compared to a reference (black; the reference in panel A is largely obscured by the 0 bp control) consisting of either only the donor probe or only the acceptor probe under the same conditions. Faster donor (**A**) and delayed acceptor (**B**) fluorophore dynamics were observed with 11 bp (blue) but not the 0 bp (red) overlap probes compared to the reference (100 nM donor alone or 100 nM acceptor alone in the presence of 1 mM $(HL)_3$-ST DNA in the same buffer). Data shown from 100 nM of oligonucleotides mixed with a preformed 1 mM $(HL)_3$-ST DNA complex at pH 6.2.

A potential effect of the peptides $(HL)_3$ and TVQFHMH on their own was tested with 500 nM hybridisation probe. This concentration was chosen because after the potential denaturation of oligo E/F by $(KL)_5$ a reduction of the hybridisation level was expected; also this relatively high concentration gave a good signal to noise ratio. The NaCl concentration of the buffer (10 mM MES) was set to 0, 50, or 150 mM NaCl. The pH was set to pH 6.2 for $(HL)_3$ and pH 6.5 for TVQFHMH in order to give them a calculated net +2 charge as used for $(HL)_3$-ST DNA complexes and TVQFHMH-ST DNA complexes (see below; Figure 6-42, Figure 6-44, Figure 6-45, and Figure 6-46).

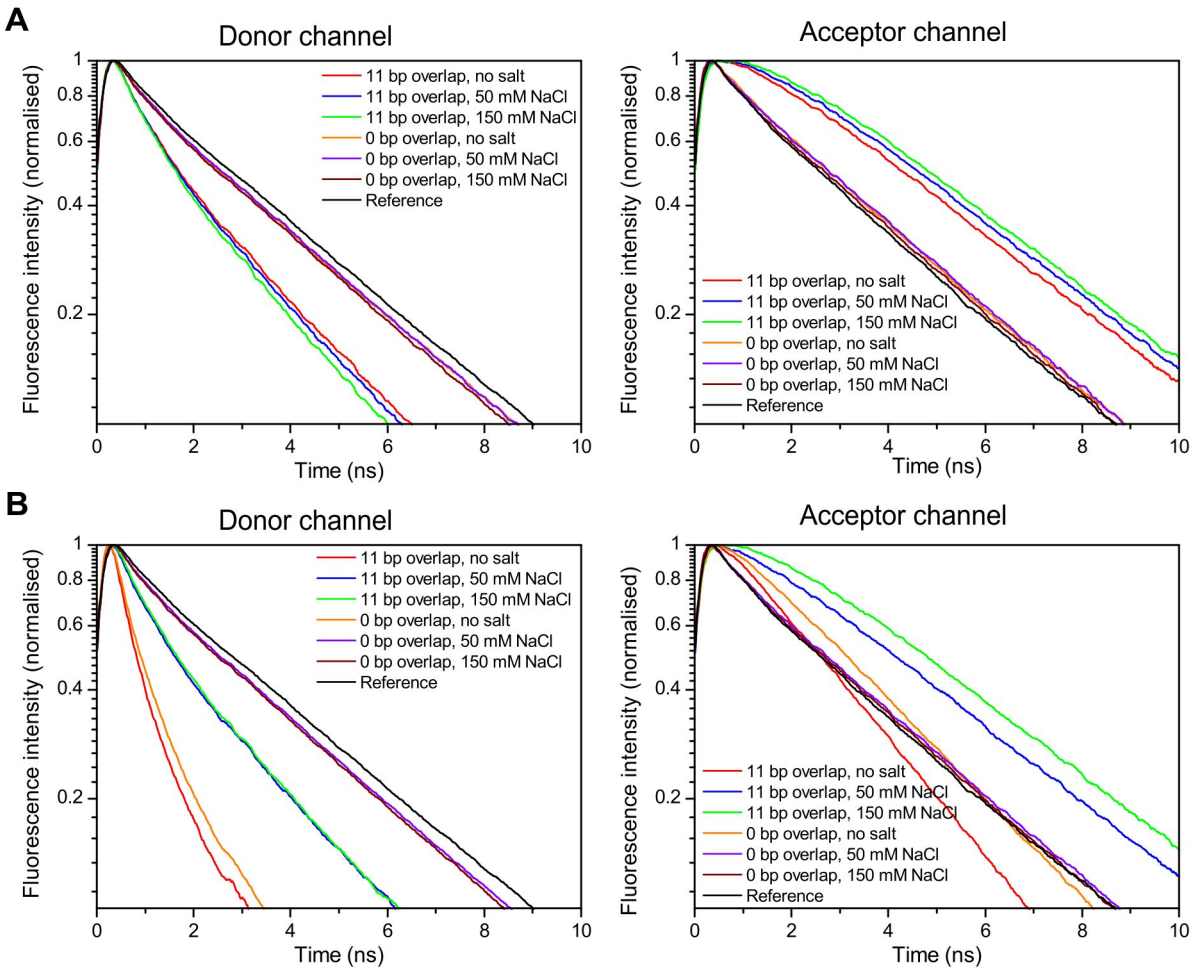

Figure 6-42: FRET assay on $(HL)_3$ and TVQFHMH (peptide alone) with 500 nM hybridisation probes. (**A**) *Effect of $(HL)_3$ on hybridisation probe fluorescence decay.* 500 nM hybridisation probes were incubated with 1 mM $(HL)_3$ in 10 mM MES pH 6.2 with 0, 50, or 150 mM NaCl. (**B**) *Effect of TVQFHMH on hybridisation probe fluorescence time courses.* 500 nM hybridisation probes were incubated with 1 mM TVQFHMH in 10 mM MES pH 6.5 with 0, 50, or 150 mM NaCl.

$(HL)_3$ had an influence on the fluorescence decay of the 11 bp donor and acceptor pairs at 500 nM each (see Figure 6-42 A): Donor fluorescence decay was faster to a level comparable to the presence of 1 M NaCl (also at 500 nM probe concentration; compare

to Figure 6-40), while the acceptor fluorescence decay was delayed indicating FRET at all NaCl concentrations (0, 50, and 150 mM) explored. The 0 bp overlap probes were much less affected: The donor fluorescence decay showed a slightly faster decay comparable to 20 mM NaCl (also at 500 nM probe concentration; compare to Figure 6-40).

TVQFHMH had a dramatic effect on both 11 bp overlap and 0 bp overlap probes in the absence of NaCl, with a very fast donor decay showing (see Figure 6-42 B). But the acceptor fluorescence decay showed an unusual decay, with an initial delay followed by faster fluorescence decay than the reference. The hint a FRET occurring with the 0 bp overlap probes was unexpected because the probes lack the 11 bp overlap sequences in order to hybridise to each other, which would bring donor and acceptor fluorophore within their Förster radius. Taken together, the unusual acceptor decay and the FRET signal with the 0 mM overlap probes suggested that the fluorophore system was unable to correctly report on hybridisation under these conditions (0 mM NaCl). In the presence of 50 and 150 mM NaCl a pattern similar to $(HL)_3$ (see Figure 6-42 A) emerged with a FRET signal at 150 mM NaCl comparable to the presence of 1 M NaCl (see Figure 6-40), while in the absence of NaCl there was only a weak effect.

Please note that for both the $(HL)_3$ and TVQFHMH control the references used were not recorded in the presence of either of the peptides, but in the corresponding buffer (pH 6.2 or pH 6.5) with 150 mM NaCl; there were no detectable differences between donor only or acceptor only curves at different NaCl concentrations (data not shown).

The importance of the 0-bp-overlap controls became clear when the effect of $(KL)_5$-DNA and $(HL)_5$-DNA complexes on hybridisation levels was examined (see Figure 6-43). The $(KL)_5$-ST DNA caused faster fluorescence decay of both donor and acceptor and a loss of fluorescence intensity (visible before normalisation of fluorescence intensity; data not shown) even with the 0 bp overlap control probes as well as with the references (donor only or acceptor only without the corresponding hybridising probe), indicating quenching of the ATTO fluorophores instead of FRET effects. $(HL)_5$-ST DNA caused faster fluorescence decay of the donor, including the 0 bp overlap probes and the donor reference. The acceptor references were not affected, but the time courses of the samples containing both donor and acceptor were unusual (compare to Figure 6-40, Figure 6-41, Figure 6-42, or Figure 6-45). The 11 bp overlap probes gave rise to an additional faster decay of the donor than the 0 bp overlap probes, but the reduced dynamic range and the unusual acceptor time courses made it not seem worthwhile to work with these peptides.

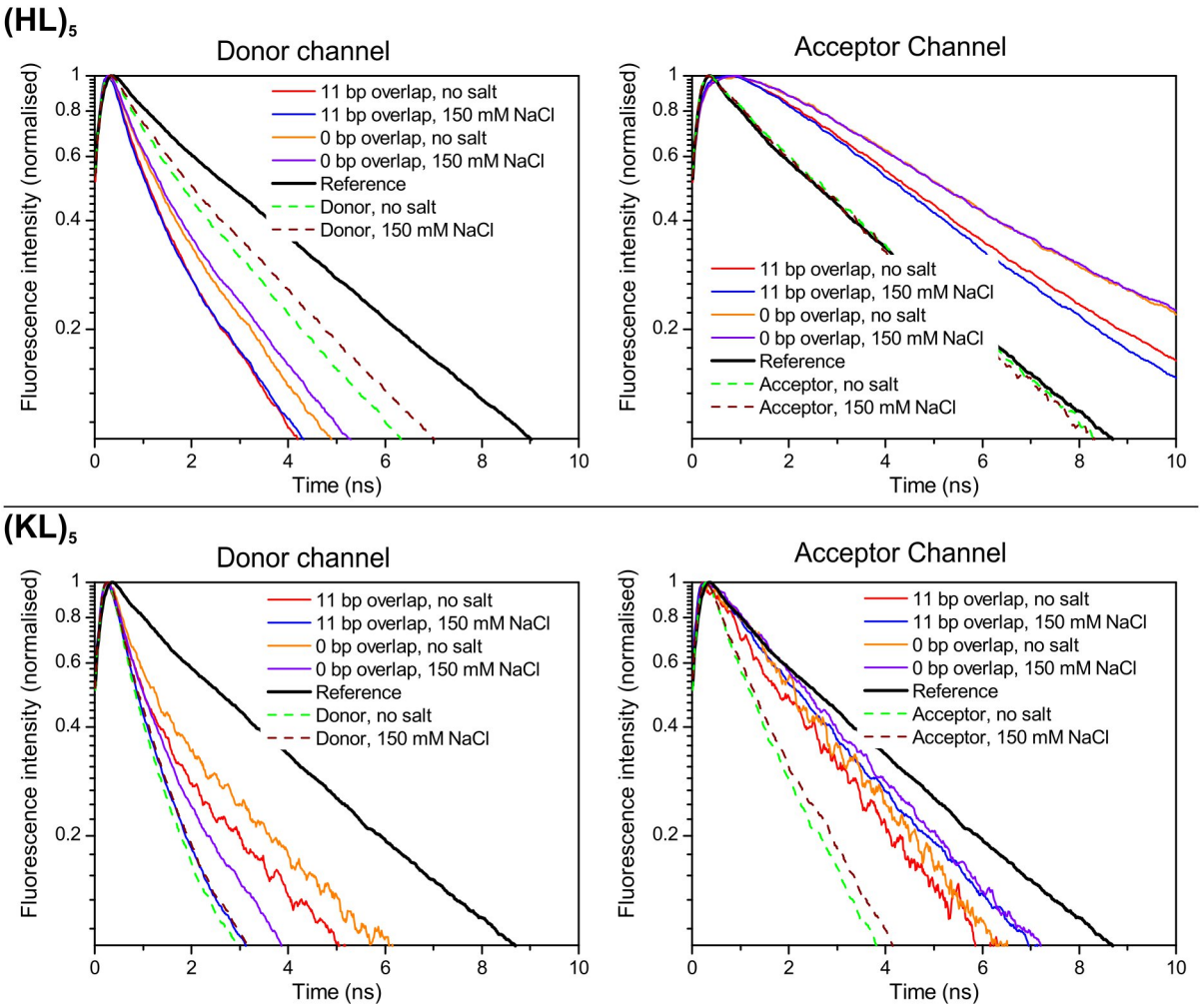

Figure 6-43: Effect of $(HL)_5$-ST DNA and $(KL)_5$-ST DNA complexes on FRET probes. 500 nM 11 bp overlap (both donor and acceptor), 0 bp overlap (both donor and acceptor), 11 bp overlap donor probe, or 11 bp acceptor probe were incubated in 0 or 150 mM NaCl with 1 mM $(HL)_5$-ST DNA at pH 6.8 (10 mM MES) or with 1 mM $(KL)_5$-ST DNA at pH 7 (10 mM HEPES). Reference was 500 nM donor probe or acceptor probe in 150 mM NaCl in the absence of peptide-ST DNA complex. (**Top**) $(HL)_5$-ST DNA caused faster fluorescence decay of the donor fluorophore for all samples including the 0 bp overlap probes and the donor only sample. The 0 bp overlap and 11 bp overlap samples showed a delayed rise and decay, but the acceptor only samples were not affected. (**Bottom**) $(KL)_5$-ST DNA caused faster

fluorescence decay of all samples in both the donor and acceptor channels, including the donor only and acceptor only control samples.

When the delayed rise and decay of the acceptor fluorophore indicated FRET, the donor decay could be used to calculate the ratio of bound, i.e. FRET-showing, to unbound donor probes. When FRET was occurring the single-exponential fluorescence decay gained an additional decay component, resulting in a double-exponential decay [209]. Division by a reference yielded the single-exponential decay caused by FRET, from which hybridisation levels could be calculated using a curve-fitting procedure (Equation 9) [152,209]. The hybridisation level of the 11 bp overlap probes was about as high with 85% hybridisation at 100 nM probe concentration as the value obtained with 500 nM probes at 150 mM NaCl during the salt titration (see Figure 6-40). This suggested that hybridisation of the 11 bp overlap probes was not hindered by the presence of ANA complex. The hybridisation level seemed relatively high given the concentration differences of the probes in the different experiments (100 nM probes in 150 mM NaCl with ANA complex vs. 500 nM in 150 mM NaCl alone). To confirm and expand these findings a titration from 20 to 800 nM probes in saturating 150 mM NaCl with or without 1 mM $(HL)_3$ ANA complex was carried out. The dissociation constant of the 11-bp-overlap probes alone was determined to be at K_d = 96 nM, but this was surprisingly clearly surpassed in the presence of the ANA complex as a dissociation constant of K_d = 18 nM was reached (see Figure 6-46). This showed that the presence of positively charged ANA complexes actually enhanced hybridisation in saturating salt conditions.

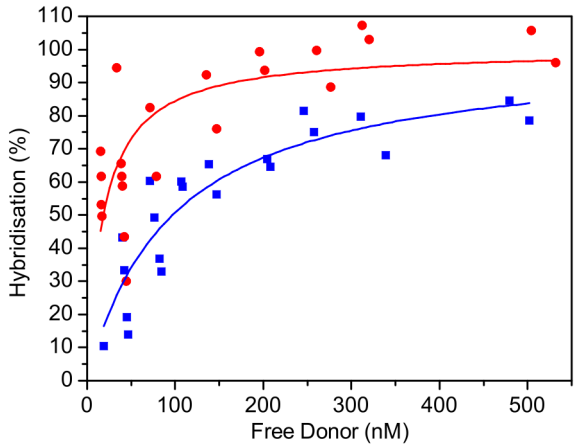

Figure 6-44: $(HL)_3$-ANA complexes enhance hybridisation. In the presence of 1 mM pre-formed $(HL)_3$-ANA complexes (red) the dissociation constant was reduced to K_d = 18 nM ± 6 nM s.d. (n = 22, r^2 = 0.48) compared to salt only (blue) with K_d = 96 ± 23 nM s.d. (n = 21, r^2 = 0.816). Probe oligonucleotides from 20 nM to 800 nM were examined with or without pre-formed ANA complexes in the presence of 150 mM NaCl and 10 mM MES pH 5.5.

The K_d reduction seemed to be mainly due to increased hybridisation levels at concentrations below the peptide-nucleic acid complex-free K_d in 150 mM NaCl only. When 20 nM and 50 nM hybridisation probes were incubated with the positively-charged peptide-ST DNA complexes of $(HL)_3$ and TVQFHMH much higher hybridisation levels than the control in 150 mM NaCl only could be detected. This was especially prominent at 20 nM probe concentration where no FRET could be detected in the absence of peptide-ST DNA complexes. $(HL)_3$-ST DNA complexes gave rise to stronger FRET signals than TVQFHMH-DNA ANA complexes, which resulted in higher hybridisation levels. The hybridisation enhancement seemed to be based on charge interactions since a mixture of negatively charged $(EL)_3$ peptide and ST DNA (see Figure 6-46) as well as increased levels of salmon testes DNA as crowding control had no effect (see Figure 6-45). The 1.0 mM ST DNA used in the peptide-ST DNA complexes had

similarly no effect. A crowding control using 3.5 mM ST DNA, which by mass corresponded to the peptide-nucleic acid complexes, did not increase hybridisation compared to buffer alone. Also, none of the peptide-ST DNA complexes had an effect on the 0-bp-overlap probes, showing that these effects were due to hybridisation of the 11-bp-overlap probes (data not shown).

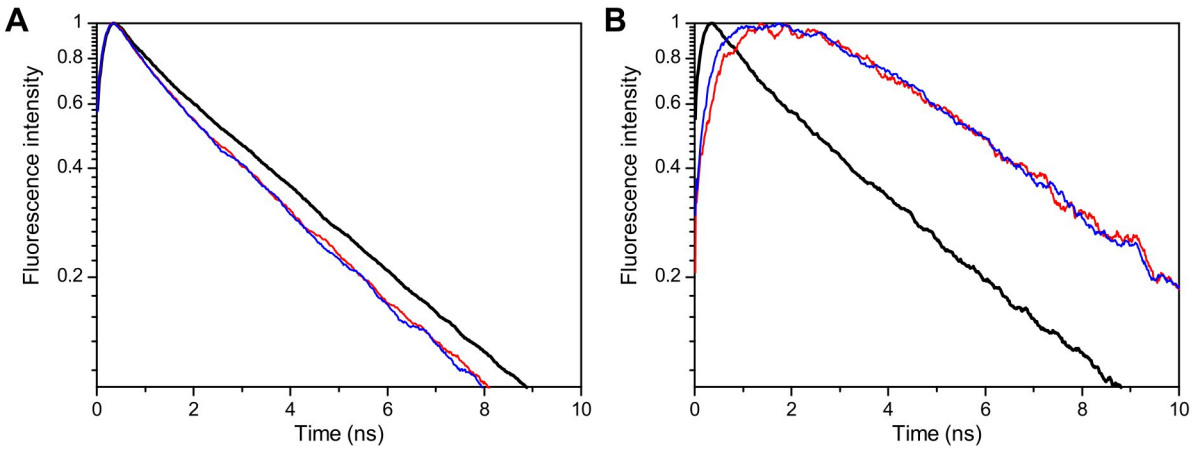

Figure 6-45: 3.5 nM DNA with 100 nM hybridisation probes. 100 nM hybridisation probes were incubated with 3.5 mM ST DNA (red) or buffer only (blue) at pH 6.2 in 10 mM MES with 150 mM NaCl. The donor fluorescence decay (A) and the acceptor, which by mass corresponded to 1 mM $(HL)_3$ with 1 mM ST DNA. The delayed rise and decay in the acceptor channels (**B**, **D**) and the slightly accelerated fluorescence decay in the donor channels (**A**, **C**) indicated that FRET occurred, although the signal was not very strong for 20 nM hybridisation probes (**C**, **D**).

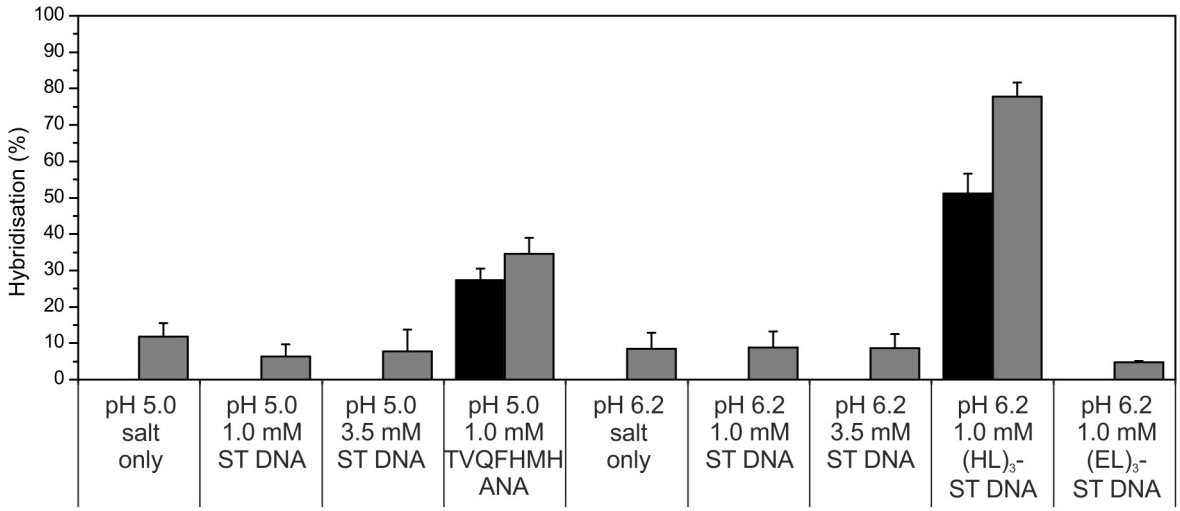

Figure 6-46: $(HL)_3$-ST DNA and TVQFHMH-ST DNA mixtures increased hybridisation at low 11 bp probe oligonucleotide concentrations. 20 nM (black)/ 50 nM (grey) 11 bp overlap probes were incubated for at least 30 minutes before measurement with 1 mM $(HL)_3$-ST DNA, 1 mM TVQFHMH-ST DNA, 1 mM (EL)3-ST DNA, 1 mM ST DNA, 3.5 mM ST DNA, or buffer. The buffer was 10 mM MES pH 5.0 or pH 6.2 (as indicated) with 150 mM NaCl. The hybridisation levels were calculated from donor fluorescence decay time courses as detailed in the methods section. The positively-charged $(HL)_3$ and TVQFHMH, but not the negatively charged $(EL)_3$ ANA complexes, enhanced hybridisation of 20 nM and 50 nM probes over control levels. 1.0 mM and 3.5 mM ST DNA did not increase hybridisation of the 20 nM and 50 nM probes compared to the 'salt only' controls.

Taken together, time-resolved FRET revealed that $(HL)_3$ and TVQFHMH promoted hybridisation of the probe oligonucleotides. This effect was not abolished in the presence of equimolar amounts of ST DNA, under which conditions amyloid fibres were shown to form (Figure 6-2, Figure 6-9, Figure 6-12). Although similar levels of FRET were observed for ANA complexes and peptide alone, ANA complexes appeared to have

slightly lower levels of non-specific interaction as highlighted by the 0 bp probe (Figs. 6-42 and 6-43). The effect of peptide on the hybridisation probe was to increase hybridisation at low probe concentrations.

7. DISCUSSION

7.1. GEL FORMATION BY THE PEPTIDES USED IN THIS WORK

Most of the peptides examined in this work did not aggregate or form gels on their own or in the presence of diethyl phosphate as a monomeric anion under the conditions explored (pH 5.0 – pH 8.0, 0 to 150 mM NaCl, room temperature; see Table 6-2, Table 6-3, Table 6-4, Table 6-5, Table 6-6, Table 6-7, and Table 6-8), suggesting that the presence of polymeric anions was essential for gel formation. This observation was consistent with previous studies by Calamai *et al.*, who have shown that polymerised charges increased amyloid formation by human muscle acylphosphatase and human lysozyme [163]. Of the peptides examined, only the basic, positively charged ones showed interaction with polyanions, while the negatively charged $(EL)_3$ showed no indication of amyloid formation in complex with nucleic or fatty acids (see Table 6-4, Figure 6-5, Figure 6-22, Figure 6-23).

The detection of gels by pipetting was a rather rough assay, but it enabled us to scan for potential associations between peptides and nucleic acids. The various peptides showed quite diverse responses regarding gel and aggregated formation when they were mixed with nucleic acids or diethyl phosphate.

Charge interactions appeared to be an important factor driving aggregation. NaCl had an effect on the balance between gel and aggregate formation by $(KL)_5$. While at 0 mM and 75 mM NaCl $(KL)_5$-PA RNA only showed aggregation, in 150 mM NaCl there was some gel formation at higher pHs (see Table 6-5). $(HL)_3$-ST DNA showed weaker gels with increasing NaCl concentrations (see Table 6-2). Taken together, this would suggest

charge interactions as a mediator between aggregation and gel formation because NaCl has been shown to have a charge-shielding effect [263]. Additionally, when TVQFHMH and $(HL)_3$ were titrated with varying ST DNA concentrations there was a preference for a 1:1 ratio between peptide and nucleic acid at pH 6.8 and pH 6.2, respectively. The peptides were calculated to carry a +2 charge under these conditions (see Table 6-1), while the nucleic acid should carry a -1 charge per phosphate and base. This would result in complexes with a +1 net charge per peptide, which in previous reports has been suggested as optimal for amyloid fibre formation from peptides on their own [142]. It was presumed that peptides with higher charge were prevented by charge repulsion from interacting and forming stable associations through β-sheet and hydrophobic interactions [142]. The formation of amyloid in complex with polyionic biomolecules was consistent with previous reports on the aggregation of Aβ [164,165], tau [4,166], α-synuclein [167], β_2-microglobulin [168], and murine PrP [6,169,170], although compensation would not be a dominant factor in all these cases charge.

Since the interactions leading to gel formation and aggregation of the peptides were based on non-covalent charge interactions the aggregation process should in principle be reversible. Dilution or introduction of peptide-nucleic acid complexes into a precursor-free environment should lead to disaggregation over time. The size of the aggregates might influence the rate of disassembly because interactions of the component polymers could only take place on the surface, or in the case of amyloid fibres, most likely at their free ends [104,264]. Future studies could concentrate on measuring the disassembly rate and try to determine the mechanism.

Interestingly, diethyl phosphate or inorganic phosphate had no detectable effect on aggregation or gel formation by $(HL)_3$, $(HL)_5$, $(KL)_3$, $(KL)_5$, or $(EL)_3$ compared to the buffer alone (see Table 6-2, Table 6-3, Table 6-4, Table 6-5, Table 6-6, Table 6-7). It seemed that monomeric phosphate (either as inorganic phosphate or a nucleic acid backbone mimetic diethyl phosphate) was not able to induce gels from most of the peptides, but longer nucleic acid strands with a series of connected negative charges (dubbed 'polymerised charges') could support gelation. An exception from this rule was TVQFHMH, which seemed to form slightly stronger gels in the presence of diethyl phosphate (see Table 6-7). However, TVQFHMH already showed a propensity to form gels on its own (see also Figure 6-11) in the presence of NaCl, so the low concentration of diethyl phosphate might have been sufficient to neutralise the charges on the peptide in order to induce fibrillisation.

While the majority of the peptides used in this study were readily water-soluble, $(HL)_5$ was quite insoluble (see chapter 6.1.3) and formed aggregates that were dominated by the formation of small (turbidity) and larger (visible) aggregates at 5 mM concentration (see Table 6-6). At 1 mM concentration only very weak gels appeared, and solely in the presence of nucleic acid. Still this peptide displayed clear cross-β patterns (see Figure 6-14). Further studies will be required to examine the effect of the (HL) pattern expansion that led from the soluble $(HL)_3$ to the insoluble $(HL)_5$.

$(KL)_3$ –DNA mixtures were quite bad at forming gels at 5 mM concentration (see Table 6-3). This was in contrast to $(KL)_5$, which was two (KL) units longer (see Table 6-5 and discussion below). The concentration of $(KL)_3$ might have been too low to support the formation of gels or aggregation. Higher concentrations used for fibre diffraction sample

preparation (>10 mM; see Table 5-4, Figure 6-15 and Figure 6-16) did form stronger gels. This could suggest that a minimum concentration was required for strong $(KL)_3$-nucleic acid interactions and potential amyloid formation that was higher than 5 mM.

$(KL)_5$, $(HL)_3$ and TVQFHMH showed some differential effects towards ST DNA and PA RNA: While with peptide-ST DNA mixtures generally showed earlier and stronger gel formation, the corresponding peptide-PA RNA mixtures displayed a trend towards aggregation and weaker gels (see Table 6-2, Table 6-5 and Table 6-7). One could speculate that the persistence length of double-stranded genomic DNA (60 nm (about 176 bp); [265]) and single-stranded artificial poly(A) RNA (about 2 bases; [265,266]) might have influenced the type of peptide-nucleic acid complex toward gels or aggregates. Thus a shorter persistence length might allow higher flexibility in the gels, potentially driving towards tighter aggregates based on the RNA being able to fold back on itself much easier than the stiffer dsDNA.

In summary, it seemed that the peptides $(HL)_3$, $(HL)_5$, $(KL)_3$, $(KL)_5$, $(KL)_4$, and $(KL)_{3.5}$ required polymerised charges in order to aggregate into gels or larger, potentially amorphous, aggregates. Aggregation seemed to be concentration-dependent with weaker gels at lower concentrations. The influence of NaCl concentration (0 mM, 75 mM or 150 mM) on the complexes usually resulted in weaker gels at higher salt concentration, which suggested charge interactions as a major factor in the aggregation of the peptides. This was additionally supported by the increased gel strength of $(HL)_3$-ST DNA and TVQFHMH-ST DNA mixtures close to 1:1 molar and calculated charge ratio.

7.2. STRUCTURES

The mixtures of peptides with nucleic acids not only formed aggregates (see section 7.1; Table 6-2, Table 6-3, Table 6-5, Table 6-6, Table 6-7), but contained fibres that were compatible with previously reported morphologies of amyloid fibres (see Figure 6-9, Figure 6-10, Figure 6-11, and Figure 6-12) [2,44,72,94,183,267,268]. The gel formation seemed to favour stronger interactions of $(HL)_3$ and TVQFHMH with nucleic acids under conditions (pH and near equimolar concentration of peptide and polyanion; Table 6-2 and Table 6-7) that gave the peptides-nucleic acid complexes a +1 net charge, which was previously described ideal for amyloid fibrillisation [142]. Indeed nearly all of the examined peptide-nucleic acid combinations showed a clear cross-β pattern (see Figure 6-14, Figure 6-15, Figure 6-17), which was indicative of amyloid formation. The requirement for nearly equimolar amounts of nucleic acid in almost all cases (with exception of TVQFHMH (Figure 6-17) and maybe $(HL)_3$ (Figure 6-25) again supported the idea of nucleic acids as an important component for the formation of amyloid fibres from $(HL)_3$, $(HL)_5$, $(KL)_3$, and $(KL)_5$. Such complexes of amyloid fibre and nucleic acid were called 'ANA' complexes for 'Amyloid-Nucleic Acid' [152].

Since the majority of the peptides used in this work seemed to require interactions with polyanions to form amyloid, they were not recognised by current computational algorithms used to find amyloidogenic peptides. So far the algorithms have not been trained to recognise polypeptide sequences that required ionic interaction partners other than themselves. Such ionic binding partners could neutralise the majority or all of the charges, which as a first approximation might allow prediction of such peptide sequences. Further research into this area could greatly improve these algorithms, simplifying the search for new self-aggregating polypeptide sequences that could be

used for nano-technological fibre production, and might help in finding essential cofactors for amyloid nucleation associated with pathological amyloidoses.

An interesting feature of TVQFHMH was its ability to form fibres on its own, either from a stock solution at pH >6 (used for X-ray fibre diffraction; Figure 6-17) or at pH 6.5 with 150 mM NaCl (used for electron microscopy; Figure 6-11). At least in the latter case the pH was known, and the peptide was calculated to carry a +2 net charge, which has been suggested previously by de la Paz *et al.* as being probably not compatible with ordered amyloid aggregation due to charge repulsion [142]. One feature that distinguished TVQFHMH from the other peptides used in this study was the presence of the aromatic residue phenylalanine. Such residues have been suggested to be important drivers of the formation of amyloid fibrils by Aβ, serum amyloid A protein, α-synuclein, and some artificial peptides derived from these examples [154,231,269]. Particularly the π-stacking interactions and high hydrophobicity have been suggested to greatly influence the propensity of peptides to aggregate [154]. Such interactions might also have played a role in the TVQFHMH fibre formation, although further studies would be needed to confirm this.

While TVQFHMH on its own, and in complex with ST DNA or PA RNA, showed a cross-β pattern the equatorial reflections were quite weak (see Figure 6-17) when compared to $(HL)_3$-ST DNA (see Figure 6-14) or $(KL)_3$- and $(KL)_5$-ST DNA (see Figure 6-15) patterns, or examples from the literature, e.g. TTR fibres [79,134,230]. The classical amyloid fibre-based cross-β pattern contained an equatorial reflection at about 10 Å, but an alternative structure could be a β-helix. β-helices have first been described as a fold in native globular proteins like pectate lyase [270], *Bordella pertussis* haemagglutinin

adhesin [239], or the phage P22 tailspike protein [134,271]. The most compelling evidence for their presence in amyloid fibres comes from a yeast prion, i.e. the prion domain of Het-s in *Podospera anserina* [134,237], and the core of PrP amyloid fibres [134]. Interestingly, all of these examples were larger proteins or full protein domains, which might help to fulfil a potential peptide length requirement, since all amyloid β-helices so far were shown to require the peptide backbone to run at least 1 (but usually more) full circumferences around a hydrophobic core [24,235,237]. The 7mer TVQFHMH on its own would probably be too short to form a β-solenoid core with a single molecule. It might be possible that 3 or more peptide strands could form such a core (2 would most likely form a β-sheet sandwich), but such a structure has not yet been described. An alternative to the β-solenoid would be a water-filled nanotube as suggested by Perutz *et al.*, which in contrast to the structures mentioned above did not have a hydrophobic core, but had a core comprised of water [235]. Such a structure would require an even longer peptide to make one circumference around the water core. Also, the nanotubes were based on the diffraction pattern of a polyglutamine peptide (D2Q15K2) which could present hydrophilic amino acid residues both to the inside and the outside of the tube, while TVQFHMH with its alternating pattern of hydrophobic and hydrophilic residues could not. Additionally, it was suggested that such a water-core tube would collapse upon drying into a β-sandwich-like structure with a corresponding diffraction pattern [235]. The diffraction patterns collected of TVQFHMH, TVQFHMH-ST DNA and TVQFHMH-PA RNA were from dried stalks, so they should have presented a classical cross-β pattern with a strong equatorial reflection at 10 Å [79,134,230]; the weak equatorial reflection in that area (see Figure 6-17) would contradict the assumption of a nanotube collapse upon drying [235] and made the formation of a water-filled nanotube unlikely.

Taken together, the weak equatorial reflection of the TVQFHMH diffraction patterns might suggest the formation of a β-solenoid around either a hydrophobic or a water core, but the shortness of the peptide (7mer), the propensity of β-solenoids to be present in functional yeast prion amyloid (e.g. Het-s) and the absence of the equatorial 10 Å reflection in the dried state made the formation of a β-sheet sandwich more likely, especially since such a structure would be more associated with disease-associated misfolded proteins and artificial short peptides. Further studies would be necessary to elucidate the structure of TVQFHMH fibres, for example by solid-state NMR which was used to determine the structure of the Het-s β-solenoid [134,237].

$(KL)_3$ showed some unusual meridional reflections in the two patterns recorded involving this peptide (see Figure 6-15 (top row) and Table 6-12). In one case a triple reflection at 5.03 Å, 4.77 Å, and 4.50 Å was seen from $(KL)_3$ in complex with herring testes DNA (see Figure 6-15, top left), and in the other an unexpectedly small meridional reflection at 4.62 Å with (KL)3 in complex with salmon testes DNA (see Figure 6-15, top right). The narrower reflection of $(KL)_3$-ST DNA might be explained by a tighter packing of the peptides within the β-sheets. Alternatively, a 4.7 to 4.8 Å reflection might be absent in this particular pattern because of interference leading to its extinction. Reflections close to 4.6 Å have been reported before [230], so this pattern might in general agree with amyloid formation. On the other hand, the triple reflections of $(KL)_3$-HT DNA would suggest that an unknown fibrous structure was formed. Further studies would be necessary to determine the structure. From the limited data available it was not clear if the diffraction patterns might be influenced by the different types of nucleic acids (HT DNA vs. ST DNA).

The other structures agreed with a cross-β pattern indicative of amyloid formation (see Figure 6-14, Figure 6-15, Figure 6-17; [2,41,79,142,230]). As described in chapter 6.1.70, equatorial reflections found in addition to the major 10 Å reflection for $(HL)_5$-PA RNA, $(KL)_5$-ST DNA, and may $(KL)_3$-ST DNA might suggest either a very ordered lateral packing of fibrils, or the presence of a protofibrillar structure with β-sheet sandwiches winding around each other in the amyloid fibril of these peptides [79,230,232]. Further studies would be required to confirm this, maybe using magnetic fields or stretch frames in order to generate better aligned fibre diffraction samples [272].

None of the diffraction patterns of ANA complexes showed a clear pattern of nucleic acids (see Figure 6-14, Figure 6-15, Figure 6-17). The single-stranded poly(A) RNA would exhibit only a very weak pattern on its own, probably comparable to that of heat-denatured DNA (see Figure 6-18), which would probably disappear in the background of a strong cross-β pattern. On the other hand, double-stranded salmon testes DNA diffracted well and displayed a strong pattern as described before (see Figure 6-18; [233]). It might be possible that DNA and amyloid fibres were not in a collinear arrangement therefore the nucleic acid pattern did not show. On the other hand, $(HL)_3$-ST DNA seemed to be somewhat collinear as seen in the confocal images (see Figure 6-13). Perhaps the nucleic acid fibres were not packed regularly and densely enough in order to be detected. In the case of $(KL)_5$-ST DNA the peptide might have denatured the nucleic acid, resulting in at least a conformational change and probably also strand separation, so that maybe only a DNA pattern similar to heat-denatured ST DNA remained (see Figure 6-18). This would agree with the findings of the PicoGreen (see Figure 6-34) and BIAcore assays (see Figure 6-37). It remained generally unclear if DNA

or RNA would be stable under the conditions explored in the presence of the peptides in a dried fibre diffraction stalk, or if they would be denatured.

7.3. PEPTIDE AGGREGATION INDUCED BY NUCLEIC ACIDS

The effect of nucleic acids or other negatively-charged biopolymers on amyloid formation has been examined before [163], albeit on amyloidogenic full-length proteins. It was shown that the number of charged phosphate groups on an adenosine nucleoside influences the amyloid formation dynamics of acylphosphatase, with more polymerised charges improving amyloid formation [163]. This work expanded on that: Peptides not able to form amyloid fibres on their own under the conditions explored could be induced to form amyloid complexes by charge-charge interactions with nucleic acids as suggested by weakened gel formation at increased NaCl concentrations and increased gel strength close to a 1:1 charge ratio (see chapter 6.1.3), increased binding of ThT or Congo Red (see chapter 6.1.4), fibre formation as detected by EM (see chapter 6.1.5), and cross-β patterns shown by X-ray fibre diffraction (chapter 6.1.7). The mechanism of amyloid aggregation remained unclear, but it might involve nucleation on the nucleic acid by concentrating the peptides. In the studies described here, the peptide-nucleic acid interactions that promoted amyloid formation must have occurred with sequences that contributed to the core of the cross-β fibril. The lack of decorating sequences may have allowed direct interaction of the cross-β core with polyanions to induce fibre formation. The same effect of concentrating amyloidogenic polypeptides should also work with positive polymerised charges, as shown for certain collagen stretches interacting with β_2-microglobulin in dialysis-related amyloidosis [20,273].

Unlike most of the peptides used in this work, STVIIE did not require nucleic acids to form amyloid [142]. But it was greatly affected in its folding behaviour by the presence of very low levels of oligo E (1:100 by charge, 1:3300 on a molecular level) in both the final conformation and the folding route taken to it. This emphasised the major effect that simple charge-charge interactions could have on the nucleation of amyloid fibres. This could potentially be exploited to influence the aggregation behaviour and potentially final conformations of a multitude of amyloidogenic polypeptides, as was shown before for the aggregation of Huntingtin polyglutamine tracts where short artificial oligonucleotides could prevent aggregation [195,196].

7.4. Peptide Aggregation Induced by Fatty Acids

The polymerised charges did not necessarily have to be covalently linked to each other, as it is the case for nucleic acids, heparan sulphate and collagen [20,163]. The surface of fatty acid vesicles also seemed to be an enhancer of amyloid formation as shown by ThT assays and by the presence of reflections compatible with the presence of amyloid structures in the fibre diffraction assays, highlighting the importance of cellular membranes on amyloid nucleation as previously described [112]. Stability of the polyanionic membrane surface might have been an important factor for $(KL)_3$ aggregation, as was suggested by the increased ThT signal for liposomes comprised of the longer oleic acid than palmitoleic and myristoleic acid liposomes, which would suggest increased liposome stability with increased hydrophobic chain length. Interactions of the aliphatic fatty acid tail with the peptide seemed less likely since hydrophobic interactions with the peptide would involve the hydrophobic leucine residues that would be expected to be buried within the β-sheet sandwich of an amyloid fibre [137,138]. However without more detailed studies of the structure of the products

of lipid-peptide interactions, the exact mechanism of formation may be difficult to establish. While the integrity of the membranes in this trial was not directly examined, the interactions of amyloid with cellular membranes has been scrutinized before, showing mainly deleterious effects like increased permeabilisation and pore formation [112,124,274]. This seemed to be mainly an effect of oligomeric amyloid precursors, but not mature fibres [107-112], which might fit with the loss of liposomes during the formation of complexes from $(KL)_3$ and fatty acid vesicles (see light microscopy images in Figure 6-20, Figure 6-21). It might be possible that the fatty acid membranes of the liposomes had a similar effect on the peptides used in these experiments as membranes on the aggregation of some amyloidogenic proteins have been shown to [22,112,174,175,177]. This might encourage the use of fatty acid liposomes as model membranes instead of the more difficult to prepare phospholipid membranes when only the polyanionic nature of the surface is of interest. Also, fatty acid membranes are of particular interest as model membranes for protocells during very early evolution of life [210,243,275-278].

The acceleration of fatty acid vesicle formation by Montmorillonite clay as shown by Hanczyc *et al.* followed a saturation curve [210]. This differed from the behaviour of the peptide-fatty acid mixtures shown in Figure 6-19 where a peak in turbidity quickly developed before disappearing. This would suggest that liposome formation was not the only process occurring; it might be accompanied by the generation of fibrous and/ or amorphous aggregates that registered in the light scattering assay (see also Figure 6-20 and Figure 6-21). This might have included amyloid formation by the positively charged $(KL)_3$ (as suggested by the Thioflavin T assay; Figure 6-22), but the peptide also seemed to disintegrate liposome membranes in the process. This might be a cause for the

reduction in turbidity over time (see Figure 6-19) and the lower numbers of liposomes visible by light microscopy (see Figure 6-20 and Figure 6-21). Importantly, the light microscopy samples consisted of liposome solutions to which the peptide was added, so the peptide could not interfere with liposome assembly. Both $(KL)_3$ and $(HL)_3$ seemed to tear the fragile membranes apart, a behaviour that might be similar to amyloidogenic peptides and proteins that interfered with membrane function [112,240]. Unlike the sometimes specific interactions between peptide and membrane, for example Aβ with membranes, the interactions between $(KL)_3$ and fatty acid (membranes) were probably based on charge interactions (similar to $(KL)_3$-nucleic acid interactions). This again would be similar to the mechanism Hanczyc *et al.* suggested for the montmorillonite-fatty acid interactions: High charge density on the clay and associated counterions were the main driving factors for liposome formation and growth from fatty acid micelle solutions [210]. This mechanism might also apply for initial $(KL)_3$-fatty acid interactions. The formation of amorphous aggregates in $(HL)_3$-fatty acid mixtures and the lack of evidence for $(EL)_3$ influencing liposome formation might further support charge interactions as primary drivers of complex formation; $(HL)_3$ had a calculated +0.5 net charge, and $(EL)_3$ a calculated -3 net charge (see Table 6-1). On the other hand, the side chain properties of lysine, histidine and glutamic acid would vary considerably [201], so that a pure charge-caused effect could not be proven here.

7.5. Peptide-Nucleic Acid Interactions

$(KL)_5$ showed a reduction of PicoGreen fluorescence with the hybridising oligo E and F (see Figure 6-34), and seemed to reduce the amount of hybridised oligonucleotide associated with the BIAcore chip surface (see Figure 6-37). This suggested that this peptide might be able to denature DNA. On the other hand, $(HL)_3$ showed no influence

on hybridisation of oligo E and oligo F to each other on the BIAcore (see Figure 6-38), and $(HL)_3$ and TVQFHMH seemed to support and enhance hybridisation (see Figure 6-42, Figure 6-43, Figure 6-44, and Figure 6-46). It might be possible that of the examined peptides only $(KL)_5$ influenced nucleic acid structure negatively, but more work would need to be done on all the peptides in order to get a general idea about what properties (side chain identity, pH, salt type and concentration etc.) might influence this behaviour.

With regard to the enhancement of hybridisation by $(HL)_3$ and TVQFHMH, it might be possible that they acted similar to polyamines such as spermine and spermidine [279]. The binding of µM amounts of spermidine induced the condensation of DNA into toroidal structures of about 80 nm diameter with an internal opening of about 30 nm [280]. No such structures were seen during the recording of electron microscopy images of peptide-ST DNA complexes (see Figure 6-9 for $(HL)_3$-ST DNA and $(HL)_5$-ST DNA, Figure 6-10 for $(KL)_3$-PA RNA and $(KL)_4$-PA RNA, and Figure 6-11 and Figure 6-12 for TVQFHMH-ST DNA and TVQFHMH alone). Additionally, this image was taken in a buffer containing 150 mM NaCl, where interactions similar to spermine/spermidine-DNA complexes would be weakened [281,282].

DNA was found to maintain B-conformation in the presence of spermine or spermidine [281], although binding of spermidine to DNA could induce conformational transition of poly(dG-me5dC) from B-DNA to Z-DNA under low ionic strength conditions [283]. For condensation of DNA a minimum of 3 positive charges on the amine seemed to be required [279,284], in competition to monovalent and divalent cations [284]. This agreed with a weakening of the spermine-DNA interactions that were abolished above certain ionic strength thresholds ([279,285]), and about 100 mM Na+ have been found

to inhibit DNA condensation independent of spermidine [285]. A higher concentration of Na+ was present in the 150 mM NaCl-containing buffers often used in the experiments presented here.

An alternative mechanism for the enhancement of hybridisation by $(HL)_3$ and TVQFHMH is based on the concentration of the probe oligonucleotides on the surface of positively charged ANA complexes such that hybridisation was promoted at concentrations below the solution K_d. This hypothesis is supported by a number of observations: Firstly, confocal microscopy showed intimate association of peptides and nucleic acids in ANA complexes. In these complexes, excess charges on the surface of the fibres would likely associate with and concentrate free oligonucleotides. Secondly, assays carried out with ANA complexes under NaCl concentrations (150mM) that saturated hybridisation in solution still showed strong promotion of hybridisation (see Figure 6-40). This would suggest that the peptides were not merely required to neutralise the phosphate backbone charge to promote hybridisation as this function was already likely to be provided by Na^+ ions. Instead the effect was more likely to result from the ability of the peptides or ANA complex to concentrate the DNA probes. Thirdly, oligonucleotides as well as longer dsDNA were shown to promote the formation of Congo Red-binding aggregates from $(KL)_5$ (see Figure 6-7), suggesting that the interactions of both short and long DNA with peptides generate amyloid structures. Fourthly, the enhancement of hybridisation on surfaces has been described and exploited for hybridisation microarrays before [254,286]. Dextran-poly-L-lysine block co-polymer conjugates have been suggested to promote hybridisation by increasing local DNA concentrations and increasing the nucleation of hybridisation [287]. The enhancement was thought to occur by restricting oligonucleotides on a 2-dimensional surface instead of in a 3-dimensional

volume. The ANA fibres might take this a step even further by providing a 1-dimensional 'search channel' for associated probes to find their respective binding partners (see Figure 7-1).

Contrary to $(HL)_3$ and TVQFHMH, $(KL)_5$ showed some hints that it was able to denature nucleic acids in the PicoGreen assay (see Figure 6-34). It was not clear if the signal was due to the peptide interfering with PicoGreen fluorescence or whether the peptide denatured nucleic acids. BIAcore analysis revealed that $(KL)_5$ seemed to be able to denature DNA (see Figure 6-37). It might be possible that the denaturation of DNA was dependent on the charge density of the peptide since $(HL)_3$ seemed to promote nucleic acid hybridisation (see Figure 6-38, Figure 6-41, Figure 6-44, and Figure 6-46). Further studies will be required to gain insight into the mechanism by which charge-based peptide/ complexes to interfere with or enhance hybridisation.

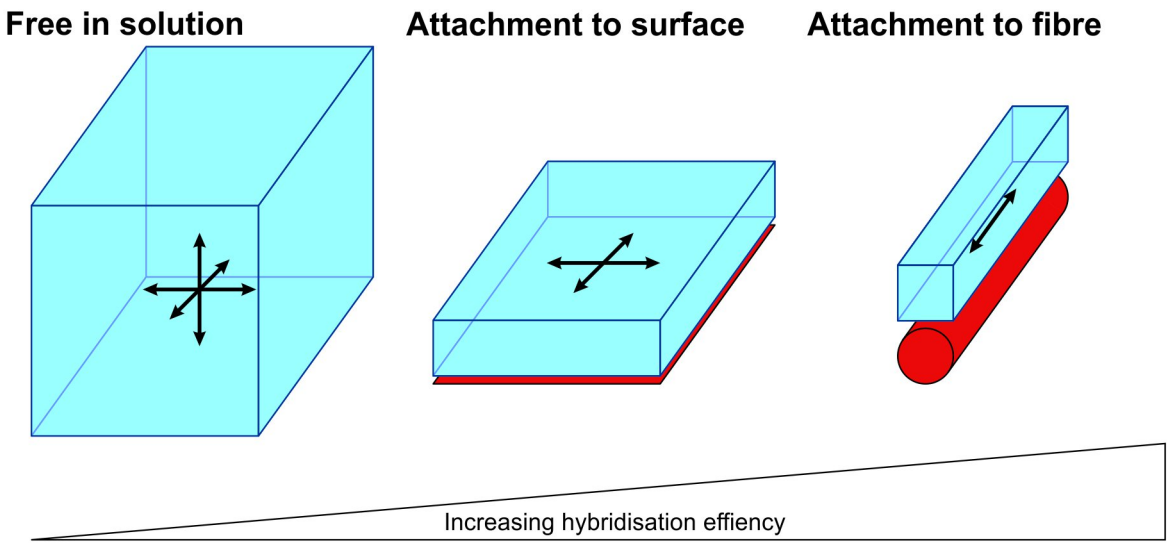

Figure 7-1: Enhancement of hybridisation by limitation of search space. Oligonucleotides floating free in solution would have to search in 3 dimensions to find binding partners. The association to a surface (red plane) would reduce that to a 2-dimensional search in a smaller volume. Oligonucleotides associated with an ANA fibre (red cylinder) would have to search only in one dimension in an even more reduced volume, further increasing the hybridisation efficiency.

The promotion of hybridisation by amyloid fibrils might support the use of aptamers, 3-dimensionally folded RNA molecules, for therapeutic purposes [288-292]. It might be possible to generate aptamers that would be only active in the vicinity of an amyloid fibril because it promotes hybridisation and proper folding of the 3-dimensional structure. This could for example interfere with the formation of toxic oligomeric species and promote their incorporation into less harmful mature fibrils.

7.6. Applications for ANA Complexes

The stable and repetitive nature of amyloid fibres would make them an interesting target for biotechnological applications. The cross-β core structure could be decorated with functional domains. One application could be the immobilisation of enzymes for bioreactors, as shown before during the search for the inactivation mechanism of the Sup35 prion [27]. It would be independent of chemical immobilisation methods that often interfere with the activity of the enzymes attached. In the mentioned example the attached enzymes were still active catalysts, albeit with reduced activity depending on the substrate size. Optimisation could overcome this issue, for example by increasing the spacing between the enzyme domains by including peptides lacking those domains.

Most of the examined ANA complexes have proven surprisingly soluble apart from the aggregation-prone $(HL)_5$ (see Table 6-6). No phase separation was observed, so ANA complexes might help to keep the immobilised enzymes in solution and to prevent phase transition to an aggregated state and denaturation. The regular structure of the β-sheets in amyloid fibres has been used to construct light harvesting complexes via attached fluorophores [293,294]. Another potential use could be nanowires, either by decorating amyloid fibres with cytochrome c [183], by casting wires in hollow amyloid tubes [63] or by depositing metals on the fibres [295]. Binding partners like nucleic acids might provide triggers for a fast conversion from monomers into amyloid fibres.

ANA complexes could also be exploited as hydrogels due to their strong gel formation. A major research focus in this field is on fibres based on α-helical peptides in the form of coiled-coil structures [296,297]. Amyloid fibres nucleated and/ or supported by nucleic acids should in principle be able to provide the same functionality, but would be based on shorter peptides, reducing the costs of the assembly. Although amyloid fibres usually contain only a single polypeptide sequence mixed amyloids have been reported [298]. This in combination with decorating domains on the core structure would allow the creation of branches as engineered in SAF fibres [297]. Again, the attachment of full domains could give the fibres properties as needed, for example cell adhesion sites and signals [299].

8. REFERENCES

1. Chiti F, Dobson CM (2006) Protein misfolding, functional amyloid, and human disease. Annu Rev Biochem 75: 333-366.

2. Harrison RS, Sharpe PC, Singh Y, Fairlie DP (2007) Amyloid peptides and proteins in review. Rev Physiol Biochem Pharmacol 159: 1-77.

3. Knauer MF, Soreghan B, Burdick D, Kosmoski J, Glabe CG (1992) Intracellular accumulation and resistance to degradation of the Alzheimer amyloid A4/beta protein. Proceedings of the National Academy of Sciences of the United States of America 89: 7437-7441.

4. Giasson BI, Forman MS, Higuchi M, Golbe LI, Graves CL, *et al*. (2003) Initiation and synergistic fibrillization of tau and alpha-synuclein. Science 300: 636-640.

5. Lee VM, Goedert M, Trojanowski JQ (2001) Neurodegenerative tauopathies. Annu Rev Neurosci 24: 1121-1159.

6. Cherny D, Hoyer W, Subramaniam V, Jovin TM (2004) Double-stranded DNA Stimulates the Fibrillation of [alpha]-Synuclein in vitro and is Associated with the Mature Fibrils: An Electron Microscopy Study. J Mol Biol 344: 929-938.

7. Poirier MA, Li H, Macosko J, Cai S, Amzel M, *et al*. (2002) Huntingtin spheroids and protofibrils as precursors in polyglutamine fibrilization. The Journal of biological chemistry 277: 41032-41037.

8. Scherzinger E, Lurz R, Turmaine M, Mangiarini L, Hollenbach B, *et al*. (1997) Huntingtin-encoded polyglutamine expansions form amyloid-like protein aggregates in vitro and in vivo. Cell 90: 549-558.

9. Huang CC, Faber PW, Persichetti F, Mittal V, Vonsattel JP, *et al*. (1998) Amyloid formation by mutant huntingtin: threshold, progressivity and recruitment of normal polyglutamine proteins. Somatic cell and molecular genetics 24: 217-233.

10. Wille H, Bian W, McDonald M, Kendall A, Colby DW, *et al*. (2009) Natural and synthetic prion structure from X-ray fiber diffraction. Proc Natl Acad Sci U S A 106: 16990-16995.

11. Cobb NJ, Surewicz WK (2009) Prion diseases and their biochemical mechanisms. Biochemistry 48: 2574-2585.

12. Prusiner SB (1982) Novel proteinaceous infectious particles cause scrapie. Science 216: 136-144.

13. Prusiner SB (1991) Molecular biology of prion diseases. Science 252: 1515-1522.

14. Makarava N, Kovacs GG, Bocharova O, Savtchenko R, Alexeeva I, *et al*. (2010) Recombinant prion protein induces a new transmissible prion disease in wild-type animals. Acta Neuropathol 119: 177-187.

15. Legname G, Baskakov IV, Nguyen HO, Riesner D, Cohen FE, *et al*. (2004) Synthetic mammalian prions. Science 305: 673-676.

16. Supattapone S (2010) What Makes a Prion Infectious? Science 327: 1091-1092.

17. Deleault NR, Kascsak R, Geoghegan JC, Supattapone S (2010) Species-dependent differences in cofactor utilization for formation of the protease-resistant prion protein in vitro. Biochemistry 49: 3928-3934.

18. Geoghegan JC, Valdes PA, Orem NR, Deleault NR, Williamson RA, *et al*. (2007) Selective Incorporation of Polyanionic Molecules into Hamster Prions. Journal of Biological Chemistry 282: 36341-36353.

19. Li J, Browning S, Mahal SP, Oelschlegel AM, Weissmann C (2010) Darwinian evolution of prions in cell culture. Science 327: 869-872.

20. Relini A, Canale C, De Stefano S, Rolandi R, Giorgetti S, *et al*. (2006) Collagen plays an active role in the aggregation of beta2-microglobulin under physiopathological conditions of dialysis-related amyloidosis. J Biol Chem 281: 16521-16529.

21. Dupuis NF, Wu C, Shea J-E, Bowers MT (2011) The Amyloid Formation Mechanism in Human IAPP: Dimers Have Œ≤-Strand Monomer‚àíMonomer Interfaces. Journal of the American Chemical Society 133: 7240-7243.

22. Konno T, Oiki S, Morii T (2007) Synergistic action of polyanionic and non-polar cofactors in fibrillation of human islet amyloid polypeptide. FEBS Lett 581: 1635-1638.

23. Ivanova MI, Sievers SA, Sawaya MR, Wall JS, Eisenberg D (2009) Molecular basis for insulin fibril assembly. Proc Natl Acad Sci U S A.

24. Greenwald J, Riek R (2010) Biology of amyloid: structure, function, and regulation. Structure 18: 1244-1260.

25. Halfmann R, Jarosz DF, Jones SK, Chang A, Lancaster AK, *et al*. (2012) Prions are a common mechanism for phenotypic inheritance in wild yeasts. Nature 482: 363-368.

26. Wickner RB (1994) [URE3] as an altered URE2 protein: evidence for a prion analog in Saccharomyces cerevisiae. Science 264: 566-569.

27. Baxa U, Speransky V, Steven AC, Wickner RB (2002) Mechanism of inactivation on prion conversion of the Saccharomyces cerevisiae Ure2 protein. Proc Natl Acad Sci U S A 99: 5253-5260.

28. Shorter J, Lindquist S (2005) Prions as adaptive conduits of memory and inheritance. Nat Rev Genet 6: 435-450.

29. Tuite MF, Cox BS (2003) Propagation of yeast prions. Nat Rev Mol Cell Biol 4: 878-890.

30. Shorter J, Lindquist S (2008) Hsp104, Hsp70 and Hsp40 interplay regulates formation, growth and elimination of Sup35 prions. Embo J 27: 2712-2724.

31. Baxa U, Keller PW, Cheng N, Wall JS, Steven AC (2011) In Sup35p filaments (the [PSI+] prion), the globular C-terminal domains are widely offset from the amyloid fibril backbone. Molecular Microbiology 79: 523-532.

32. Coustou V, Deleu C, Saupe S, Begueret J (1997) The protein product of the het-s heterokaryon incompatibility gene of the fungus Podospora anserina behaves as a prion analog. Proceedings of the National Academy of Sciences of the United States of America 94: 9773-9778.

33. Maddelein ML, Dos Reis S, Duvezin-Caubet S, Coulary-Salin B, Saupe SJ (2002) Amyloid aggregates of the HET-s prion protein are infectious. Proc Natl Acad Sci U S A 99: 7402-7407.

34. Fowler DM, Koulov AV, Alory-Jost C, Marks MS, Balch WE, *et al*. (2006) Functional amyloid formation within mammalian tissue. PLoS Biol 4: e6.

35. Maji SK, Perrin MH, Sawaya MR, Jessberger S, Vadodaria K, *et al*. (2009) Functional amyloids as natural storage of peptide hormones in pituitary secretory granules. Science 325: 328-332.

36. Westermark P, Eriksson L, Engstrom U, Enestrom S, Sletten K (1997) Prolactin-derived amyloid in the aging pituitary gland. Am J Pathol 150: 67-73.

37. Wang X, Hammer ND, Chapman MR (2008) The molecular basis of functional bacterial amyloid polymerization and nucleation. The Journal of biological chemistry 283: 21530-21539.

38. Garcia MC, Lee JT, Ramsook CB, Alsteens D, Dufrene YF, *et al*. (2011) A role for amyloid in cell aggregation and biofilm formation. PLoS One 6: e17632.

39. Capstick DS, Jomaa A, Hanke C, Ortega J, Elliot MA (2011) Dual amyloid domains promote differential functioning of the chaplin proteins during Streptomyces aerial morphogenesis. Proceedings of the National Academy of Sciences of the United States of America.

40. Bartels T, Choi JG, Selkoe DJ (2011) alpha-Synuclein occurs physiologically as a helically folded tetramer that resists aggregation. Nature 477: 107-110.

41. Fandrich M, Fletcher MA, Dobson CM (2001) Amyloid fibrils from muscle myoglobin. Nature 410: 165-166.

42. Fandrich M, Zandomeneghi G, Krebs MR, Kittler M, Buder K, *et al*. (2006) Apomyoglobin reveals a random-nucleation mechanism in amyloid protofibril formation. Acta Histochem 108: 215-219.

43. Fandrich M, Forge V, Buder K, Kittler M, Dobson CM, *et al*. (2003) Myoglobin forms amyloid fibrils by association of unfolded polypeptide segments. Proc Natl Acad Sci U S A 100: 15463-15468.

44. Pertinhez TA, Bouchard M, Tomlinson EJ, Wain R, Ferguson SJ, *et al*. (2001) Amyloid fibril formation by a helical cytochrome. FEBS Lett 495: 184-186.

45. Jimenez JL, Guijarro JI, Orlova E, Zurdo J, Dobson CM, *et al*. (1999) Cryo-electron microscopy structure of an SH3 amyloid fibril and model of the molecular packing. Embo J 18: 815-821.

46. Relini A, Torrassa S, Rolandi R, Gliozzi A, Rosano C, *et al*. (2004) Monitoring the Process of HypF Fibrillization and Liposome Permeabilization by Protofibrils. Journal of Molecular Biology 338: 943-957.

47. Anfinsen CB (1973) Principles that govern the folding of protein chains. Science 181: 223-230.

48. Tenidis K, Waldner M, Bernhagen J, Fischle W, Bergmann M, *et al*. (2000) Identification of a penta- and hexapeptide of islet amyloid polypeptide (IAPP) with amyloidogenic and cytotoxic properties. J Mol Biol 295: 1055-1071.

49. Fraser PE, McLachlan DR, Surewicz WK, Mizzen CA, Snow AD, *et al*. (1994) Conformation and fibrillogenesis of Alzheimer A beta peptides with selected substitution of charged residues. J Mol Biol 244: 64-73.

50. Balbach JJ, Ishii Y, Antzutkin ON, Leapman RD, Rizzo NW, *et al*. (2000) Amyloid fibril formation by A beta 16-22, a seven-residue fragment of the Alzheimer's beta-amyloid peptide, and structural characterization by solid state NMR. Biochemistry 39: 13748-13759.

51. Tjernberg LO, Callaway DJ, Tjernberg A, Hahne S, Lilliehook C, *et al*. (1999) A molecular model of Alzheimer amyloid beta-peptide fibril formation. J Biol Chem 274: 12619-12625.

52. Sawaya MR, Sambashivan S, Nelson R, Ivanova MI, Sievers SA, *et al*. (2007) Atomic structures of amyloid cross-[bgr] spines reveal varied steric zippers. Nature 447: 453-457.

53. Hasegawa K, Ohhashi Y, Yamaguchi I, Takahashi N, Tsutsumi S, *et al*. (2003) Amyloidogenic synthetic peptides of beta2-microglobulin--a role of the disulfide bond. Biochem Biophys Res Commun 304: 101-106.

54. Gasset M, Baldwin MA, Lloyd DH, Gabriel JM, Holtzman DM, *et al*. (1992) Predicted alpha-helical regions of the prion protein when synthesized as peptides form amyloid. Proc Natl Acad Sci U S A 89: 10940-10944.

55. Nelson R, Sawaya MR, Balbirnie M, Madsen AO, Riekel C, *et al*. (2005) Structure of the cross-[beta] spine of amyloid-like fibrils. Nature 435: 773-778.

56. Inoue M, Konno T, Tainaka K, Nakata E, Yoshida HO, *et al*. (2012) Positional effects of phosphorylation on the stability and morphology of tau-related amyloid fibrils. Biochemistry 51: 1396-1406.

57. Gazit E (2005) Mechanisms of amyloid fibril self-assembly and inhibition. Model short peptides as a key research tool. Febs J 272: 5971-5978.

58. Balbirnie M, Grothe R, Eisenberg DS (2001) An amyloid-forming peptide from the yeast prion Sup35 reveals a dehydrated beta-sheet structure for amyloid. Proc Natl Acad Sci U S A 98: 2375-2380.

59. Colletier JP, Laganowsky A, Landau M, Zhao M, Soriaga AB, *et al*. (2011) Molecular basis for amyloid-beta polymorphism. Proc Natl Acad Sci U S A 108: 16938-16943.

60. Goux WJ, Kopplin L, Nguyen AD, Leak K, Rutkofsky M, *et al*. (2004) The formation of straight and twisted filaments from short tau peptides. J Biol Chem 279: 26868-26875.

61. el-Agnaf OM, Irvine GB (2002) Aggregation and neurotoxicity of alpha-synuclein and related peptides. Biochem Soc Trans 30: 559-565.

62. Bodles AM, Guthrie DJ, Greer B, Irvine GB (2001) Identification of the region of non-Abeta component (NAC) of Alzheimer's disease amyloid responsible for its aggregation and toxicity. J Neurochem 78: 384-395.

63. Reches M, Gazit E (2003) Casting metal nanowires within discrete self-assembled peptide nanotubes. Science 300: 625-627.

64. Andreola A, Bellotti V, Giorgetti S, Mangione P, Obici L, *et al*. (2003) Conformational switching and fibrillogenesis in the amyloidogenic fragment of apolipoprotein a-I. J Biol Chem 278: 2444-2451.

65. Inouye H, Kirschner DA (2003) X-ray fibre diffraction analysis of assemblies formed by prion-related peptides: Polymorphism of the heterodimer interface between PrPC and PrPSc. Fibre Diffraction Review 11: 102-112.

66. Virchow R (1854) Zur Celluslose-Frage. Virchows Arch 6: 415-426.

67. Sipe JD, Cohen AS (2000) Review: History of the Amyloid Fibril. Journal of Structural Biology 130: 88-98.

68. Missmahl HP, Hartwig M (1953) Polarisationsoptische Untersuchungen an der Amyloidsubstanz. Virchows Arch Path Anat 324: 489-508.

69. Vassar PS, Culling CF (1959) Fluorescent stains, with special reference to amyloid and connective tissues. Archives of pathology 68: 487-498.

70. Klunk WE, Pettegrew JW, Abraham DJ (1989) Quantitative evaluation of congo red binding to amyloid-like proteins with a beta-pleated sheet conformation. J Histochem Cytochem 37: 1273-1281.

71. Klunk WE, Jacob RF, Mason RP (1999) Quantifying amyloid beta-peptide (Abeta) aggregation using the Congo red-Abeta (CR-abeta) spectrophotometric assay. Analytical Biochemistry 266: 66-76.

72. Nilsson MR (2004) Techniques to study amyloid fibril formation in vitro. Methods 34: 151-160.

73. Puchtler H, Sweat F, Levine M (1962) ON THE BINDING OF CONGO RED BY AMYLOID. Journal of Histochemistry & Cytochemistry 10: 355-364.

74. LeVine H, 3rd (1999) Quantification of beta-sheet amyloid fibril structures with thioflavin T. Methods in enzymology 309: 274-284.

75. Krebs MR, Bromley EH, Donald AM (2005) The binding of thioflavin-T to amyloid fibrils: localisation and implications. J Struct Biol 149: 30-37.

76. Cohen AS, Calkins E (1959) Electron microscopic observations on a fibrous component in amyloid of diverse origins. Nature 183: 1202-1203.

77. Koscielska-Kasprzak K, Otlewski J (2003) Amyloid-forming peptides selected proteolytically from phage display library. Protein science : a publication of the Protein Society 12: 1675-1685.

78. Eanes ED, Glenner GG (1968) X-ray diffraction studies on amyloid filaments. J Histochem Cytochem 16: 673-677.

79. Sunde M, Serpell LC, Bartlam M, Fraser PE, Pepys MB, *et al*. (1997) Common core structure of amyloid fibrils by synchrotron X-ray diffraction. Journal of Molecular Biology 273: 729-739.

80. Westermark P, Benson MD, Buxbaum JN, Cohen AS, Frangione B, *et al*. (2005) Amyloid: toward terminology clarification. Report from the Nomenclature Committee of the International Society of Amyloidosis. Amyloid : the international journal of experimental and clinical investigation : the official journal of the International Society of Amyloidosis 12: 1-4.

81. Jarrett JT, Lansbury PT, Jr. (1993) Seeding "one-dimensional crystallization" of amyloid: a pathogenic mechanism in Alzheimer's disease and scrapie? Cell 73: 1055-1058.

82. Wetzel R (2006) Kinetics and thermodynamics of amyloid fibril assembly. Acc Chem Res 39: 671-679.

83. Harper JD, Lieber CM, Lansbury PT, Jr. (1997) Atomic force microscopic imaging of seeded fibril formation and fibril branching by the Alzheimer's disease amyloid-beta protein. Chem Biol 4: 951-959.

84. Harper JD, Lansbury PT, Jr. (1997) Models of amyloid seeding in Alzheimer's disease and scrapie: mechanistic truths and physiological consequences of the time-dependent solubility of amyloid proteins. Annu Rev Biochem 66: 385-407.

85. Kelly JW (2000) Mechanisms of amyloidogenesis. Nat Struct Biol 7: 824-826.

86. Dunstan DE, Hamilton-Brown P, Asimakis P, Ducker W, Bertolini J (2009) Shear flow promotes amyloid-{beta} fibrilization. Protein Eng Des Sel 22: 741-746.

87. Hill EK, Krebs B, Goodall DG, Howlett GJ, Dunstan DE (2006) Shear flow induces amyloid fibril formation. Biomacromolecules 7: 10-13.

88. Ferguson N, Berriman J, Petrovich M, Sharpe TD, Finch JT, *et al*. (2003) Rapid amyloid fiber formation from the fast-folding WW domain FBP28. Proc Natl Acad Sci U S A 100: 9814-9819.

89. Manno M, Craparo EF, Martorana V, Bulone D, San Biagio PL (2006) Kinetics of insulin aggregation: disentanglement of amyloid fibrillation from large-size cluster formation. Biophys J 90: 4585-4591.

90. Thakur AK, Jayaraman M, Mishra R, Thakur M, Chellgren VM, *et al*. (2009) Polyglutamine disruption of the huntingtin exon 1 N terminus triggers a complex aggregation mechanism. Nat Struct Mol Biol 16: 380-389.

91. Knowles TP, Waudby CA, Devlin GL, Cohen SI, Aguzzi A, *et al*. (2009) An analytical solution to the kinetics of breakable filament assembly. Science 326: 1533-1537.

92. Chiti F, Webster P, Taddei N, Clark A, Stefani M, *et al*. (1999) Designing conditions for in vitro formation of amyloid protofilaments and fibrils. Proc Natl Acad Sci U S A 96: 3590-3594.

93. Uversky VN, Fink AL (2004) Conformational constraints for amyloid fibrillation: the importance of being unfolded. Biochim Biophys Acta 1698: 131-153.

94. Bouchard M, Zurdo J, Nettleton EJ, Dobson CM, Robinson CV (2000) Formation of insulin amyloid fibrils followed by FTIR simultaneously with CD and electron microscopy. Protein Sci 9: 1960-1967.

95. Harper JD, Wong SS, Lieber CM, Lansbury PT (1997) Observation of metastable Abeta amyloid protofibrils by atomic force microscopy. Chem Biol 4: 119-125.

96. Harper JD, Wong SS, Lieber CM, Lansbury PT, Jr. (1999) Assembly of A beta amyloid protofibrils: an in vitro model for a possible early event in Alzheimer's disease. Biochemistry 38: 8972-8980.

97. Walsh DM, Hartley DM, Kusumoto Y, Fezoui Y, Condron MM, *et al*. (1999) Amyloid beta-protein fibrillogenesis. Structure and biological activity of protofibrillar intermediates. J Biol Chem 274: 25945-25952.

98. Walsh DM, Lomakin A, Benedek GB, Condron MM, Teplow DB (1997) Amyloid beta - Protein Fibrillogenesis. Detection of a Protofibrillar Intermediate. J Biol Chem 272: 22364-22372.

99. Jansen R, Dzwolak W, Winter R (2005) Amyloidogenic self-assembly of insulin aggregates probed by high resolution atomic force microscopy. Biophys J 88: 1344-1353.

100. Kad NM, Myers SL, Smith DP, Alastair Smith D, Radford SE, *et al*. (2003) Hierarchical Assembly of [beta]2-Microglobulin Amyloid In Vitro Revealed by Atomic Force Microscopy. Journal of Molecular Biology 330: 785-797.

101. Serpell LC, Berriman J, Jakes R, Goedert M, Crowther RA (2000) Fiber diffraction of synthetic alpha-synuclein filaments shows amyloid-like cross-beta conformation. Proc Natl Acad Sci U S A 97: 4897-4902.

102. Conway KA, Harper JD, Lansbury PT (2000) Fibrils Formed in Vitro from α-Synuclein and Two Mutant Forms Linked to Parkinson's Disease are Typical Amyloid†. Biochemistry 39: 2552-2563.

103. Pease LF, 3rd, Sorci M, Guha S, Tsai DH, Zachariah MR, *et al*. (2010) Probing the nucleus model for oligomer formation during insulin amyloid fibrillogenesis. Biophysical Journal 99: 3979-3985.

104. Esler WP, Stimson ER, Jennings JM, Vinters HV, Ghilardi JR, *et al*. (2000) Alzheimer's disease amyloid propagation by a template-dependent dock-lock mechanism. Biochemistry 39: 6288-6295.

105. Chernoff YO, Lindquist SL, Ono B, Inge-Vechtomov SG, Liebman SW (1995) Role of the chaperone protein Hsp104 in propagation of the yeast prion-like factor [psi+]. Science 268: 880-884.

106. Shorter J, Lindquist S (2004) Hsp104 catalyzes formation and elimination of self-replicating Sup35 prion conformers. Science 304: 1793-1797.

107. Caughey B, Lansbury PT (2003) Protofibrils, pores, fibrils, and neurodegeneration: separating the responsible protein aggregates from the innocent bystanders. Annu Rev Neurosci 26: 267-298.

108. Caughey B, Baron GS (2006) Prions and their partners in crime. Nature 443: 803-810.

109. Hardy J, Selkoe DJ (2002) The Amyloid Hypothesis of Alzheimer's Disease: Progress and Problems on the Road to Therapeutics. Science 297: 353-356.

110. Shankar GM, Li S, Mehta TH, Garcia-Munoz A, Shepardson NE, *et al*. (2008) Amyloid-[beta] protein dimers isolated directly from Alzheimer's brains impair synaptic plasticity and memory. Nat Med 14: 837-842.

111. Mc Donald JM, Savva GM, Brayne C, Welzel AT, Forster G, *et al*. (2010) The presence of sodium dodecyl sulphate-stable Aβ dimers is strongly associated with Alzheimer-type dementia. Brain 133: 1328-1341.

112. Relini A, Cavalleri O, Rolandi R, Gliozzi A (2009) The two-fold aspect of the interplay of amyloidogenic proteins with lipid membranes. Chem Phys Lipids 158: 1-9.

113. Kremer JJ, Pallitto MM, Sklansky DJ, Murphy RM (2000) Correlation of beta-amyloid aggregate size and hydrophobicity with decreased bilayer fluidity of model membranes. Biochemistry 39: 10309-10318.

114. Bokvist M, Lindstrom F, Watts A, Grobner G (2004) Two types of Alzheimer's beta-amyloid (1-40) peptide membrane interactions: aggregation preventing transmembrane anchoring versus accelerated surface fibril formation. J Mol Biol 335: 1039-1049.

115. McDonald KL, McDonnell J, Muntoni A, Henson JD, Hegi ME, *et al*. (2010) Presence of alternative lengthening of telomeres mechanism in patients with glioblastoma identifies a less aggressive tumor type with longer survival. J Neuropathol Exp Neurol 69: 729-736.

116. Arispe N, Pollard HB, Rojas E (1993) Giant multilevel cation channels formed by Alzheimer disease amyloid beta-protein [A beta P-(1-40)] in bilayer membranes. Proc Natl Acad Sci U S A 90: 10573-10577.

117. Arispe N, Rojas E, Pollard HB (1993) Alzheimer disease amyloid beta protein forms calcium channels in bilayer membranes: blockade by tromethamine and aluminum. Proc Natl Acad Sci U S A 90: 567-571.

118. Kawahara M, Kuroda Y (2000) Molecular mechanism of neurodegeneration induced by Alzheimer's [beta]-amyloid protein: channel formation and disruption of calcium homeostasis. Brain Research Bulletin 53: 389-397.

119. Choo-Smith LP, Garzon-Rodriguez W, Glabe CG, Surewicz WK (1997) Acceleration of amyloid fibril formation by specific binding of Abeta-(1-40) peptide to ganglioside-containing membrane vesicles. J Biol Chem 272: 22987-22990.

120. Yip CM, McLaurin J (2001) Amyloid-beta peptide assembly: a critical step in fibrillogenesis and membrane disruption. Biophys J 80: 1359-1371.

121. Lorenzo A, Razzaboni B, Weir GC, Yankner BA (1994) Pancreatic islet cell toxicity of amylin associated with type-2 diabetes mellitus. Nature 368: 756-760.

122. Janson J, Ashley RH, Harrison D, McIntyre S, Butler PC (1999) The mechanism of islet amyloid polypeptide toxicity is membrane disruption by intermediate-sized toxic amyloid particles. Diabetes 48: 491-498.

123. Green JD, Kreplak L, Goldsbury C, Li Blatter X, Stolz M, *et al*. (2004) Atomic force microscopy reveals defects within mica supported lipid bilayers induced by the amyloidogenic human amylin peptide. J Mol Biol 342: 877-887.

124. Volles MJ, Lansbury PT, Jr. (2002) Vesicle permeabilization by protofibrillar alpha-synuclein is sensitive to Parkinson's disease-linked mutations and occurs by a pore-like mechanism. Biochemistry 41: 4595-4602.

125. Volles MJ, Lee SJ, Rochet JC, Shtilerman MD, Ding TT, *et al*. (2001) Vesicle permeabilization by protofibrillar alpha-synuclein: implications for the pathogenesis and treatment of Parkinson's disease. Biochemistry 40: 7812-7819.

126. Aguzzi A, Calella AM (2009) Prions: protein aggregation and infectious diseases. Physiol Rev 89: 1105-1152.

127. Baglioni S, Casamenti F, Bucciantini M, Luheshi LM, Taddei N, *et al*. (2006) Prefibrillar amyloid aggregates could be generic toxins in higher organisms. J Neurosci 26: 8160-8167.

128. Bucciantini M, Calloni G, Chiti F, Formigli L, Nosi D, *et al*. (2004) Prefibrillar amyloid protein aggregates share common features of cytotoxicity. J Biol Chem 279: 31374-31382.

129. Bucciantini M, Giannoni E, Chiti F, Baroni F, Formigli L, *et al*. (2002) Inherent toxicity of aggregates implies a common mechanism for protein misfolding diseases. Nature 416: 507-511.

130. Fandrich M, Meinhardt J, Grigorieff N (2009) Structural polymorphism of Alzheimer Abeta and other amyloid fibrils. Prion 3: 89-93.

131. Krishnan R, Lindquist SL (2005) Structural insights into a yeast prion illuminate nucleation and strain diversity. Nature 435: 765-772.

132. Toyama BH, Kelly MJ, Gross JD, Weissman JS (2007) The structural basis of yeast prion strain variants. Nature 449: 233-237.

133. Makarava N, Baskakov IV (2008) The same primary structure of the prion protein yields two distinct self-propagating states. J Biol Chem 283: 15988-15996.

134. Jahn TR, Makin OS, Morris KL, Marshall KE, Tian P, *et al*. (2010) The common architecture of cross-beta amyloid. J Mol Biol 395: 717-727.

135. Nelson R, Eisenberg D (2006) Recent atomic models of amyloid fibril structure. Curr Opin Struct Biol 16: 260-265.

136. Richardson JS, Richardson DC (2002) Natural beta-sheet proteins use negative design to avoid edge-to-edge aggregation. Proc Natl Acad Sci U S A 99: 2754-2759.

137. Broome BM, Hecht MH (2000) Nature disfavors sequences of alternating polar and non-polar amino acids: implications for amyloidogenesis. J Mol Biol 296: 961-968.

138. Wang W, Hecht MH (2002) Rationally designed mutations convert de novo amyloid-like fibrils into monomeric beta-sheet proteins. Proc Natl Acad Sci U S A 99: 2760-2765.

139. Fandrich M, Dobson CM (2002) The behaviour of polyamino acids reveals an inverse side chain effect in amyloid structure formation. Embo J 21: 5682-5690.

140. Rose GD, Fleming PJ, Banavar JR, Maritan A (2006) A backbone-based theory of protein folding. Proc Natl Acad Sci U S A 103: 16623-16633.

141. Kammerer RA, Kostrewa D, Zurdo J, Detken A, Garcia-Echeverria C, *et al*. (2004) Exploring amyloid formation by a de novo design. Proc Natl Acad Sci U S A 101: 4435-4440.

142. Lopez De La Paz M, Goldie K, Zurdo J, Lacroix E, Dobson CM, *et al*. (2002) De novo designed peptide-based amyloid fibrils. Proc Natl Acad Sci U S A 99: 16052-16057.

143. Lopez de la Paz M, Serrano L (2004) Sequence determinants of amyloid fibril formation. Proc Natl Acad Sci U S A 101: 87-92.

144. West MW, Wang W, Patterson J, Mancias JD, Beasley JR, *et al*. (1999) De novo amyloid proteins from designed combinatorial libraries. Proc Natl Acad Sci U S A 96: 11211-11216.

145. Vendruscolo M, Dobson CM (2007) Chemical biology: More charges against aggregation. Nature 449: 555.

146. Maury CP (2009) Self-propagating beta-sheet polypeptide structures as prebiotic informational molecular entities: the amyloid world. Orig Life Evol Biosph 39: 141-150.

147. Hammarstrom P, Ali MM, Mishra R, Salagic B, Svensson S, *et al*. (2010) An Auto-Catalytic Surface for Conformational Replication of Amyloid Fibrils-Genesis of an Amyloid World? Origins of life and evolution of the biosphere : the journal of the International Society for the Study of the Origin of Life.

148. Milner-White EJ, Russell M (2008) Predicting the conformations of peptides and proteins in early evolution. Biology Direct 3: 3.

149. Gilbert W (1986) The RNA World. Nature 319: 618.

150. Robertson MP, Joyce GF (2010) The Origins of the RNA World. Cold Spring Harb Perspect Biol.

151. Dale T (2006) Protein and nucleic acid together: a mechanism for the emergence of biological selection. J Theor Biol 240: 337-342.

152. Braun S, Humphreys C, Fraser E, Brancale A, Bochtler M, *et al*. (2011) Amyloid-associated nucleic Acid hybridisation. PLoS One 6: e19125.

153. Braun S, Humphreys C, Dale T (2012) Evolutionary Routes from a prebiotic ANA-world. Communicative & Integrative Biology 5: 1-4.

154. Marshall KE, Morris KL, Charlton D, O'Reilly N, Lewis L, *et al*. (2011) Hydrophobic, aromatic, and electrostatic interactions play a central role in amyloid fibril formation and stability. Biochemistry 50: 2061-2071.

155. Claessen D, Rink R, de Jong W, Siebring J, de Vreugd P, *et al*. (2003) A novel class of secreted hydrophobic proteins is involved in aerial hyphae formation in Streptomyces coelicolor by forming amyloid-like fibrils. Genes Dev 17: 1714-1726.

156. de Groot NS, Sabate R, Ventura S (2009) Amyloids in bacterial inclusion bodies. Trends Biochem Sci 34: 408-416.

157. Cannon MJ, Williams AD, Wetzel R, Myszka DG (2004) Kinetic analysis of beta-amyloid fibril elongation. Anal Biochem 328: 67-75.

158. Carulla N, Caddy GL, Hall DR, Zurdo J, Gairi M, *et al*. (2005) Molecular recycling within amyloid fibrils. Nature 436: 554-558.

159. Cherny D, Hoyer W, Subramaniam V, Jovin TM (2004) Double-stranded DNA stimulates the fibrillation of alpha-synuclein in vitro and is associated with the mature fibrils: an electron microscopy study. J Mol Biol 344: 929-938.

160. Deleault NR, Lucassen RW, Supattapone S (2003) RNA molecules stimulate prion protein conversion. Nature 425: 717-720.

161. Ginsberg SD, Galvin JE, Chiu TS, Lee VM, Masliah E, *et al*. (1998) RNA sequestration to pathological lesions of neurodegenerative diseases. Acta neuropathologica 96: 487-494.

162. Nandi PK, Nicole JC (2004) Nucleic Acid and Prion Protein Interaction Produces Spherical Amyloids which can Function in vivo as Coats of Spongiform Encephalopathy Agent. J Mol Biol 344: 827-837.

163. Calamai M, Kumita JR, Mifsud J, Parrini C, Ramazzotti M, *et al*. (2006) Nature and significance of the interactions between amyloid fibrils and biological polyelectrolytes. Biochemistry 45: 12806-12815.

164. Castillo GM, Ngo C, Cummings J, Wight TN, Snow AD (1997) Perlecan binds to the beta-amyloid proteins (A beta) of Alzheimer's disease, accelerates A beta fibril formation, and maintains A beta fibril stability. J Neurochem 69: 2452-2465.

165. McLaurin J, Franklin T, Zhang X, Deng J, Fraser PE (1999) Interactions of Alzheimer amyloid-beta peptides with glycosaminoglycans effects on fibril nucleation and growth. Eur J Biochem 266: 1101-1110.

166. Goedert M, Jakes R, Spillantini MG, Hasegawa M, Smith MJ, *et al*. (1996) Assembly of microtubule-associated protein tau into Alzheimer-like filaments induced by sulphated glycosaminoglycans. Nature 383: 550-553.

167. Cohlberg JA, Li J, Uversky VN, Fink AL (2002) Heparin and other glycosaminoglycans stimulate the formation of amyloid fibrils from alpha-synuclein in vitro. Biochemistry 41: 1502-1511.

168. Yamaguchi I, Suda H, Tsuzuike N, Seto K, Seki M, *et al*. (2003) Glycosaminoglycan and proteoglycan inhibit the depolymerization of beta2-microglobulin amyloid fibrils in vitro. Kidney Int 64: 1080-1088.

169. Nandi PK, Leclerc E, Nicole JC, Takahashi M (2002) DNA-induced partial unfolding of prion protein leads to its polymerisation to amyloid. J Mol Biol 322: 153-161.

170. Cordeiro Y, Machado F, Juliano L, Juliano MA, Brentani RR, *et al*. (2001) DNA converts cellular prion protein into the beta-sheet conformation and inhibits prion peptide aggregation. J Biol Chem 276: 49400-49409.

171. Kampers T, Friedhoff P, Biernat J, Mandelkow EM, Mandelkow E (1996) RNA stimulates aggregation of microtubule-associated protein tau into Alzheimer-like paired helical filaments. FEBS Lett 399: 344-349.

172. Geoghegan JC, Valdes PA, Orem NR, Deleault NR, Williamson RA, *et al*. (2007) Selective incorporation of polyanionic molecules into hamster prions. J Biol Chem 282: 36341-36353.

173. Wang F, Wang X, Yuan CG, Ma J (2010) Generating a prion with bacterially expressed recombinant prion protein. Science 327: 1132-1135.

174. Wang F, Yang F, Hu Y, Wang X, Wang X, *et al*. (2007) Lipid Interaction Converts Prion Protein to a PrPSc-like Proteinase K-Resistant Conformation under Physiological Conditions,Ä†. Biochemistry 46: 7045-7053.

175. Wang F, Wang X, Yuan C-G, Ma J (2010) Generating a Prion with Bacterially Expressed Recombinant Prion Protein. Science 327: 1132-1135.

176. Deleault NR, Lucassen RW, Supattapone S (2003) RNA molecules stimulate prion protein conversion. Nature 425: 717-720.

177. Deleault NR, Harris BT, Rees JR, Supattapone S (2007) Formation of native prions from minimal components in vitro. Proceedings of the National Academy of Sciences 104: 9741-9746.

178. Ellis RJ, Minton AP (2003) Cell biology: join the crowd. Nature 425: 27-28.

179. Minton AP (2000) Implications of macromolecular crowding for protein assembly. Curr Opin Struct Biol 10: 34-39.

180. White DA, Buell AK, Knowles TP, Welland ME, Dobson CM (2010) Protein aggregation in crowded environments. Journal of the American Chemical Society 132: 5170-5175.

181. Koga T, Taguchi K, Kobuke Y, Kinoshita T, Higuchi M (2003) Structural regulation of a peptide-conjugated graft copolymer: a simple model for amyloid formation. Chemistry 9: 1146-1156.

182. Kawahara M, Kuroda Y, Arispe N, Rojas E (2000) Alzheimer's beta-amyloid, human islet amylin, and prion protein fragment evoke intracellular free calcium elevations by a common mechanism in a hypothalamic GnRH neuronal cell line. J Biol Chem 275: 14077-14083.

183. Baldwin AJ, Bader R, Christodoulou J, MacPhee CE, Dobson CM, *et al*. (2006) Cytochrome Display on Amyloid Fibrils. Journal of the American Chemical Society 128: 2162-2163.

184. Liu Y, Gotte G, Libonati M, Eisenberg D (2001) A domain-swapped RNase A dimer with implications for amyloid formation. Nat Struct Mol Biol 8: 211-214.

185. Findeis MA (2000) Approaches to discovery and characterization of inhibitors of amyloid beta-peptide polymerization. Biochim Biophys Acta 1502: 76-84.

186. Lendel C, Bolognesi B, Wahlstrom A, Dobson CM, Graslund A (2010) Detergent-like interaction of Congo red with the amyloid beta peptide. Biochemistry 49: 1358-1360.

187. Bard F, Cannon C, Barbour R, Burke RL, Games D, *et al*. (2000) Peripherally administered antibodies against amyloid beta-peptide enter the central nervous system and reduce pathology in a mouse model of Alzheimer disease. Nat Med 6: 916-919.

188. Wilcock DM, Rojiani A, Rosenthal A, Subbarao S, Freeman MJ, *et al*. (2004) Passive immunotherapy against Abeta in aged APP-transgenic mice reverses cognitive deficits and depletes parenchymal amyloid deposits in spite of increased vascular amyloid and microhemorrhage. J Neuroinflammation 1: 24.

189. Wilcock DM, Rojiani A, Rosenthal A, Levkowitz G, Subbarao S, *et al*. (2004) Passive amyloid immunotherapy clears amyloid and transiently activates microglia in a transgenic mouse model of amyloid deposition. J Neurosci 24: 6144-6151.

190. Magga J, Puli L, Pihlaja R, Kanninen K, Neulamaa S, *et al*. (2010) Human intravenous immunoglobulin provides protection against Abeta toxicity by multiple mechanisms in a mouse model of Alzheimer's disease. J Neuroinflammation 7: 90.

191. DeMattos RB, Bales KR, Cummins DJ, Dodart JC, Paul SM, *et al*. (2001) Peripheral anti-A beta antibody alters CNS and plasma A beta clearance and decreases brain A beta burden in a mouse model of Alzheimer's disease. Proc Natl Acad Sci U S A 98: 8850-8855.

192. Lobello K, Ryan JM, Liu E, Rippon G, Black R (2012) Targeting Beta amyloid: a clinical review of immunotherapeutic approaches in Alzheimer's disease. Int J Alzheimers Dis 2012: 628070.

193. Sun N, Funke SA, Willbold D (2012) A survey of peptides with effective therapeutic potential in Alzheimer's disease rodent models or in human clinical studies. Mini Rev Med Chem.

194. Funke SA, Willbold D (2012) Peptides for therapy and diagnosis of Alzheimer's disease. Curr Pharm Des 18: 755-767.

195. Skogen M, Roth J, Yerkes S, Parekh-Olmedo H, Kmiec E (2006) Short G-rich oligonucleotides as a potential therapeutic for Huntington's Disease. BMC Neurosci 7: 65.

196. Parekh-Olmedo H, Wang J, Gusella JF, Kmiec EB (2004) Modified single-stranded oligonucleotides inhibit aggregate formation and toxicity induced by expanded polyglutamine. J Mol Neurosci 24: 257-267.

197. Brazier SP, Ramesh B, Haris PI, Lee DC, Srai SK (1998) Secondary structure analysis of the putative membrane-associated domains of the inward rectifier K+ channel ROMK1. Biochem J 335 (Pt 2): 375-380.

198. Lewis RN, Prenner EJ, Kondejewski LH, Flach CR, Mendelsohn R, *et al*. (1999) Fourier transform infrared spectroscopic studies of the interaction of the antimicrobial peptide gramicidin S with lipid micelles and with lipid monolayer and bilayer membranes. Biochemistry 38: 15193-15203.

199. Tartaglia GG, Vendruscolo M (2008) The Zyggregator method for predicting protein aggregation propensities. Chem Soc Rev 37: 1395-1401.

200. Maurer-Stroh S, Debulpaep M, Kuemmerer N, Lopez de la Paz M, Martins IC, *et al*. (2010) Exploring the sequence determinants of amyloid structure using position-specific scoring matrices. Nat Methods 7: 237-242.

201. Voet D, Voet JG (2004) Biochemistry: John Wiley & Sons.

202. Abramoff MD, Magalhaes PJ, Ram SJ (2004) Image Processing with ImageJ. Biophotonics International 11: 36-42.

203. Rasband W (1997-2011) ImageJ. US National Institutes of Health, Bethesda, Maryland, USA.

204. Rasband WS (1997-2009) ImageJ. Bethesda: US National Institutes of Health.

205. Bian W, Wang H, McCullough I, Stubbs G (2006) WCEN: a computer program for initial processing of fiber diffraction patterns. Journal of Applied Crystallography 39: 752-756.

206. Makin OS, Serpell CS (2002) X-Ray Diffraction Studies of Amyloid Structure. Amyloid Proteins: Methods and Protocols: Springer. pp. 67-80.

207. Makin OS, Sikorski P, Serpell LC (2007) CLEARER: a new tool for the analysis of X-ray fibre diffraction patterns and diffraction simulation from atomic structural models. Journal of Applied Crystallography 40: 996-972.

208. Perrins RD, Orchard C, Zavodszky M, Kasry A, Nikolaev N, *et al*. (2011) Doing More with Less: A Method for Low Total Mass, Affinity Measurement Using Variable-Length Nanotethers. Analytical chemistry.

209. Perrins RD, Orchard C, Zavodszky M, Kasry A, Nikolaev N, *et al*. (2011) Doing more with less: a method for low total mass, affinity measurement using variable-length nanotethers. Anal Chem 83: 8900-8905.

210. Hanczyc MM, Fujikawa SM, Szostak JW (2003) Experimental Models of Primitive Cellular Compartments: Encapsulation, Growth, and Division. Science 302: 618-622.

211. Henin O, Barbier B, Brack A Simple polyanionic peptides as artificial PPases. Proceedings of the First International Meeting on Inorganic Pyrophosphatases.

212. Barbier B, Brack A (1992) Conformation-controlled hydrolysis of polyribonucleotides by sequential basic polypeptides. Journal of the American Chemical Society 114: 3511-3515.

213. Brack A, Barbier B (1990) Chemical activity of simple basic peptides. Orig Life Evol Biosph 20: 139-144.

214. Fried MG, Bloomfield VA (1984) DNA gelation in concentrated solutions. Biopolymers 23: 2141-2155.

215. Team RC (2012) R: A Language and Environment for Statistical Computing. Vienna, Austria: R Foundation for Statistical Computing.

216. Groenning M, Olsen L, van de Weert M, Flink JM, Frokjaer S, *et al*. (2007) Study on the binding of Thioflavin T to beta-sheet-rich and non-beta-sheet cavities. J Struct Biol 158: 358-369.

217. Kelenyi G (1967) On the histochemistry of azo group-free thiazole dyes. The journal of histochemistry and cytochemistry : official journal of the Histochemistry Society 15: 172-180.

218. Khurana R, Coleman C, Ionescu-Zanetti C, Carter SA, Krishna V, *et al*. (2005) Mechanism of thioflavin T binding to amyloid fibrils. Journal of Structural Biology 151: 229-238.

219. Ilanchelian M, Ramaraj R (2004) Emission of thioflavin T and its control in the presence of DNA. Journal of Photochemistry and Photobiology A: Chemistry 162: 129-137.

220. Nielsen L, Khurana R, Coats A, Frokjaer S, Brange J, *et al*. (2001) Effect of environmental factors on the kinetics of insulin fibril formation: elucidation of the molecular mechanism. Biochemistry 40: 6036-6046.

221. Khurana R, Uversky VN, Nielsen L, Fink AL (2001) Is Congo red an amyloid-specific dye? J Biol Chem 276: 22715-22721.

222. Schutz AK, Soragni A, Hornemann S, Aguzzi A, Ernst M, *et al*. (2011) The amyloid-Congo red interface at atomic resolution. Angew Chem Int Ed Engl 50: 5956-5960.

223. Biancalana M, Koide S (2010) Molecular mechanism of Thioflavin-T binding to amyloid fibrils. Biochim Biophys Acta 1804: 1405-1412.

224. Montoliu L, Bock CT, Schutz G, Zentgraf H (1995) Visualization of large DNA molecules by electron microscopy with polyamines: application to the analysis of yeast endogenous and artificial chromosomes. J Mol Biol 246: 486-492.

225. Younghusband HB, Inman RB (1974) The electronmicroscopy of DNA. Annu Rev Biochem 43: 605-619.

226. Griffith JD, Christiansen G (1978) Electron microscope visualization of chromatin and other DNA-protein complexes. Annu Rev Biophys Bioeng 7: 19-35.

227. Stoeckenius W (1961) ELECTRON MICROSCOPY OF DNA MOLECULES "STAINED" WITH HEAVY METAL SALTS. The Journal of Biophysical and Biochemical Cytology 11: 297-310.

228. Vollenweider HJ, Sogo JM, Koller T (1975) A routine method for protein-free spreading of double- and single-stranded nucleic acid molecules. Proceedings of the National Academy of Sciences of the United States of America 72: 83-87.

229. Rich A, Nordheim A, Wang AH (1984) The chemistry and biology of left-handed Z-DNA. Annu Rev Biochem 53: 791-846.

230. Blake C, Serpell L (1996) Synchrotron X-ray studies suggest that the core of the transthyretin amyloid fibril is a continuous beta-sheet helix. Structure 4: 989-998.

231. Makin OS, Atkins E, Sikorski P, Johansson J, Serpell LC (2005) Molecular basis for amyloid fibril formation and stability. Proc Natl Acad Sci U S A 102: 315-320.

232. Sunde M, Blake CCF (1998) From the globular to the fibrous state: protein structure and structural conversion in amyloid formation. Quarterly Reviews of Biophysics 31: 1-39.

233. Arnott S (2006) Historical article: DNA polymorphism and the early history of the double helix. Trends in Biochemical Sciences 31: 349-354.

234. Wing R, Drew H, Takano T, Broka C, Tanaka S, *et al*. (1980) Crystal structure analysis of a complete turn of B-DNA. Nature 287: 755-758.

235. Perutz MF, Finch JT, Berriman J, Lesk A (2002) Amyloid fibers are water-filled nanotubes. Proc Natl Acad Sci U S A 99: 5591-5595.

236. Wetzel R (2002) Ideas of Order for Amyloid Fibril Structure. Structure 10: 1031-1036.

237. Wasmer C, Lange A, Van Melckebeke H, Siemer AB, Riek R, *et al*. (2008) Amyloid fibrils of the HET-s(218-289) prion form a beta solenoid with a triangular hydrophobic core. Science 319: 1523-1526.

238. Kishimoto A, Hasegawa K, Suzuki H, Taguchi H, Namba K, *et al*. (2004) beta-Helix is a likely core structure of yeast prion Sup35 amyloid fibers. Biochem Biophys Res Commun 315: 739-745.

239. Kajava AV, Cheng N, Cleaver R, Kessel M, Simon MN, *et al*. (2001) Beta-helix model for the filamentous haemagglutinin adhesin of Bordetella pertussis and related bacterial secretory proteins. Mol Microbiol 42: 279-292.

240. McLaurin J, Chakrabartty A (1996) Membrane disruption by Alzheimer beta-amyloid peptides mediated through specific binding to either phospholipids or gangliosides. Implications for neurotoxicity. J Biol Chem 271: 26482-26489.

241. Hargreaves WR, Deamer DW (1978) Liposomes from ionic, single-chain amphiphiles. Biochemistry 17: 3759-3768.

242. Blochliger E, Blocher M, Walde P, Luisi PL (1998) Matrix Effect in the Size Distribution of Fatty Acid Vesicles. The Journal of Physical Chemistry B 102: 10383-10390.

243. Zhu TF, Szostak JW (2009) Coupled growth and division of model protocell membranes. J Am Chem Soc 131: 5705-5713.

244. Manno M, Craparo EF, Podesta A, Bulone D, Carrotta R, *et al*. (2007) Kinetics of different processes in human insulin amyloid formation. J Mol Biol 366: 258-274.

245. Lindgren M, Hallbrink M, Prochiantz A, Langel U (2000) Cell-penetrating peptides. Trends Pharmacol Sci 21: 99-103.

246. Greenfield NJ, Fasman GD (1969) Computed circular dichroism spectra for the evaluation of protein conformation. Biochemistry 8: 4108-4116.

247. Greenfield NJ (2006) Using circular dichroism spectra to estimate protein secondary structure. Nature protocols 1: 2876-2890.

248. Venyaminov S, Baikalov IA, Shen ZM, Wu CS, Yang JT (1993) Circular dichroic analysis of denatured proteins: inclusion of denatured proteins in the reference set. Analytical Biochemistry 214: 17-24.

249. Condon EU (1937) Theories of Optical Rotatory Power. Reviews of Modern Physics 9: 432.

250. Singer VL, Jones LJ, Yue ST, Haugland RP (1997) Characterization of PicoGreen reagent and development of a fluorescence-based solution assay for double-stranded DNA quantitation. Anal Biochem 249: 228-238.

251. Cosa G, Vinette AL, McLean JR, Scaiano JC (2002) DNA damage detection technique applying time-resolved fluorescence measurements. Anal Chem 74: 6163-6169.

252. Cosa G, Focsaneanu KS, McLean JR, McNamee JP, Scaiano JC (2001) Photophysical properties of fluorescent DNA-dyes bound to single- and double-stranded DNA in aqueous buffered solution. Photochem Photobiol 73: 585-599.

253. Alwine JC, Kemp DJ, Stark GR (1977) Method for detection of specific RNAs in agarose gels by transfer to diazobenzyloxymethyl-paper and hybridization with DNA probes. Proceedings of the National Academy of Sciences of the United States of America 74: 5350-5354.

254. Maskos U, Southern EM (1993) A study of oligonucleotide reassociation using large arrays of oligonucleotides synthesised on a glass support. Nucleic Acids Res 21: 4663-4669.

255. Lemieux B, Aharoni A, Schena M (1998) Overview of DNA chip technology. Molecular Breeding 4: 277-289.

256. Zipper H, Brunner H, Bernhagen J, Vitzthum F (2004) Investigations on DNA intercalation and surface binding by SYBR Green I, its structure determination and methodological implications. Nucleic Acids Res 32: e103.

257. Nieba L, Nieba-Axmann SE, Persson A, Hamalainen M, Edebratt F, *et al*. (1997) BIACORE analysis of histidine-tagged proteins using a chelating NTA sensor chip. Anal Biochem 252: 217-228.

258. Jensen KK, Orum H, Nielsen PE, Norden B (1997) Kinetics for hybridization of peptide nucleic acids (PNA) with DNA and RNA studied with the BIAcore technique. Biochemistry 36: 5072-5077.

259. Wood SJ (1993) DNA-DNA Hybridization in Real Time Using BIAcore. Microchemical Journal 47: 330-337.

260. Nilsson P, Persson B, Uhlen M, Nygren PA (1995) Real-time monitoring of DNA manipulations using biosensor technology. Analytical Biochemistry 224: 400-408.

261. Gotoh M, Hasegawa Y, Shinohara Y, Shimizu M, Tosu M (1995) A new approach to determine the effect of mismatches on kinetic parameters in DNA hybridization using an optical biosensor. DNA research : an international journal for rapid publication of reports on genes and genomes 2: 285-293.

262. Ryu J, Joung HA, Kim MG, Park CB (2008) Surface plasmon resonance analysis of Alzheimer's beta-amyloid aggregation on a solid surface: from monomers to fully-grown fibrils. Anal Chem 80: 2400-2407.

263. Jelesarov I, Dürr E, Thomas RM, Bosshard HR (1998) Salt Effects on Hydrophobic Interaction and Charge Screening in the Folding of a Negatively Charged Peptide to a Coiled Coil (Leucine Zipper)†. Biochemistry 37: 7539-7550.

264. Smith AM, Scquah SFA, Bone N, Kroto HW, Ryadnov MG, *et al*. (2005) Polar Assembly in a Designed Protein Fiber. Angew Chem Int Ed Engl 44: 325-238.

265. Yoffe AM, Prinsen P, Gopal A, Knobler CM, Gelbart WM, *et al*. (2008) Predicting the sizes of large RNA molecules. Proc Natl Acad Sci U S A 105: 16153-16158.

266. Abels JA, Moreno-Herrero F, van der Heijden T, Dekker C, Dekker NH (2005) Single-molecule measurements of the persistence length of double-stranded RNA. Biophys J 88: 2737-2744.

267. Krebs MRH, MacPhee CE, Miller AFM, Dunlop IED, Dobson CM, *et al*. (2004) The formation of spherulites by amyloid fibrils of bovine insulin. Proceedings of the National Academy of Sciences of the United States of America 101: 14420-14424.

268. MacPhee CE, Dobson CM (2000) Formation of Mixed Fibrils Demonstrates the Generic Nature and Potential Utility of Amyloid Nanostructures. J Am Chem Soc 122: 12707-12713.

269. Kim W, Hecht MH (2006) Generic hydrophobic residues are sufficient to promote aggregation of the Alzheimer's Abeta42 peptide. Proc Natl Acad Sci U S A 103: 15824-15829.

270. Yoder MD, Keen NT, Jurnak F (1993) New domain motif: the structure of pectate lyase C, a secreted plant virulence factor. Science 260: 1503-1507.

271. Steinbacher S, Baxa U, Miller S, Weintraub A, Seckler R, *et al*. (1996) Crystal structure of phage P22 tailspike protein complexed with Salmonella sp. O-antigen receptors. Proc Natl Acad Sci U S A 93: 10584-10588.

272. Inouye H, Fraser PE, Kirschner DA (1993) Structure of beta-crystallite assemblies formed by Alzheimer beta-amyloid protein analogues: analysis by x-ray diffraction. Biophysical Journal 64: 502-519.

273. Giorgetti S, Rossi A, Mangione P, Raimondi S, Marini S, *et al*. (2005) {beta}2-Microglobulin isoforms display an heterogeneous affinity for type I collagen. Protein Science 14: 696-702.

274. Lin H, Bhatia R, Lal R (2001) Amyloid beta protein forms ion channels: implications for Alzheimer's disease pathophysiology. Faseb J 15: 2433-2444.

275. Schrum JP, Zhu TF, Szostak JW (2010) The origins of cellular life. Cold Spring Harb Perspect Biol 2: a002212.

276. Mansy SS, Szostak JW (2008) Thermostability of model protocell membranes. Proc Natl Acad Sci U S A 105: 13351-13355.

277. Chen IA, Salehi-Ashtiani K, Szostak JW (2005) RNA catalysis in model protocell vesicles. J Am Chem Soc 127: 13213-13219.

278. Szostak JW, Bartel DP, Luisi PL (2001) Synthesizing life. Nature 409: 387-390.

279. Bloomfield VA (1997) DNA condensation by multivalent cations. Biopolymers 44: 269-282.

280. Gosule LC, Schellman JA (1976) Compact form of DNA induced by spermidine. Nature 259: 333-335.

281. Gosule LC, Schellman JA (1978) DNA condensation with polyamines I. Spectroscopic studies. J Mol Biol 121: 311-326.

282. Chattoraj DK, Gosule LC, Schellman A (1978) DNA condensation with polyamines. II. Electron microscopic studies. J Mol Biol 121: 327-337.

283. Vertino PM, Bergeron RJ, Cavanaugh PF, Jr., Porter CW (1987) Structural determinants of spermidine-DNA interactions. Biopolymers 26: 691-703.

284. Widom J, Baldwin RL (1980) Cation-induced toroidal condensation of DNA studies with Co3+(NH3)6. J Mol Biol 144: 431-453.

285. Pelta J, Jr., Durand D, Doucet J, Livolant F (1996) DNA mesophases induced by spermidine: structural properties and biological implications. Biophys J 71: 48-63.

286. Chan V, Graves DJ, McKenzie SE (1995) The biophysics of DNA hybridization with immobilized oligonucleotide probes. Biophysical Journal 69: 2243-2255.

287. Wu L, Shimada N, Kano A, Maruyama A (2008) Poly(l-lysine)-graft-dextran copolymer accelerates DNA hybridization by two orders. Soft Matter 4: 744-747.

288. Ylera F, Lurz R, Erdmann VA, F¸rste JP (2002) Selection of RNA Aptamers to the Alzheimer's Disease Amyloid Peptide. Biochem Biophys Res Commun 290: 1583-1588.

289. Zhou J, Li H, Li S, Zaia J, Rossi JJ (2008) Novel dual inhibitory function aptamer-siRNA delivery system for HIV-1 therapy. Mol Ther 16: 1481-1489.

290. McNamara JO, 2nd, Andrechek ER, Wang Y, Viles KD, Rempel RE, *et al*. (2006) Cell type-specific delivery of siRNAs with aptamer-siRNA chimeras. Nat Biotechnol 24: 1005-1015.

291. Stoltenburg R, Reinemann C, Strehlitz B (2007) SELEX--a (r)evolutionary method to generate high-affinity nucleic acid ligands. Biomol Eng 24: 381-403.

292. Uphoff KW, Bell SD, Ellington AD (1996) In vitro selection of aptamers: the dearth of pure reason. Curr Opin Struct Biol 6: 281-288.

293. Channon KJ, Devlin GL, MacPhee CE (2009) Efficient energy transfer within self-assembling peptide fibers: a route to light-harvesting nanomaterials. J Am Chem Soc 131: 12520-12521.

294. Channon KJ, Devlin GL, Magennis SW, Finlayson CE, Tickler AK, *et al*. (2008) Modification of fluorophore photophysics through peptide-driven self-assembly. J Am Chem Soc 130: 5487-5491.

295. Scheibel T, Parthasarathy R, Sawicki G, Lin XM, Jaeger H, *et al*. (2003) Conducting nanowires built by controlled self-assembly of amyloid fibers and selective metal deposition. Proc Natl Acad Sci U S A 100: 4527-4532.

296. Gribbon C, Channon KJ, Zhang W, Banwell EF, Bromley EH, *et al*. (2008) MagicWand: a single, designed peptide that assembles to stable, ordered alpha-helical fibers. Biochemistry 47: 10365-10371.

297. Woolfson DN, Ryadnov MG (2006) Peptide-based fibrous biomaterials: Some things old, new and borrowed. Curr Opin Chem Biol 10: 559-567.

298. MacPhee CE, Woolfson DN (2004) Engineered and designed peptide-based fibrous biomaterials. Current Opinion in Solid State and Materials Science 8: 141-149.

299. Gras SL, Tickler AK, Squires AM, Devlin GL, Horton MA, *et al*. (2008) Functionalised amyloid fibrils for roles in cell adhesion. Biomaterials 29: 1553-1562.

300. Joyce GF (2002) The antiquity of RNA-based evolution. Nature 418: 214-221.

301. Wolf YI, Koonin EV (2007) On the origin of the translation system and the genetic code in the RNA world by means of natural selection, exaptation, and subfunctionalization. Biology Direct 2.

302. Szathm·ry Er (1999) The origin of the genetic code: amino acids as cofactors in an RNA world. Trends in Genetics 15: 223-229.

303. Alberti S (1997) The Origin of the Genetic Code and Protein Synthesis. Journal of Molecular Evolution 45: 352-358.

304. Franchi M, Ferris JP, Gallori E (2003) Cations as Mediators of the Adsorption of Nucleic Acids on Clay Surfaces in Prebiotic Environments. Origins of Life and Evolution of Biospheres 33: 1-16.

305. Ertem G, Ferris JP (1998) Formation of RNA Oligomers on Montmorillonite: Site of Catalysis. Origins of Life and Evolution of Biospheres 28: 485-499.

306. Ferris JP, Ertem G (1992) Oligomerization of ribonucleotides on montmorillonite: reaction of the 5'-phosphorimidazolide of adenosine. Science 257: 1387-1389.

307. Ferris JP, Hill AR, Jr., Liu R, Orgel LE (1996) Synthesis of long prebiotic oligomers on mineral surfaces. Nature 381: 59-61.

308. Lincoln TA, Joyce GF (2009) Self-sustained replication of an RNA enzyme. Science 323: 1229-1232.

309. McGinness KE, Joyce GF (2002) RNA-catalyzed RNA ligation on an external RNA template. Chem Biol 9: 297-307.

310. Wochner A, Attwater J, Coulson A, Holliger P (2011) Ribozyme-catalyzed transcription of an active ribozyme. Science 332: 209-212.

311. Ellington AD, Szostak JW (1990) In vitro selection of RNA molecules that bind specific ligands. Nature 346: 818-822.

312. Ellington AD, Szostak JW (1992) Selection in vitro of single-stranded DNA molecules that fold into specific ligand-binding structures. Nature 355: 850-852.

313. Tuerk C, Gold L (1990) Systematic evolution of ligands by exponential enrichment: RNA ligands to bacteriophage T4 DNA polymerase. Science 249: 505-510.

314. Zhang B, Cech TR (1997) Peptide bond formation by in vitro selected ribozymes. Nature 390: 96-100.

315. Ryadnov MG, Woolfson DN (2007) Self-assembled templates for polypeptide synthesis. J Am Chem Soc 129: 14074-14081.

316. Turk RM, Chumachenko NV, Yarus M (2010) Multiple translational products from a five-nucleotide ribozyme. Proceedings of the National Academy of Sciences of the United States of America 107: 4585-4589.

317. Chen IA, Roberts RW, Szostak JW (2004) The emergence of competition between model protocells. Science 305: 1474-1476.

9. APPENDIX

9.1. CONGO RED ABSORBANCE ASSAY NORMALISATION

To test the Congo Red absorbance assay independent of the plate reader and to test normalisation methods of the samples containing 1 mM TVQFHMH, 1 mM salmon testes DNA, 20 mM HEPES pH 7.0 and 500 µM Congo Red were incubated for 30 minutes before the first recording of the absorbance spectra on a NanoDrop ND-1000. They were kept at room temperature for 2 days before the repeat measurement was carried out. The higher Congo Red concentrations used when compared to the plate reader assay were necessary to generate a sufficient absorbance signal.

The raw spectra showed great variation in absorbance levels based on different levels of aggregation that kept material outside the light path (see Supplementary Figure 1 A and Supplementary Figure 2 A). This was a general problem with this assay and was encountered previously [72,186]. Several options for normalisation were explored, limited by the available filters on the plate reader. Also, the spectra generally undergo some shape changes, leading to a shift in the absorbance maxima of the amyloid peak around 540 nm. A normalisation to 403 nm, a potential isosbestic point [71], created the biggest changes in the spectra (see Supplementary Figure 1 C and Supplementary Figure 2 C), while the normalisation to the Congo Red absorbance peak at 487 nm had a much smaller effect (see Supplementary Figure 1 B). The normalisation to 450 and 485 nm chosen for the plate reader was intermediate (see Supplementary Figure 1 D and Supplementary Figure 2 D).

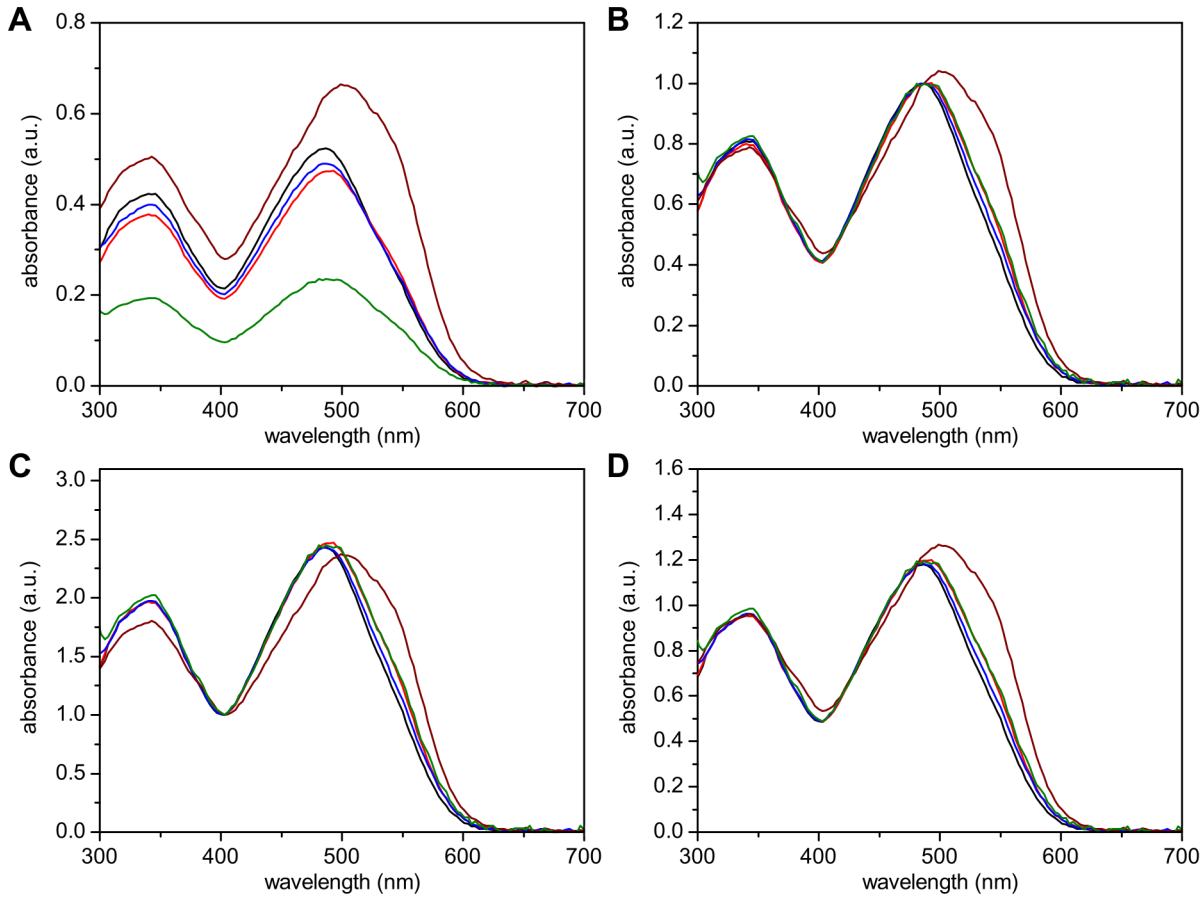

Supplementary Figure 1: Congo Red normalisation with TVQFHMH-DNA sample on day 0. The Congo Red absorbance spectra (**A**) were normalised either to the maximum at 487 nm (**B**), a potential isosbestic point at 403 nm (**C**), or the average of 450 and 485 nm (**D**). The appearance of a shoulder at about 540 nm is indicative of amyloid formation, which in this case is directly eminent for TVQFHMH alone (brown). The insulin amyloid positive control (red), DNA alone (blue), and TVQFHMH-DNA ANA complex (green) are much weaker.

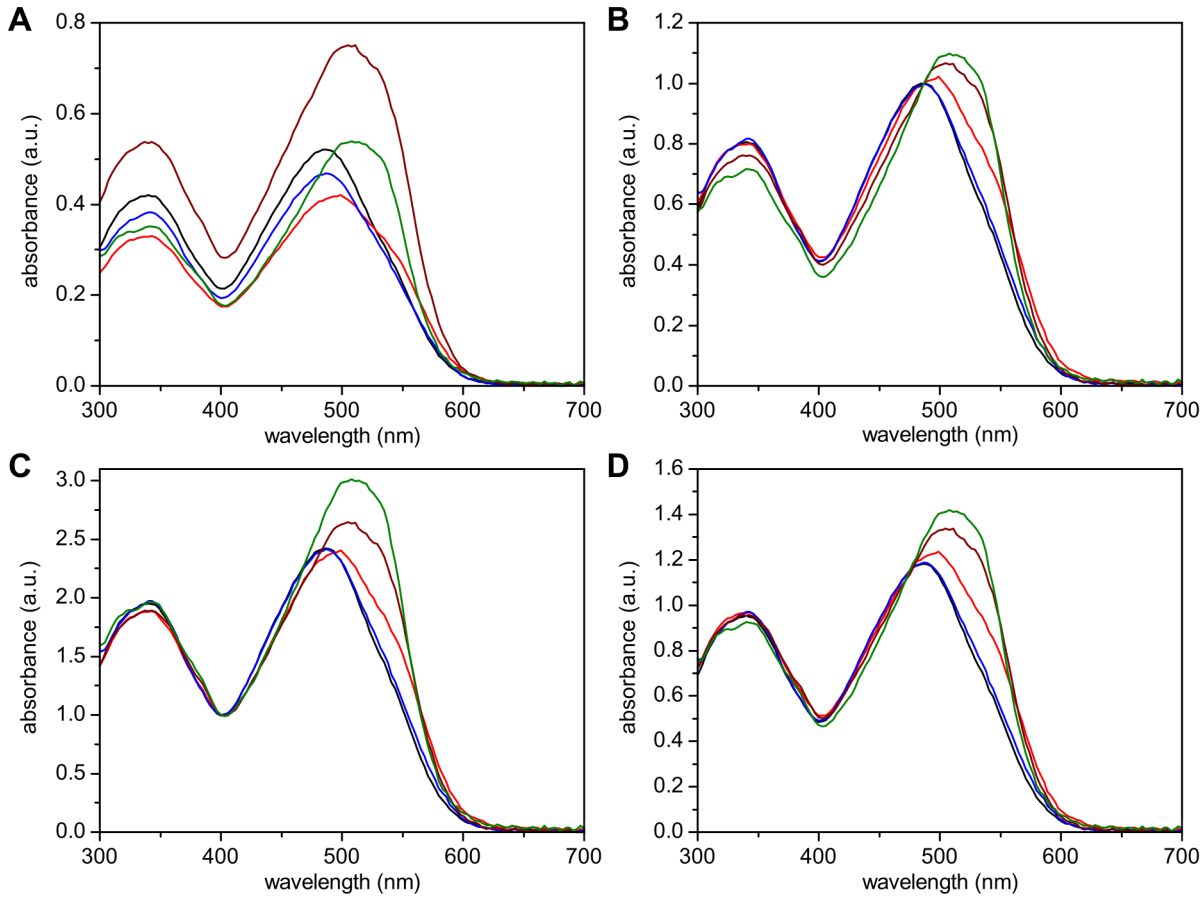

Supplementary Figure 2: Congo Red normalisation with TVQFHMH-DNA sample on day 2. The Congo Red absorbance spectra (**A**) were normalised either to the maximum at 487 nm (**B**), a potential isosbestic point at 403 nm (**C**), or the average of 450 and 485 nm (**D**). The appearance of a shoulder at about 540 nm is indicative of amyloid formation, which after 2 days was given for both TVQFHMH alone (brown) and TVQFHMH-DNA ANA complex (green). The insulin amyloid control (black) was clearly positive in this assay, and DNA alone (blue) negative.

The difficulty of using Congo Red became apparent by the weak insulin amyloid positive control on day 0, most likely because no Congo Red-binding aggregate was present in the light path of the NanoDrop. The TVQFHMH-DNA complex absorbance might have

been quite low because the dye had problems penetrating the gel to bind to the amyloid fibres. The same effect could have led to the low signal of the insulin amyloid positive control, but interestingly this was not an issue during Thioflavin T assays. So the assay was negative for TVQFHMH-ANA complexes after only 30 minutes incubation with Congo Red, but was positive after 2 days It was unclear if this was due to the dye finally penetrating the gel and binding the amyloid material or if the dye induced the amyloid formation during this time period.

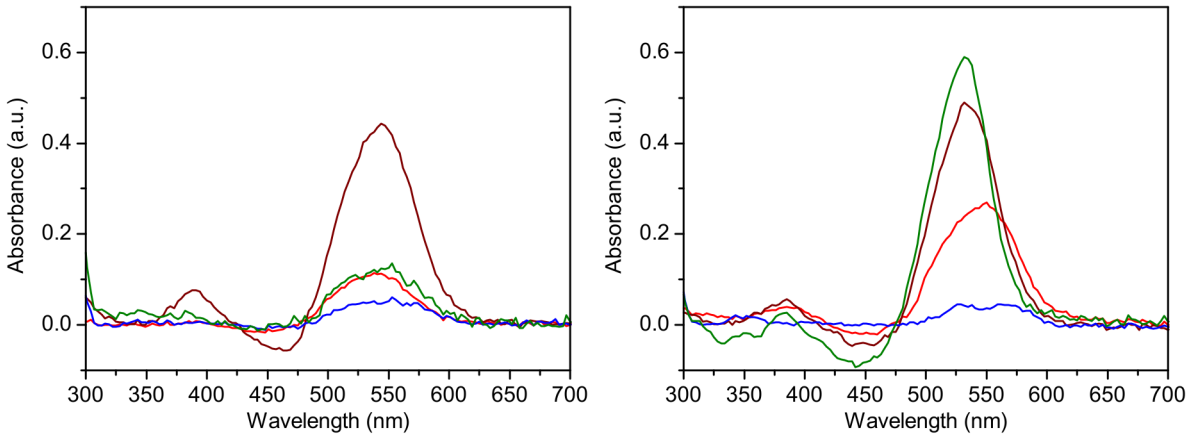

Supplementary Figure 3: Congo Red shoulder peaks after normalisation to 450 and 485 nm background subtraction. Congo Red absorbance spectra after 0 (left) and 2 days (right) in the presence of 50 µM insulin amyloid (red), 1 mM ST DNA (blue), 1 mM TVQFHMH (brown), or 1 mM TVQFHMH-DNA ANA complex (green) were normalised to the absorbance at 450 and 485 nm before the Congo Red background was subtracted. A peak at about 540 nm is indicative of amyloid formation. The peaks of DNA and peptide alone remain largely stable, while the ones for insulin amyloid and TVQFHMH-DNA ANA complex increase.

The shifts in the absorbance shoulders were also notable and visible after subtraction of the original Congo Red (see Supplementary Figure 3). Insulin amyloid appeared to develop a red-shift in the absorbance shoulder over time. Samples containing TVQFHMH were even further blue-shifted to 532 nm. This could pose a potential problem when comparing the absorbances at 544 nm of different samples, but should not be an issue for the same peptide and with the 10 nm band pass filter of the BMG FLUOStar.

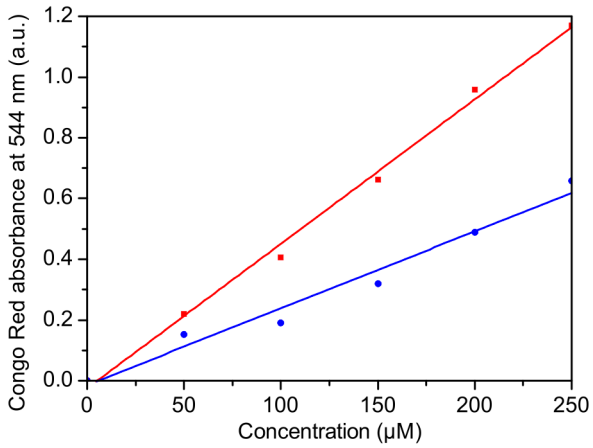

Supplementary Figure 4. Comparison of Congo Red absorbance normalisation with insulin amyloid titration. Spectra of 0 to 250 250 µM insulin amyloid with 500 µM Congo Red were recorded and normalised to 403 nm (red; n = 6, r^2 = 0.995) or blue (blue; n = 6, r^2 = 0.966). Note that the exceeding of 1 a.u. is due to the normalisation and did not occur during recording of the spectra.

A comparison of the Congo Red normalisation methods using a titration of 0 to 250 µM insulin amyloid showed little difference between them (see Supplementary Figure 4). While the absolute values differed, the normalisation to 403 nm was only slightly (r^2 = 0.995) better than normalisation to 450 and 485 nm (r^2 = 0.966). Since the plate reader could not be equipped with a matching filter for 403 nm due to capacity issues, the normalisation to 450 and 485 nm was used, because it seemed that there would be little deviation from the optimum.

9.2. STATISTICAL PARAMETERS

Supplementary Table 1: Statistical Parameters

sample 1	n_1	sample 2	n_2	*t*	degrees of freedom	*p*		Origin
$(HL)_3$	4	$(HL)_3$-ST DNA	4	-15.1534	3.489	0.0002622	***	Figure 6-2 on page 90
$(HL)_3$	4	buffer	4	0.6405	5.044	0.5498	n.s.	
$(HL)_3$-ST DNA	4	ST DNA	4	4.9009	3.526	0.01103	*	
$(KL)_3$	4	$(KL)_3$-ST DNA	4	30.5519	4.132	$5.031 \cdot 10^{-6}$	***	Figure 6-3 on page 93
$(KL)_3$	4	buffer	4	1.0393	5.999	0.3387	n.s.	
$(KL)_3$-ST DNA	4	ST DNA	4	8.4217	5.142	0.0003372	***	
$(KL)_5$	4	buffer	4	2.9717	3	0.05899	n.s.	Figure 6-7 on page 100
$(KL)_5$-ST DNA	4	ST DNA	4	-13.272	5.703	$1.668 \cdot 10^{-5}$	***	
$(KL)_5$-ST DNA	4	$(KL)_5$	4	-9.113	5.33	0.0001895	***	
$(KL)_5$-oligo E	3	$(KL)_5$- ST DNA	4	-0.8168	2.63	0.4815	n.s.	
$(KL)_5$-oligo E	3	oligo E	4	-6.6414	2.157	0.01801	*	
$(KL)_5$-oligo E	3	$(KL)_5$	4	-4.7361	3.288	0.01447	*	
$(HL)_3$-ST DNA pH 5.5	4	ST DNA pH 5.5	4	13.7878	4.384	$8.91 \cdot 10^{-5}$	***	Figure 6-4 on page 94
$(HL)_3$-ST DNA pH 6.0	4	ST DNA pH 6.5	4	17.3298	4.927	$1.32 \cdot 10^{-5}$	***	
$(HL)_3$-ST DNA pH 6.5	4	ST DNA pH 6.5	4	3.5654	5.784	0.1261	*	
$(HL)_3$-ST DNA pH 8.0	4	ST DNA pH 8.0	4	2.494	5.186	0.05316	n.s.	
Myristoleic acid	3	Myristoleic acid – $(EL)_3$	3	3.4233	2.439	0.05693	n.s.	Figure 6-22 on page 143
Myristoleic acid	3	Myristoleic acid – $(HL)_3$	3	9.753	2.03	0.00985	*	
Myristoleic acid	3	Myristoleic acid – $(KL)_3$	3	76.8414	2.039	0.0001467	***	
Palmitoleic acid	3	Palmitoleic acid – $(EL)_3$	3	1.0239	3.974	0.3641	n.s.	
Palmitoleic acid	3	Palmitoleic acid – $(HL)_3$	3	4.1485	3.152	0.02311	*	
Palmitoleic acid	3	Palmitoleic acid – $(KL)_3$	3	7.7302	2.008	0.01614	*	
Oleic acid	3	Oleic acid – $(EL)_3$	3	-0.565	2.469	0.9592	n.s.	
Oleic acid	3	Oleic acid – $(HL)_3$	3	27.6066	2.579	0.0002936	***	
Oleic acid	3	Oleic acid – $(KL)_3$	3	5.3438	2	0.03328	*	
$(EL)_3$	3	buffer	3	-3.6022	2.367	0.05354	n.s.	
$(HL)_3$	3	buffer	3	-1.7214	2.439	0.2043	n.s.	
$(KL)_3$	3	buffer	3	1.1305	2.659	0.3498	n.s.	

An unpaired Student's t-test was employed to determine if the differences between samples shown in Figure 6-2, Figure 6-3, Figure 6-7, and Figure 6-4 were significant using R [215]. The

number of replicates of both samples n_1 and n_2, the *t*-value, degrees of freedom and the *p*-value are listed here. * = $p < 0.05$; ** = $p < 0.01$; *** = $p < 0.001$; n.s. = not significant.

9.3. Results of Dye-Binding Assays

This table summarises the results of the dye-binding tests that were carried out to test for amyloid formation in various peptide-nucleic acid combinations. The majority of the samples did not show positive results, i.e. no increased Thioflavin T fluorescence or Congo Red absorbance at 544 nm in comparison to peptide alone or nucleic acid alone.

Supplementary Table 2: Qualitative Results of dye-binding assays.

Peptide	Thioflavin T	Congo Red
$(HL)_5$-ST DNA	No signal at 50 µM, 500 µM, or 5 mM each	No signal at 50 µM, 500 µM, and 5 mM
$(KL)_3$-ST DNA	Significant binding at 50 µM	No signal at 50 µM or 5 mM each
$(HL)_3$-ST DNA	Significant binding at 50 µM	No signal at 50 µM or 5 mM each
$(KL)_5$-ST DNA	No signal at 50 µM or 5 mM each	Significant binding at 0.2 mM $(KL)_5$ with 1 mM ST DNA
TVQFHMH-ST DNA	No signal at 50 µM, 1 mM or 5 mM each	No signal at 50 µM, 1 mM or 5 mM each
TVQFHMH alone	No signal at 1 mM or 5 mM each	No signal at 1 mM or 5 mM each
STVIIE	No signal at 0.8 mM	n.d.

Supplementary Table 2: The Thioflavin T or Congo Red assays were carried out as described in the methods section. All buffers contained 150 mM NaCl and 50 µM Congo Red or Thioflavin T, and were usually based on 10 mM MES or 10 mM HEPES. $(HL)_5$-ST DNA, $(KL)_3$-ST DNA, $(HL)_3$-ST DNA, $(KL)_5$-ST DNA and TVQFHMH-ST DNA were tested at pH 5.0, 5.5 6.0, 6.5, 7.0, and 8.0, while TVQFHMH alone was examined at pH 6.5. The Thioflavin T test on STVIIE was run at pH 2.6 in 20 mM glycine.

9.4. INSTRUMENT RESPONSE FUNCTION OF THE FRET SETUP

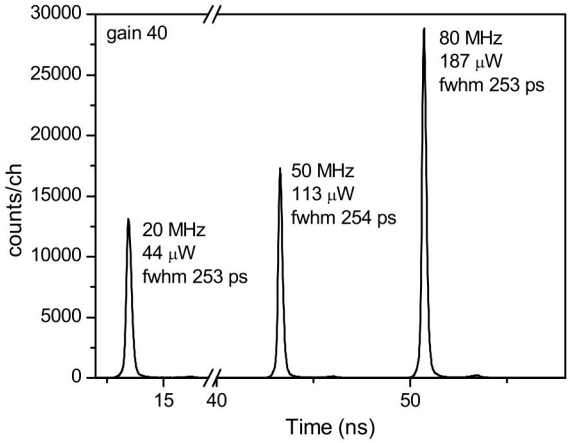

Supplementary Figure 5: Instrument Response Function. A 50 ps laser pulse was reflected by a glass coverslip in the sample holder and recorded by the photomultipliers. Identical results were obtained with a silver mirror to ensure it was truly the response coming from the laser and the detector, not the sample (data not shown). The response curves closely followed a Gaussian distribution and showed the reaction of the instrument to an instantaneous event, which in this case was simulated by the 50 ps laser pulse. The full width at half maximum (fwhm) determined the time resolution of the instrument; at 20 MHz the time resolution was 253 ps.

This data was kindly provided by Paola Borri (Cardiff University), who designed, ran and analysed this experiment.

9.5. Additional STVIIE + Oligo E Time Courses

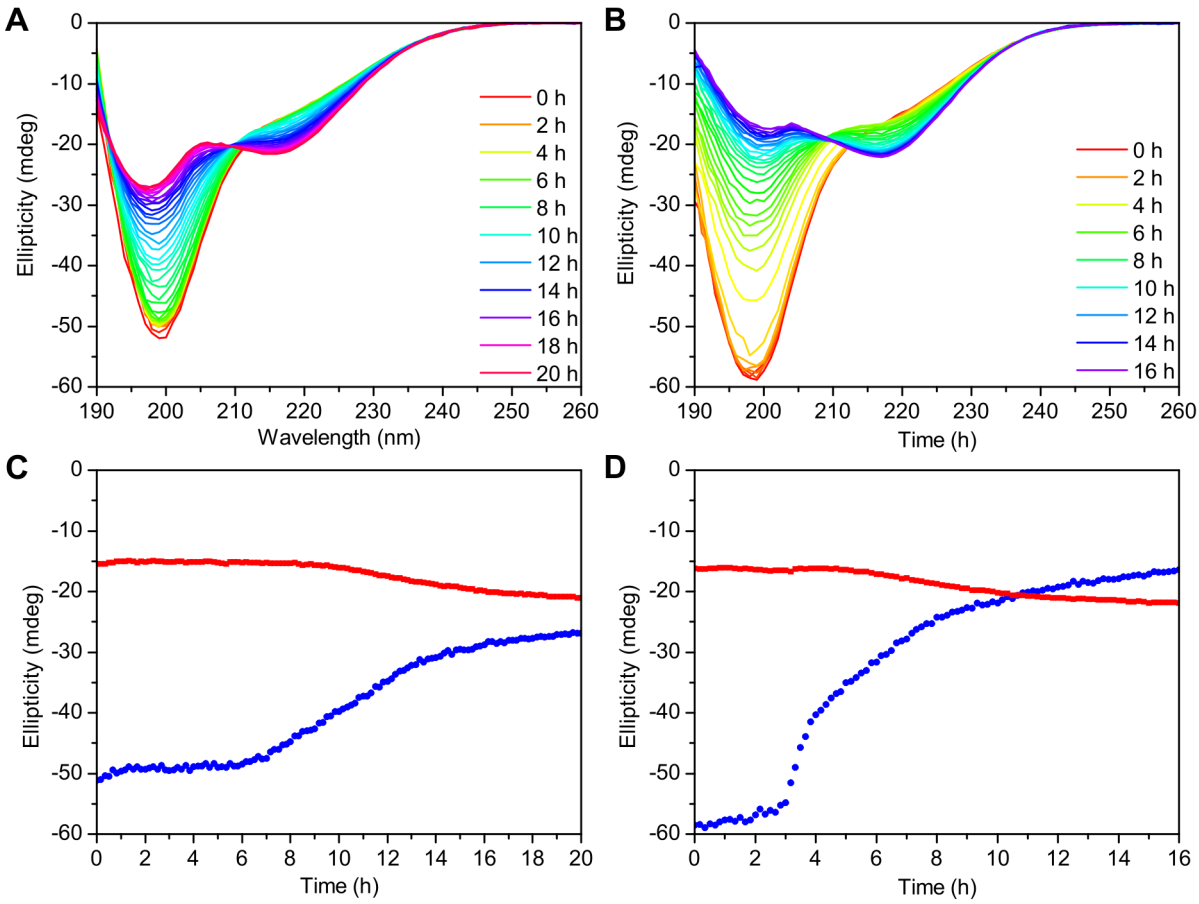

Supplementary Figure 6. Circular dichroism time courses of STVIIE + oligo E without direct comparison to STVIIE alone. 0.8 mM STVIIE were incubated with 8 µM oligo E at pH 2.6 at room temperature, taking a spectrum every 10 minutes. The spectra indicated a change from pure random coil (minimum at 208 nm) to a mixed conformation containing high levels of β-sheet (minimum at 218 nm) over the time course of several hours. Note the large difference in lag time length between samples that were prepared in the same way, but not from the same stock solutions and not closely matched (see also Figure 6-26, Figure 6-28, and Figure 6-29).

9.6. Overlay Comparisons of Fibre Diffraction Patterns

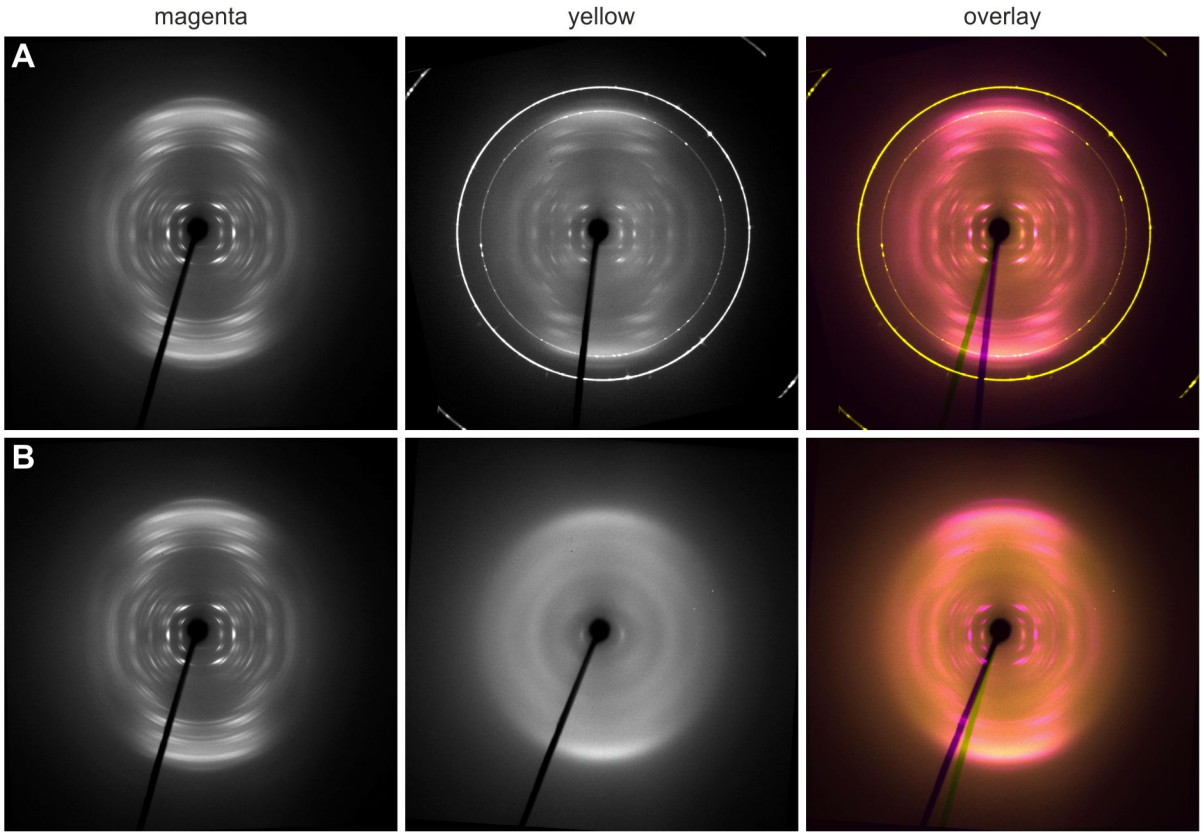

Supplementary Figure 7: Comparison of DNA diffraction patterns. (**A**) A comparison of DNA with (right) or without (left) 150 mM NaCl shows that the main DNA diffraction pattern was not influenced by the presence of the salt, but it might be possible that the strong salt ring suppressed it. (**B**) Denatured DNA (right) gained its weak features from some of the strongest reflections of the dsDNA diffraction pattern (left). The good agreement at the 3.4 Å reflections suggests that the base stacking is retained during and after the denaturation process and primarily the base pairing was lost.

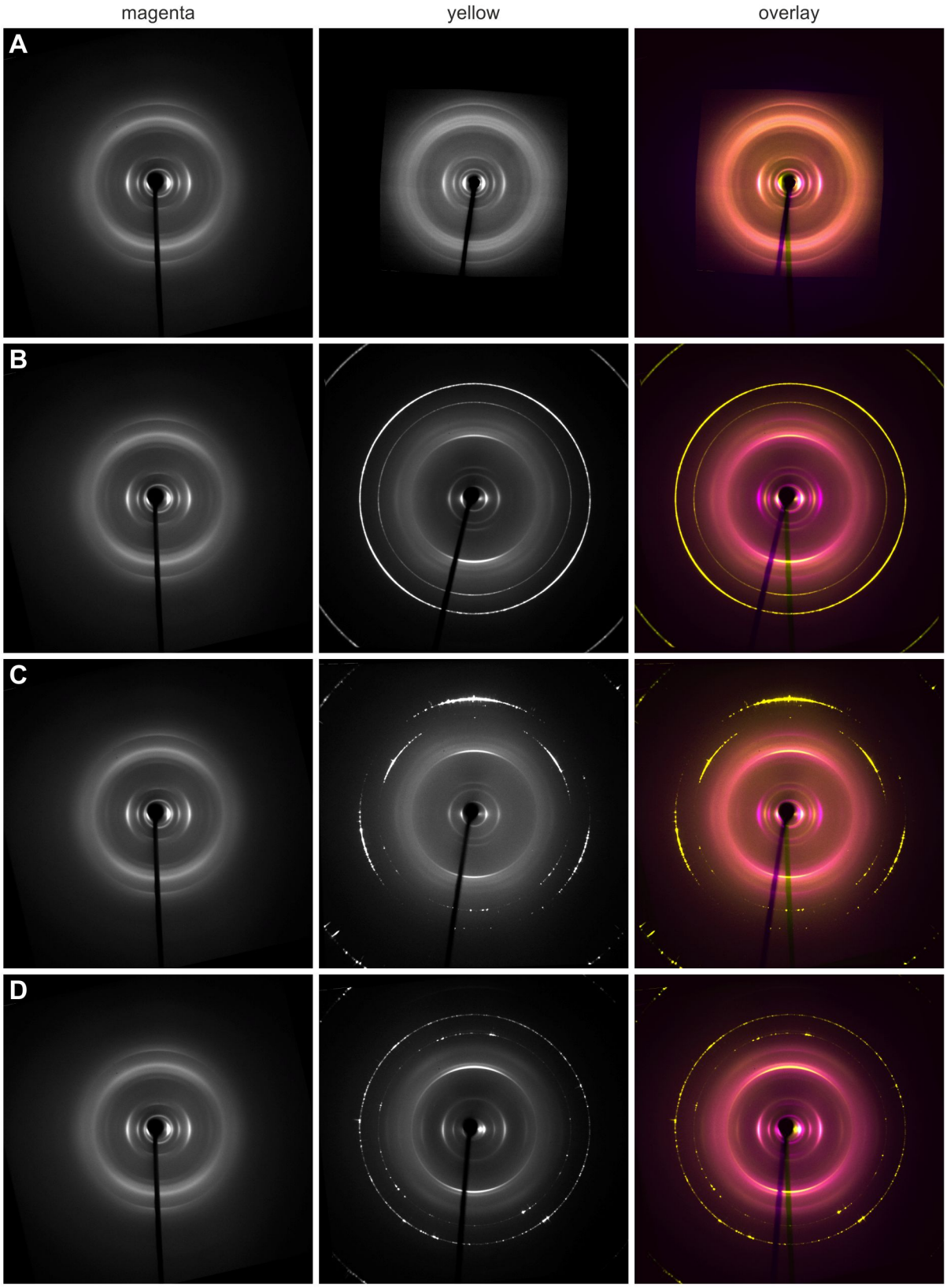

Supplementary Figure 8: Comparison of $(KL)_3$ with $(HL)_3$ and $(KL)_5$ diffraction patterns.

Although there are big differences at the 4.8 A meridional reflection the two diffraction

patterns of $(KL)_3$ in complex with DNA (**A**) are virtually identical. The comparison of $(KL)_3$ with $(HL)_3$ (**B** and **C**) reveals that the packing in fibre direction is very similar, but there are large differences in the lateral packing of the fibres. This was due to the different length of the varying side chains or different interactions with DNA that lead to different fibre packing. The comparison of $(KL)_3$ with $(KL)_5$ (**D**) shows no big differences, suggesting that both peptides have very similar lateral packing.

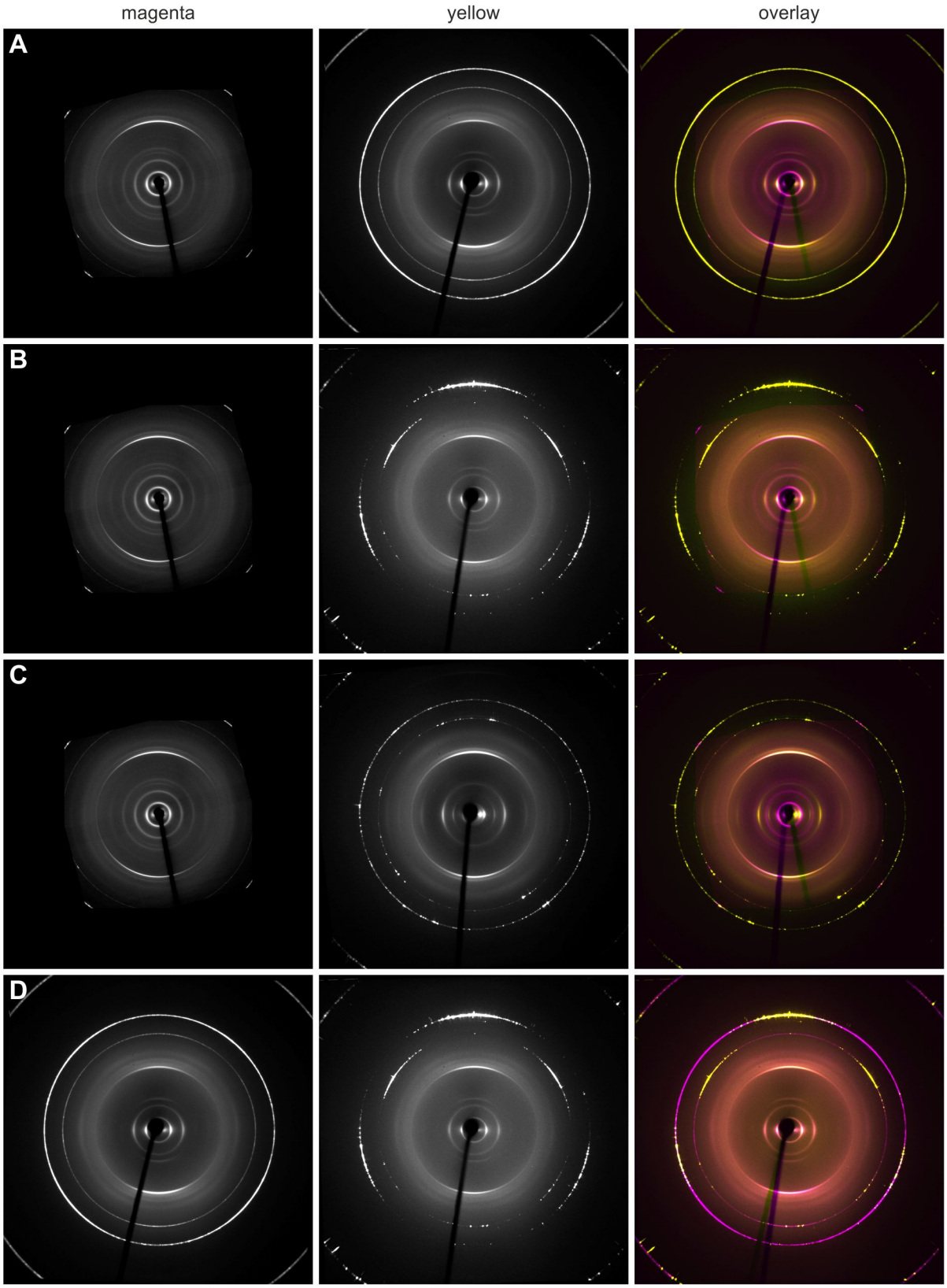

Supplementary Figure 9: Comparison of $(HL)_5$, $(HL)_3$ and $(KL)_5$ diffraction patterns. As expected, there are not big differences in meridional direction, showing that the peptide

backbones are similarly aligned in the fibre for all peptides. The comparison of $(HL)_5$ with $(HL)_3$ (**A** and **B**) indicates that there are no major differences in the lateral fibre packing, although there are more reflections visible in the $(HL)_5$ pattern. The fibres of $(KL)_5$-DNA complexes are wider apart from each other than (KL)5-RNA complexes (**C**), suggesting either some influence of the nucleic acid (poly(A) RNA vs. salmon testes DNA) or the different length of the side chains gave rise to different fibre distances. The two patterns of $(HL)_3$ in 150 mM and 50 mM NaCl buffers (**D**) reveal no differences in the peptide reflections, showing that the amyloid core structure is not influenced by the NaCl concentrations chosen here during formation.

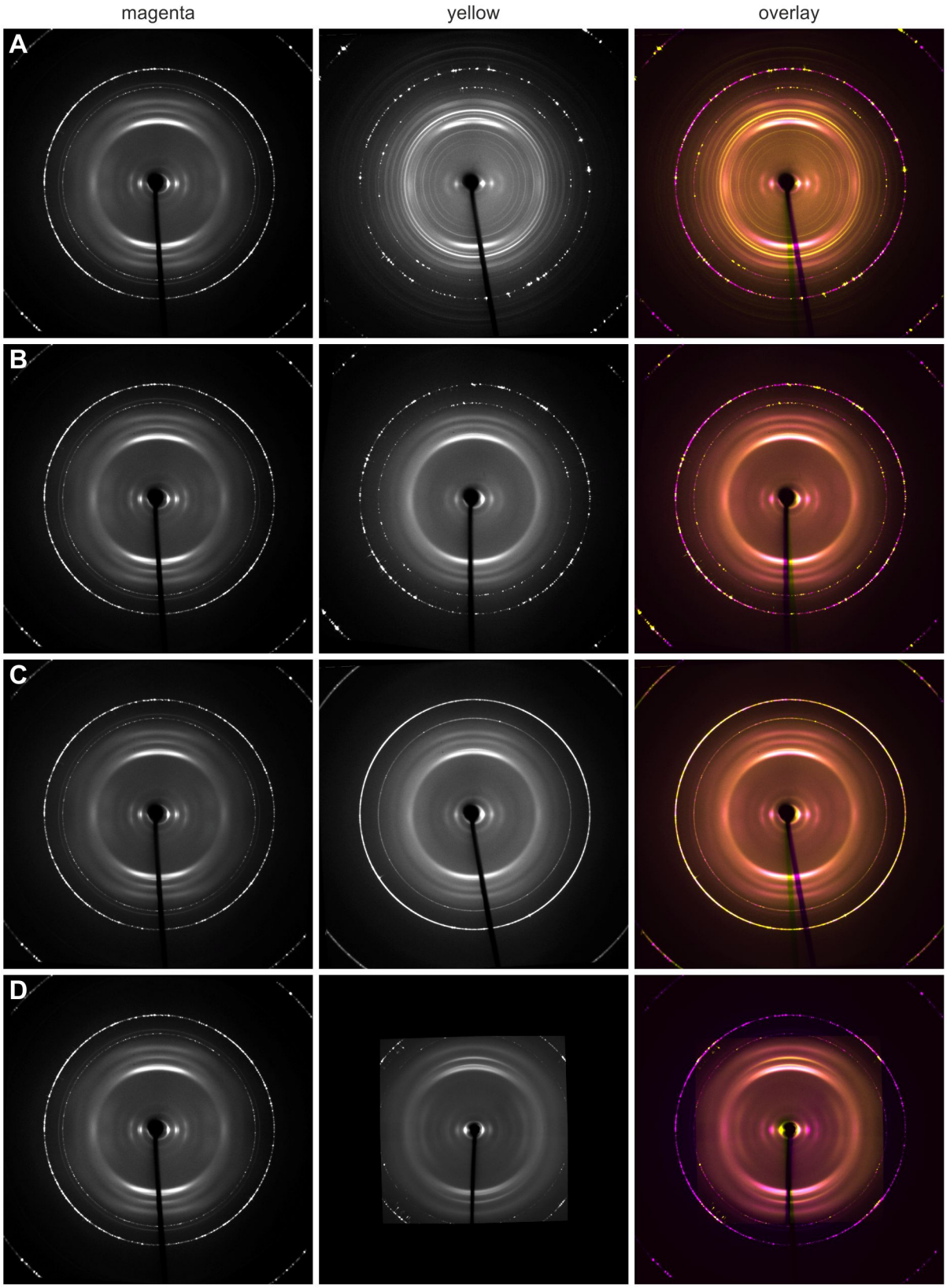

Supplementary Figure 10: Comparison of TVQFHMH diffraction patterns. The comparison of the various TVQFHMH diffraction patterns reveals that the TVQFHMH amyloid structure is

largely independent of pH (**B** and **C**), nucleic acid (**D**) or microstructure of the stalk used for fibre diffraction (**A**; powder diffraction pattern due to enclosed microcrystals).

9.7. FATTY ACID SPECTRA

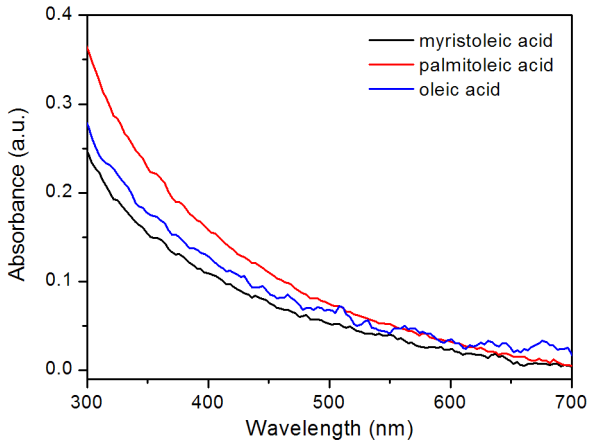

Supplementary Figure 11: Fatty acid liposome spectra. 10 mM myristoleic acid (red), palmitoleic acid (blue), or oleic acid (green) or 1 mM $(KL)_3$ were incubated in 200 mM bicine pH 8.5 for 1 hour before spectra were taken on a NanoDrop ND-1000 spectrophotometer. Buffer background was subtracted. Please note that the path length differed from the plate reader setup used for Figure 6-19.

9.8. TVQFHMH CD SPECTRA

The CD spectra of TVQFHMH did not agree with the published standard CD spectra and were not reproducible. Occasionally different spectra could be recorded for TVQFHMH that was incubated for 1 hour with 1:100 molar ratio oligo E compared to peptide alone (see Supplementary Figure 12 below), but the spectra could not be interpreted because of reproducibility issues and very high HT values. This made them unusable for time course experiments as shown in chapter 6.1.9.

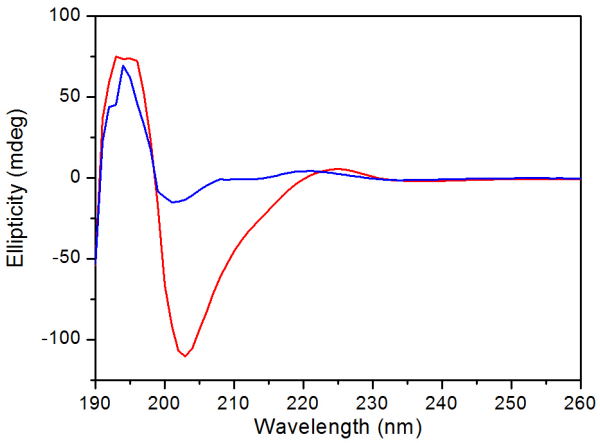

Supplementary Figure 12: TVQFHMH CD spectra. 1 mM TVQFHMH was incubated with (blue) and without (red) 0.01 mM oligo E for 1 hour in 10 mM MES pH 6.5 with 150 mM NaCl before CD spectra from 190 to 260 nm were recorded. A buffer spectrum was subtracted. Note that the HT values exceeded 800 V below 206 nm so that the ellipticity values recorded there were not reliable.

9.9. HYPOTHESIS: THE AMYLOID-NUCLEIC ACID (ANA) WORLD AS TRANSITION FROM THE RNA WORLD

The mutually beneficial interactions of amyloid and nucleic acids could provide an explanation for a puzzling problem in the current models of the development of life. So far the most convincing theory is the 'RNA-world', which is solely based on the catalytic activity of 3-dimensionally folded RNA molecules that are both enzymatic catalysts and genomic material, carrying out all the functions necessary for reproduction and survival [300]. A major issue with this theory is that it is devoid of interactions between nucleic acids and proteins. Such interactions are crucial in modern life in the regulation of essential cellular function, for example protein and nucleic acid synthesis [201]. The existing models do not provide a convincing hypothesis on how the nucleic acids of the RNA world might profit from contacts with peptides or proteins. In most cases, the binding of single amino acids is envisaged to improve the catalytic activity of RNAzymes [301-303]. On the other hand, the related hypothesis of an 'amyloid-world' that was based on the high stability of the amyloid regarding hot conditions state does not provide how the tight interactions with nucleic acids arose [146,148]. Its model for inheritance was based on the propagation of the amyloid fold to new incoming peptide as proposed for prions, but it was lacking interactions with nucleic acids.

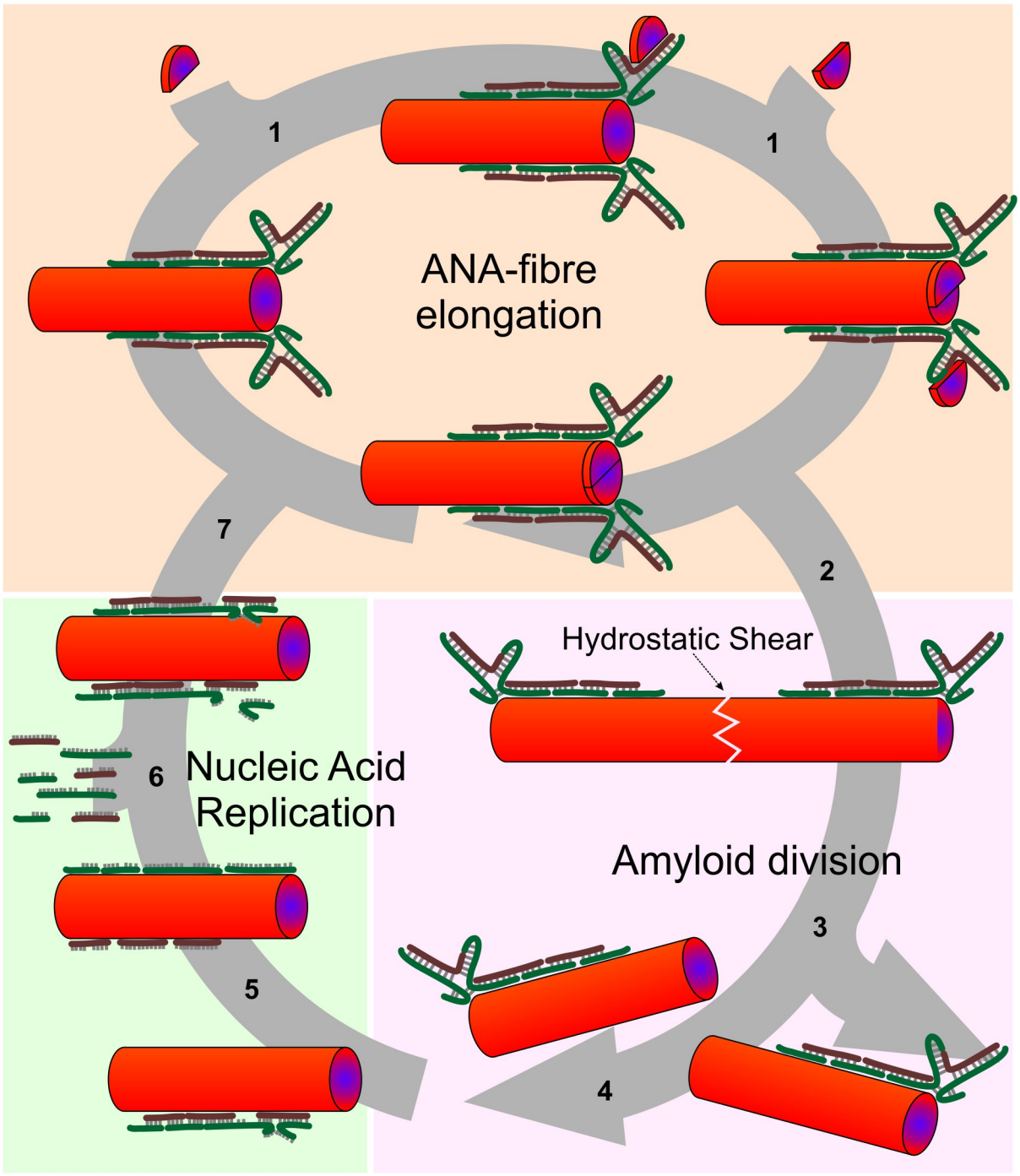

Supplementary Figure 13: Interlocking cycles of amyloid growth and nucleic acid replication. (**1**) Nucleic acids recruit short basic amyloidogenic peptides to the growing end of the amyloid fibril primarily through charge interactions with the phosphate backbone. (**2**) With increasing length, the amyloid fibrils become vulnerable to hydrostatic forces, (**3**) eventually causing them to shear. This generates daughter fibrils that inherit associated nucleic acids, which were replicated on the fibre (see **5** and **6**) and are therefore related. (**4**)

The associated nucleic acids denature on the amyloid fibre, and (**5**) are separated into their composite oligonucleotides. (**6**) Complementary oligonucleotides hybridise to the ones associated with the fibre, which (**7**) refold to their 3-dimensional structure. Adapted from Braun *et al*. (2011) [152].

Here we propose a model in which peptides, not single amino acids, and nucleic acids interacted right from the beginning of biological life (see Supplementary Figure 13) [151-153]. Similar to the 'RNA world' hypothesis, nucleic acids are the main carrier of genetic information and catalytic activity. Positively charged amyloid fibrils provide a growing compartment that restricts the enzymatic activity of RNAzymes towards co-localised and therefore related nucleic acids [304]. Attachment of nucleic acids to surfaces such as clay particles has been suggested before, primarily in combination with their prebiotic synthesis [210,304-307]. The major difference of amyloid fibres to clays like montmorillonite as a compartment lies in the ability of amyloid fibres to grow. The negatively-charged phosphate backbone of nucleic acids interacts with positively-charged peptides to increase the amyloid growth rate. The amyloid enhances hybridisation of attached nucleic acids, which are able to move freely along the fibre. This allows formation of (partial) double strands by overlapping short oligonucleotides. The longer nucleic acid strands provide a larger negative charge density that increases the concentration of basic peptides in the vicinity of the fibre, accelerating the rate of fibre elongation [151]. Attached nucleic acids would be protected from the environment, potentially inhibiting hydrolysis of the phosphate backbone [18]. The growing fibre then provides more attachment sites for oligonucleotides, but it also becomes susceptible to hydrostatic shearing. This breakage of ANA fibrils has been repeatedly encountered

during pipetting work for the EM sample preparation and was visible in the EM images. Hydrostatic shear creates daughter fibrils with attached genetically related nucleic acids which represent the individuals that are subject to selection. ANA complexes making best use of the mutually beneficial interactions of its components would grow faster, replicate both amyloid fibre and nucleic acid more efficiently, and divide more often.

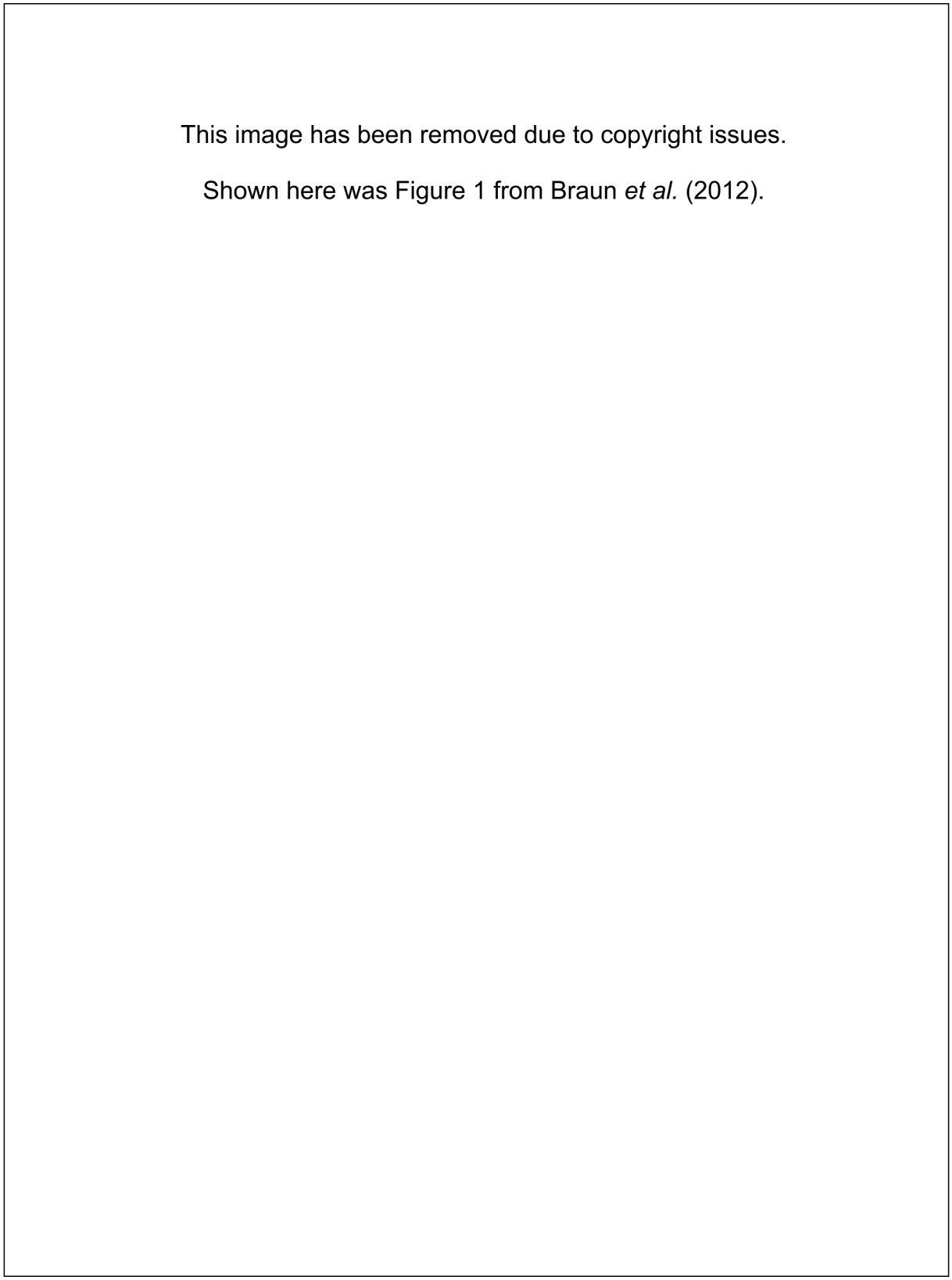

Supplementary Figure 14: Evolutionary routes from a prebiotic ANA-world. (**A**) *ANA world life cycle*. Nucleic acids recruit short basic amyloidogenic peptides to the growing end of the

amyloid fibril primarily through charge interaction with the phosphate backbone. With increasing length, the amyloid fibrils become vulnerable to hydrostatic forces, eventually causing them to shear. This generates daughter fibrils that inherit associated and the therefore related nucleic acids. The amyloid fibril might promote nucleic acid replication by enhancing hybridisation. Inter- and intra-molecular hybridisation allows nucleic acids to adopt secondary structures, some of which may enhance the incorporation of amyloidogenic peptides. This might allow the formation of nucleic acid structures that could promote amyloid elongation or nucleic acid replication, which could evolve ribosome-like or polymerase/ligase-like activities respectively. (**B**) *Elongase Evolution*. Only peptides of the sufficient length with an alternating pattern of hydrophobic (triangles) and hydrophilic (circles) residues are incorporated into the amyloid fibre (red). If peptides of sufficient length (e.g., 6 residues) are unavailable, RNAzymes associated with the fibril might generate suitable peptides by ligating or extending shorter ones. RNA-specific recognition of suitable amino acid sequences could evolve into the ribosome (purple). (**C**) *Replicase Evolution*. Initially, the amyloid promotes hybridisation and double-strand formation from short overlapping oligonucleotides. The resulting longer strands provide a higher charge density and therefore associate more strongly with the fibre to enhance its elongation. Evolution of nucleic acid ligase or polymerase activities enhances the quantity and length of associated nucleic acids under conditions of limiting polynucleotides. This process advances through selection to generate protein fibre-associated nucleic acid polymerases. (**D**) *Separation of Function*. Initially, both elongase and replicase RNAzymes are required to be on a single fibre. With the incorporation of ANA fibres within membrane vesicles, the elongase and replicase functions could evolve on different fibres since the importance of the fibre for compartment formation would be removed. Adapted from Braun *et al*. (2012) [153].

Natural selection would favour the fastest growing ANA complexes which would be able to expand and spread in a population of ANA complexes competing for limited resources like abiotically synthesized oligonucleotides and peptides, putting selective pressure on both nucleic acid replication and amyloid fibre elongation. The overlapping oligonucleotides could, additionally supported by the amyloid fibre, develop an RNAzyme with ligase activity to create longer nucleic acid strands. A system employing an RNAzyme ligase chain reaction has already been developed, suggesting that a similar reaction could take place in a prebiotic context [308,309]. This could then evolve further into a RNA-based polymerase, in a pathway similar to the one taken in the *in vitro* evolution of such a ribozyme (see Supplementary Figure 14) [150,152,153,300,310]. The increased efficiency in the generation of long nucleic acid strands provides the basis for the development of longer and more complex RNAzymes that could potentially provide additional functions.

Since shearing of long amyloid fibres is the proposed division mechanism an increased growth rate would result in production of more 'offspring' ANA complexes and be selected for. Amyloid elongation could be improved by specific selection of peptides with sequences of alternating polar and apolar residues by aptamer-like nucleic acid molecules, thereby concentrating more suitable peptides around the ANA complex and maybe even promoting the conformational switch to β-sheet for incorporation into the fibre [288,311-313]. The initial recognition of suitable peptides could be improved by catalysis of peptide ligation [314,315]and/ or expansion [316] to yield peptides of suitable sequence and length. This initial recognition of suitable peptides would eventually be driven towards development of template-dependent polypeptide synthesis by a ribosomal activity (see Supplementary Figure 11).

Longer peptides allow the formation of 3-dimensionally folded functional domains that due to their higher variability compared to RNA would take over the majority of enzymatic function, while still covalently linked to the amyloid fibre via amyloidogenic sequence elements [27,183]. With encapsulation in lipid membranes the compartment function of the amyloid fibre becomes secondary. The aggregation potential would actually become harmful for the protocells so that finally amyloid would be counter-selected, leading to the suppression of this conformation as it is found today [136].

Encapsulation into a lipid membrane is not strictly necessary in the beginning, but could provide a mechanism to prevent ANA complexes to clump together. Fatty acid membranes are the most likely candidates in a prebiotic setting to form membranes [210,317]. Their growth and division would be supported by the accumulation of polymers in their lumen, driving osmotic swelling [243,277,317]. Additionally, the growing ANA fibres could push the membranes outwards, forcing the membranes to grow, which might help then in the competition with other protocells [317]. Also, encapsulation of ANA complexes in membranes would reduce the selective pressure to maintain all enzymatic functions, be it RNAzymes or globular protein domains linked to the amyloid fibre, on the same fibre (see Supplementary Figure 13).

This hypothesis of prebiotic evolution provides compartmentalisation, replication of nucleic acids and amyloid fibre, selection and inheritance, essential prerequisites for Darwinian evolution. It could provide the answer to the breakout problem by including the nucleic acid and polypeptide interaction right from the beginning of life.